Collisions in a cloud of metastable helium near quantum degeneracy

Signe Seidelin

N° d'ordre : 7676

INSTITUT D'OPTIQUE THÉORIQUE ET APPLIQUÉE
LABORATOIRE CHARLES FABRY

UNIVERSITÉ PARIS XI
U.F.R. SCIENTIFIQUE D'ORSAY

THÈSE

présentée pour obtenir

le GRADE de DOCTEUR EN SCIENCES

DE L'UNIVERSITÉ PARIS XI ORSAY

par

Signe Louise SEIDELIN

Sujet :

COLLISIONS DANS UN GAZ D'HÉLIUM MÉTASTABLE AU VOISINAGE DE LA DÉGÉNÉRESCENCE QUANTIQUE

Soutenue le 3 novembre 2004 devant la Commission d'examen :

M.	A. ASPECT	Directeur de thèse
M.	J. BAUDON	Rapporteur
M.	G. BIRKL	Rapporteur
M.	M. INGUSCIO	Rapporteur
M.	K. MØLMER	Examinateur
M.	P. PILLET	Président
M.	W. D. PHILLIPS	Membre invité
M.	C. WESTBROOK	Membre invité

Remerciements

Mes travaux de thèse ont étés réalisés au Laboratoire Charles Fabry de l'Institut d'Optique. Je remercie tout d'abord son directeur, Pierre CHAVEL, non seulement de m'y avoir accueilli, mais aussi de l'authentique intérêt qu'il a montré pour mon travail, et de l'attention qu'il porte aux travaux des doctorants en général.

Je suis à la fois très fière et très reconnaissante d'avoir eu l'opportunité de faire une thèse sous la direction d'Alain ASPECT. En effet, ma première passion pour la physique est née en lisant des livres populaires décrivant ses expériences exceptionnelles sur les inégalités de Bell. Je le remercie donc de m'avoir fait découvrir la richesse et la beauté de la physique en premier lieu et, ensuite, de m'avoir acceptée en tant que doctorante dans son équipe avec tout ce que cela implique. En particulier, j'ai énormément bénéficié de ses talents de pédagogue lors de nos réunions de groupe, ainsi que de sa clarté d'esprit lors de la rédaction d'articles.

Jacques BAUDON, Gerhard BIRKL et Massimo INGUSCIO ont eu la gentillesse d'accepter de rapporter cette thèse. Je les remercie de leur intérêt pour mon travail ainsi que de leurs commentaires et corrections sur mon manuscrit. Je remercie également Pierre PILLET d'avoir accepté de présider mon jury de thèse et pour ses commentaires sur le manuscrit. Je tiens aussi à remercier vivement Bill PHILLIPS pour l'agréable surprise qu'il m'a faite en assistant à ma soutenance, d'autant plus qu'il a accepté au dernier moment de faire partie du jury. J'en suis sincèrement honorée.

Je voudrais aussi exprimer ma reconnaissance envers Klaus MØLMER. C'est grâce à lui que j'ai connu le groupe Optique Atomique en premier lieu, et sans son soutient et son aide dans de nombreuses occasions, tout aurait été bien plus difficile pour moi ! Je le remercie également d'avoir accepté de faire partie du jury.

Mon travail de thèse a été guidé par Chris WESTBROOK. En discutant avec Chris, j'ai très vite compris le sens de ce que l'on appelle "intuition" et "recul sur la physique". Aussi, malgré ses grandes responsabilités administratives, j'ai toujours senti que Chris était vraiment passionné par notre travail au laboratoire, et je le remercie de m'avoir communiqué en continu sa motivation pour faire avancer l'expérience.

Denis BOIRON lui aussi a guidé ce travail, et il a joué un rôle primordial pendant ma thèse. Je ne peux pas le remercier suffisament. C'est non seulement au niveau de l'expérience, mais particulièrement lors de l'analyse des données, où il a apporté une aide précieuse, que j'ai pu admirer son sens remarquable de la rigueur et de la perseverance, souvent au cœur de la reussite en physique experimentale. Par dessus tout, je le remercie mille fois de ses lectures et relectures de mon manuscrit, ce qui n'a pas toujours dû être très drôle...en particulier certaines annexes, que je pense que Denis est le seul à avoir lus plusieurs fois !

C'est Olivier SIRJEAN qui m'a initiée à l'expérience hélium, et j'ai eu le plaisir de travailler à ses côtés pendant deux ans. Je lui suis reconnaissante de m'avoir communiqué sa maîtrise de l'expérience ainsi que ses connaissances théoriques, ce qui m'a permis de terminer, avec l'équipe, les expériences que nous avons démarrées ensemble. J'ai commencé ma thèse en même temps que Jose GOMES, et Rodolphe HOPPELER nous a rejoint un an après. Je les remercie tous les deux de notre collaboration, et je tiens à préciser qu'une grande partie des résultats présentés ici sont évidemment aussi les leurs. Je leur souhaite beaucoup de succès pour la suite ! Martijn SCHELLEKENS a démarré sa thèse au moment où nous avons entrepris le changement du détecteur de l'expérience, et Aurélien PERRIN nous a rejoint cette année. Je regrette beaucoup de ne pas avoir pu passer plus de temps avec eux au laboratoire ! Je les remercie d'avoir accepté la grande responsabilité liée à la continuation d'une expérience difficile. Je les remercie également de leurs conseils sur l'utilisation délicate de LaTeX lors de la préparation de mes transparents pour ma soutenance !

J'ai adoré ce temps au cœur du groupe Optique Atomique. Chacun de ses membres, sans exception, m'ont apporté quelque chose et je les remercie tous d'avoir rendu ce temps passionnant. Même s'il est impossible de remercier chaque membre du groupe individuellement, Jocelyne RETTER mérite un remerciement particulier pour ses corrections fabuleuses sur mon manuscrit. Au début, je lui avais demandé son aide d'un point de vue linguistique, mais ses corrections portaient bien au-delà : Jocelyne m'a impressionnée par sa capacité à comprendre ce qui est incompréhensible et à le rendre lisible en utilisant nettement moins de mots ! J'ai rédigé ma thèse en parallèle avec Jérôme ESTEVE et Marie FAUQUEMBERGUE. Leur amitié, soutient moral et encouragements ont beaucoup facilité cette période un peu difficile ! Une autre personne du groupe qui a été particulière importante pour moi - peut-être sans s'en rendre compte - est Isabelle BOUCHOULE. Son écoute, ses conseils (physique ou pas) et sa bonne humeur ont éclairé mon esprit et mes journées. Je la remercie aussi de l'excellent "leverpostej" (pâté de foie danois) qu'elle a fait pour mon pot de thèse et qui a impressionné même ma mère, qui est pourtant une vraie experte en ce domaine. Je dois aussi mes

remerciements à Frédéric MORON et André VILLING, non seulement pour leur assistance technique (la réparation de toutes ses boîtes "qui bizarrement ne marchent plus...") mais aussi de leur amitié. C'est aussi grâce à André que j'ai été tenue au courant des affaires essentielles ayant lieu dans mon pays d'origine. Je remercie aussi Philippe BOUYER (et Joanna !) pour les invitations généreuses qui m'ont permis de connaître une cuisine bien plus sophistiquée que celle du Danemark !

J'étais très triste de voir Antoine BROWAEYS quitter notre groupe seulement quelques mois avant que je commence ma thèse, en croyant que je n'allais jamais profiter de ses grands talents de physicien. C'était donc une chance énorme pour moi (et l'expérience hélium en général !) qu'Antoine soit revenu à l'institut. Car même si Antoine est maintenant membre permanent dans le groupe Optique - non Atomique - mais Quantique, il nous a pourtant maintes fois fait bénéficier de son aide précieuse. En particulier, il a pris le temps de nous conseiller sur les modifications que nous avons apporté à un dispositif expérimental qu'il connaît mieux que personne. Mais ce n'est pas tout ; Antoine a lu et corrigé mon manuscrit et il m'a également beaucoup aidé dans la phase précédant la soutenance par ses conseils et participations aux répétitions...!

Je dois aussi mes remerciements à Fabrice GERBIER, un autre "ancien" du groupe. J'ai pu à la fois admirer et profiter de sa lucidité et de ses grandes connaissances dans de nombreuses occasions. J'espère que nos chemins se croiseront de nouveau.

Je remercie sincèrement Lionel JACUBOWIEZ de la confiance qu'il m'a accordée en me laissant assurer des cours à SupOptique. Sur le plan plus personnel (mais tout aussi important !) je le remercie d'avoir été la source d'inspiration de nombreux voyages et j'espère pouvoir continuer à profiter de son expérience sur le plan aventurier. Je suis également très reconnaissante envers Thierry AVIGNON de ses conseils et de son soutient technique lors de mon enseignement, ainsi que de sa gentillesse et de sa bonne humeur.

Enfin, je souhaite remercier mes parents, pour tout ce qu'ils ont fait pour moi et pour leur compréhension et leur grande tolérance envers ma vie parfois mouvementée. Je les remercie de m'avoir laissé une liberté complète tout en me faisant bénéficier de leurs précieux conseils. Surtout, je les remercie de la confiance qu'ils m'ont montrée au long de toutes ces années d'étude...

Sans Yann rien n'aurait été possible. Son soutient et ses conseils ont été exceptionnels. Même pendant ses moments les plus stressants, (à savoir que Yann travaillait souvent sur trois expériences en parallèle !) il est toujours venu à mon secours quand c'était nécessaire. Non seulement ses talents de

physicien m'ont été utiles, mais aussi ses grandes connaissances dans des domaines très divers m'ont profondément impressionnées et m'ont permis d'élargir mon horizon au-delà du sous-sol. Je souhaite de tout mon cœur pouvoir continuer à partager mon temps avec lui, où que nous soyons dans ce monde...

The quest for certainty blocks
the search for meaning.
Uncertainty is the very condition
to impel man to unfold his powers.

La quête de la certitude fait obstacle
à la quête du sens.
L'incertitude est la condition même
qui pousse l'homme à découvrir ses pouvoirs.

Contents

Resumé

Dans ce travail de thèse nous avons étudié les propriétés d'un gaz dilué d'atomes froids, piégés à l'aide d'un potentiel magnétique.

Pour un tel gaz, la physique essentielle des interactions peut être décrite sous la forme des collisions interatomiques. Il existe deux catégories de collisions : les collisions élastiques et les collisions inélastiques. Par définition, les collisions élastiques ne changent pas l'état interne des atomes, tandis que les collisions inélastiques peuvent changer l'état des atomes de sorte qu'ils ne soient plus confinés par le champ magnétique de piégeage.

Nous avons étudié en particulier un gaz d'atomes ultrafroid au voisinage de la condensation de Bose-Einstein. Un condensat de Bose-Einstein d'atomes en phase gazeuse, obtenu dans un piège magnétique, consiste en une accumulation macroscopique d'atomes dans le niveau fondamental du potentiel de piégeage. Cet état de la matière est décrit par une seule fonction d'onde macroscopique et se forme si la température de l'échantillon est suffisamment basse et la densité suffisamment élevée.

Pour un gaz d'atomes à une température au voisinage de celle où se produit la condensation de Bose-Einstein, les collisions élastiques sont entièrement caractérisées par un seul paramètre appelé "la longueur de diffusion dans l'onde s", dénoté en général par la lettre a. La section efficace des collisions élastiques ne dépend que de ce paramètre. De plus, pour un échantillon dilué, l'effet des interactions se décrit entièrement à l'aide de ce paramètre. En effet, le vrai potentiel qui décrit l'interaction entre deux atomes est très complexe, mais ceci peut être remplacé par un pseudo-potentiel très simple, qui ne dépend que de la longueur de diffusion et la densité de l'échantillon.

Nous utilisons l'atome d'hélium dans l'état 2^3S_1, appelé hélium métastable, dans notre expérience. La durée de vie de l'état métastable est très longue (environ 9000 s), et ne limite en rien son utilisation dans nos expériences. Pour un tel échantillon, les collisions inélastiques les plus importantes sont les collisions ionisantes dites Penning. Pour les densités atomique obtenues, les collisions entre deux ou trois atomes d'hélium métastable sont responsables d'un flux d'ions produit par le nuage d'atomes. Ces deux processus d'ionisation sont caractérisés par les constantes de collisions, dénotées par β et L pour les collisions à deux ou trois corps, respectivement.

Pour décrire et interpréter le comportement d'un gaz d'hélium métastable, il est donc utile, voire nécessaire, de connaître non seulement la longueur de diffusion mais également ces constantes de collisions. Le travail de thèse présenté ici consiste en partie à mesurer ces paramètres afin de permettre

une compréhension plus profonde du comportement d'un gaz d'hélium métastable.

Une autre partie du travail présenté a consisté en une étude de la production des ions en tant qu'outil pour observer le nuage atomique. Plus précisément, la production continue d'ions provenant d'un nuage atomique piégé permet de sonder, et ceci d'une manière non-invasive, les propriétés de l'échantillon, en particulier la densité ; le taux de collision à deux ou trois corps en dépendent. Utilisant une galette de micro-cannaux, nous pouvons enregistrer le flux d'ions produit et en extraire l'information sur le nuage. En particulier, nous pouvons déterminer, à partir du flux d'ions, le seuil de la condensation de Bose-Einstein, c'est à dire le moment où commencent à s'accumuler les atomes dans l'état d'énergie le plus bas. Plus concrètement, au seuil de la condensation, le taux d'ions augmente très soudainement en raison d'une augmentation forte de densité. Ceci est illustré dans la figure 1, où la rupture de pente, indiquée par la flèche, correspond au seuil de la condensation. Cette indication du seuil se rélève un outil important nous ayant permis de mesurer la longueur de diffusion. De même, si nous connaissons les constantes de collisions, nous pouvons traduire le signal d'ions en une densité de sorte que nous puissions suivre en temps réel la densité de l'échantillon, ce qui est une motivation forte pour déterminer ces constantes.

Dans la suite nous allons présenter de manière très brève les principaux résultats obtenus lors de ce travail de thèse.

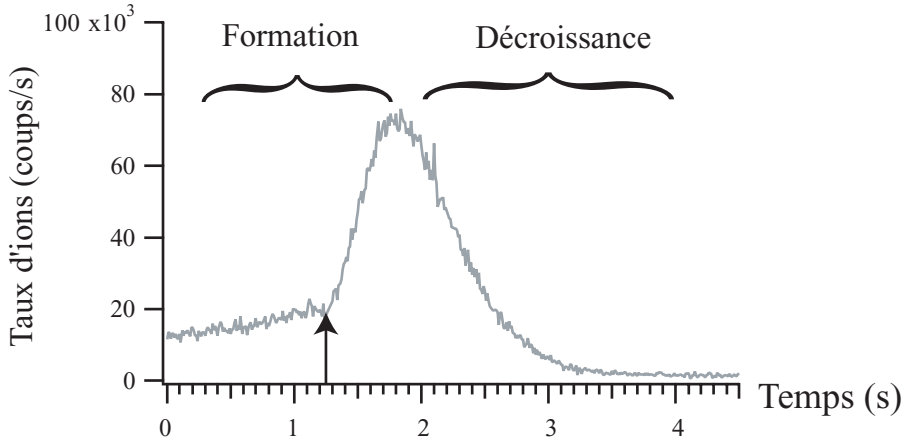

Figure 1: *Taux d'ions pendant la formation (et décroissance) d'un condensat. La flèche indique une rupture de pente dans le signal d'ions, ce qui nous signale le seuil de la condensation.*

Détermination des constantes de collisions

Pour déterminer les constantes de collisions, nous utilisons un condensat de Bose-Einstein. Le taux d'ions Φ normalisé par le nombre d'atomes N en fonction de la densité au centre n_0 s'écrit:

$$\Gamma_{\mathrm{BEC}} = \frac{\Phi}{N} = \frac{1}{\tau_i} + C_1\,\beta\,n_0 + C_2\,L\,n_0^2. \tag{1}$$

Dans cette expression, τ_i est la durée de vie limitée par de collisions ionisantes avec le gaz résiduel, C_1 et C_2 sont des facteurs numériques connus, et β et L sont les constantes de collisions à deux et trois corps.

Pour déterminer β et L, nous avons mesuré le taux d'ions pour un grand nombre de nuages ayant des densités différentes. Pour ce faire, nous enregistrons avec la galette de micro-cannaux le taux d'ions suivi par une technique de Temps-de-Vol (TdV). Le TdV se fait en coupant le potentiel de piégeage et laissant s'étendre le nuage. Ce dernier tombe sous l'effet de la gravité sur la même galette de micro-cannaux, qui est aussi capable de détecter les atomes neutres métastable du fait de leur grande énergie interne. Le TdV nous donne l'énergie du condensat, ce que nous appelons le potentiel chimique, denoté par μ. La densité au centre du nuage est reliée à cette énergie :

$$n_0 = \frac{m}{4\pi\hbar^2} \times \frac{\mu}{a}$$

Grâce à cette relation nous obtenons la densité. Cependant, la valeur de la longueur de diffusion étant encore mal connu, nous deduisons la densité paramétrisée en terme de cette dernière. Les données sont montrées dans la figure 2.

En ajustant les données qui consistent en Γ_{BEC} en fonction de la densité, utilisant l'équation 1, nous déduisons les constantes de collisions β et L. Comme la densité dépend de a, β et L, eux aussi, dépendront de ce paramètre. Nous obtenons donc : $\beta(a)$ et $L(a)$.

Mesure de la longueur de diffusion

Pour attribuer des valeurs absolues aux constantes de collisions, la longueur de diffusion est indispensable. Pour avancer, l'idée de base consiste à chercher "une troisième équation". En effet, nous avons déjà les deux équations $\beta(a)$ et $L(a)$, mais 3 inconnus : β, L et a. La dernière équation manquante peut être obtenue de la manière suivante : pour un nuage exactement au seuil de la condensation, le taux d'ions peut être exprimé non pas en fonction de la densité mais en fonction de la température et des constantes de collisions. Ceci est dû à une relation entre nombre d'atomes et température, uniquement valable au seuil de la condensation :

$$N_{\mathrm{c}} = 1.202 \left(\frac{k_B T_{\mathrm{c}}}{\hbar\bar{\omega}}\right)^3, \tag{2}$$

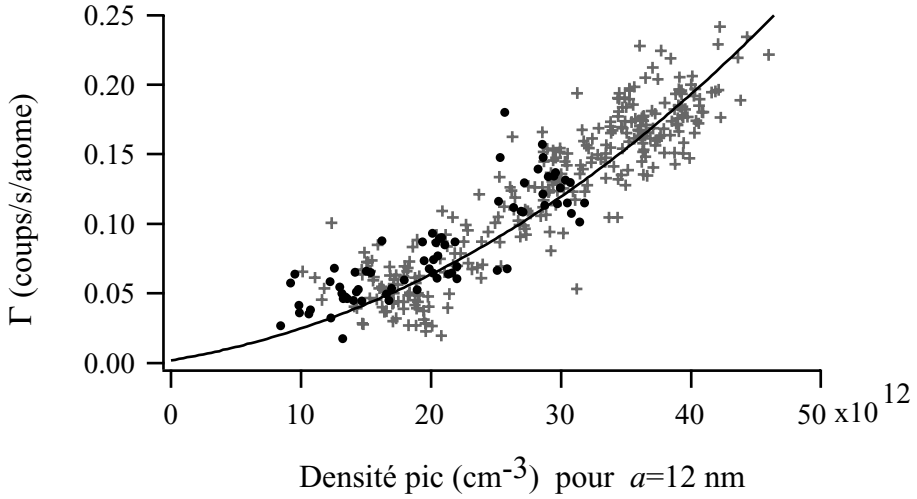

Figure 2: *Taux d'ions normalisé en fonction de la densité pic. La courbe en trait continu est un ajustement utilisant l'équation 1 et nous permet d'extraire les constantes de collisions.*

où $\overline{\omega} = (\omega_{\|}\omega_{\perp}^2)^{1/3}$ est la moyenne des fréquence d'oscillation du piège. Nous obtenons l'expression suivante pour le taux d'ions au seuil (modèle du gaz idéal) :

$$\Phi_{\rm c} = (\frac{\omega_{\rm c}}{\overline{\omega}})^3 \times \left[\frac{1}{\tau_i}1.20 + \frac{\beta(a)}{\lambda_{\rm c}^3}0.33 + \frac{L(a)}{\lambda_{\rm c}^6}0.22\right]. \qquad (3)$$

Dans cette expression nous avons défini : $\omega_{\rm c} \equiv k_B T_{\rm c}/\hbar$ et $\lambda_{\rm c} \equiv \lambda(T_{\rm c}) = h/\sqrt{2\pi m k_B T}$.

Expérimentalement, grâce à l'augmentation forte dans le signal d'ions au seuil de la condensation, nous pouvons identifier, et en conséquence produire, un nuage au seuil de condensation. Nous enregistrons le taux d'ions, et par la technique de Temps-de-Vol, nous obtenons également la température du nuage.

Les résultats sont montrés dans la figure 3. Toutes les données montrées représentent des nuages au seuil de condensation selon l'indication du taux d'ions. Cependant, nous jugeons, à partir d'une analyse plus sophistiquée basée sur le signaux de TdV, que les données indiquées en gris ne correspondent pas exactement à des tels nuages, et en conséquence elles ne sont pas incluses dans l'analyse finale. Pour obtenir la longueur de diffusion, nous ajustons ces données avec l'équation 3 (en réalité, nous prenons plutôt une expression plus complexe qui inclue les interactions entre atomes dans le

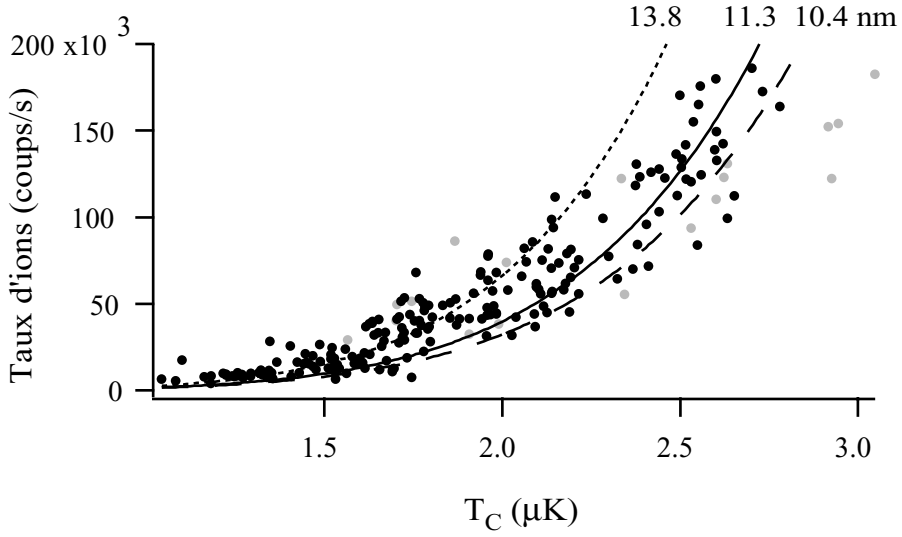

Figure 3: *La longueur de diffusion est obtenue en ajustant ces données (en incluant uniquement les points noirs) avec l'équation 3. L'ajustement donne* 11.3 *nm (la courbe en trait continu). Les barres d'erreurs sont obtenues en ajustant separemment les points en dessous et au-dessus* 2 *μK (cette fois incluant les points gris). Ces deux ajustements sont indiqués en trait pointillé et trait tireté, respectivement.*

gaz). Le seul paramètre libre dans l'ajustement est la longueur de diffusion. Nous obtenons

$$a = 11.3^{+2.5}_{-1.0} \text{ nm}$$

Les barres d'erreur sont également indiquées dans la figure 3. Elles sont obtenues en ajustant la partie des données correspondant à des températures faibles et élevées separemment afin de tenir en compte d'une légère erreur non expliquée, qui se traduit par une valeur ajustée de la longueur de diffusion plus élevée pour de températures faibles que pour de températures plus élevées. A cela nous avons ajouté quadratiquement la petite erreur provenant de l'incertitude sur les mesures des constantes de collisions. Finalement, nous obtenons aussi les constantes de collisions :

$$\beta = 0.9^{+2.0}_{-0.8} \times 10^{-14}\ \mathrm{cm}^3/\mathrm{s}$$

$$L = 2.5^{+5.3}_{-1.7} \times 10^{-27}\ \mathrm{cm}^6/\mathrm{s}$$

La valeur de la longueur de diffusion ainsi que les constantes des collisions se montrent en bon accord avec les estimations theoriques.

Conclusion

La détermination des constantes de collisions ainsi que la longueur de diffusion ouvre la porte d'études complexes basées sur un gaz d'hélium métastable. Entre autre, il est possible d'étudier la dynamique de formation d'un condensat, utilisant le signal d'ions : connaissant les constantes de collisions, la densité peut être déduite de ce signal. Ceci donne donc un moyen de suivre en temps réel l'évolution de la densité durant la formation, contrairement aux expériences habituelles, où la mesure de densité est destructive.

Le signal d'ions n'est pas le seul avantage d'hélium métastable. L'énergie interne des atomes neutres permet aussi en principe de les détecter un par un avec la galette de micro-cannaux. Notre prochaine expérience profite de cela : en faisant tomber un nuage froid et en détectant l'intervalle de temps entre l'arrivée de chaque atome, nous pouvons déduire les fonctions de corrélation temporelles des atomes du nuage - pas seulement pour un nuage thermique ou un condensat de Bose-Einstein, mais aussi pour un nuage ayant une température et densité qui le place entre ces deux régimes distincts. Les functions de correlation des atomes appartenant à un nuage entre ces deux régimes n'ont pas été étudiées d'une manière directe – c'est à dire en observant les atomes un par un – jusqu'à présent, et c'est vers cette étude que s'oriente désormais notre recherche expérimentale.

Introduction and outline of Ph.D. thesis

If this thesis had been written around 1995, where the first Bose-Einstein condensate (BEC) of a dilute atomic gas was experimentally observed [1, 2], the introduction should necessarily have contained a solid motivation for choosing to do experiments with ultracold atoms. Nonetheless, the explosion of the domain of cold atoms during the last decade entirely proves not only the richness but also the importance of the field, and shows that the modern physics society indeed find a general interest therein. For instance, the list of different elements having been condensed continue to get longer every year: today, Bose-Einstein condensation has been observed for all alkali atoms [1, 2, 3, 4, 5, 6], hydrogen [7], metastable helium [8, 9] and ytterbium [10]! The possibility of condensing yet other species are currently being tested, of particular interest from our point of view is metastable neon [11, 12, 13]. However, among other things, the short intrinsic lifetime of the metastable state being only 14.7 seconds [11] makes it a serious challenge.

Instead of listing the various motivations behind cold atoms physics, let us therefore simply try to place the field in a context of general modern physics and see in which direction it tends to evolve. Today, no universal model describing the entirety of all observable phenomena has been developed. Depending on the energy or size of the system, one particular model is always better than another, because systems of different size behave qualitatively very different, at least according to our way of perceiving them. For very large scale systems, general relativity is essential, while particle physics is related to extremely small, high-energy systems. It is somewhere in the wide range between these extremes, we can find systems, which are neither microscopic nor macroscopic, or, if one prefer, both. Three important examples are superfluidity, superconductivity and lasing. All three phenomena have one point in common: each of them involves a macroscopic occupation of one single quantum state, exactly as BEC of an atomic dilute gas[1][14, 15, 16]. In addition to the intrinsic interest in obtaining experimentally this new state of matter, one of the advantages of BEC[2] are the weak

[1] Note that lasing is different in the sense that it is a state which is not in thermodynamical equilibrium.

[2] In the following the word BEC is used only for dilute atomic gasses even though rigorously speaking, superfluidity, superconductivity and lasing are all different manifestations of Bose-Einstein condensation.

interactions between particles. In a laser field interactions are absent[3], and in the superfluid or superconducting phase, they are too dominant to be modelled in a relatively simple way. For a BEC however, the interactions are weak enough to treat them using perturbation theory; this was indeed one of the initial motivations for studying BEC physics. It is therefore interesting and somewhat paradoxical to realize that today, the interest in BEC physics is shifted towards engineering and even deliberate increasing the interactions in the systems, in order to go beyond the validity of the perturbative regime. Here, phenomena as quantum depletion [17] can be observed, where atoms are pushed out of the BEC state because of strong interactions, or other deviations from the predictions following a perturbative approach. The strength of the interactions is related to the scattering length of the atoms, and this "constant" can in some cases be engineered by applying magnetic field: this is the Feshbach resonance [18]. By using a Feshbach resonance, the interaction can also be increased in order to convert the ultra-cold atoms into ultra-cold *molecules* [19, 20, 21, 22, 23] and these molecules can even form a molecular BEC [24, 25, 26]! Another way to create and even trap ultracold molecules is *via* photoassociation of cold atoms (see Ref. [27] and references therein), and in analogy with the above schemes, this could be referred to as "optical Feshbach resonances".

It is also possible to apply the magnetic Feshbach resonance in such a way that the molecules formed are extremely loosely bound, and become similar to cooper pairs of electrons in a metal. The BEC of these molecules is therefore in many aspects equivalent to a BCS (Bardeen-Cooper-Schrieffer) state in a metal and as the atoms forming the molecules can be fermions, this pushes the analogy even further [28, 29, 30, 31]. As the BEC of atoms is a superfluid state, the BEC of loosely bound molecules bear resemblance to a super conducting state. The full understanding and experimental realization of a true BCS state of molecules is one of the topics which attracts great interest at the moment. Finally, not only degenerate gases of *either* bosons or fermions have been observed. Experiments investigating the *simultaneous* existence of a Bose-Einstein condensate and a gas of fermions are being performed, and the mutual interactions have been studied [32, 33]. These studies open the door towards the exploitation of Feshbach resonances between bosons and fermions, and all the exciting physics which follows therefrom.

The spirit behind

In 2001, six years after the first rubidium condensate was obtained, the first BEC of metastable atoms was observed. It was metastable helium (helium in the 2^3S_1 state) and it happened a cold winter night in our group in

[3]Note that this is not true if the photons propagate in non-linear media. In this case, the Schrödinger equation becomes non-linear, and the system will behave as if the photons interact.

Orsay[4] [8]. Very shortly afterwards, the group of Michèle Leduc and Claude Cohen-Tannoudji at Ecole Normale Supérieure also succeeded in condensing metastable helium [9].

I joined the metastable helium experiment in Orsay just a few months after the first BEC was obtained, and our first project was to study the formation of the condensate. Metastable atoms present an advantage compared to ground state atoms for studying the formation processes, because they offer a non-destructive monitoring tool, in the form of a continuous ionization signal. In fact, in a sample of metastable atoms, ionizing collisions between an atom from the background gas and a trapped metastable helium atom can take place: under a collision, the internal energy of the helium atom can be transferred to the background atom, which ionizes. The helium atom decays to the ground state. Therefore, a trapped cloud of helium atoms creates continuously a flux of ions, which can be detected with a micro-channel plate. The ionization rate will here depend on the number of trapped helium atoms and the background pressure. Even though the ionization signal is high enough to be easily detectable, the loss of atoms due to ionization is small and does not destroy the cloud, as we will show later. If the sample becomes very dense, collisions between two or even three helium atoms become dominant. The rate of these collisions will depend on the *density* of the sample. In this case, the ionization rate is a probe of the sample-density. Our idea was to study the density evolution of the cloud during BEC formation using this ion signal as measurement tool.

The traditional way of studying the density evolution during BEC formation is based on the technique called Time-Of-Flight. Here, the velocity distribution of the cloud is measured by switching off the potential which confines the atoms, let the cloud expand, and then make an image. From the velocity distribution, the density distribution can be traced back. However, by switching off the trap potential, the atoms are lost. Therefore, to measure an evolution of the density, the experiment must be repeated many times, under exactly the same conditions. This requires a very stable experiment! Therefore, the non-destructive monitoring *via* the ionization rate seemed to be a very good solution.

As it happens very often in research, the solution of a first problem gives rise to the next and so it continues. This was definitely the case for the work performed during these past three years. The problem was that to exploit the ion rate in a quantitative way, the 2- and 3- body rate constants for the ionizing collisions were necessary. Theoretically, only estimates for these constants existed, and we therefore decided to measure them. Unfortunately, to do this, we need a way to measure the density of the sample. As we will see later, we could only obtain the density parameterized by the s-wave scattering length a. Consequently, the 2- and 3-body rate constants obtained were also a function of a.

[4]To be honest, I don't know if it was cold, I had not joined the experiment yet, and I was probably sleeping. But I sounds more poetic like that, and I know that it was winter!

However, as the scattering length for metastable helium was not very precisely known, these results could not be exploited quantitatively. We had three "unknowns": the two rate constants and the scattering length, but only two "equations" - one for each rate constant! A third equation was therefore needed to obtain the absolute values for the rate constants and the scattering length. Fortunately, there was a way to obtain this third equation: as we will explain later, for clouds exactly at the Bose-Einstein phase transition point, the ion rate can be written in terms of the temperature (together with the rate constants and the scattering length). Because we could identify threshold using the ion rate (this will be discussed in chapter 3), we could measure the ionization rate as a function of temperature exactly at this point, and we could consequently establish this third – and missing – equation. And thereby obtain rate constants and the scattering length.

In this way, one of the main result of this thesis became the measurement of the scattering length, even though we never actually decided that it should be so! However, from my point of view, the true result is not the scattering length, but it is rather to be found in *the way* we had to go to obtain this result: all the physics encountered and used along the way is definitely not only interesting, but also very subtle.

Outline of the thesis

This thesis is meant to guide the reader through the different measurement done along the way, including all the interesting physics which has been necessary to understand on the way in order to obtain the most precise value of the scattering length.

As the reader will soon discover, in this manuscript it will happens that the interpretation of some results require data obtained later in the thesis, and sometimes it even happens that we must use a sort of iterative procedure to extract the desired information. This makes it very difficult to write a manuscript which remains coherent all the way through. I have tried to order the results in a way which is essentially chronological. However, in order not to interrupt certain discussions before their natural end, I have sometimes been obliged to use information, which only became available at a later stage.

The manuscript is divided into five chapters. The subject of the first chapter is a general introduction to collisions. Elastic collisions are discussed in order to give a definition of the scattering length and a motivation for why it is an important parameter in cold atom physics. Inelastic collisions, in particular ionizing collisions, are the backbone of all measurement here described. Chapter 2 describes the experiment. It is meant to provide the minimum knowledge required in order to understand the technical details discussed in this thesis, and allow the reader to place the experiments here described in their true surroundings. If the reader is interested in more experimental details, much better discussions can be found in Ph.D. of former

students [34, 35, 36, 37]. Chapter 3 presents the ionization signal, and shows how it can be used to extract information about the sample. In particular, it shows how this signal, provided one knows the ionization rate constants, can be use to monitor non-perturbatively the density of the sample. This leads directly to chapter 4, which describes our measurement of these rate constants. They are given in terms of the scattering length, but in chapter 5 we present a measurement of this constant, which also allows us to deduce the absolute values of the rate constants. Finally the manuscript contains seven appendices. They generally contain details, longer calculations or additional illustrations which could be omitted in the main text. The content of the last appendix is different: it contains the articles related to the results obtained during the last three years.

A part of the results contained in this thesis have been obtained in collaboration with O. Sirjean with whom I was working during the first 2 years of my Ph.D. In particular, the preliminary study of the ionization rate discussed in chapter 3 as well as the measurements of the rate constants parameterized by the scattering length described discussed in chapter 4. These results are therefore also discussed in his thesis [37], even though his approach is somewhat different. I would like to mention that results here presented also "belong" to J. Gomes and R. Hoppeler, who have also been participating in these experiments.

CHAPTER 1

Elastic and inelastic collisions

After studying a particular subject for a while, physicists often get so absorbed in it that they start to develop a language which is specific to this domain. For instance, in BEC physics, one will often hear the words "good collisions" and "bad collisions". While an ordinary person would think that all collisions are bad - collisions between two freight trains for instance - a BEC physicist will immediately know what a good collision is, namely an elastic collision which allows an effective cooling of a sample of trapped atoms. On the other hand, a bad collision is an inelastic collision, which will make one lose atoms without decreasing the temperature. One of the main results presented in this thesis is a measurement of a parameter which describes the good collision: the s-wave scattering length, denoted by a. To complicate the story, the measurements are obtained *via* bad (inelastic) collisions, which consequently become good collisions, at least for us! Hang on, the goal of this chapter is to clarify these concepts...

In the first part of this chapter, we will give a general definition of the s-wave scattering length. This parameter does not only describe the elastic collision properties, but dictates the cold gas behavior in a large variety of physical phenomena, and some examples will be given. We then discuss generally how the scattering length can be obtained from theory and from experiments. We then turn to the specific case of metastable helium, giving a state of the art: we will discuss the current precision of the existing calculations and measurement of the scattering length of metastable helium. As mentioned above, our way of obtaining the scattering length is very unusual compared to previous measurements: it is indirectly obtained from the inelastic collisions through measurements of the ionizing rate constants. Therefore the second part of the chapter is devoted to inelastic collisions in a sample of metastable helium, giving the necessary background for understanding the measurements reported in this thesis.

1.1 Elastic collisions and scattering theory

The s-wave scattering length is a parameter which is defined in the framework of quantum scattering theory. This subject is often encountered in the literature, and for a simple and short introduction, I personally recommend [38]. A more general reference is [39], and a nice discussion of quantum scattering with a focus on BEC physics can be found in [40, 41]. This is an extremely rich domain of physics, and it would be impossible to give a complete description. Here, we will summarize some of the main ideas.

We will study the case of an elastic collision between two identical particles, denoted 1 and 2, each of mass M. The particles interact through a potential $V(\mathbf{r}_1 - \mathbf{r}_2)$. The corresponding Hamiltonian is

$$\hat{H} = \frac{\hat{p}_1^2}{2M} + \frac{\hat{p}_2^2}{2M} + V(\hat{\mathbf{r}}_1 - \hat{\mathbf{r}}_2). \tag{1.1}$$

Defining the center of mass operators $\hat{R}_{\mathrm{CM}} = (\hat{\mathbf{r}}_1 + \hat{\mathbf{r}}_2)/2$ and $\hat{P}_{\mathrm{CM}} = \hat{\mathbf{p}}_1 + \hat{\mathbf{p}}_2$ and the relative variables $\hat{\mathbf{r}} = \hat{\mathbf{r}}_1 - \hat{\mathbf{r}}_2$ and $\hat{\mathbf{p}} = (\hat{\mathbf{p}}_1 - \hat{\mathbf{p}}_2)/2$ the Hamiltonian can be written as

$$\hat{H} = \frac{\hat{P}_{\mathrm{CM}}^2}{4M} + \frac{\hat{p}^2}{M} + V(\hat{\mathbf{r}}). \tag{1.2}$$

Of course, we can always choose a coordinate system where the total momentum of the particles is zero. In such a coordinate system, the dynamics of the collision can be uniquely given by the position and momentum of a fictive particle of mass $\mu = M/2$ moving in a potential $V(\hat{\mathbf{r}})$, with an energy $E = \hbar^2 k^2 / 2\mu$. This simplifies the following discussion. However, the meaning of the position coordinate $\hat{\mathbf{r}}$ must be kept in mind for future interpretations: it is the relative distance between the two particles.

1.1.1 Partial waves and the cross section

In quantum mechanics, we need to describe the fictive particle in terms of a time-dependent wave packet. We write the time-dependent wave packet as an expansion on a basis of stationary states. These stationary states are solutions to the equation

$$\left(\frac{\hat{p}^2}{2\mu} + V(\hat{\mathbf{r}}) \right) \psi_{\mathbf{k}}(\mathbf{r}) = E_k \psi_{\mathbf{k}}(\mathbf{r}), \tag{1.3}$$

each with eigenvalues $E_k = \hbar^2 k^2 / 2\mu$. In the asymptotic limit the solution can be written as a superposition of an incident plane wave (with momentum $\mathbf{k}$) and a scattered spherical wave with an amplitude $f(k, \theta)$:

$$\psi_{\mathbf{k}}(\mathbf{r}) \sim e^{i\mathbf{k}\cdot\mathbf{r}} + f(k, \theta) \frac{e^{ikr}}{r}. \tag{1.4}$$

The amplitude of the scattered spherical wave $f(k, \theta)$ is related to the cross section by:

$$\sigma(k) = \int |f(k,\theta)|^2 \, \mathrm{d}\Omega, \tag{1.5}$$

where $\mathrm{d}\Omega$ indicates the solid angle. For $kr \gg 1$, we can use the partial wave expansion to express the incident plane wave as a sum of incoming and outgoing spherical waves [40]:

$$e^{i\mathbf{k}\cdot\mathbf{r}} \sim \frac{1}{2ikr} \sum_{l=0}^{\infty} (2l+1) P_l(\cos\theta) \left((-1)^{l+1} e^{-ikr} + e^{ikr} \right), \tag{1.6}$$

where $P_l(\cos\theta)$ are the Legendre polynomials. Inserting this expression in Eq. 1.4 gives (spherical potential)

$$\psi_{\mathbf{k}}(\mathbf{r}) \sim \frac{1}{2ikr} \sum_{l=0}^{\infty} (2l+1) P_l(\cos\,\theta) \left((-1)^{l+1} e^{-ikr} + e^{2i\delta_l} e^{ikr} \right), \tag{1.7}$$

where we have defined a phase shift δ_l by

$$f(k,\theta) = \frac{1}{2ik} \sum_{l=0}^{\infty} (2l+1) P_l(\cos\,\theta)(e^{2i\delta_l} - 1). \tag{1.8}$$

Using the fact that the Legendre polynomials are orthogonal and normalized to $2/(2l+1)$, we obtain the cross section which was defined in Eq. 1.5

$$\sigma(k) = \sum_{l=0}^{\infty} \sigma_l(k), \tag{1.9}$$

with $\sigma_l(k)$ the partial cross section

$$\sigma_l(k) = \frac{4\pi}{k^2} (2l+1) \sin^2 \delta_l(k). \tag{1.10}$$

The cross section has now been expressed in terms of a sum of phase shifts. It is interesting to note that the total cross section is obtained by by summing incoherently over the different partial cross sections, i.e. interference between different terms is absent due to the orthogonality of the Legendre polynomials.

The expression for the cross section given by Eq. 1.10, is valid for distinguishable particles. When the particles are identical, the symmetry of the wave function given in Eq. 1.7 has to be considered: for bosons, it must be symmetric while for fermions antisymmetric. This leads to a modification of the expression of the cross section, as explained in [40]. Taking this into account, the cross sections for indistinguishable particles becomes:

$$\sigma_l = \sum_{l \text{ even}}^{\infty} \frac{8\pi}{k^2}(2l+1)\sin^2\delta_l(k) \qquad \text{for bosons,} \tag{1.11}$$

and

$$\sigma_l = \sum_{l \text{ odd}}^{\infty} \frac{4\pi}{k^2}(2l+1)\sin^2\delta_l(k) \qquad \text{for fermions.} \tag{1.12}$$

Note that for bosons, we only sum over l even, while for fermions, we sum over l odd: this is because the symmetry of the wavefunction is given by $(-1)^l$. In the following we will always consider the case of bosons.

To determine the cross section form Eq. 1.11, we must determine the phase shift $\delta_l(k)$. We separate the wavefunction into a radial and angular part:

$$\psi_{\mathbf{k}}(\mathbf{r}) = \sum_{l=0}^{\infty}\sum_{m=-l}^{l} Y_l^m(\theta,\phi)\frac{u_{k,l}(r)}{r}, \tag{1.13}$$

where the $Y_l^m(\theta,\phi)$'s are the common eigenvectors of $\hat{L}^2$ and $\hat{L}_z$ ($\hat{\mathbf{L}}$ being the angular momentum operator). Using this expansion for the wavefunction in Eq. 1.3, we can obtain a radial equation[1]:

$$u''_{k,l}(r) + \left(k^2 - \frac{l(l+1)}{r^2} - \frac{2\mu V(r)}{\hbar^2}\right) u_{k,l}(r) = 0. \tag{1.14}$$

Now according to Eq. 1.7, the asymptotic form of the radial part of the wave function, for a given l, can be written as

$$u_{k,l}(r) \propto (-1)^{l+1}e^{-ikr} + e^{2i\delta_l(k)}e^{ikr}. \tag{1.15}$$

By solving the radial equation for a particular potential (in general numerically), and imposing the asymptotic form given in 1.15, the phase shift, and consequently the cross section can be obtained.

1.1.2 Ultracold collisions

When one is considering ultracold[2] collisions ($k \to 0$), the expression for the cross section becomes very simple as we will show in the following. In general, the solution to the radial equation can be written as a linear combination of spherical Bessel and Neumann functions. Consequently, also the phase shift can be expressed in terms of these functions, and by using their properties, it can by shown that [39, 42]

$$\delta_l(k) \propto k^{2l+1} \qquad \text{for } k \to 0. \tag{1.16}$$

[1] The equation is valid when $u_{k,l}(r)/r$ stays finite when $r \to 0$.

[2] We shall clarify the meaning of "ultracold" later.

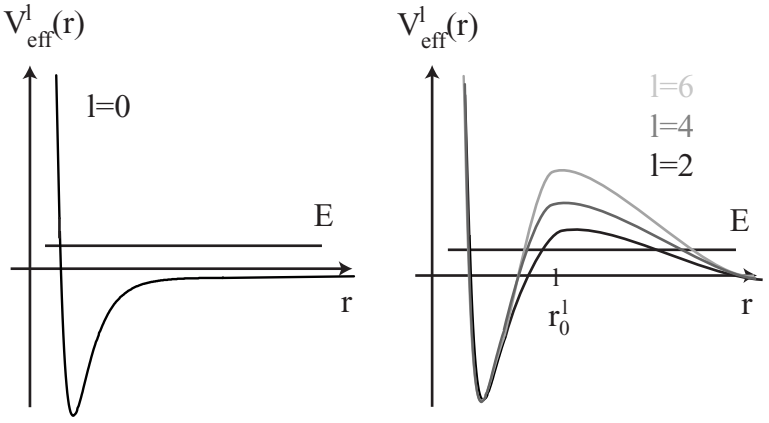

Figure 1.1: *The effective potential (defined in the text) corresponding to the different partial waves for bosons. Due to symmetry considerations, only even l partial waves contribute. For energies lower than the potential corresponding to $l = 2$ (which is the case for the energy E), only the potential for $l = 0$ contribute to the interaction, because for the other l values, a centrifugal barrier hinder the close approach of the two particles.*

This means that at very low energies, for every partial cross section:

$$\sigma_l(k) \propto \sin^2 \delta_l(k)/k^2 \to k^{4l} \to 0 \qquad \text{for } k \to 0. \tag{1.17}$$

This is true for all partial waves with $l \neq 0$. At very low energies, only the cross section corresponding to $l = 0$ (the s-wave) survives and tends to a constant value, which we will give later. To understand physically why the cross section vanishes for all partial waves corresponding to $l \neq 0$, we consider the potential for each partial wave separately. We define a new potential $V^l_{\text{eff}}(r)$ which includes both the real potential and the centrifugal barrier from the radial equation (Eq. 1.14):

$$V^l_{\text{eff}}(r) = V(r) + \frac{\hbar^2}{2\mu}\frac{l(l+1)}{r^2}, \tag{1.18}$$

where for long distances, $V(r)$ is the van der Waals potential which to lowest order in r^6 is [43]

$$V^l_{\text{eff}}(r) = \frac{l(l+1)}{m}\frac{\hbar^2}{r^2} - \frac{C_6}{r^6}, \tag{1.19}$$

where C_6 is a parameter which depends on the nature of the atomic species. The approximate form of the effective potentials for bosons for different values of l is shown in Fig. 1.1. Note that for increasing values of l, the barrier in the potential due to the centrifugal term becomes increasingly high. If the kinetic energy E is lower than the barrier, the particles will be

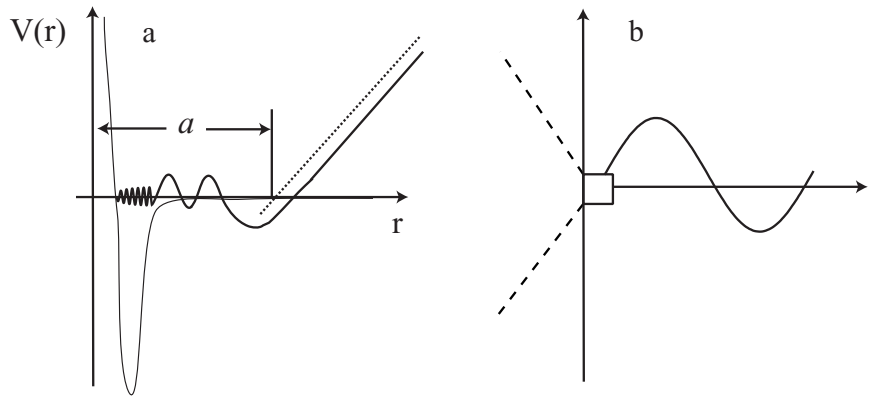

Figure 1.2: *The black solid line shows the interaction potential, while the gray solid line is the wavefunction for the scattering state. This state describes the two incoming particles having an energy just above the dissociation limit. Figure a is a zoom of b: in a we show the behavior of the wavefunction for short and intermediate values of r, while in b we show the large r behavior. For short distances, the wavefunction oscillates very rapidly (high energy region), while for intermediate distances, it tends to a straight line. This lines is actually the first lobe of the long-period sine function shown in b (free-particle behavior). This long period sine function is phase shifted from the origin due to the interaction potential. The scattering length a is defined as the zero energy crossing of the tangent to the first lobe of the long period sine function. This corresponds also to the phase shift of the sine function.*

reflected, and they will never enter the region where the interaction takes place. If the collision is ultra cold, the energy E is so low that only the s-wave ($l = 0$) will penetrate into the region where the interaction takes place. This is the case for the energy shown in the figure, and in this case, the collision is completely characterized by a quantity called the s-wave scattering length a, which we will now define.

Let us consider the wave function corresponding to two very cold atoms entering in collision. As the atoms are very cold, the kinetic energy is extremely low, and the total energy of the two atoms is just above the dissociation limit of the corresponding molecular state. The state is called the diffusion state (or scattering state). The scattering length has a geometric interpretation in terms of the wave function of this state, which is shown in Fig. 1.2. In the inner parts of the potential a, the wave function oscillates rapidly, as this is the high energy region. At very long distances, the wavefunction becomes a sine wave with an extremely long period, as shown in

the zoom in Fig. 1.2, b. In intermediate regions, the wave function tends toward a straight line, which we can write as $U_{k,0} = A \times (r - a)$, where a is the zero intersection of this line. By definition, this is the scattering length. To obtain an expression for the scattering length, we therefore rewrite the radial wavefunction given in Eq. 1.15 with $l = 0$:

$$\begin{aligned} u_{k,0}(r) &\propto -e^{-ikr} + e^{2i\delta_0(k)} e^{ikr} \\ &= 2i\, e^{i\delta_0}\, \sin(kr + \delta_0) \\ &= 2i\, e^{i\delta_0}\, [\sin(kr)\cos(\delta_0) + \sin(\delta_0)\cos(kr)]. \end{aligned} \tag{1.20}$$

When $kr \ll 1$, we can approximate $\sin(kr) \simeq kr$ and $cos(kr) \simeq 1$, and we obtain:

$$\begin{aligned} u_{k,0}(r) &\propto 2i\, e^{i\delta_0}\, [kr\cos(\delta_0) + \sin(\delta_0)] \\ &= 2i\, e^{i\delta_0}\, \cos(\delta_0)[kr + \tan(\delta_0)]. \end{aligned} \tag{1.21}$$

We can therefore now define the s-wave scattering length a

$$a = -\lim_{k\to 0} \frac{\tan[\delta_0(k)]}{k}. \tag{1.22}$$

Therefore, the effect of the interaction between the atoms is to displace the straight line describing the wave function by a distance a from the origin. As the line describing the wavefunction actually is the first lobe of a sine function with a very long period, the effect of the potential can also be interpreted as a phase shift of the partial wave corresponding to $l = 0$ by an amount a. The figure shows the case of a repulsive potential, where the wave function is shifted away from the origin relative to the non-interacting case, and the scattering length becomes consequently positive. For an attractive potential, the wave function is shifted towards the origin, and a is consequently negative.

The physically interesting parameter is the cross section given by Eq. 1.11, and in the s-wave limit we can write it in terms of a:

$$\lim_{k\to 0} \sigma_0(k) = 8\pi \frac{\sin^2[\delta_0(k)]}{k^2} \tag{1.23}$$

$$\simeq 8\pi a^2, \tag{1.24}$$

where in the last step we have approximated the sine with a tangent.

l	2	4	6
r_0^l (nm)	3.2	2.4	1.9
$V_{\text{eff}}^l(r_0^l)/k_B$ (mK)	42.6	251	841

Table 1.1: *The position and height of the potential barrier for He* corresponding to the potential shown in Fig. 1.1.*

Finally it should be mentioned that it is possible to be in the s-wave limit even when k is finite (but small). It can be shown that the cross section can be written as[3][41]

$$\sigma(k) = \frac{8\pi a^2}{1 + k^2 a^2}. \tag{1.25}$$

In the next section we will estimate the temperature requirements for the different regimes discussed above in the case for metastable helium.

Helium

We consider the 2^3S_1 metastable state of helium, see Appendix A. By differentiation of the potential given in Eq. 1.18 with $V(r)$ given by Eq. 1.19 we can calculate the position of the potential barrier r_0^l (the position where the potential is maximum), and the barrier height. We use $C_6 \sim 3.12 \times 10^{-22}$ J nm^6 [34]. The barrier height and position are given for $l = 2$, 4, 6 in table 1.1. It is interesting to note that the s-wave regime is already reached at 42.6 mK. The depth of the trap potential that we use for the He* atoms (chapter 2) is only a few millikelvin, so only atoms colder than this value are confined. Consequently, for collisions between trapped atoms, the s-wave approximation will always be valid.

On the other hand, we are not necessarily in the regime where the cross section is independent of energy. In fact, this is true only when $k^2a^2 \ll 1$. Using $E = \hbar^2k^2/2\mu = k_BT$, $\mu = m_{\text{He}}/2$ and $a = 12$ nm, we can write

$$k^2a^2 = \frac{k_B\, T\, a^2\, m_{\text{He}}}{\hbar^2} \sim 1 \times \text{T(mK)}. \tag{1.26}$$

Therefore, in order to have $k^2a^2 < 0.1$, the temperature must be less than 100 μK. If the temperature is higher, we must use Eq. 1.25 rather than Eq. 1.23 for the cross section.

[3] A more accurate expression is given by $\sigma(k) = \frac{8\pi a^2}{(1-k^2 a r_e)+k^2a^2}$ where r_e is the "effective range" of the potential, also discussed in [41].

atom	H	He	^{23}Na	^{87}Rb
a(nm)	0.06	~ 12	3.45	5.6

Table 1.2: *Scattering length for atoms commonly used for BEC. All values are given for the triplet state, see [45].*

1.1.3 The role of the s-wave scattering length

The reason why the scattering length is so important for us is that in a Bose-Einstein condensate, or a thermal cloud near the BEC phase transition, the collisions are ultra cold: only s-wave scattering takes place, and the scattering length a becomes a key parameter. In this limit, the interaction potential between atoms in a dilute (but too dense to be ideal) gas becomes very simple: in the mean field approach (see Ref. [17]), the atomic interaction potential can be described uniquely by the scattering length and the density $n(r)$

$$V_{\text{int}}(r) = \frac{4\,\pi\,\hbar^2\,a}{m} n(r) \equiv U n(r) \tag{1.27}$$

Therefore, the behavior of the sample can be predicted from the density alone, if the scattering length is known. Let us give some brief examples:

Evaporative cooling

Bose-Einstein condensation was realized in dilute gases only after the development of evaporative cooling. This cooling scheme consists of continuously ejecting the hottest atoms - with a rate which allows the sample to relax back to equilibrium, or to "thermalize". In this way, a BEC can be achieved[4]. An effective cooling requires a rapid thermalization which in turn requires a high elastic collision rate - a parameter which increases with the scattering length squared[5]. To be more precise, the essential quantity is the ratio between elastic and inelastic collisions – elastic collisions are necessary for the thermalization, while inelastic collisions destroy the sample. This is, by the way, why elastic collisions are called "good collisions" and inelastic collisions are called "bad collisions"! Therefore, the scattering length plays a key role in the feasibility of reaching BEC! This is also partly why it took considerably more time to make a hydrogen condensate compared to the "standard" alkali BEC: the scattering length of hydrogen is much lower than the BEC alkali atoms as shown in table 1.2

[4] This will be discussed more in detail in chapter 2.

[5] This is true for the zero energy cross section. For higher temperatures, it is possible to enter regimes where the cross section is independent of a, or will depend on the effective range of the potential, see [41, 44].

BEC with a negative scattering length

Not only the magnitude but also the *sign* of the scattering length is important. Positive scattering length gives rise to an repulsive mean field potential (see Eq. 1.27), whereas a negative scattering length gives rise to an attractive mean field potential[6]. Theoretically, it can be shown that in a homogeneous system, a condensate with a negative scattering length is unstable and cannot exist [3, 46, 47]. This is because the condensate contracts in order to minimize the energy of the system, until all atoms are lost due to an increase in inelastic collisions: the condensate is said to "implode". However, if the condensate is confined in a harmonic potential, such that its size is smaller than a given critical value, it can become stable because the kinetic energy, which is present to balance the trap potential, introduces an energy barrier towards collapse. One can therefore define a critical atom number, below which the condensate is stable, and above which it implodes. An example is the Bose-Einstein condensate of ^{7}Li with $a = -1.5$ nm, for which the theoretical critical atom number has been experimentally verified [46].

Shift of the critical temperature

The Bose-Einstein phase transition temperature given in the famous Einstein paper [16], is calculated for an ideal gas. Due to interactions between atoms, this critical temperature is shifted. For a weakly interacting, homogeneous gas of fixed volume[7], the critical temperature is *increased* compared to the ideal gas case. The shift depends on the scattering length and is to lowest order proportional to a, for theory, see Refs. [48, 49, 50, 51, 52, 53, 54, 55, 56, 57], and for experiments, see Refs. [58, 59] and references therein. This shift can be thought of as due to density fluctuations (critical fluctuations) which create small "high-density regions", accelerating the formation of the condensate[8]. These fluctuations are enhanced by interactions which again depends on a. In a homogeneous gas, this displacement of the critical temperature is only present beyond the mean field approximation, as discussed for instance in Ref. [60].

For a gas trapped by a harmonic potential there is an additional contribution to the shift on the critical temperature, which is even present within the mean field approximation. For a gas in a harmonic potential, the volume is not fixed, only the number of particles. The shift of the critical temperature arises because the atoms repel each other, and consequently the peak density is lowered. In order to fulfil the phase transition requirement $n\lambda_{dB}^3 = g_{3/2}(1)$, the critical temperature is *lowered*. The higher a is, the more the atoms interacts, and the more is the transition tempera-

[6] Note that the true 2-particle potential is always attractive, it is only the mean field potential arising from elastic collisions which can be either attractive or repulsive

[7] Particles in a box, for instance.

[8] This is far from being a rigorous argument, but only an intuitive way to think about it.

ture lowered. This shift dominates over the increase in critical temperature discussed above such that the overall shift is downwards.

Hydrodynamic regime

The most common way to observe a condensate is to let it expand for a while and then image it. It is often a very good approximation to assume that the cloud expands freely (ballistic expansion) after the switch-off of the trap. However, if strong interactions are present, this approximation is no longer valid, and collisions during the first milliseconds of the expansion must be taken into account. When this is the case, the gas is said to be in the hydrodynamic regime. This is the case when the rate of elastic collisions is much larger than the oscillation frequencies of the harmonic potential which traps the atoms (chapter 2). As the elastic collision rate is given by $8\pi a^2 n\bar{v}$, with n the density and $\bar{v}$ the mean relative velocity, the value of a determines whether a gas is hydrodynamic or "collision-less" for a given density and trap geometry. As we shall see later, the large scattering length for He^* requires that we take into account hydrodynamic effects when we interpret the shape of the expanded cloud.

Many more effects depend on the interactions and therefore on a and it would be impossible to mention all of them here!

1.1.4 How to measure the scattering length

In order to calculate a, the whole atom-atom interaction potential must be known, not only the long range part described by the C_6 coefficient defined in Eq. 1.19, but also the inner part[9]. Except for hydrogen, the potentials are not known accurately enough to deduce a precise value of a. Therefore the scattering length is in general determined experimentally. We will briefly discuss the different approaches, with special attention to their precision.

BEC measurements

In principle, it is straightforward to deduce the scattering length from measurements of the atom number and the width of an expanded BEC (using time-of-flight signals, which will be introduced in chapter 2). This is because for a BEC, the kinetic energy is negligible compared to interaction energy, and the expansion of the BEC arises from the latter alone, which depends only on a and the atom number N. More precisely, the width of the TOF signal is proportional to $(a\,N)^{1/5}$. By measuring the width as a function of atom number, the scattering length can be obtained. However, uncertainties on the measurements of the atom number, typically at least 10% for the alkali gases, lead to a large uncertainty on a. For He^* the uncertainty become

[9]Except for the so-called purely long range potentials, where the inner part is not required to calculate a.

even worse, as we will discuss in later chapters. Therefore, the scattering length is usually obtained from spectroscopic measurements. However, for He^* no spectroscopic measurement of the scattering length exists yet, and this is the reason why a large part of this thesis work is sacrificed to the measurement of the scattering length[10]. Even though our measurement of a is not done *via* spectroscopy such measurements for He^* are in progress in the group directed by Michèle Leduc and Claude Cohen-Tannoudji in "Ecole Normale Supérieure" in Paris [62]. As they use spectroscopy, it is therefore of general interest to briefly explain the main principles.

Spectroscopy of colliding pairs of atoms

We will summarize the main ideas concerning this topic. For a more complete discussion the reader can consult Refs. [62, 63, 64] and references given therein.

Before discussing the specific ways to do this kind of spectroscopy, let us first set the stage. The potential curves for the interaction between two colliding atoms are given in Fig. 1.3. The interaction between two atoms at large relative distance r both in the ground state (S+S) is described by the long range potential varying as $1/r^6$ at long distances. If one of the atoms is optically excited to a P state, the interaction potential is modified and varies as $1/r^3$ (S+P potential). This means that the upper S+P molecular curve corresponds to an *electronically* excited level, while the lower S+S curve is the ground state with respect to electronic excitation. For each of the two curves, in addition to the unbound scattering state, several molecular bound states exist, corresponding to different vibrational levels. With this figure in mind we will now define two types of spectroscopy: one which is based on "light-assisted collisions" and one based on photoassociation creating molecules. In both case, as we will see below, the signature of a certain transition taking place will be a trap loss of atoms. The laser frequencies for maximum loss rates then corresponds to the particular transition energies.

i) Light-assisted collisions

This method is based on the fact that a pair of ground state unbound atoms (the S+S scattering state) can absorb a laser photon and make a transition to the S+P scattering state (also an unbound state). Assume that the two S+S atoms initially are approaching each other with almost zero energy. Now one of the atoms is excited by a laser to the S+P scattering state, and the potential is therefore changed from $1/r^6$ to $1/r^3$. Consequently the atoms experience an increased acceleration towards each other. When the atom pair decays back to the S+S state, the atoms have gained kinetic energy. If initially the atoms were trapped, it is possible that they have

[10] Note however that photoassociation of cold He^* has been performed earlier, but primarily the S+P potential has been determined [61].

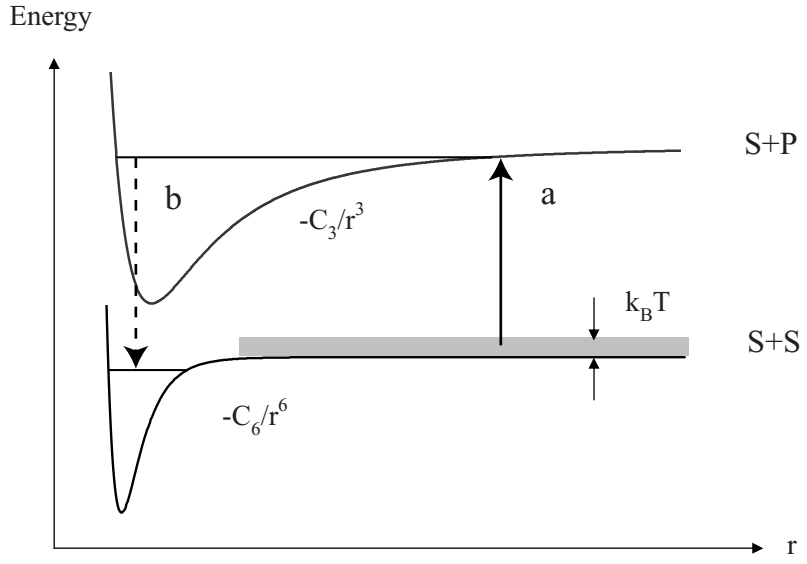

Figure 1.3: *The potential curves for the interaction between two atoms as a function of the separation distance between the atoms. The lower curve describes the interaction between two atoms in the electronic ground state (S+S), while for the upper curve, one of the atoms are in an excited level (S+P). The width of the S+S state is given by k_BT, where T is the temperature of the atoms. Inside each of the potential curves, several vibrational bound states exist. An example of photoassociation is the 2-photon Raman spectroscopy (discussed in the text): a laser induce transitions from the scattering state in the S+S potential to a bound state in the S+P potential (arrow denoted by a). Now applying a second laser, detuned by an amount corresponding to the energy difference between the scattering S+S state and the first bound state in the same potential (b) transitions to this bound state will take place, and atom losses will be observed. The detuning corresponding to maximum losses gives the energy level of the bound state, and consequently a. The figure is taken from Ref. [62] with the kind permission of the author.*

gained enough kinetic energy to escape from the trapping potential. A loss of atoms could then be the signature of a transition between the S+S and S+P curves shown in Fig. 1.3.

ii) Photoassociation

The second method is based on photon-induced transitions from the S+S scattering state to a bound molecular state. The method relies on the fact

that even though the atoms are trapped by the external potential, a molecule is not necessarily trapped by the same potential. Consequently, a transition to a molecular state results in a loss of atoms. If it is the S+S potential which is probed (this is the case when searching for the scattering length), then transitions to molecular bound state in this potential are performed. This is generally done by making a two-photon transition from the unbound S+S state *via* a virtual level to the bound state in the same potential.

Determination of the scattering length

These were the principles. How is it possible to extract the scattering length from these kind of experiments? Let us again separate the case of light-assisted collisions and photoassociation.

i) **Light-assisted collisions: probing directly the wave function of the scattering state**

The idea is based on the fact that a transition between the two scattering states S+S and S+P occurs only if the overlap between the wavefunctions of the two states is non-zero. This means that the transition strength is modulated by the spatial variations of the diffusion state for the potential (S+S), in particular by its nodal points, where the transition probability is zero. The transition is driven by a narrow linewidth laser light at a frequency ω_L. The resonant frequency for the transition depends on the interparticle distance r (see Fig. 1.3). If the long range part of the S+P potential (given by the C_3 coefficient) in addition to the asymptotic part of the S+S potential is known, the interparticle distance corresponding to a transition can be determined by the laser frequency ω_L. By measuring the transition strength as a function of laser frequency, the nodal points can be obtained as a function of position. From the nodal points, the overall phase shift of the wavefunction can be determined and from there the scattering length is obtained.

ii) **Photoassociation: probing the energy level of the last bound state of the molecular potential**

The scattering length for a given potential can also be deduced from measurements of the energy of the last vibrational bound state of the molecular potential: the energy difference ΔE between this level and the asymptote of the potential is directly related to the scattering length through [65, 66]:

$$|a| = \frac{\hbar}{\sqrt{2m\Delta E}}$$

This formula is valid when the scattering length is large ($a \gg r_e$, r_e the effective range of the potential). For helium, this formula turns out to be

a good approximation because the scattering length is relatively large compared to the range of the potential[11]. For other species such as rubidium, to calculate the scattering length, a more sophisticated model, also taking into account details concerning the inner part of the potential, is used.

The position of this energy level can be measured by Raman spectroscopy: a two-photon transition from the scattering state to the last bound state of the S+S potential (through a virtual level in the vicinity of the S+P potential). The relative detuning of the two photons corresponding to maximum losses (molecules are formed and usually lost) gives the transition energy. From there, the position of the last bound state, and consequently the scattering length, is obtained (illustrated in Fig. 1.3).

Frustrated photoassociation

A refinement of this method, known as *frustrated* photoassociation, deserves to be mentioned [67]. In this method, a *decrease* of atom losses signals the transition. The method consists of applying a first laser with a constant frequency, resonant with the transition between the scattering state of the S+S potential and a chosen bound state in the S+P potential. This creates molecules and consequently induces atom losses as discussed above. Then a frequency sweep with a second laser is performed. The frequency of this laser is swept through values corresponding to the transition energy between the chosen state in the S+P potential, and a bound state in the S+S potential. When this laser is exactly at resonance with the transition, due to the appearance of a dark state, the molecule formation rate drops and consequently the atom losses *decrease* (see for instance [64] and references therein for a more rigorous explanation).

This short overview is far from exhaustive. In the methods described above, the signature of the transition is based on atom losses. An alternative method is to use a probe laser to excite the scattering state to higher excited states, which can undergo either auto- or photo ionization. The resulting molecular ions can be detected and indicates that the transitions take place. These techniques will not be explained here, but a discussion can be found in Ref. [63] and references therein.

1.1.5 The scattering length of metastable helium: state of the art

The photoassociative methods have been performed to obtain the potential curves for most atoms used commonly for BEC: Li, Na, Rb and Cs, and from there the different scattering lengths have been deduced (for nice overviews

[11] Even though the approximation is good for helium, an even more precise way to obtain the scattering length is to use the measurements of the energy level to correct the already known form of the potential. From the corrected potential, the scattering length can be obtained. This is what the ENS group plans to do.

see Refs. [62, 64]). For hydrogen, the scattering length can be calculated due to the simplicity of the atom. However no spectroscopic measurements for He^* has until now given the scattering length. This does not mean that the scattering length is completely unknown: in this section we will give an overview of how precise the current theoretical and experimental estimates are.

Theory

Two metastable helium atoms in the 2^3S_1 state, each of spin 1, can interact *via* 3 different potentials according to the total spin of the two atoms. The 3 potentials[12] are denoted by $^1\Sigma_g^+$, $^3\Sigma_u^+$ and $^5\Sigma_g^+$ and corresponds to a total spin of 0, 1, or 2, respectively[13]. The total spin depends on the relative orientation of the individual spins of the two atoms: in an unpolarized sample, the total spin can be 0, 1 and 2, while in a polarized sample, all the spins are aligned, and the total spin is necessarily 2. In the magnetic trap (see chapter 2), the spin is polarized, and consequently, the interaction is always described by $^5\Sigma_g^+$ potential. Therefore, the scattering length governing the physics in our magnetically trapped sample corresponds to this potential. The difficulty in calculating a precise value of a springs out of the fact that for this potential, the last vibrational bound state is very close to the dissociation limit. This means that the scattering length is extremely sensitive to the potential well depth: if the well depth is slightly decreased, the last bound level approaches rapidly the potential asymptote so that $a \to \infty$ ($\Delta E \propto 1/a^2$). If it is decreased further, this last level just becomes unbound (ΔE becomes very small and negative), and a jumps to a large *negative* value. The total decrease required to make this level unbound is very small, and consequently, even a small uncertainty in the calculated well depth corresponds to a very high uncertainty on a. The variation of the scattering length as a function of the well depth in Kelvin is illustrated in Fig. 1.4. The solid vertical line at $\sim$ 1488 K gives the well depth for which the last bound state (assuming a higher well depth) just becomes unbound.

The first precise calculation of this potential was done by J. Stärk and W. Meyer in 1994 [68]. They found that the well supports 15 bound vibrational states, and they claim and uncertainty of 1 % on the potential depth. Their central value for the well depth is 1505 K, indicated by the dashed lines in Fig. 1.4. The grey bands indicate their uncertainty. Even though the uncertainty on the potential is only 1 % this leads to huge variations on a as shown in Fig. 1.4: a varies between 4 and 60 nm around a central value of 8 nm! In 2000, V. Venturi and I. B. Whittingham published a refined calculation of a. It is based on the potential from J. Stärk and W. Meyer, but the connection between the inner and outer part of the potential is better.

[12] The same notation is often used to indicate the molecular state.

[13] For long distances between the atoms, the potentials become equivalent and tend toward the $-C_6/r^6$ potential (the S+S potential shown above).

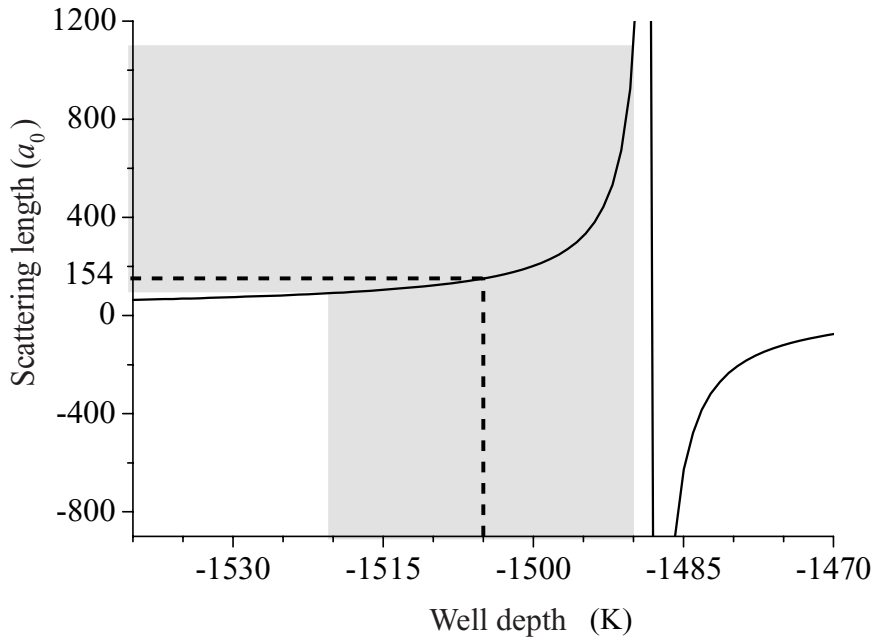

Figure 1.4: *Variation of a in Bohr radius units ($a_0 = 0.053$ nm.) according to variations in the potential. The dashed lines indicate the well depth and corresponding value for the scattering length obtained in Ref. [68], and the gray bands corresponds to the claimed uncertainty of 1 % of the potential. The figure is again from Ref. [62].*

They give the same central value for a, but reduce the error-bars confining a to the interval between 5 and 25 nm [69]. In 2002, F. X. Gadéa, T. Leininger and A. S. Dickinson published new calculations of the potential [70]. In their abstract they state that "*...there are certainly 15 vibrational levels and that the dissociation energy is most probably 1045.2 ± 1 cm^{-1}...*". Their final value of a is 15.4 nm, but they stress that this is only an upper limit. Before starting the experiments described in this thesis, these values for the scattering length were the most precise theoretical estimates available. After our determination of a described in this thesis, a second paper from A. S. Dickinson *et al.* was published and gave an improved result: a should be between 8.0 and 12.2 nm [71], the most probable value being the upper limit. This is to our knowledge the most precise theoretical value published, and as we will see in this thesis, it turns out to be consistent with our results.

Experiments

In 2001, a Bose-Einstein condensate of He^* was almost simultaneously produced for the first time in the ENS group and in our group. Using these condensates, a measurement of the scattering length was estimated. Our group published $a = 20 \pm 10$ nm [8], while the ENS group published $a = 16 \pm 8$ nm [9]. In both cases, the large uncertainty was due to difficulties in direct measurements of the atom number in the condensate.

As mentioned above, spectroscopic measurements of the scattering length are already underway in the ENS group in Paris and a precision of less than a nm is expected. The ENS group is implementing an off-resonant two-photon Raman transitions to determine the position of the last bound state, and from there deduce a. They are also exploring the 2-photon scheme based on frustrated photoassociation. One-photon transitions to the upper S+P state have been successfully implemented [72, 62].

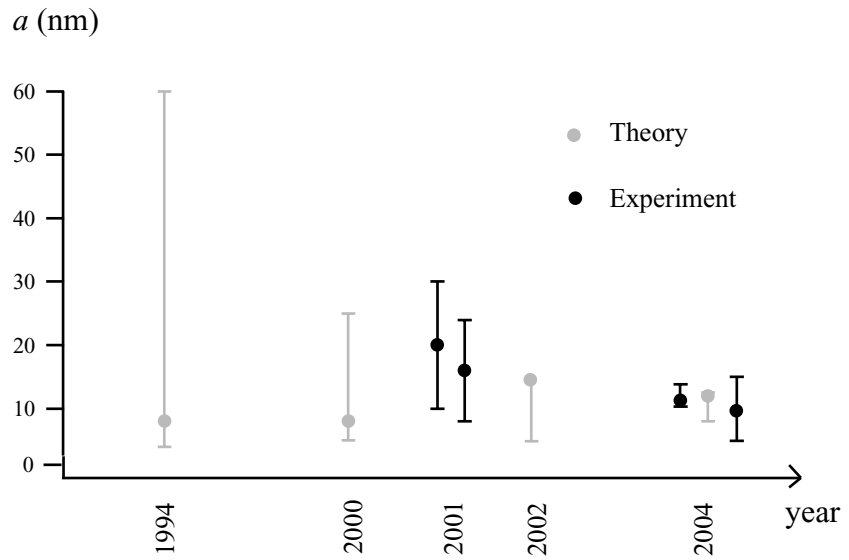

Figure 1.5: *Estimates for the scattering length. The first value comes from J. Stärk and W. Meyer, the second from V. Venturi and I. B. Whittingham. The next two experimental values come from BEC measurements (our group and ENS), followed by a theoretical value from F. X. Gadea et al. (2002). The most precise theoretical value is published two years later (2004), and comes from this same group. The first measurement in 2004 is from our group, and will be discussed in detail in this thesis. The last indicated measurement comes from the group of W. Vassen:* $|a| = 10 \pm 5$ *nm [73].*

A summary of the different values for a, theory and experiment, is given in Fig. 1.5. To the values discussed in this section, one experimental value is added: $a = 11.3^{+2.5}_{-1.0}$ nm. This is one of the main results of this Ph.D. thesis.

It is a new and quite atypical measurement of a, and it is the most precise value to date. Our measurement of a is based on the ion signals from a BEC and a thermal cloud. These ions are produced in inelastic collisions ("bad collisions"), which will be discussed in the next section. In chapter 5, we will explain how these ion rates lead to a measurement of the scattering length.

1.2 Inelastic collisions

If an excited particle A* collides with particle B, the latter can be ionized if its ionization energy is less than the excitation energy of A:

$$A^* + B \rightarrow A + B^+ + e^-$$

This reaction is an example of an inelastic collision, because the internal state of the atom is modified. For He* the internal excitation energy is 19.8 eV. This is several times higher than the ionization energy for a collision with another He* atom (4.77 eV), and also higher the ionization energies for collisions with the dominant background molecules, H_2O (12.5 eV) and H_2 (15.5 eV) [74]. In the experiments described in this thesis, we detect the ions produced by these collision using a micro-channel plate (see chapter 2) to use the ion signal to infer the properties of the trapped cloud.

These ionizing collisions are called *Penning collisions*[14], and occur when the particles entering in the collision get sufficiently close to each other, provided that the energy requirement is fulfilled. Therefore, in a trapped dense sample of He*, the rate of ionizing collisions increases with the density. The Penning collisions are essential in the work performed in this thesis, and we will in the following provide an overview of the collisions as well as their dependence on the sample density. A more detailed description of the Penning collisions in He* systems figures several times in literature, see for instance [34, 37, 76, 77].

Each time a He* atom is ionized, it is lost from the trap. Penning collisions therefore induce atom losses. We will also explain why these atom losses turn out to be lower than one might expect, and therefore do not prevent the formation of a dense sample of atoms or a Bose-Einstein condensate.

1.2.1 Penning collisions

A Penning collision can occur both between a trapped He* atom and a background molecules, and between two or more trapped He* atoms. Both types of collisions are present, but depending on the density of the sample, not the same reactions will dominate. We will below consider each of the collisions separately.

[14] The name is given after the Dutch physicist F.M. Penning who already suggested this process in 1927 [75].

$\mathbf{He^* + X}$

When the density of the sample is sufficiently low, collisions between trapped atoms become rare and the collisions with the background gas dominate[15]. This is the case for our magnetically trapped sample, before we start the rf-evaporation (see chapter 2). A collision with a background molecule can be written as[16]:

$$\mathrm{He}^*(2^3S_1) + \mathrm{X} \rightarrow \begin{cases} \mathrm{He}(1^1S_0) + \mathrm{X}^+ + e^- \\ \mathrm{He}X^+ + e^-, \end{cases} \tag{1.28}$$

where X represents a background gas molecules (H_2O, H_2). Each of the two reactions yield an ion, and in both cases one He^* atom is lost from the trap (neither the created ground state He atom nor the molecular ion is confined in the trap). The subsequent local density loss is given by[17]

$$\left.\frac{dn(\mathbf{r})}{dt}\right]_{ion} = -\alpha \times n(\mathbf{r}) \times n'(\mathbf{r}). \tag{1.29}$$

The density of the trapped sample of He^* is denoted $n(\mathbf{r})$ while $n'(\mathbf{r})$ is the density of the background gas. We define α as the *ionizing* rate constant for background collisions. With this definition, the density loss is due to ionizing collisions alone, and not other inelastic processes (indicated by the subscript *ion* in the equation). As α and $n'(\mathbf{r})$ are constants, we can rewrite Eq. 1.29 as:

$$\left.\frac{dn(\mathbf{r})}{dt}\right]_{ion} = -\frac{n(\mathbf{r})}{\tau_i}. \tag{1.30}$$

The quantity τ_i is in fact the background limited lifetime of the sample due to *ionizing* collisions[18], and $n(\mathbf{r})$ the local density. The total loss rate is obtained by integrating the density loss over the spatial extent of the sample

$$\left.\frac{dN}{dt}\right]_{ion} = -\frac{1}{\tau_i}\int n(\mathbf{r})\mathrm{d}\mathbf{r} = -\frac{N}{\tau_i}. \tag{1.31}$$

This loss rate is independent of the density of the sample. As one ion is created for one atom lost, the ionization rate arising from this kind of collisions is simply given by

$$\Phi = \frac{N}{\tau_i}. \tag{1.32}$$

[15] For a typical background pressure of $\simeq 10^{-11}$ mbar, this is true when the average density of the cloud is below $\langle n \rangle < 10^8$ cm^{-3}).

[16] This collision is sometimes called a "one-body" collision because only one atom from the trapped sample participates.

[17] One could also imagine that the collisions result in a heating and a subsequent additional density loss. However, as secondary collisions (collisions with decay products from the first reaction) are negligible, so is the heating (see Refs. [13, 37]).

[18] Note that the total density loss (not only due to ionizing collisions as above) would be written as $\frac{dn(\mathrm{r})}{dt} = -\frac{n(\mathrm{r})}{\tau}$, with τ the total lifetime of the sample.

$\mathbf{He^* + He^*}$

When the density of the sample is increased, collisions between two He^* atoms become probable. Also in this type of Penning collision, two reactions can take place: either one He^* decays to the ground state, transferring its internal energy to the other He^* atom which is consequently ionized, or a molecular ion is formed [78]:

$$\mathrm{He}^*(2^3S_1) + \mathrm{He}^*(2^3S_1) \rightarrow \begin{cases} \mathrm{He}(1^1S_0) + \mathrm{He}^+ + e^- \\ \mathrm{He}_2^+ + e^- \ . \end{cases} \tag{1.33}$$

Here, the collision rate depends on the He^* density squared and therefore the density loss is given by

$$\left.\frac{dn(\mathrm{r})}{dt}\right]_{ion} = -\beta\, n(\mathrm{r})^2, \tag{1.34}$$

where we have defined the two-body ionization rate constant β. The ionization rate can be written again by integrating and by noting that two atoms are lost for each ion created

$$\Phi = \frac{1}{2}\,\beta \int n(\mathrm{r})^2 \mathrm{d}\mathbf{r}, \tag{1.35}$$

This can be written in a simpler notation by defining a "density-weighted average" as[19]

$$\langle X(\mathbf{r})\rangle = \frac{\int X(\mathbf{r}) n(\mathbf{r}) d\mathbf{r}}{\int n(\mathbf{r}) d\mathbf{r}} = \frac{\int X(\mathbf{r}) n(\mathbf{r}) d\mathbf{r}}{N}.$$

We get

$$\Phi = \frac{1}{2}\beta \langle n(\mathrm{r})\rangle\, N. \tag{1.36}$$

$\mathbf{He^* + He^* + He^*}$

When the density gets very high (above 10^{12} cm^{-3}), three-body collisions start to contribute to the loss processes[20]. This happens in the end of the rf-evaporation, in the vicinity of the Bose-Einstein condensation. The three-body collision can be written as [79]:

$$\begin{array}{rcll} \mathrm{He}^* + \mathrm{He}^* + \mathrm{He}^* & \rightarrow & \mathrm{He}_2^* & +\mathrm{He}^*(\sim 400\ \mu\mathrm{K}) \\ & & \hookrightarrow & \mathrm{He}^+ + \mathrm{He}(1S) + e^-. \end{array} \tag{1.37}$$

The collision produces an excited molecule (He_2*) and a hot He^* atom[21]. The He_2* molecule is supposed to decay very fast, giving a ground state He

[19] Note that the brackets defined contain a dimension – they replace a volume.

[20] The contribution from two-body and three-body processes becomes equal for a density of $\sim 10^{13}$ cm^{-3}

[21] The acquired energy of this atom corresponds to the binding energy of the He_2* molecule, i.e. $\sim \hbar^2/2ma^2$.

atom, and an ion, which we can detect. Again we write the density loss due to this process:

$$\left.\frac{dn(\mathrm{r})}{dt}\right]_{ion} = -Ln(\mathrm{r})^3, \tag{1.38}$$

where we now have defined the three-body ionizing rate constant L. In this process, three atoms are lost for each ion created, so the ionization rate becomes

$$\Phi = \frac{1}{3}L\int n(\mathrm{r})^3 \mathrm{d}\mathbf{r} = \frac{1}{3}L\langle n(\mathrm{r})^3\rangle = \frac{1}{3}L\langle n(\mathrm{r})^2\rangle\, N. \tag{1.39}$$

The total ionization rate

Finally, the total ionization rate is obtained by summing the contributions due to background, two- and three-body collisions:

$$\Phi = \frac{N}{\tau_i} + \frac{1}{2}\beta\langle n(\mathrm{r})\rangle N + \frac{1}{3}L\langle n(\mathrm{r})^2\rangle N. \tag{1.40}$$

In this thesis, we will most often use the normalized ionization rate, which we denote by Γ

$$\Gamma = \frac{1}{\tau_i} + \frac{1}{2}\beta\langle n(\mathrm{r})\rangle + \frac{1}{3}L\langle n(\mathrm{r})^2\rangle, \tag{1.41}$$

because a graph of the normalized ionization rate as a function of density can be written in a way which has an obvious geometrical interpretation: if it is a straight line, the dominating collisions are two-body processes, while a three-body dominance gives a parabola.

In chapter 3 we will give some examples on how we can exploit the ion signal arising from the Penning collision to obtain information about the sample, and in chapter 4, we will present measurements of the two- and three-body rate constants β and L in a pure BEC. In the same chapter, we will also present measurements of ionization rates in a cold thermal cloud.

For later use, we will therefore in the following list the explicit expressions for the ionization rate in these two cases by using the fact that the density distribution in the two cases are well-known.

1.2.2 Ionization rates in a thermal cloud

The density distribution for a thermal cloud far from BEC threshold can be described by a Gaussian function. In this case, $\langle n(\mathrm{r})^2\rangle = 8/(3\sqrt{3})\langle n(\mathrm{r})\rangle^2$ and the ionization rate can be written as

$$\Gamma_{\mathrm{Th}} = \frac{1}{\tau_i} + \frac{1}{2}\,\beta\,\langle n\rangle + \frac{1}{3}\,\frac{8}{3\sqrt{3}}L\,\langle n\rangle^2. \tag{1.42}$$

This expression for the ionization rate will be used in chapter 4 to fit the measured ionization rate as a function of density[22].

[22] One could also choose to write the ionization rate in terms of the peak density as we will do for the BEC (see below). For a Gaussian distribution, we have $\langle n(\mathrm{r})\rangle = \frac{1}{2\sqrt{2}}n_0$

1.2.3 Ionization rates in a Bose-Einstein condensate

In our measurements using a pure BEC, we will not measure directly the density, but the chemical potential. From this chemical potential, the peak density, n_0, can be deduced. We will therefore write the ionization rate as a function of n_0 instead of average density as we did for the thermal cloud. In our case, the pure condensate is well described by the Thomas-Fermi distribution, corresponding to an inverted parabola [17]. Using this distribution, the relations between the density weighted average values and peak density n_0 can be obtained:

$$\langle n(\mathrm{r})\rangle = \frac{4}{7}n_0 \quad \text{and} \quad \langle n(\mathrm{r})^2\rangle = \frac{8}{21}n_0^2. \tag{1.43}$$

Substituting into Eq. 1.40, and writing the ionization rate per atom Γ, we obtain

$$\Gamma_{\mathrm{BEC}} = \frac{1}{\tau_i} + \frac{1}{2}\frac{4}{7}\beta' n_0 + \frac{1}{3}\frac{8}{21}L' n_0^2. \tag{1.44}$$

Importantly, note that we have added a prime to the rate constants. The reason is that the rate constants given in Eq. 1.40 are defined for a thermal cloud and due to quantum statistics, they are different for a Bose-Einstein condensate. However, the rate constants for a BEC is related in a simple way to the rate constants in a thermal cloud:

$$\beta' = \frac{1}{2!}\beta \qquad \text{and} \qquad L' = \frac{1}{3!}L.$$

so we can rewrite Eq. 1.44 as

$$\Gamma_{\mathrm{BEC}} = \frac{\Phi}{N} = \frac{1}{\tau_i} + \frac{1}{2!}\frac{1}{2}\frac{4}{7}\beta n_0 + \frac{1}{3!}\frac{1}{3}\frac{8}{21}L n_0^2. \tag{1.45}$$

"Quantum reduction factors"

The added factors ("quantum reduction factors") arise from the fact that in a BEC, the particles are all in the same energy level, while in a thermal cloud, the particles are spread over different energy levels. In both cases the wavefunction must be symmetric, as the He^* atoms are bosons. For N Bose-Einstein condensed atoms entering in a collision (in the mean field approximation) the wavefunction is

$$|\Psi_{\mathrm{BEC}}\rangle = \overbrace{|\phi_i\rangle|\phi_i\rangle....|\phi_i\rangle}^{N}, \tag{1.46}$$

where the ground state of the many-body wavefunction is denoted by $|\phi_i\rangle$. This wavefunction is symmetric with respect to exchange of particles. However, for a thermal cloud with the different energy levels denoted by $i, j, k...$, the simple product wavefunction is not symmetric as it should be:

and $\langle n(\mathrm{r})^2\rangle = \frac{3\sqrt{3}}{8}n_0^2$, and the ionization rate is then $\Gamma_{\mathrm{Th}} = \frac{1}{\tau_i} + \frac{1}{2}\frac{1}{2\sqrt{2}}\beta n_0 + \frac{1}{3}\frac{3\sqrt{3}}{8}L n_0^2$.

$$|\Psi_{\rm Th}\rangle = \overbrace{|\phi_i\rangle|\phi_j\rangle...|\phi_k\rangle}^{N}. \tag{1.47}$$

The correctly symmetrized wavefunction is:

$$|\Psi_{\rm Th}\rangle = \frac{1}{\sqrt{N!}} \overbrace{\{|\phi_i\rangle|\phi_j\rangle...|\phi_k\rangle + ... + |\phi_j\rangle|\phi_k\rangle...|\phi_i\rangle\}}^{N!\ \text{terms}}. \tag{1.48}$$

Now the probability P of having a collision between N particles can be written as $|\langle\Psi_{\rm final}|V|\Psi_{\rm initial}\rangle|^2$, with $|\Psi_{\rm initial}\rangle$ the N particle wavefunction and V the particle interaction. For a N-body collision in a BEC we have

$$P_{\rm BEC} \propto |\langle\Psi_{\rm final}|V|\phi_i\rangle|\phi_i\rangle...|\phi_i\rangle|^2, \tag{1.49}$$

while for a N-body collision in a thermal cloud

$$P_{\rm Th} \propto \frac{1}{N!}|\langle\Psi_{\rm final}|V|\overbrace{\phi_i\rangle|\phi_j\rangle...|\phi_k\rangle + ... + |\phi_j\rangle|\phi_k\rangle...|\phi_i\rangle}^{N!\ \text{terms}}|^2. \tag{1.50}$$

If we assume that the matrix elements of V for the different states are equal so that $\langle\Psi_{\rm final}|V|\phi_i\rangle|\phi_j\rangle...|\phi_k\rangle = \langle\Psi_{\rm final}|V|\phi_i\rangle|\phi_i\rangle...|\phi_i\rangle$, then

$$P_{\rm Th} \propto \frac{1}{N!}|N! \times P_{\rm BEC}|^2 = N! \times P_{\rm BEC}. \tag{1.51}$$

Thus the collision probability is reduced for a BEC with respect to a thermal cloud by a factor of $N!$. This is the reason why we must insert 1/2! and 1/3! in Eq. 1.44 if we keep the rate constants as they are defined for thermal cloud.

Further corrections to this expression turn out to be necessary. These corrections arise from the fact that not all the atoms are part of the condensate wavefunction: this is due to the so-called quantum depletion arising from interactions between the atoms. Also the fact that the condensate is not at zero temperature results in the fact that some of the atoms are outside the condensate. However, in order to understand these corrections, more background knowledge of the experiment is needed, which will be given in chapter 2. These corrections will therefore first be discussed in chapter 4, where we will use Eq. 1.44 to fit experimental data to obtain the rate constants.

1.2.4 Ionizing rate constants: predictions

So far we have not given any orders of magnitude for the ionization rates, because in addition to the density dependence, it also depends on which kind of trap we use: if the atoms are confined in a MOT, they are not spin polarized (see chapter 2) while in the magnetic trap, they are. This changes dramatically the ionization rates, as we will explain in the following.

The Penning collision arises to first order from an electrostatic interaction. In this kind of interaction, the total spin must be conserved. This is impossible in a two-body Penning ionization between spin polarized atoms. Consider the spin of the initial and final particles

$$\begin{array}{ccccccccc} \mathrm{He}^*(2^3S_1) & + & \mathrm{He}^*(2^3S_1) & \rightarrow & \mathrm{He}(1^1S_0) & + & \mathrm{He}^+ & + & e^-. \\ 1 & + & 1 & \rightarrow & 0 & + & \frac{1}{2} & + & \frac{1}{2} \end{array}$$

In general, the total spin of the initial state can be 0,1 or 2, while that of the final state can be 0 or 1. If the He^* atoms are spin polarized, the total initial spin is necessarily 2, a value which is impossible to reach for the final total spin. The interaction is therefore forbidden.

This is true when one consider only the electrostatic interaction, but another type of interaction is possible. The atoms can interact *via* their magnetic moment associated with their spin (spin-dipole interaction). This interaction can couple states having a different total spin, giving rise to a non-zero ionization rate. The interaction is very weak compared to the electrostatic one, however, and is only non-negligible whenever the latter is forbidden. It has been predicted theoretically, that the ratio of the two types of interactions is around 10^5 [79, 80], reducing the ionization rate constant for a polarized sample with the same factor. Let us give some orders of magnitudes for the rate constants. In general, the rate constants depend on the magnetic field, but below 100 Gauss (which is the case for the magnetic trap in which the BEC is produced, see chapter 2), they are field independent [79, 80, 81]. Moreover, the rate constants depend on temperature, but below approximately 10 mK they are approximately constant[23]. The two-body ionizing rate constant $\beta_{\mathrm{non-pol}}$ corresponding to non-polarized atoms has been estimated theoretically to be $\simeq 5 \times 10^{-10}$ cm^3/s at zero temperature [82]. Its value has also been measured at temperatures around 1 mK [83, 84, 85, 86, 87], and agrees approximately with the theoretical estimations. The two-body rate constant for a polarized sample is about 10^5 times weaker, thus we expect $\beta \simeq 5 \times 10^{-15}$ cm^3/s in the magnetic trap. The three-body rate constant L is estimated theoretically to be $\simeq 4 \times 10^{-27}$cm^6/s (for $a \sim 12$ nm) for a spin polarized sample for low temperatures and magnetic fields [88].

Note that it is due to this suppression of Penning collision that it is at all possible to achieve BEC. In a non-polarized sample with a density of $\simeq 10^{12}$ cm^{-3}, the ionizing lifetime of the sample is only 2 ms, much shorter than the duration of the experimental cooling sequence. In a polarized sample, the lifetime for the same density becomes background limited, and for typical background pressures, it is around 100 s, three times longer than the average duration of the cooling sequence. In this case, the sample is sufficiently stable to reach BEC.

[23] Above 10 mK, the dominant loss process is no longer ionizing collisions, but spin relaxation [79].

Chapter summary and outlook

In this chapter, we have discussed elastic collisions and provided the reader with a definition of the s-wave scattering length. At the low temperatures realized in our experiment, most physical properties can be predicted by the scattering length alone. In addition, as we will see in chapter 4, if we know the scattering length, we have a precise way of measuring the density for a BEC, namely *via* the chemical potential. This is why the scattering length is an extremely useful parameter to know. In this chapter we have presented the existing values, theoretical as well as experimental, for the scattering length. Moreover, we mention the fundamental reason why it is so difficult to calculate this constant: the last bound level in the two-atom potential is very close to the dissociation limit. Therefore the scattering length is very sensitive to even minor changes in the two-atom potential, and a small uncertainty in this calculated potential leads to a huge uncertainty in the scattering length. Therefore, the best way to obtain this parameter is through experiments – and this is one of the motivation behind the measurements described in this thesis.

A large part of this thesis work is related to the measurement of the ionizing rate constants. Therefore, the ionizing processes are also discussed in detail in this chapter, and should give the theoretical background for understanding these experiments. Also our measurement of the scattering length presented in chapter 5 is based on these inelastic collisions, even though this must still appear paradoxical at this stage of the reading. Some insight into the experiment itself is necessary to clarify how this can be true – and will allow one to place the work performed in this thesis in a larger context. The goal of the next chapter is therefore to provide the reader with this insight.

CHAPTER 2

A Bose-Einstein condensate of metastable helium

The nature of the physicist exhibits a peculiar desire of wanting to go to a lot of bother, the sole recompense being the personal satisfaction gained in reaching the goal[1]. One might think that this was also the case when physicists first attacked the problem of Bose-Einstein condensation of metastable helium. It had already been proven that Bose-Einstein Condensation was experimentally possible, and not only for one atomic species, but for all of H, Li, Na and Rb. This time, however, the recompense went far beyond personal satisfaction. As we will see in this thesis, the BEC of He^* offers a new and very useful tool for the physicist: thanks to the internal energy of the atoms, one can use a micro-channel plate for detection of a cloud of neutral atoms. Moreover, due to a continuous production of ions in the cloud, one can use the same micro-channel plate to monitor the sample without disturbing the natural evolution of the cloud.

In this chapter, we will first give an ultrashort introduction to the physics describing the Bose-Einstein condensation, and introduce some concepts needed later on. However, this chapter is primarily devoted to an overview of the different steps required to produce and characterize a Bose-Einstein condensate. It will be far from exhaustive, but it should at least give the necessary background for understanding the experiments presented in this thesis. If the reader desires more details on the apparatus, this can be found in Refs. [34, 35, 36, 37]. We will in this chapter concentrate on the detection of atoms as well as ions with a micro-channel plate, which is of particular importance for these experiments. A very careful study of the micro-channel plate was performed by O. Sirjean, and a more complete description can be found in Ref. [37].

[1] This is, by the way, the reason why a lot of physicists are mountaineers in their spare time.

2.1 Bose-Einstein condensation

Many excellent review articles, Ph.D. theses and even books about Bose-Einstein condensation already exist (see for instance [17, 45, 89, 90]). In this section, we will just remind the reader some concepts which will be needed in later chapters.

Bose-Einstein condensation is the macroscopic occupation of a single quantum state. For the typical Bose-Einstein condensates in the gas phase, the single quantum level is the ground state of the external trapping potential (neglecting at the moment atomic interactions). The starting point is therefore this potential, which is a harmonic potential, experimentally realized by using magnetic fields, as discussed below. This potential can be written as

$$V_{\text{ext}}(\vec{r}) = \frac{1}{2}\, m\omega_x^2\, x^2 + \frac{1}{2}\, m\omega_y^2\, y^2 + \frac{1}{2}\, m\omega_z^2\, z^2,$$

where ω_x, ω_y and ω_z are the trap oscillation frequencies. The ground state of N non-interacting bosons in this potential can be written as the product of N identical wavefunctions, each solution to the time-independent Schrödinger equation:

$$\left(-\frac{\hbar^2\nabla^2}{2m} + V_{\text{ext}}(\vec{r})\right)\phi(\vec{r}) = E\phi(\vec{r}), \tag{2.1}$$

i.e. each described by a Gaussian function, which is the ground state corresponding to a harmonic oscillator potential. Because of interaction between atoms, the Schrödinger equation is modified. These interactions introduce a non-linear term as expressed in the Gross-Pitaevskii equation (see for instance [17]):

$$\left(-\frac{\hbar^2\nabla^2}{2m} + V_{\text{ext}}(\vec{r}) + U\phi^2(\vec{r})\right)\phi(\vec{r}) = \mu\phi(\vec{r}). \tag{2.2}$$

The atomic interactions is proportional to the particle density, and the strength of the interactions described by $U = \frac{4\pi\hbar^2 a}{m}$, with a the s-wave scattering length discussed in detail in chapter 1. Note that if a is negative, the potential is attractive, and if a is positive, it is repulsive. The energy μ is the chemical potential. Even though we include interactions (as long as they do not become too strong), we can still write the total wavefunction as a product of the N individual wavefunctions. This is the mean field approximation. To determine the single particle wavefunction, we must solve Eq. 2.2. Very often in the experiments however, the kinetic energy is negligible compared to the interaction energy. In that case Eq. 2.2 has a very simple solution:

$$\phi(\vec{r}) = \sqrt{\frac{\mu - V_{\text{ext}}(\vec{r})}{U}}, \tag{2.3}$$

for $\mu > V_{\text{ext}}$ and $\phi(\vec{r}) = 0$ outside. The density is obtained from $n(\vec{r}) = \phi^2(\vec{r})$, i.e. it has the shape of an inverted parabola. This is the Thomas-Fermi approximation. By requiring $N = \int n(\vec{r})d\vec{r}$, we can obtain a relation between chemical potential and atom number:

$$\mu = \frac{\hbar\bar{\omega}}{2}\left(\frac{15Na}{\sigma}\right)^{2/5},$$

where $\bar{\omega} = (\omega_x^2\omega_y^2\omega_z^2)^{1/3}$ and $\sigma = (\hbar/m\bar{\omega})^{1/2}$. The peak density n_0 is the maximum density (the density at $\vec{r} = 0$) and can also be obtained from the chemical potential:

$$n_0 = \frac{\mu}{U} = \frac{m}{4\pi\hbar} \times \frac{\mu}{a}.$$

We will use these relations extensively in chapter 4 to obtain the atom number and peak density from measurements of the chemical potential for the condensate.

2.2 Experimental apparatus

Let us start with an overview of the setup used for making our Bose-Einstein condensate. It is shown in Fig. 2.1. The setup can be separated into four main parts:

- The source (A): an atomic beam of helium atoms is generated, and the atoms are excited to the 2^3S_1 metastable state (defined in Appendix A).
- The transverse collimation of the atomic beam (B): it consists of two pairs of retro-reflected laser beams, resonant with the $2^3S_1 \rightarrow 2^3P_2$ transition.
- The Zeeman Slower (C): the longitudinal velocity of the atoms is decreased giving a slow atomic beam.
- The ultrahigh vacuum chamber (D): the atoms are collected in a magneto-optical trap before being transferred to a magnetic trap for further cooling. It is also here that the detection of the cold atomic clouds with a micro-channel plate takes place.

In the following we will go more into detail with the description of these four zones.

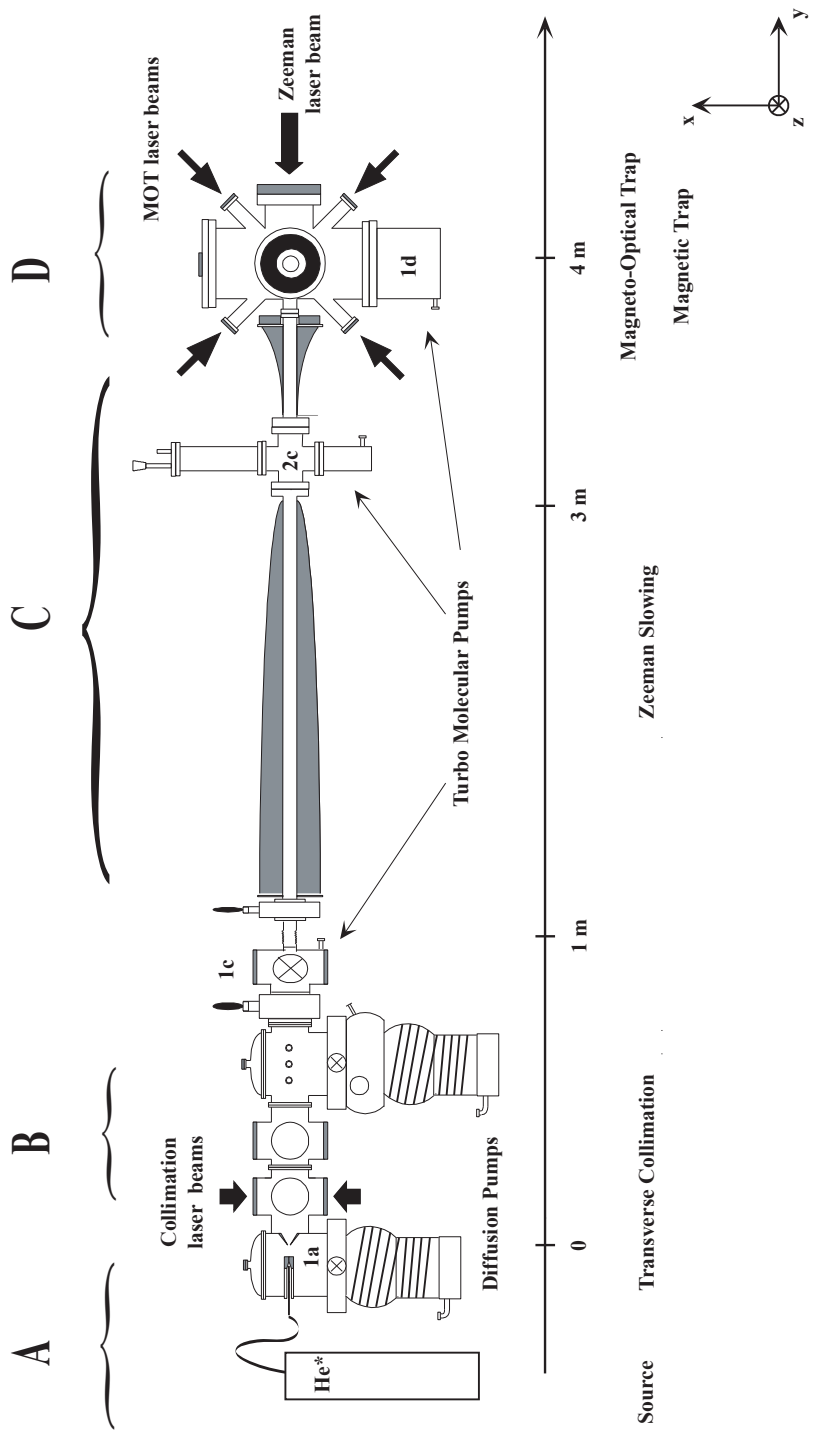

Figure 2.1: *The experimental apparatus for producing a BEC of He*. The different parts are described in the text.*

2.2.1 The source zone

The ground state helium atoms come out of a bottle attached to the extreme left of the setup in Fig. 2.1 A, and enter the first zone of the vacuum system. This part of the vacuum system is pumped by a diffusion pump (3000 ℓ/s)[2], which is the first pump indicated in Fig. 2.1. The pressure obtained is around 10^{-7} mbar when the atomic beam is switched off, and increases to around 2×10^{-4} mbar, when the experiment is running. When the bottle is opened, the ground state helium atoms are guided through a narrow opening in a copper block (1a in the figure). The copper block is cooled by liquid nitrogen, in order to decrease the initial velocity of the atoms. The smooth operation of the experiment is extremely dependent on this cooling process – a small increase (5-10 %) of the temperature of the copper block makes it impossible to obtain a Bose-Einstein condensate. For instance, the temperature of the block is increased if the nitrogen flow is hindered by the presence of small nitrogen crystals, stuck in the thin pipes. Having passed the block, the atoms explode into the vacuum, forming a supersonic atomic beam [91, 92]. The excitation to the metastable state happens between a needle held at a voltage of around 3 kV and a skimmer, which is grounded (1a in the figure). The needle is situated parallel to the beam before the copper block. The needle is separated from the copper block by boron nitrite, which in addition to its high thermal conductance isolates electrically, assuring that the discharge happens between the needle and the skimmer, and not between the needle and the copper. The excitation efficiency is of the order of one atom excited out of 10^4 atoms remaining in the ground state. When the experiment is running smoothly, the initial flux of the beam produced is $\simeq 10^{12}$ atoms/s and the longitudinal velocity is of the order of 1200 m/s. The divergence of the beam is $\simeq 40$ mrad [34].

2.2.2 Transverse collimation of the atom beam

After leaving the source, the atoms enter the transverse collimation region B. The vacuum here is also maintained by a diffusion pump. Due to the small size of the opening in the skimmer, the conductance between the source and the transverse collimation region is small, and a differential pressure is established: the vacuum in the collimation zone is maintained at 10^{-7} mbar, even when the atomic beam is on. The transverse collimation consists of two pairs of retro-reflected laser beams perpendicular to the propagation of the atomic beam (Ox and Oz in Fig. 2.1). As indicated in the figure, a second pair of windows situated next to the first one is present. It was designed to apply the transverse collimation a second time, but it turns out not to be necessary. The laser beams are resonant with the 2^3S_1–2^3P_2 transition, and by using curved wave fronts, interaction with atoms from a broader velocity range [93, 94, 95] is possible. The beams have an elongated profile,

[2]This is the efficiency for helium, while for nitrogen, it is 2400 ℓ/s [34].

the longest side parallel with the beam, in order to increase the interaction time. The effect of the transverse collimation is twofold. First, it decreases the divergence of the atomic beam, which is essential because the Zeeman slowing requires a long propagation (3 meters) of the beam. Second, it eliminates a large fraction of the ground state atoms in the beam: as the collimation only affects the atoms in the metastable state, only these atoms are collimated. By subsequently passing the beam through a small pinhole (4 mm), a large fraction of the ground state atoms are filtered away. To avoid a perturbation of the experiments in the ultrahigh vacuum chamber due to the continuous atomic beam, a mechanical shutter is situated before the pinhole, in order to cut off the atomic beam once a sufficient number of atoms has been collected in our trap.

After the transverse collimation, the beam contains $\simeq 2 \times 10^{11}$ atoms/s and the divergence is reduced to about 2 mrad. This produces an increase of the atomic beam intensity *after* propagation in the Zeeman of approximately a factor of 70 [36].

2.2.3 Zeeman Slowing of the atomic beam

The next part of the experiment is the Zeeman Slower C. This part is separated from the source and transverse collimation vacuum system by a valve, which is closed when the experiment is not running. The vacuum in the Zeeman Slower is maintained by two turbo molecular pumps, 1c and 2c, with pumping speeds of 250 ℓ/s and 50 ℓ/s, respectively. A diaphragm is situated near the second turbo molecular pump, in order to eliminate as many as possible of the remaining ground state atoms[3]. The small diameter of the inner tube of the Zeeman Slower (43 mm) in combination with the diaphragm leads to a low conductance and hence a differential vacuum: it is 3×10^{-8} mbar immediately after the valve and decreases along the Zeeman Slower to the ultrahigh vacuum chamber, where the pressure is less than 10^{-10} mbar.

The Zeeman Slower has become a standard tool in cold atom experiments [96]. A counter-propagation laser beam combined with a longitudinally decreasing magnetic field slow the atomic beam down due to the simultaneous presence of the Zeeman and Doppler effect. Result: the He^* atoms are slowed down from 1200 m/s to around 100 m/s, and the beam flux is reduced to $\sim 5 \times 10^9$ atoms/s. As the beam has diverged during the propagation due to spontaneous emission (the beam diameter is increased from few millimeters to around 4 cm), the profile of the beam is larger than the capture area of the magneto-optical trap (see later in this chapter), limiting the loading rate. In addition, because of geometric limitations, there is a gap between the end

[3]Even when using the pinhole, far from all ground state atoms are eliminated. On arrival at the vacuum chamber, the beam still contains 150 times more ground state atoms than metastable atoms. As they are not loaded into the trap, they will contribute to the background pressure before they are pumped away.

of the Zeeman Slower and the center of the trapping region, which also decreases the loading rate. We measure a loading rate of the magneto-optical trap of $\sim 5 \times 10^8$ atoms/s.

A remarkable thing about our Zeeman Slower is it length – it is almost three meters long, much longer than the typical Zeeman Slowers used in rubidium experiments, for instance. The reason follows from the expression of the length, which can be written as [34]:

$$L = \frac{mv^2}{\hbar k \Gamma} \propto \frac{k_B T_{\text{init}}}{\hbar k \Gamma}. \tag{2.4}$$

For He^*, both the linewidth of the transition and the wave number $k = 2\pi/\lambda$ is small compared to rubidium, making the required length of the Zeeman Slower larger. Note that this length does not depend on the atom mass, but only of the properties of the atomic transition.

2.2.4 The ultrahigh vacuum chamber

The heart of the experiment is the ultrahigh vacuum (UHV) chamber (D in Fig. 2.2), which is a large metallic chamber. Most often BEC experiments are done in small glass cells, because it represents several advantages compared to a large metallic chamber. For instance, as the volume is smaller (and glass can be cleaner), it is easier to reach a low pressure. In addition to this, the small size of a glass cell allows the coils used for generating trapping magnetic fields to be placed very close to the atoms. Consequently, it is easier to create stronger fields with lower currents. Finally, no eddy currents can be induced in the glass which generates perturbing stray fields. In our case however, practical considerations prevent us from using a glass cell: we use a micro-channel plate (section 2.4), which requires connections to electronics outside the vacuum and a large space (the micro-channel plate is in our case situated 5 cm below the trapping region). Moreover, since glass is a non-conducting material, the inner surfaces of the cell can become polarized, perturbing the electric fields applied to the micro-channel plate. Consequently, the glass cell is not a possible choice, and one must instead deal with the difficulties arising from the use of a large metallic vacuum chamber.

The volume of the chamber is 8 ℓ, and the material used is stainless steel. The geometry has been chosen in order to bring the exit of Zeeman Slower as close as possible to the center of the trapping region, without blocking the optical path of the laser beams used for the magneto-optical trap. In order to minimize the distance between the magnet coils used for trapping the atoms (section 2.3) and the atomic cloud, re-entrant flanges are used, as shown in Fig. 2.2. Shortening this distance minimizes the current necessary to generate the desired fields. Despite the re-entrant flanges, the current still needs to be quite high (240 A), and to obtain an efficient cooling, the coils are made of hollow wires, inside which water flows under pressure. An

alternative solution would be to bring the coils closer to the trapping zone by placing them *inside* the vacuum system, but when working at UHV, the less one puts inside the chamber (especially something which needs water cooling), the better it is.

The chamber is pumped by a turbo molecular pump (500 ℓ/s) with a high compression ratio for hydrogen and helium (5×10^6 and 5×10^7, respectively). The pressure obtained with the turbo molecular pumps alone is around 10^{-10} mbar, which is not sufficiently low. Therefore the pressure is further decreased by using titanium sublimation [34]. After sublimation the pressure reaches $\sim 10^{-11}$ mbar[4], corresponding to a lifetime of a magnetically trapped cloud of approximately 100 s.

2.3 Towards cold clouds and Bose-Einstein condensates

After this overview of the main parts of the setup, we can now turn to the production of cold clouds and condensates. We will describe briefly the sequence step by step: the magneto-optical trap, the magnetic trap, radio-frequency evaporation and how we detect the atomic cloud and ions produced.

2.3.1 The magneto-optical trap: millikelvin regime

We load the atoms from the slow beam directly into magneto-optical trap (MOT). This type of trap was first proposed by J. Dalibard and later experimentally realized [97]. It consists of 3 pairs of red-detuned, circular polarized, counter-propagating laser beams (σ^+ and σ^-) and magnetic field gradients. By Doppler and Zeeman shifts, the atoms are both confined to the trap center and cooled down. When polarization gradient cooling is neglected, the theoretical lower temperature limit T for atoms trapped in a MOT is [98]:

$$T = T_{\mathrm{D}} \left(1 + \frac{2I}{I_{\mathrm{sat}}} + \left(\frac{2\Delta}{\Gamma} \right)^2 \right) \frac{\Gamma}{2|\Delta|}, \tag{2.5}$$

with I the the intensity and Δ the detuning of the MOT beams relative to the atomic transition. The constant Γ is the natural linewidth, T_{D} the Doppler temperature and I_{sat} the saturation intensity. Appendix A gives these values for He*. For the MOT beams that we use, $\frac{I}{I_{\mathrm{sat}}} \simeq 25$. Equation 2.5 allows one to deduce the optimal detuning Δ_{opt} corresponding to the lowest temperature:

$$\Delta_{\mathrm{opt}} = \frac{\Gamma}{2}\sqrt{1 + \frac{2I}{I_{\mathrm{sat}}}}. \tag{2.6}$$

[4]The given pressure is an estimate – it is too low to obtain a precise measurement.

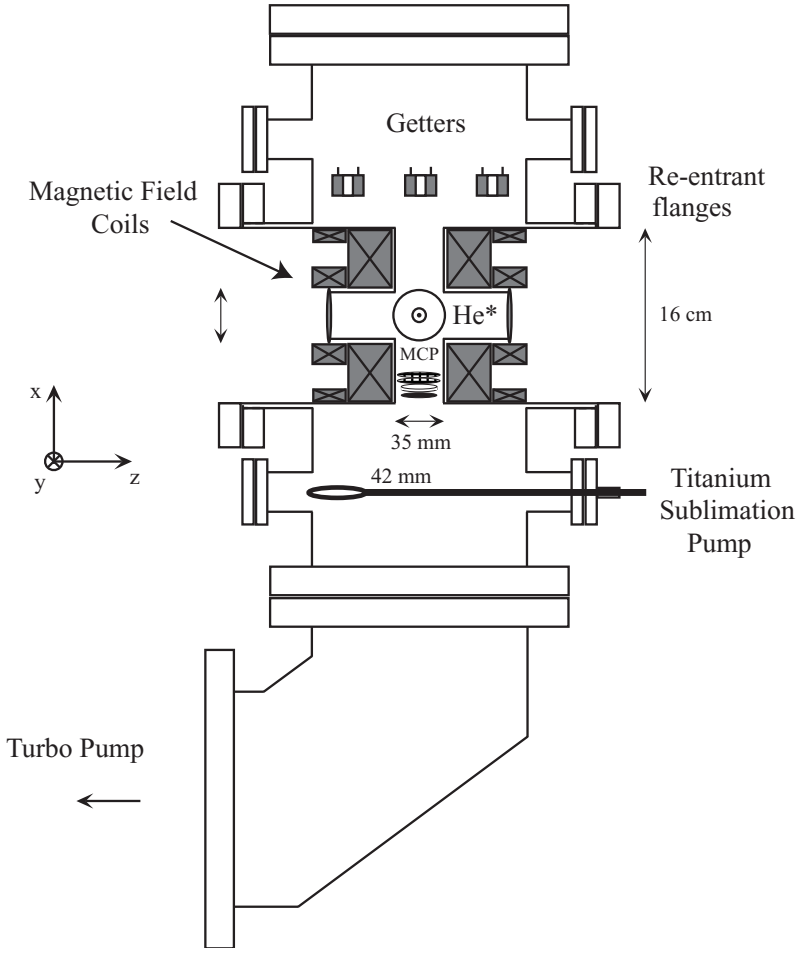

Figure 2.2: *The UVH chamber where the BEC of He* is produced. The diagram is approximately drawn to scale. The Zeeman Slower is situated behind the chamber, perpendicular to the projection of the chamber shown in the figure.*

This gives $\Delta_{\text{opt}} = 3.6\ \Gamma$. Although this minimizes the temperature, the most important quantity for us is the atom number, and the detuning plays a critical role for atom losses. In a MOT, the He* atoms are not spin polarized, and therefore the two-body Penning collisions are allowed (chapter 1). In addition, laser light near resonance tends to increase further the collision rate. This is because the interaction between two atoms is stronger, when a non-negligible fraction of atoms is excited to a P state [76, 77, 86, 87, 99]. To minimize this effect, the MOT laser light is detuned more than corresponding to the optimal detuning given in Eq. 2.6. This reduces the number of atoms in the P state and thereby the destructive Penning collisions. The optimal detuning turns out to be 25 Γ [34]. Detuning the laser light decreases the

trapping strength of the MOT, and to compensate this, the gradient of the magnetic field is increased. When the gradient reaches 50 G/cm, the atom number saturates at a value of 5×10^8 atoms. The rms width of the cloud is 2 mm, the peak density is $n_0 \sim 4 \times 10^8$ atoms/cm^3 and the measured temperature is around 1 mK.

2.3.2 Optical molasses and transfer to magnetic trap

The minimum temperature reached in a MOT is limited by the presence of the laser light, which heats the sample through spontaneous emission. The next step in the cooling process is therefore to trap the atoms without use of laser light, namely in a purely magnetic trap. Here the confinement is provided by the interaction between the magnetic moment of the atoms and an external magnetic field. To obtain a good transfer to the magnetic trap, the temperature needs to be lowered further before this transfer is done. This is achieved by using a 3-D optical molasses: the magnetic fields are switched off, and the former MOT beams constitute the optical molasses. Without the magnetic field present during the MOT, the cloud becomes sensitive to residual stray magnetic fields. These fields are compensated by using small additional magnetic coils. The result of the optical molasses is a cloud containing approximately 4×10^8 atoms with a measured temperature of 300 μK. This is higher than what is expected – the reason might be that the sample is too dense to reach the expected Doppler temperature.

To optimize the transfer, the size of the cloud should be kept constant during the transfer [34]. This is done by matching the magnetic trap curvature to the initial size of the cloud so that the latter neither expands nor contract in the new trap. Therefore the magnetic trap must be in a "non-compressed" configuration (discussed below). Another important thing is that for He* in the 2^3S_1 level, only the $m_J = 1$ level is a trapping state (m_J is the projection of **J** on the quantization axis). In the MOT, the atoms consist of an equal mixture of $m_J = -1$, $m_J = 0$ and $m_J = 1$. In order not to lose two thirds of the atoms, an optical pumping pulse is applied to pump all atoms into $m_J = 1$. This is done by applying a retro-reflected, σ^+ polarized laser beam 30 μs [34]. Once all the atoms are in the $m_J = 1$ level, the sample is said to be spin polarized. In general we manage to transfer close to 100 % of the atoms in the MOT into the magnetic trap.

2.3.3 The magnetic trap: towards the microkelvin regime

In the following we will explain the principles of magnetic trapping, and give some characteristics of the trap that we use for metastable helium.

Principles of magnetic trapping

The principle of magnetic trapping is based on the interaction between the permanent magnetic moment of an atom μ with an external magnetic field

$\mathbf{B}(\mathbf{x})$. The interaction energy can by written as $U(\mathbf{x}) = -\boldsymbol{\mu} \cdot \mathbf{B}(\mathbf{x}) = \hbar\,\omega_L$, where we have defined the Larmor frequency ω_L, the frequency of the precession of the magnetic moment of the atom around the magnetic field. For an atomic level having a total angular momentum $\mathbf{J}$, the magnetic moment can be written as $\boldsymbol{\mu} = -g_J \frac{\mu_B}{\hbar} \mathbf{J}$, with g_J the Landé factor and μ_B the Bohr magneton. If the Larmor frequency is large compared to the rate of change of the external magnetic field, the magnetic moment will adiabatically follow the external field. The magnetic moment is then always parallel to the direction the external field, and in this case the interaction potential simplifies to

$$U(\mathbf{x}) = g_J \frac{\mu_B}{\hbar} m_J\, B(\mathbf{x}), \tag{2.7}$$

where $B(\mathbf{x})$ is the modulus of the magnetic field $\mathbf{B}(\mathbf{x})$. The adiabatic condition is always fulfilled for the parameters we use in our experiment. If the external field is harmonic, atoms with $g_J\, m_J > 0$ will experience a minimum in the potential, around which they can be trapped. For He* (2^3S_1), $g_J = +2$, so only the $m_J = 1$ level is a trapping state. When g_J is positive, $\boldsymbol{\mu}$ and $\boldsymbol{B}(\mathbf{x})$ are anti-parallel. The potentials are shown in Fig. 2.3.

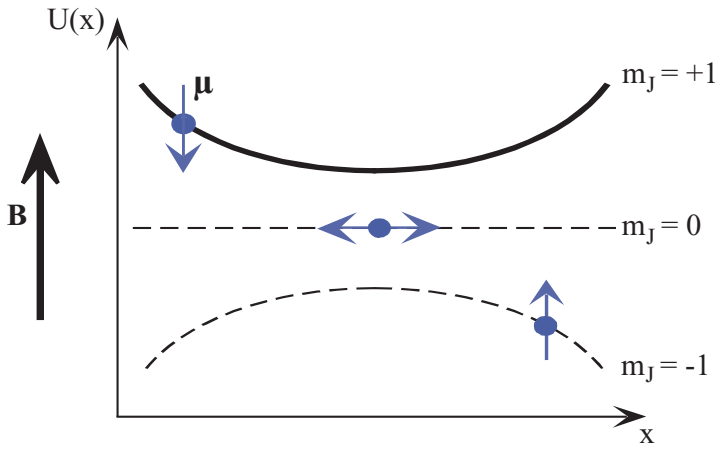

Figure 2.3: *Potentials created by the interaction of the magnetic moment of an atom with an external magnetic field of harmonic shape. If the magnetic moment of the atom is parallel to the external field ($m_J = -1$), the potential has a maximum, and no trapping force exists. If the magnetic moment is anti-parallel to the field ($m_J = 1$), the atoms can be trapped in the minimum of the potential. If the magnetic moment is perpendicular to the field ($m_J = 0$), the atom is insensitive to this field.*

Characteristics of the magnetic trap

The trap configuration used in our experiment is the Ioffe-Pritchard cloverleaf trap [100]. This choice is partly based on geometry considerations: as it is preferable to avoid having magnetic coils in the vacuum chamber, the cloverleaf trap combined with re-entrant flanges allows one to bring the coils close to the atoms. Also, the Ioffe-Pritchard configuration posses a non-zero field minimum, in order to avoid non-adiabatic transitions to non-trapping states [101]. Twelve coils are used to generate the fields required for the

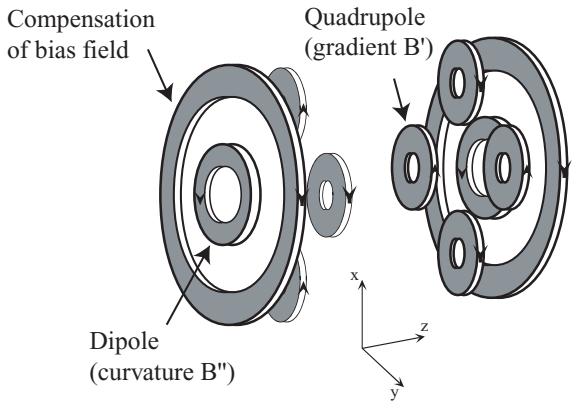

Figure 2.4: *Coils in the Ioffe-Pritchard configuration used to create the magnetic trapping potential. The pair of four elliptic coils create a gradient and confine the atoms in the transverse direction while the pair of small circular coils creates a harmonic dipole potential with a given curvature in the axial direction. The large circular coils is used to compensate the bias field and consequently compress the trap, see text.*

trapping potential as shown in Fig. 2.4. A pair of four small elliptic coils creates a quadrupole field (gradient B') which traps the atoms in the transverse plane (x, y). A pair of coils with the current running in the same direction, adds a confining potential in the axial direction (z). These coils are separated by more than in the Helmholtz configuration, and create a harmonic dipole field with a curvature B''. The value of this field at the trap center is called the bias field and is denoted by B_0. To be able to adjust this bias field, a second pair of coils is added, this time in Helmholtz configuration and with the current running in the opposite direction relative to the dipole coils. This gives rise to a field which is uniform in the axial direction, allowing one to reduce or almost cancel the bias field. As we will see below, the value of the bias field also influences the radial confinement of the atoms: by reducing the bias field, we can compress the trap.

The total magnetic field can be written in terms of the bias field B_0, the

gradient B' of the dipole field and the curvature B'' of the quadrupole field. Neglecting terms higher than second order in x, y, and z, the magnetic field $\mathbf{B}(x,y,z)$ in the vicinity of the trap center can be written as

$$\mathbf{B}(x,y,z) \simeq \begin{pmatrix} 0 \\ 0 \\ B_0 \end{pmatrix} + B' \begin{pmatrix} x \\ -y \\ 0 \end{pmatrix} + B'' \begin{pmatrix} -xz \\ -yz \\ z^2 - \frac{1}{2}(x^2+y^2) \end{pmatrix} . \quad (2.8)$$

where B_0 is the sum of the field contribution from the compensation coils and the other coils. The atom-field coupling depends on the modulus of $\mathbf{B}(x,y,z)$ which is

$$B(x,y,z) \simeq \sqrt{\left(B_0 + B''\left(z^2 - \frac{x^2+y^2}{2}\right)\right)^2 + B'^2(x^2+y^2)} . \quad (2.9)$$

The exploration of the different regimes

One can define two working regimes for the Ioffe-Pritchard trap, depending on the size (temperature) of the cloud. If $z \ll \sqrt{\frac{B_0}{B''}}$ and $\sqrt{x^2+y^2} \ll \frac{B_0}{B'}$, which corresponds to the requirement[5] $k_B T \ll 2\mu_B B_0$, a second order development of the expression 2.9 is a good approximation:

$$B(x,y,z) \simeq B_0 + \left(\frac{B'^2}{2B_0} - \frac{B''}{2}\right)(x^2+y^2) + B''z^2 . \quad (2.10)$$

The field is therefore harmonic in the three dimensions with an axial curvature B'' and a radial curvature equal to $\left(\frac{B'^2}{2B_0} - \frac{B''}{2}\right)$. Therefore, by decreasing the bias field, the radial curvature can be increased. This approximation is valid for low temperatures or high bias field. The other regime corresponds to high temperatures and low bias fields. In this limit, the trap potential becomes linear in the radial directions (with a gradient B') and harmonic in the axial direction with a curvature B''. The trap is said to be *semi-linear*.

[5] We write the energy in one direction as $k_B T \sim 2\mu_B B'' \langle z^2 \rangle$. Now for the approximation to be valid $\langle z^2 \rangle \ll \sqrt{B_0/B''}$, and it follows that $k_B T \ll 2\mu_B B$.

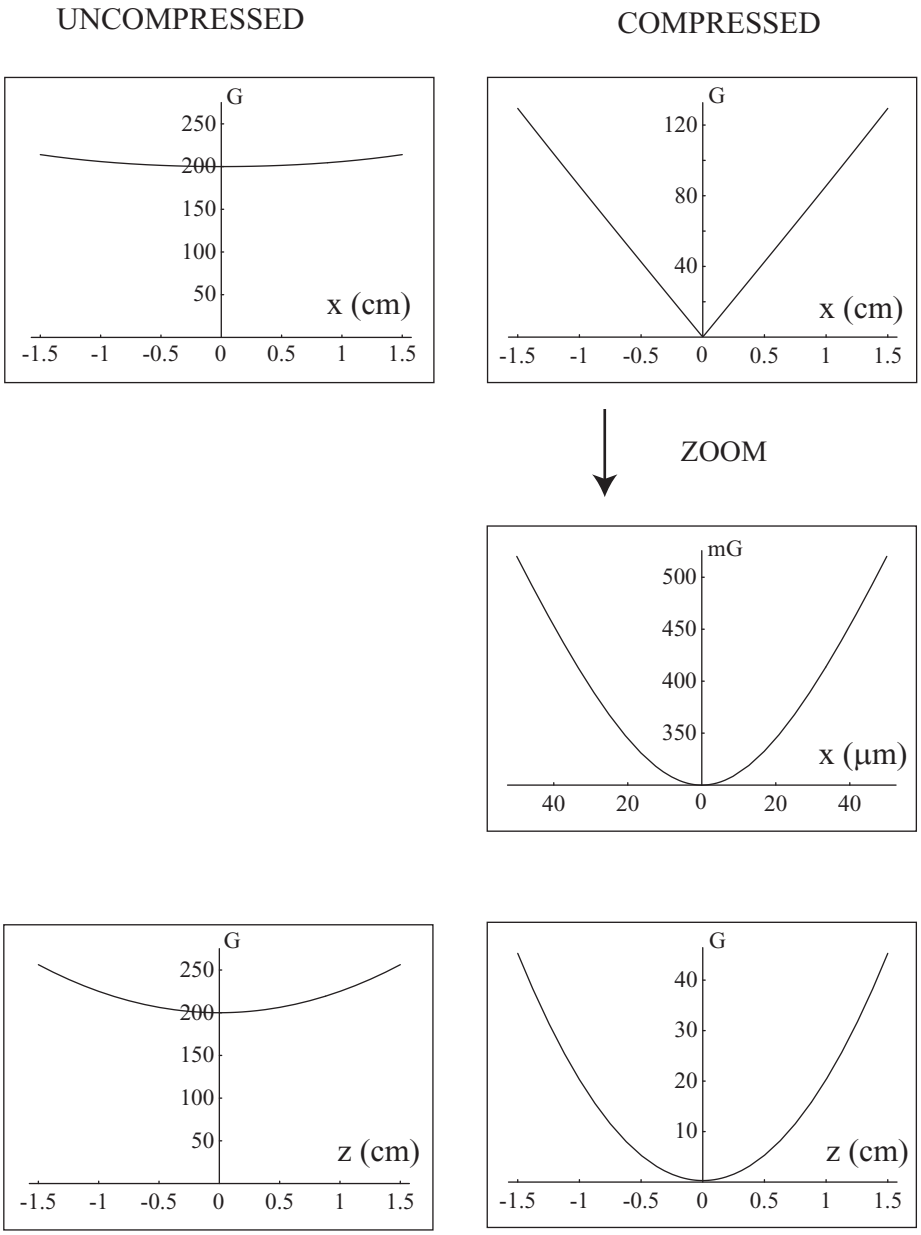

Figure 2.5: *Profile of the magnetic field as a function of radial (x) and axial (y) directions. The left column shows the characteristics of an uncompressed trap, while the right column corresponds to a compressed trap (see text). The uncompressed trap remains harmonic for all directions independent of the temperature of the cloud. A compressed trap becomes semi-linear in the radial directions if the cloud explores a large zone (top graph in the right column), while the central zone explored by a cold cloud remains harmonic (second graph in the same column). In the axial direction, the potential is always harmonic (bottom graphs).*

The two regimes are both explored during the cooling sequence. Not only does the temperature of the cloud change, but the magnetic fields (B_0, B' and B'') are deliberately varied in order to optimize the performance of the trap during the different steps in the cooling process. In order to optimize the loading, the currents in the trap coils will be chosen such that the trap potential allows the cloud to conserve its size given by the optical molasses. Later in the cooling process, to make the evaporative cooling efficient (see later), the trap will be compressed, by lowering the bias field, in order to increase the elastic collision rate. As the atoms are still relatively hot, they will be exploring a semi-linear trap. Evaporative cooling then decreases the temperature of and consequently the size of the cloud, and the atoms will finally be confined to the purely harmonic region. The magnetic field corresponding to the different regimes are shown in Fig. 2.5. In the left column, the graphs show an uncompressed trap, which is always harmonic independent of the temperature in both the radial and axial direction. In the right column, the trap is compressed by lowering the bias field: the graph at the top shows the behavior of the magnetic field in the transverse direction relatively far from the origin, corresponding to the region explored by a hot cloud. The second graph is a zoom on the central region of the trap. In this zone, explored by a cold cloud, the trap is harmonic. In the axial direction the potential remains harmonic for all temperatures, even for a compressed cloud. To give some numbers, let us divide the cooling sequence into parts according to the characteristics of the magnetic trap:

- During loading from the optical molasses: $B' \sim 85$ G/cm and $B'' \sim 25$ G/cm^2. The current in the compensation coils is zero, leaving the bias field high: $B_0 \sim 190$ G. The temperature of the cloud is around 1 mK, such that $\frac{k_B T}{2\mu_B B_0} \sim 0,01$, and we are then in the regime described by Eq. 2.10, namely an anisotropic harmonic potential with a radial curvature of 7 G/cm^2 and an axial curvature of 25 G/cm^2.

- Compression of the trap: This is done by decreasing the bias field B_0. According to Eq. 2.10, this increases the curvatures in the radial plane. A typical value of the bias field after compression is 300 mG. As the compensation coils are not perfectly Helmholtz, the axial curvature is also slightly modified. After compression, the bottom of the trap is then very anisotropic, with a radial curvature of 12000 G/cm^2 and an axial curvature of 20 G/cm^2. The atoms, however, explore a much wider zone of the trap: as the bias field has decreased without any decrease in the temperature of the cloud, $\frac{k_B T}{2\mu_B B_0} \sim 25$, and the atoms feel a semi-linear trapping potential with a gradient of 85 G/cm and a radial curvature of 20 G/cm^2 (see Fig. 2.5). Note that the semi-linear potential is steeper than the corresponding harmonic potential, and this enhances favorably the elastic collision rate in the beginning of the evaporation.

- After evaporation the temperature has decreased down to $\sim$ 1 μK and $\frac{k_B T}{2\mu_B B_0} \sim 0.02$. Consequently, the atoms now only explore the harmonic zone of the trapping potential (12000 G/cm^2 and an axial curvature of 20 G/cm^2).

Finally we will relate the magnetic fields to the trapping potential experienced by the atoms in the harmonic regime. To do this we define the trap oscillation frequencies ω_x, ω_y and ω_z

$$U(\vec{r}) = \frac{1}{2} m\omega_x^2 x^2 + \frac{1}{2} m\omega_y^2 y^2 + \frac{1}{2} m\omega_z^2 z^2,$$

By comparing Eq. 2.7 and Eq. 2.10, we see that the oscillation frequencies are related to the magnetic field in the following way:

$$\omega_{x,y} \equiv \omega_\perp = \sqrt{\frac{4\mu_B}{m}\left(\frac{B'^2}{2B_0} - \frac{B''}{2}\right)} \sim \sqrt{\frac{4\mu_B}{m}\frac{B'^2}{2B_0}}, \tag{2.11}$$

and

$$\omega_z \equiv \omega_\parallel = \sqrt{\frac{4\mu_B}{m} B''}, \tag{2.12}$$

with $B' \simeq 85$ G/cm and $B'' \simeq 20$ G/cm^2. A bias field of $B_0 = 360$ mG gives $\omega_\perp/2\pi \simeq 1200$ Hz and $\omega_\parallel/2\pi \simeq 50$ Hz. Experimentally, it is hard to obtain precise values of the oscillation frequencies, because direct measurement of B' and B'' in the trap center is impossible. However, measurements by parametric heating of the cloud is possible: when the trapping magnetic field is modulated with a frequency two times higher than the trap oscillation frequency, a pronounced heating of the cloud is observed [37]. In our case we have two ways of observing a heating: either by an atom loss observed in the Time-Of-Flight signal, or by a sudden decrease in the ion signal (this signal is discussed in chapter 3). The frequencies measured in this way agrees with the ones calculated using approximate values of the magnetic fields.

The trap oscillation frequencies are important because they determine the density of the sample, which governs the collisions, in particular the elastic collisions, responsible for an efficient evaporative cooling, as we will see below.

2.3.4 Radio-frequency evaporative cooling

Once the atoms are trapped in a magnetic trap, they can be cooled further by evaporative cooling. The basic idea is to eliminate atoms with an energy larger than a certain limit and let the sample restore thermal equilibrium *via* elastic collisions ("good collisions"). The procedure is repeated, decreasing progressively the energy limit, above which atoms are ejected. The restoration of thermal equilibrium is called thermalization, and the more it happens fast, the more efficient is the cooling.

In practice, the ejection of atoms are achieved using a radio-frequency (rf) field which transfers high-energy atoms to non-trapped or anti-trapped states. The principle is shown in Fig. 2.6. An rf-field of frequency ν_{rf} driving the transitions is applied to the sample. Atoms with an energy greater than or equal to E_{limit} will be resonant with the transition towards $m_J = 0$ or $m_J = -1$ and therefore ejected from the trap. This provides a selection of the atoms based on their energy. When E_{limit} is progressively decreased (this is called *forced* evaporation), the average energy per atom decreases, and the sample can be cooled down until a pure BEC is reached. In general,

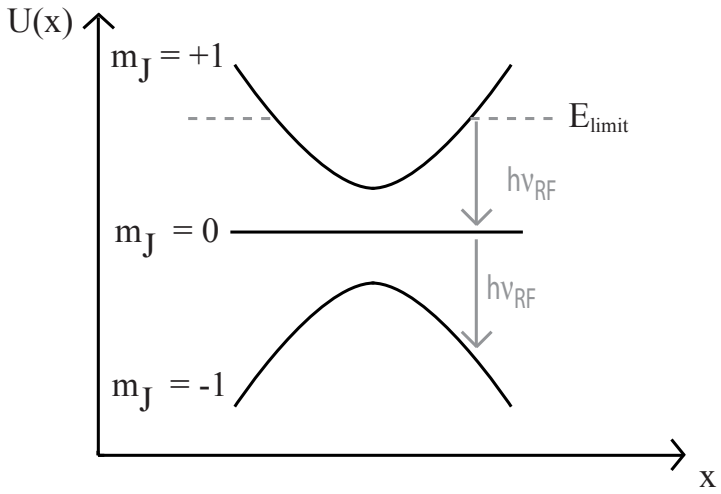

Figure 2.6: *The principles of evaporative cooling. The trapped state corresponds to $m_J = 1$, $m_J = 0$ is a non-trapping state and $m_J = -1$ is an anti-trapping state. Atoms with an energy higher than E_{limit} will be resonant with the applied radio-frequency field, and transferred to non- or anti-trapping states, and consequently ejected from the trap.*

the BEC will fast decay to a thermal cloud due to heating of the sample. However, the rf-frequency can be kept constant at the final value, in order to continuously eject the hot atoms. This is called an rf-shield, and it allows one to keep a pure BEC. On the other hand, if the rf-frequency is decreased beyond the energy of the condensate, all the atoms will be abruptly ejected. It is therefore important to know exactly at which rf-frequency a pure BEC is formed: to do we observe either the cloud or the ions produced by the cloud. The cloud can be observed by switching off the trapping potential and let the entire cloud fall on our detector: the shape of the cloud tells us if we have reached a pure BEC (see section 2.5), and we can therefore see at which rf-frequency this happens. We can also identify the rf-frequency corresponding to a pure BEC from the ionization rate: the ionization rate drops abruptly to zero when this rf-frequency is reached. This is because in that case, the rf knife expels all atoms, and without atoms in the trap,

no ions are produced. How we in practice observe the atomic cloud and the ions is the subject of the next section.

2.4 Electronic detection of atoms and ions

The fact that the helium atoms are in a metastable state with a large excitation energy opens the door for an electronic detection scheme using a micro-channel plate (MCP). The internal energy of one He^* atom is large enough to eject an electron from a surface, depending on the material of this latter. By amplifying this electron signal, using the same principle as in a photo multiplier, one can detect the atoms one by one. In addition to the neutral metastable atoms, the ions created by collisions can also be detected with an MCP: with electric fields, the ions can be accelerated and thereby gaining enough kinetic energy to eject electrons from the surface. To distinguish between atoms and ions, we can add a metallic grid above the MCP. The voltage of this grid can be varied: if we put a positive voltage we repel all positive ions, and the signal is due to neutral metastable atoms alone[6]. If we put a negative voltage we detect both atoms and ions.

In all experiment described in this thesis, we use an MCP for the detection of atoms and ions. As mentioned at the beginning of this chapter, a detailed discussion of our micro-channel plate (MCP) can be found in [37]. For non French reading people, more general articles about the topic exist, see for instance [102, 103, 104]. In this section, we will give a brief overview of how our MCP works, and discuss the detection efficiency as well as eventual saturation problems.

2.4.1 The micro-channel plate: working principle

The principle of the detector is illustrated in Fig. 2.7. The upper surface is held at -2 kV, the lower surface at 0 kV. The first electrons created in the entrance of the channel therefore experience an acceleration along the propagation inside the channel, and the probability for emission of secondary electrons increases progressively. At the exit of the channel a measurable current is generated. A micro-channel plate consists of a thin glass plate with a very large number of microscopic channels, which are slightly tilted relative to the surface normal direction. Therefore, a particle arriving perpendicular to the surface of the MCP, will hit the internal surface of the channel, and an electron can be ejected. Each of the channels works individually as an electron multiplier, as illustrated in Fig. 2.8, where one single channel is shown. The surface of each micro-channel is coated such that the probability of emission of secondary electrons becomes close to one. The two outer surfaces of the MCP are metal-coated in order to connect electrically the different channels. Since the channels are semi-conducting, a current will

[6] Even though we put a positively biased grid, we do not detect the electrons, due to the MCP voltage of -2 kV.

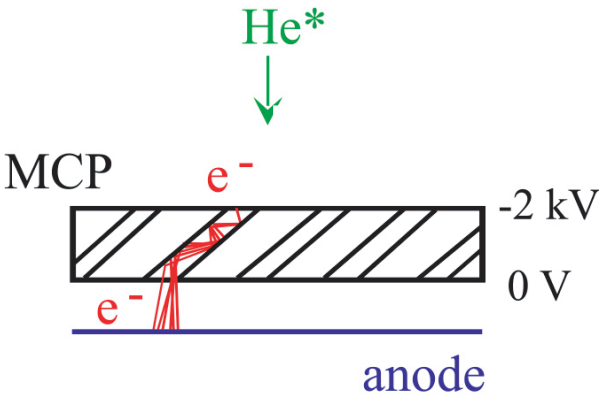

Figure 2.7: *Illustration of the micro-channel plate. When a He* atom falls on the micro-channel plate (MCP), the internal energy of the atom can be transferred to the surface of the detector, where an electron consequently is ejected. This electron is multiplied inside a micro-channel, and at the exit of the channel, enough electrons are present to create a measurable current.*

then circulate between the two surfaces of the MCP. This current, called the "strip current" will depend on the voltage applied, and the resistance of the MCP (≈ 100 MΩ). In practice, to increase the gain, the MCP used in our experiments is composed of two superposed micro-channel plates (a 2-stage MCP, see the technical documentation [105]). The working principle is the same, but due to the higher gain, the detection efficiency is increased.

2.4.2 Atoms and ions: two different regimes

As mentioned in the end of section 2.3.4, we can observe the entire atomic cloud by switching off the trap potential and let the cloud fall on the detector. We will call this a Time-Of-Flight (TOF) signal. When we record a TOF signal, the metastable atoms from the entire cloud arrives almost simultaneously (within ~ 10 ms) on the MCP. For instance, a BEC containing 10^5 atoms creates a maximum flux as high as 10^7 atoms/s. The flux of ions produced by collisions in the cloud being held trapped, is much lower than the atom flux corresponding to a TOF signal. For the most dense clouds, the ionization rate reaches maximum 3×10^5 ions/s. To adapt the detection to the flux, we will use the MCP in two different modes:

Atom detection

As the flux is very high precautions must be taken to avoid saturation. In this context saturation means that the signal from the micro-channel plate

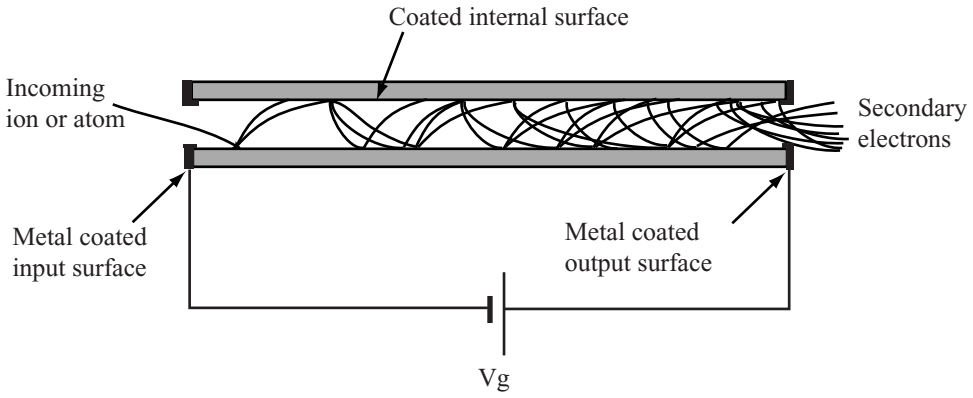

Figure 2.8: *One separate channel from the MCP. The channel is for simplicity shown horizontally, but in the MCP, all the channel are only slightly tilted relative to vertical. An ion or atom entering a channel, is multiplied due to the special coating of the inner surface of the channel, and at the exit of the channel, enough electrons are present to be easily detected. As indicated, a voltage difference is applied between the input and output surface. This accelerates the electrons inside the channel, and increases the gain.*

is no longer directly proportional to the number of incident particles. In order not to saturate the MCP, the voltage applied is limited to a value, for which the detector works in a *low-gain regime*. In practice, we apply 1.75 kV. In this regime, each channel can multiply simultaneously several particles, avoiding saturation even for a high flux of atoms. Using an signal-integrator, we obtain a continuous current coming from the MCP, with an amplitude proportional to the incident flux. We say that the detector works in *analogue mode*.

Ion detection

To detect the ions, we will increase the applied MCP voltage in order to run the detector in the *high-gain regime*. A typical voltage applied is 2.1 kV. With this voltage, each ion creates an avalanche of electrons, giving rise a single current pulse coming out from the MCP. The pulses are peaked and relatively narrow, and by using a discriminator we can in principle obtain a discrete signal for each ion detected. We then use a "National Instrument counting card" to register the counts and obtain the ionization rate. The detector is used in *counting mode*.

Experimentally, we can change between the two regimes by using an electronic switch, in order to switch the signal from the fast amplifier (required

for the counting mode) connected to the counting card, to the slower amplifier used in the analogue mode. We can perform the switch fast, but this generally not necessary: the ions which we detect come from a trapped cloud and the atoms from a cloud which has undergone a given Time-Of-Flight. This means that we have got all the time during the Time-Of-Flight, to switch from one amplifier to another; for a cold cloud this time is 100 ms.

2.4.3 Detection efficiency

Assuming that we do not saturate the detector, the number of incident particles can be determined from the signal. In analogue mode, the relationship between signal and incident flux depends on the gain, while in counting mode, the pulse height is without importance, as long as it remains higher than the discriminator level. In both modes, the detection efficiency depends on the quantum efficiency of the MCP and geometrical considerations. First we consider the geometrical limitations, which are identical for both atoms and ions. It arises from two contributions: the open (active) surface of the micro-channel plate corresponding to the entrance of channels, and the shielding by the two metallic grid used to manipulate the ions. In numbers, the open surface is 60 % of the total MCP surface. The geometric transmission of each grid is approximately 0.84 and the total transmission of the grids is therefore $0.84^2 \simeq 0.7$. Consequently, the efficiency is intrinsically equal to or less than $0.6 \times 0.7 = 0.42$ (taking into account the open surface and the two grids). Two assumptions have been made: for the ion detection, we have assumed that the ions are not guided through the openings in metallic grid due to the stronger electric fields behind the grids created by the MCP. This could actually increase the transmission above the one given by the geometric area. In addition, both for ion and atom detection, even the coefficient taking into account the open area of the MCP itself could be overestimated. One could imagine that electrons generated by atoms or ions falling on the dead area of the MCP are guided along the surface to the active area, and then could be detected. This would also increase the coefficient above the one corresponding to the open surface alone.

However, as we do not have any good estimate for the probability for those processes, we will in the following assume that the 0.42 is the correct factor, for atoms as well as ions. In addition to this factor, we have the quantum efficiency for the detection to take into account. This is different for atoms and ions, so we treat the two cases separately below.

Ion detection efficiency

To determine the overall ion detection efficiency, we write the detected ionization rate I_{det} as a function of the real ionization rate I_{real}:

$$I_{\mathrm{det}} = 0.42 \times \epsilon_{\mathrm{ion}} \times I_{\mathrm{real}} \equiv \alpha \times I_{\mathrm{real}}$$

We have assumed that due to the negative voltage applied to the metallic grids positioned above the MCP all ions arrive on the MCP[7]. The quantum efficiency for the ion detection is denoted ϵ_{ion}. It has been experimentally shown that for an applied MCP voltage above 2 kV, every ion entering a micro-channel ejects at least one electron [103, 106], implying that the quantum efficiency is close to one. Therefore at low temperatures, the total detection efficiency is expected to be limited only by the open area of the MCP (metallic grid and open surface), and should therefore be close to 0.42. At this stage, we do not have a good estimate for the uncertainty on the ion detection efficiency, but in chapter 5, based on measurements presented in later chapters, we will be able to give a strict lower limit for this quantity.

The various saturation mechanisms are described in [37]. We will here only give a number: for the ion detection in counting regime, the saturation limit of the MCP has been estimated to $\simeq 2\times10^5$ ions/s. This value is lower than the ionization rate produced by our most dense clouds. Consequently, when absolute ionization rate measurements are needed, we only produce clouds which are sufficiently dilute so that their ionization rate becomes inferior to the saturation limit.

Atom detection efficiency

In analogue mode, the relationship between the detected signal and incident flux depends on the gain (which again depends on the MCP voltage). In order to relate the analogue MCP signal V_{out} to the atom flux initially created by the cloud F we write:

$$V_{\text{out}} = 0.42 \times \beta(T) \times \epsilon_{\text{atom}} \times G\, e\, R \times F$$

$\beta(T)$ takes into account the fact that only a limited fraction of the initially created atoms arrive on the MCP. When the temperature of the cloud is low (BEC or vicinity), $\beta(T)$ is equal to one. The quantum efficiency, ϵ_{atom} - the probability that an electron is ejected when a He* atom touches the internal surface of a micro-channel - is not very well known, but it is estimated to be close to one [86]. The gain G is the average number of secondary electrons per electron initially ejected, which is estimated to be 5×10^4 for an applied MCP voltage of 1.75 kV, and 2×10^5 for 1.85 kV [37]. The charge of the electron is denoted by e and R is the resistance of the amplifier used, which is 6.8 MΩ. In total, for 1.75 kV we have $V_{\text{out}} = F_{\text{inc}} \times 2.3\times10^{-8}\,\text{V s}$ while for 1.85 kV $V_{\text{out}} = F_{\text{inc}} \times 9.2\times10^{-8}\,\text{V s}$. In most of our experiments we have used 1.75 kV.

The saturation limit in the analogue detection mode for a MCP voltage of 1.75 kV is estimated to be around 10^7 atoms/s [37]. This corresponds to the maximal flux for our largest BEC, and we can therefore assume that

[7] Tests show that this is the case when the cloud is sufficiently cold, i.e. below 500 μK [37]

the detector always works below the saturation limit when we are using it in the analogue mode.

Resolution

The MCP used for the experiments described in this thesis gives the arrival time for the incident particles, but is not position resolved. In analogue mode, the time resolution is limited by the RC filter of the integrator, which is 0.4 ms. For a high temporal resolution, the detector must be used in counting mode. Here the time resolution is given by the precision of our National Instruments counting card. The card counts the separation time between the two particles in multiples of 50 ns, so in principle we could use 50-ns bins, which would therefore be the time resolution. However, as our flux is low (in 50 ns we expect much less than one count in average), we need to increase the bin size, in in order to obtain a good signal-to-noise ratio. Typically, we choose a bin size of ~ 5 ms, which is therefore our time resolution.

2.5 Time-Of-Flight signals

Having discussed the MCP, we will now give some more details on how the TOF signal is recorded. To observe the cloud after a completed sequence, we switch off the magnetic fields. Now if the cloud is hot (millikelvin) it explodes symmetrically in space due to the kinetic energy of the atoms, and only a fraction corresponding to the solid angle of the MCP is detected. In this thesis however, the clouds observed will generally be very cold (microkelvin), and gravity governs the evolution: the cloud expands little and all the atoms arrive on the MCP (see Appendix C for details). We will therefore concentrate on cold clouds.

The TOF signal is observed on an oscilloscope. Examples of TOF signals are shown in Fig. 2.9. The gray curve is the experimental signal, and the black curve is a gaussian fit. The amplitude is given in arbitrary units. The TOF signals are plotted as a function of arrival time of the atoms. The fall of 5 cm takes around 100 ms when the atoms have zero initial velocity, which is the case in the TOF signals shown. The first TOF signal corresponds to a typical cold thermal cloud, far from the BEC threshold. It is well described by a Gaussian function, indicating that the Maxwell-Boltzmann distribution is valid [107]. The second TOF signal shows a cloud which is cooled past BEC threshold. The narrow central peak indicates the presence of a BEC, while the broad wings with a Gaussian shape indicates that thermal atoms, i.e. atoms which are not in the condensate wavefunction, are present. In the last TOF signal, almost all the atoms are in the condensate wavefunction, and no thermal wings can be discerned.

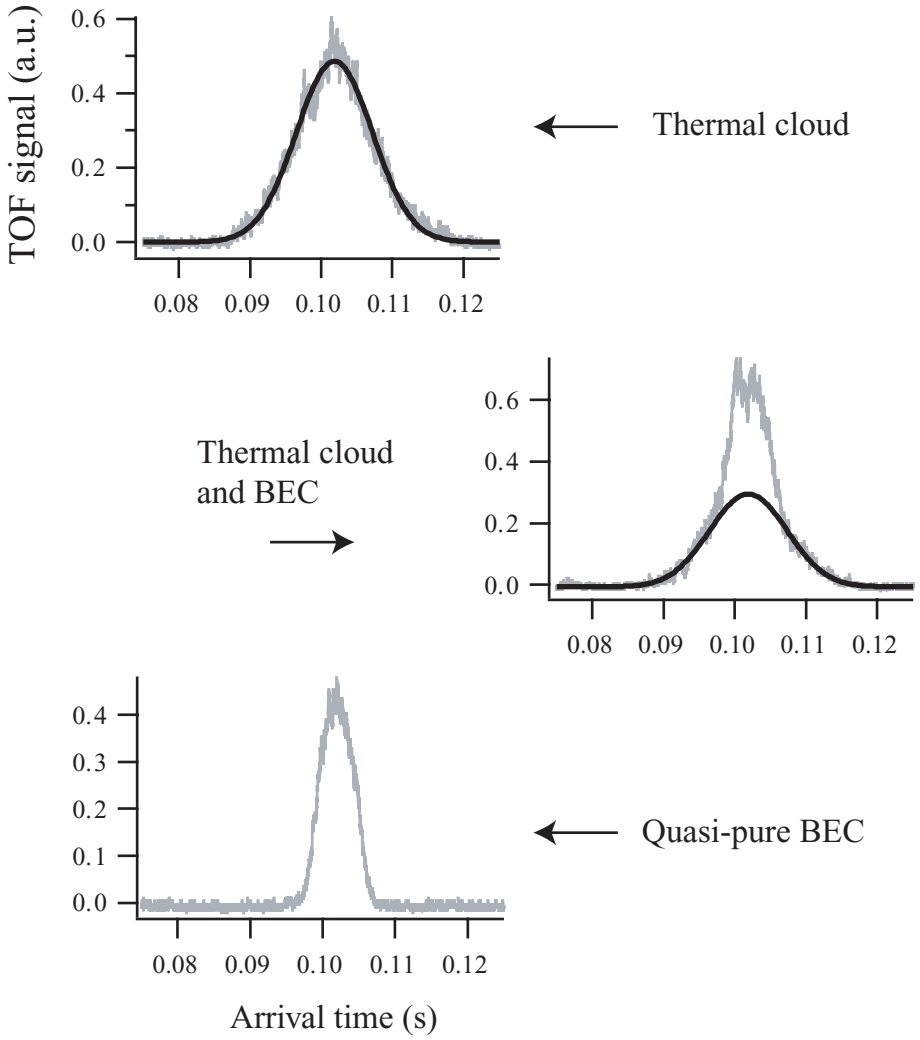

Figure 2.9: *Example of three recorded TOF signals (gray curves), corresponding to clouds released at different moments during the evaporative cooling. The first one is released relatively early in the cooling sequence, and the TOF signal shows a thermal cloud. The second TOF signal contains both a macroscopic fraction in the condensate wavefunction and thermal atoms. Both of these TOF signals are accompanied by a Gaussian fit to the wings*[9] *(black curves). In the last TOF signal, an almost pure BEC is shown.*

To interpret a TOF signal – to characterize it qualitatively (thermal cloud, cloud at BEC threshold or pure BEC) and quantitatively (atom number, temperature or chemical potential) a fit must be done. The fit function depends on the nature of the cloud. If it is purely thermal, a Gaussian function works well, while for a cloud near threshold, a Bose function must be used. For a pure BEC, a Thomas-Fermi profile is chosen. The fit functions used for the data analysis presented in this thesis are described in Appendix C, and the fitting procedure for thermal clouds will be discussed in chapter 5.

When we say that we let the atoms fall on the micro-channel plate in order to record the TOF signal, things seem very simple. It is not. A strange behavior of the magnetic fields during cut-off of the trap in addition to stray magnetic fields during the Time-Of-Flight complicate the detection process. The result is that it becomes very difficult to deduce directly the number of atoms in the cloud from the TOF signal. We will now explain why this is so.

2.5.1 Population transfer between magnetic levels

In section 2.4 we mentioned that for a very cold cloud (BEC or vicinity) all the atoms arrive on the MCP. This was based on temperature considerations alone. When a hot cloud is released from the trap, it explodes symmetrically, and only a fraction corresponding to the solid angle is detected by the MCP ($\sim$ 0.5 %). In this case the gravity is negligible compared to the thermal energy. For a very cold cloud, it is the opposite: gravity dominates the evolution, and all the atoms fall like snow on a day with no wind onto the MCP. This is only valid so far as the atoms are not influenced by magnetic fields during the Time-Of-Flight. However, stray magnetic fields due to eddy currents induced by the trap switch-off are present during the Time-Of-Flight, and this makes it very improbable that magnetic field sensitive atoms arrive on the MCP. Nevertheless, we observe an almost unperturbed TOF signal on the MCP. The reason is the following: during the switch-off of the trap, the bias field changes in an uncontrolled way from a positive value to a high negative value, see Fig. 2.10. When it passes through zero, non-adiabatic transitions from the trapping state $m_J = 1$ towards the $m_J = 0$ level take place. Now the atoms transferred to the $m_J = 0$ level are insensitive to the stray magnetic field, and fall unperturbed on the MCP. It is therefore essentially $m_J = 0$ atoms that we observe. For a nice discussion of this phenomena, see [36]. We can verify that this is the case by applying an additional magnetic gradient, stronger than the stray field, along the vertical direction. This is realized by adding a magnetic coil above the atoms. This field will accelerate $m_J = 1$ atoms towards the MCP. The signal on the MCP with and without this additional gradient is shown in Fig. 2.11. We see that the initial TOF signal (gray curve) is not modified when we apply a gradient (black curve), indicating that these atoms are

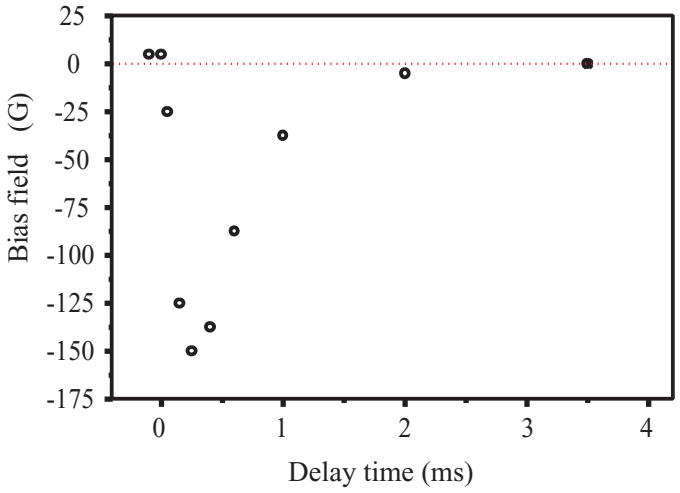

Figure 2.10: *The evolution of the bias field after trap switch-off. The origin corresponds to the switch-off of the magnetic trap. The bias field decreases very abruptly, passing through zero. This induces non-adiabatic transitions to the $m_J = 0$ level. The atoms transferred to this state constitutes the TOF signal. The measurements of the field shown in the figure where performed by A. Robert, and experimental details can be found in her thesis [36].*

insensitive to magnetic fields. In contrast, a second peak is present when we apply the gradient. This peak is very narrow and corresponds to the $m_J = 1$ atoms which are accelerated towards the MCP, and which therefore arrive earlier than the $m_J = 0$ atoms. We can also observe $m_J = -1$ atoms by adding a coil below the atoms. However, the fraction transferred to this state turns out to be negligible.

Distortion of signal due to the presence of $m_J = 1$ atoms

Even though the $m_J = 1$ atoms are mainly directed away from the MCP, a small part of them will arrive together with the $m_J = 0$ atoms on the detector and be present in the TOF signal. Since the trajectories of these $m_J = 1$ atoms are perturbed by the stray field, the TOF signal will be slightly distorted. In order to avoid this effect, we apply a horizontal magnetic gradient in order to push away atoms from the MCP. In this way, the TOF signal consists of the $m_J = 0$ atoms alone. In Fig. 2.12 we show two examples of TOF signal corresponding to a thermal cloud and their fit: one in the absence of the applied magnetic gradient (gray curve), and one where it is present (black curve). The fit is clearly very bad in the first case, because of the distortion of the signal due to $m_J = 1$ atoms. In the latter case, the

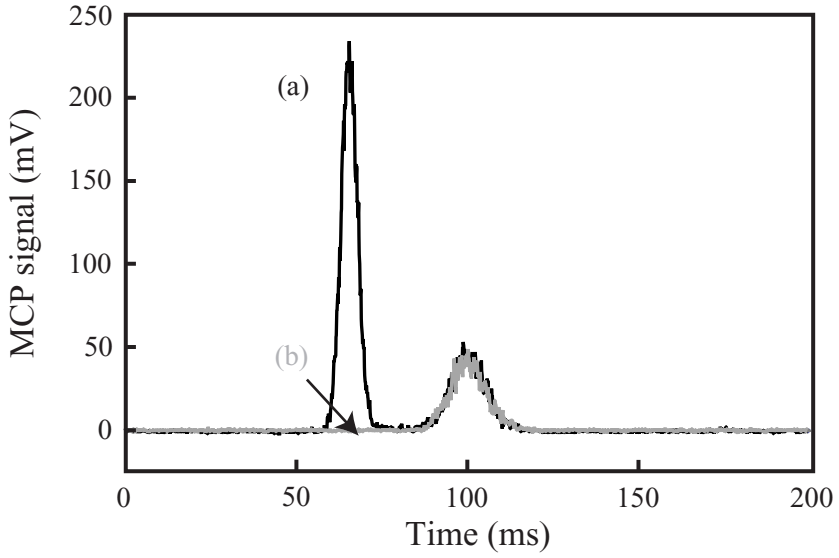

Figure 2.11: *TOF signals in presence (black curve, a) and in absence (gray curve, b) of an applied external magnetic gradient. The black curve corresponds to atoms in the $m_J = 1$ level, while the gray curve is $m_J = 0$ atoms. Note that the TOF signal for the $m_J = 0$ atoms is unchanged when the gradient is applied.*

fit is much better. The efficiency of the gradients on the $m_J = 1$ atoms depends on the temperature of the cloud: the colder it is, the more easily we manage to push away $m_J = 1$ atoms from the detector, and more easily is the TOF signal "purified". In general, this procedure is possible for clouds with a temperature below $5\,\mu$K. In order to obtain reliable fits, we always apply a gradient during the fall of the atoms.

Unknown transfer fraction

If the uncontrolled transfer between the $m_J = 1$ and $m_J = 0$ level were not present, we would never have observed an unperturbed TOF signal on the MCP. At the same time, this transfer also has an inconvenience: we do not know very well the fraction of atoms which are transferred from $m_J = 1$ to $m_J = 0$. Consequently, the amplitude of the detected TOF signal does not correspond to the number of atoms initially present in the trap, making atom number measurement very hard. To use the amplitude of the detected TOF signal to deduce the atom number, one must know the "correction factor" $\mathcal{F}$, which gives the ratio between the true atom number and the detected atom number: $\mathcal{F} = [N(m_J = 1) + N(m_J = 0)]/N(m_J = 0)$. In the

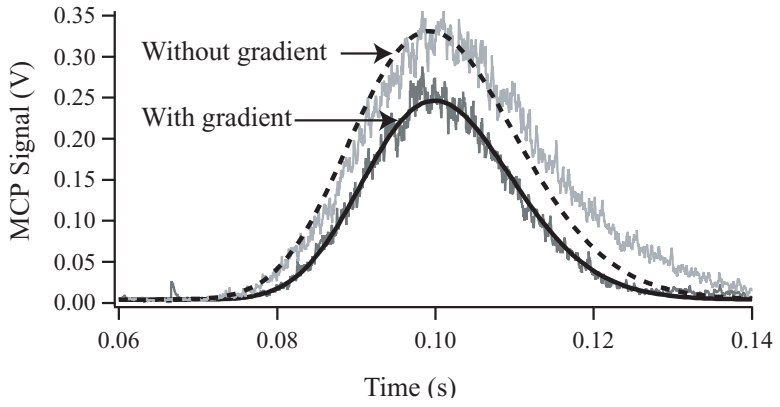

Figure 2.12: *Two TOF signals, each corresponding to a cloud at 4 μK. In the gray curve, no magnetic gradient is applied, and the TOF signal is consequently perturbed by $m_J = 1$ atoms, whose trajectories are disturbed by stray fields. In the black curve, a gradient pushes away these atoms, and the TOF signal (corresponding to $m_J = 0$ atoms alone) is unperturbed.*

first published paper about the He* BEC from our group [8], the scattering length was measured based on the expansion of TOF signals from pure BEC, as explained in chapter 1. They first deduced $\mathcal{F}$ for a cloud at the transition point: at this point, the atom number can be deduced directly from the temperature alone (and the trap oscillation frequencies) which can be measured reliably[10]. This gives the true atom number, corresponding to the atoms initially trapped. The detected atom number is obtained from the amplitude of the fit. The correction factor $\mathcal{F}$ obtained was then used to deduce the atom number in a pure BEC. The scattering length was extracted: $a = 20 \pm 10$ nm. In chapter 5 we deduce a different value for the scattering length: $a = 11.3^{+2.5}_{-1.0}$ nm. We also show that $\mathcal{F}$ it is not the same for a BEC and a thermal cloud, but differs almost by a factor of two. This explains why the first measurement of the scattering length (assuming $\mathcal{F}$ to be the same for a BEC and a thermal cloud) is almost a factor of two different from the value, which we now believe is the correct one.

2.5.2 Controlled population transfer *via* Raman transitions

An alternative, and more direct method to obtain a better estimation of the atom number, is to make a controlled transition of *all* the atoms to the $m_J = 0$ level, without switching off the trap. This should be possible using Raman transitions [108, 109], where it should be possible to transfer 100 %

[10] This will be discussed in detail in chapter 5.

of all the atoms to the $m_J = 0$ level, without switching off the trap. We have indeed implemented such a Raman transition scheme during my thesis work, and a detailed discussion of our results will be presented in the Ph.D. thesis of J. Gomes. Briefly, we observed Rabi oscillations between the two states, at the correct oscillation frequency, given the laser intensities. Also the arrival time of the TOF signal corresponding to the Raman-transferred atoms was as we expected from our timing of the sequence. However, even though we managed to empty the trap (we observed only the Raman signal while the initial TOF signal was absent), the amplitude of this signal was smaller than what we expected. We therefore think that we have an atom loss during the transfer, that we do not yet understand. We believe that in the near future we will understand this loss process and be able to exploit Raman transitions as a controlled way of coupling the atoms out of the trap.

A controlled switch-off using an optical dipole trap

A second way to control the outcoupling of atoms from the trap is the use of a so-called optical dipole trap. In this type of trap, the atoms are confined in a focused off-resonant laser beam, due to an interaction between their electric dipole moment and electric field of the light. The advantages of the dipole trap is that the trap switch-off being simply the switch-off of the laser beam, would not give rise to stray magnetic fields.

In a dipole trap, atoms can be trapped in all m_J levels. The ideal solution would be to use the $m_J = 0$ level. In this case, all atoms would arrive unperturbed on the MCP. However, for atoms in the $m_J = 0$ level, Penning ionizations would not be suppressed and give rise to high losses. Therefore, a better solution would be still to use the $m_J = 1$ level. In this case, however, other small stray fields present during the fall of the atoms, would in need to be compensated, in order not to perturb the trajectory of the atoms.

Chapter conclusion and outlook

In this section, we have showed how we produce and manipulate a Bose-Einstein condensate of He^*. In particular, we have showed how we can identify degeneracy using the TOF signal. One advantage among others of metastable helium is that we have a second observational tool: the ion signal. Like the TOF signal, the ionization rate can give us information about the state of the cloud, but the advantage of the ionization rate is that is "non-destructive". How the ion signal can be used is the topic of the next chapter.

CHAPTER 3

Ionization rate as a monitoring tool

During collisions between trapped He^* atoms, the internal energy of one atom can be transferred to another. The latter is thereby ionized and lost from the trap. These collisions are the *Penning* collisions, and were discussed in chapter 1. The ions are lost from the trap, but can be detected with the micro-channel plate. The resulting ion signal gives information about the collisions in the sample, and consequently about the density. This way of monitoring does not destroy the sample, making the ionization rate a powerful tool. In this chapter we will demonstrate how we can exploit the ion signal, either accompanied with Time-Of-Flight (TOF) signals or alone, in order to extract information about the behavior of the sample. In particular, the ionization rate can be used to follow in *real-time* the evolution of the atom cloud while it is cooled beyond the phase transition, and therefore gives insight into the formation and decay process of a Bose-Einstein condensate.

3.1 Dynamics of the cold atomic cloud

The ion signal can be optimally exploited only when an unambiguous mapping between the instantaneous value of the ionization rate and the density is accessible. A prerequisite for this mapping are the ionizing rate constants corresponding to the dominating collision processes. This is the subject of chapter 4. There, we obtain values for the rate constants, which will allow one to interpret the ion signal directly as a density. Here, we will concentrate on the direct measurable quantity, the ion signal itself, and we will investigate its behavior during the formation and decay of the condensate. In order to understand qualitatively the behavior of the ion signal, we will compare it with corresponding TOF signals at different instants during the formation and decay processes.

We first record an ion signal which we would like to investigate. The goal is then to obtain a series of corresponding TOF signals for different instants during the evolution of the ionization rate, overcoming the difficulty that the TOF technique is destructive. This means that each TOF signal necessarily comes from an independent experimental run, but if we require that the ionization rate produced by each cloud is identical to the ionization rate which we are investigating up to the switch-off time, we can consider all the

different TOF signals as being part of one single sequence. In this way, the ionization rate is used *via* post-selection of data to overcome experimental problems in the sense of repeatability. This way of exploiting the ionization rate will be used in the study of the formation and decay discussed below.

3.1.1 Formation of the Bose-Einstein condensate

We will in the following give a particular example of an ionization rate and the corresponding TOF signals during the formation. The ionization rate during the whole formation and decay is recorded in one single run, as shown in Fig. 3.1 1a. The last evaporation ramp starts at time zero and the pure BEC is formed two seconds later. The sequence has been repeated six times, and for each run, the trap has been switched off at different instants. The vertical dashed lines indicate at which moment the trap has been released, and the corresponding TOF signals with their Gaussian fit has been shown in 2a-2f in Fig. 3.1. As discussed above, each TOF signal shown has an ionization rate which, until the time where the trap is released, is identical to the one-run ionization rate shown in 1a. To give the reader some experimental details: to obtain a series of six TOF signals all having the same initial ionization rate, at least 100 ion rates were acquired. This gives an idea of the fluctuations in the ionization rate.

The TOF signals enable us to determine the state of the cloud. The first two TOF signals (2a, 2b) show a typical thermal cloud, well fitted by the Gaussian function. The corresponding ionization rate is slowly increasing. After this, there is a break in the slope in the ionization rate, and it starts to increase more rapidly. This corresponds to an increase in the density. Looking at the first TOF signal recorded immediately after the break in the ionization rate (2c), one observes for the first time a double structure, indicating the presence of a condensed part. The cloud can no longer be fitted by a simple Gaussian. It is therefore reasonable to suppose that the break in the slope signals the onset of BEC. This is a very important feature, which we will develop further in section 3.2, and use extensively in chapter 5. Following the TOF signals, we see that the condensed parts progressively grows larger (2d and 2e) and that a pure BEC is finally obtained (2f). Note that a pure BEC does not correspond to the maximum ionization rate (and therefore, maximum density) as one could expect. The reason is that during the very last part of evaporation (between 1.8 and 2.0 s in the figure) the density is strongly increasing and consequently the losses due to collisions increase. Therefore, the density decreases during the last 200 ms before a pure BEC is reached.

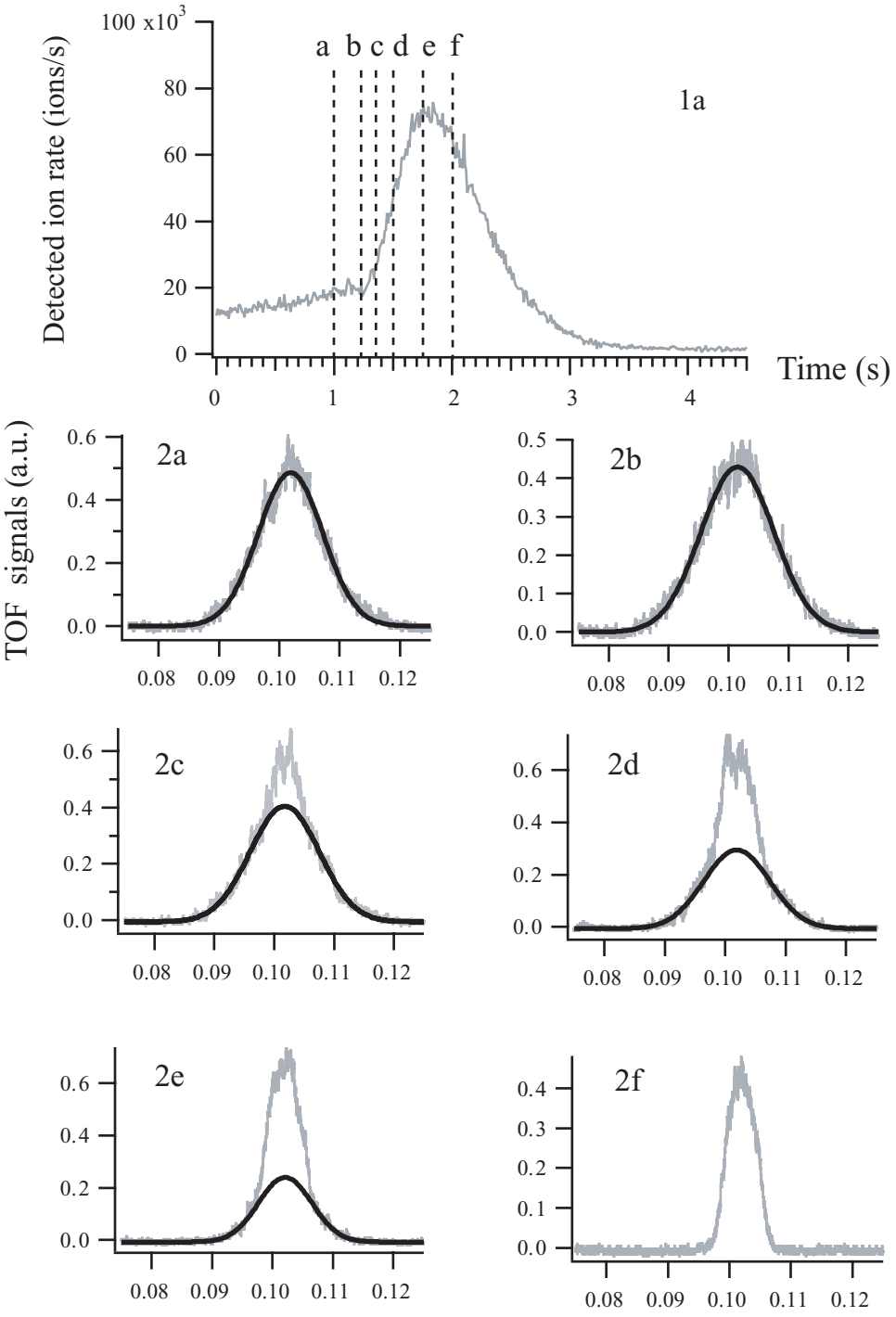

Figure 3.1: *In 1a we show the ion signal. The vertical dashed lines show the switch-off time of the trap. In 2a-2f the TOF signals as a function of time (in ms) are shown. The black curves in 2a-2f are Gaussian fits.*

In order to compare the ion signal with a theoretical model, the (so far unknown) inelastic rate constants are needed. However, a qualitative model can reproduce the characteristic shape of the observed ion signal such as the break in the slope at the critical point and the final decrease in the signal before BEC is reached, without knowledge of the rate constants. A model for the ionization rate has been developed by O. Sirjean, and is described in [37].

It should be noted that in this kind of experiment, the time scales for the formation is dictated by the choice of the final evaporation ramp. The two seconds it takes from the onset of BEC until a pure BEC is formed is not universal, but related to the rate of change of the rf-frequency. In order to study the universal time scales for bosonic stimulation, the experiment must be independent of the characteristics of the evaporation ramp. This can be done by cooling a cloud to a temperature very near the critical temperature, and then suddenly apply a short rf pulse, which quenches it below the critical point. The time scales for relaxation towards BEC is then independent of evaporation ramp. Such an experiment has been first performed in the group of W. Ketterle [110] and later by J. Walraven [111].

Let us also mention the formation experiment performed in the group of Hänsch [112]. Here, the cloud is continuously cooled through phase transition, and the growth time therefore depends on the evaporation ramp, as in our case. Finally, another formation experiment, similar to the Hänsch experiment, is under progress in the laboratory next door to the He^* laboratory, under the responsibility of P. Bouyer and A. Aspect. In this experiment, the goal is to study not only the dynamics of the density, but also the coherence properties of the condensate during the formation process.

The advantage of all these formation experiments is that they measure directly the density, while the inconvenient is that the detection is destructive. We hope that once we have established an unambiguous relation between the ionization rate and the density, we will have an ideal setup to monitor the dynamics of cold atomic clouds.

3.1.2 Decay of the Bose-Einstein condensate

We also study the decay of the condensate by comparing ionization rate with TOF signals. In Fig. 3.2 we show the ionization rate and corresponding TOF signals as before. Two different ion signals are shown (black and gray curve), corresponding to two types of decay:

- **Gray Curve:** After formation of the BEC, the rf-field is kept on at the final value of the evaporation frequency. This acts as an rf-shield, expelling hot atoms and thus preventing heating of the cloud. In this way the cloud remains a pure BEC, as indicated by the corresponding TOF signals shown above the ionization rate. As we lose atoms due to the rf-knife, the size of the BEC decreases.

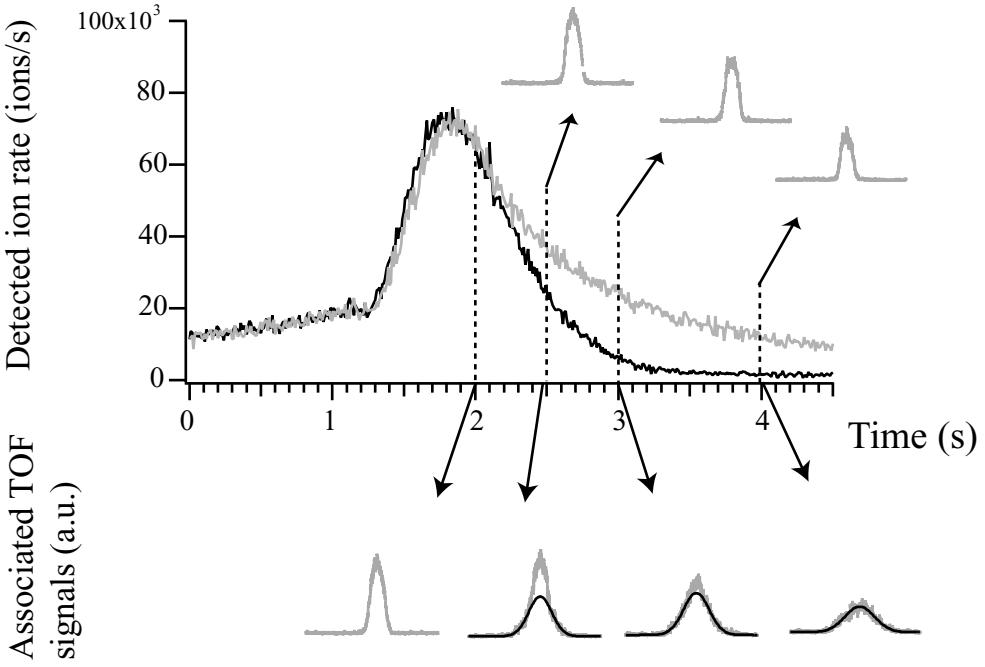

Figure 3.2: *The ionization rate accompanied with TOF signals. We here concentrate on the decay of the BEC. The gray ionization rate shows a decay in presence of an rf-knife, and the corresponding TOF signals shown above indicate the that BEC stays pure. The black curve is in absence of the rf knife, and the TOF signals below show the appearance of thermal wings.*

- **Black Curve:** The other type of decay corresponds to the situation where we have switched off the rf field after formation, and let the cloud evolve freely. This corresponds to the black ionization rate shown in Fig. 3.2, with the TOF signals shown below. In the absence of an rf-shield, the ionization rate decays much faster. Since the total number of atoms must be higher than in the case where atoms are expelled by the rf-field[1], the faster decrease in ionization rate is attributed to a loss in density (and not in atom number) resulting from heating. This is confirmed by the TOF signals, which reveals the appearance of thermal wings.

The heating rate of the sample in the absence of an rf-field can be determined by fitting the thermal wings of the TOF signals. From these fits the temperature, deduced from the width of the TOF signals, as a function of time is found. This is shown in Fig. 3.3, where the time scale is the same as in Fig. 3.2. We see that the sample heats 1.2 μK in 2.5 s, a heating rate of

[1] Assuming that the trap is deep enough to keep the heated atoms trapped.

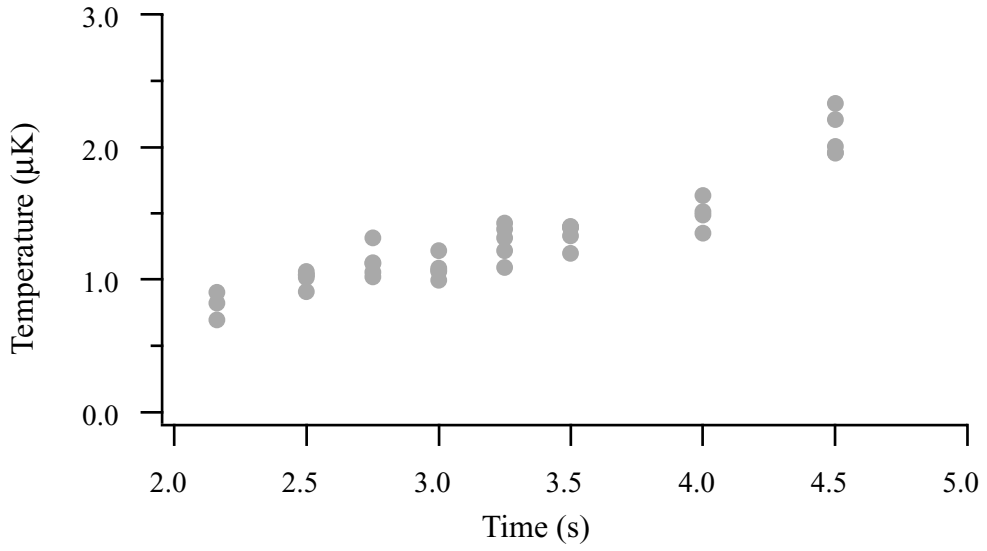

Figure 3.3: *The temperature as a function of time for the decaying sample in the absence of an rf-shield. The time scale is the same as in Fig. 3.2. The temperature is extracted from a fit of the wings of the TOF signal. For each of the different times observed, four measurements have been performed, each one of them being plotted in the graph.*

$\simeq 0.5$ μK/s. For each different time, four separate measurements have been made, as indicated in the figure. All the measurements were selected on the basis of identical initial conditions, as determined by the ionization rate.

We have not studied the processes causing the heating, but we suspect them to several. In particular, heating can be caused by elastic collisions between hot He^* atoms which are created in Penning collisions and the cold, trapped atoms (elastic, secondary collisions, see Ref. [13]). Also collisions with hot background gas atoms, and fluctuations in the magnetic field are examples of phenomena causing heating of the sample.

Another interesting source of heating has been studied in the group of G. Birkl and W. Ertmer. The fact that the collision rate is highest in high-density regions of the atomic cloud, leads to a heating: the largest atom loss happens in the high density region, where the atoms are coldest. Therefore cold atoms are dominantly lost, which therefore leads to an "anti-evaporation". This mechanism is studied in Ref. [113] in the case of metastable neon, and accounts for the heating observed in these experiments. This mechanism might equally well explain the heating observed in our sample of metastable helium.

The heating rate measured in the metastable helium group in ENS is much larger than ours: they measure $\simeq 20$ μK/s [62]! However, this heating rate is measured for a sample with a density one order of magnitude higher than in our case. This increases the rate of secondary collisions, and consequently the heating rate. We have not investigated this quantitatively, however.

3.1.3 Atom number dynamics and heating

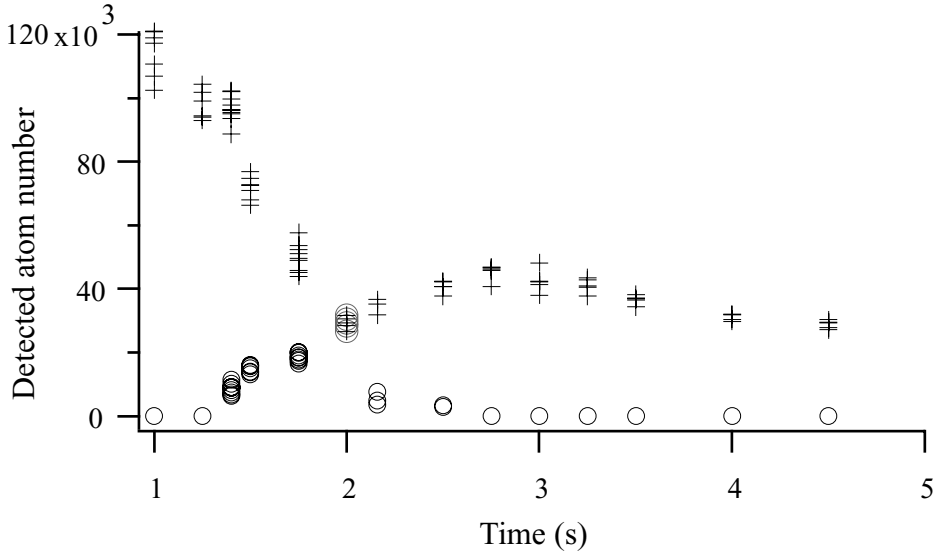

Figure 3.4: *Evolution of the atom number, obtained from fits to the TOF signals. The circles give the atom number for the BEC, while the crosses give the total atom number (BEC and thermal cloud). The time scale is the same as in Fig. 3.2, where a pure BEC is formed at $t = 2$. The increase in the total atom number between $t = 2$ and $t = 3$ should not be taken literally, as discussed in the text.*

The fits of the TOF signal shown in Fig. 3.1 and 3.2 give us the atom number during the formation and decay. For the decay, we use the TOF signals corresponding to the situation where the rf-shield is absent. This atom number is plotted in Fig. 3.4. The time scale is again the same as in the other figures, i.e. $t = 2$ s corresponds to a pure BEC. The crosses give the total atom number (thermal cloud and BEC), while the circles are for the BEC alone. The atom number is deduced directly from the amplitude of the TOF signal, and the fact that only a fraction of the atoms are detected is not taken into account. The atom number shown is therefore smaller than what is in reality. We see that up to $t = 2$ s the total number decreases (hot atoms are expelled by the rf-field), while the number of atoms in the condensate increases. After a pure BEC is reached, the condensate heats

(rf-field absent), and atoms are transferred to the thermal cloud. Therefore the number of atoms in the BEC part decreases. Strangely, the total atom number seems to be increasing, but of course, this increase cannot be real. It must be related to the fact that the detection efficiency is higher for a thermal cloud than for a BEC. This means that if atoms are transferred from a BEC to a thermal cloud without losing atoms, it would look as if the atom number increases. As explained in chapter 2, we detect only atoms which are transferred from the trapped $m_J = 1$ level to the field-insensitive $m_J = 0$ level during trap switch-off. It is possible that this transition occurs with higher probability for a cloud which is more spread out in space, i.e. a thermal cloud, than for a pure BEC. In chapter 5, we show that the fraction of detected atoms compared to the "true" number of atoms is around two times higher for a thermal cloud, than for a pure BEC, agreeing with this hypothesis.

3.2 Ionization rate as indicator of the phase transition

The series of TOF signals in Fig. 3.1 indicates that the break in the slope in the ionization rate coincides with the appearance of a double structure in the TOF signal. This gives an experimental indication that the break in the slope corresponds to the Bose-Einstein phase transition. If this is true, the ionization rate gives a new signature of the onset of BEC. We will use this feature in the measurements of the scattering length presented in chapter 5. There, we will need to produce clouds exactly at BEC threshold. The reason is that for a cloud exactly at BEC threshold, the density can be deduced directly from the temperature, which can be reliably measured.

As we want to use the ionization rate as an indicator of threshold, let us first see if this can be justified theoretically.

3.2.1 A definition of the phase transition

Let us discuss briefly what is actually meant by the BEC threshold point. This point corresponds to the point where the temperature of the gas reaches its critical value, T_c, defined according to:

$$n_0 \lambda^3(T_c) = 2.612, \tag{3.1}$$

where n_0 is the peak density of the cloud, and $\lambda(T_c) = h/\sqrt{(2\pi m k_B T_c)}$. In the ideal gas model, this temperature has a clear physical meaning: the condensed fraction is zero for all temperatures higher than T_c, and for temperatures below, it is given by:

$$\frac{N_c}{N} = 1 - \left(\frac{T}{T_c}\right)^3 \tag{3.2}$$

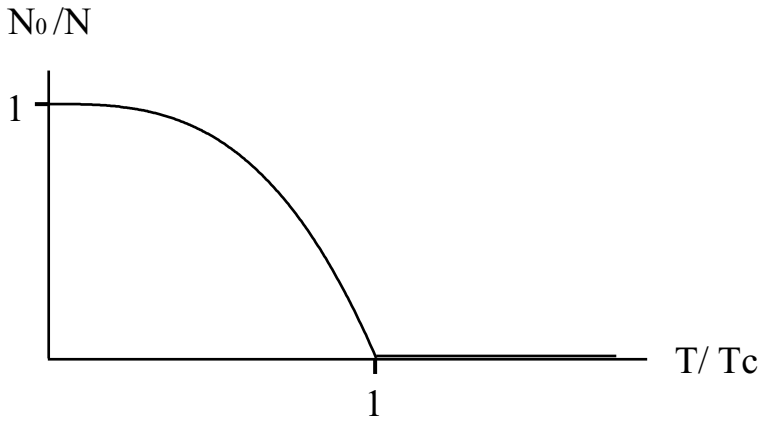

Figure 3.5: *The fraction of atoms in the condensate as a function of temperature in units of T_c. The curve is valid only for an ideal gas.*

This distribution is shown in Fig. 3.5, and the phase transition corresponds to the discontinuity in the curve. Does this point correspond to the break in the slope in the ionization rate? Let us first see if this is the case using an extremely simple (definitely too simple!) model. We assume that: *i*) the temperature decreases linearly at all time, *ii*) no atom losses are present, *iii*) the number of atoms in the BEC varies according to Eq. 3.2, and the atom number in the thermal cloud is constant until T_c and then decreases linearly, and finally *iv*) the density in the BEC varies as $N_c^{2/5}$ (see chapter 4, section 4.3), and the density in the thermal cloud varies as $(T/T_c)^{-3/2}$ (according to a Gaussian distribution). We then calculate the ionization rate, and also here we make a crude approximation: we do not take into account collisions between thermal cloud and BEC, so we take the ionization rate as the sum of ions produced by the BEC and the thermal cloud. We use the theoretical estimates for the rate constants given in chapter 1, section 1.2.4. The obtained ionization rate is shown in Fig. 3.6, where the thin solid line gives the BEC contribution, the dashed line gives the thermal cloud distribution, and the thick solid line gives the total ionization rate. The inset shows the evolution of the atom number for the BEC (solid line) and for the thermal cloud (dashed line). The units on the horizontal axis is temperature in units of T_c. What is important is that at the critical temperature, the ionization rate exhibits a break in the slope. Therefore, this naive model supports the idea that the break in the slope is the phase transition point.

The above model is of course far too simple to give any quantitative information – it is just meant to give a first intuition for why threshold should correspond to the break in the slope in the ionization rate. A much

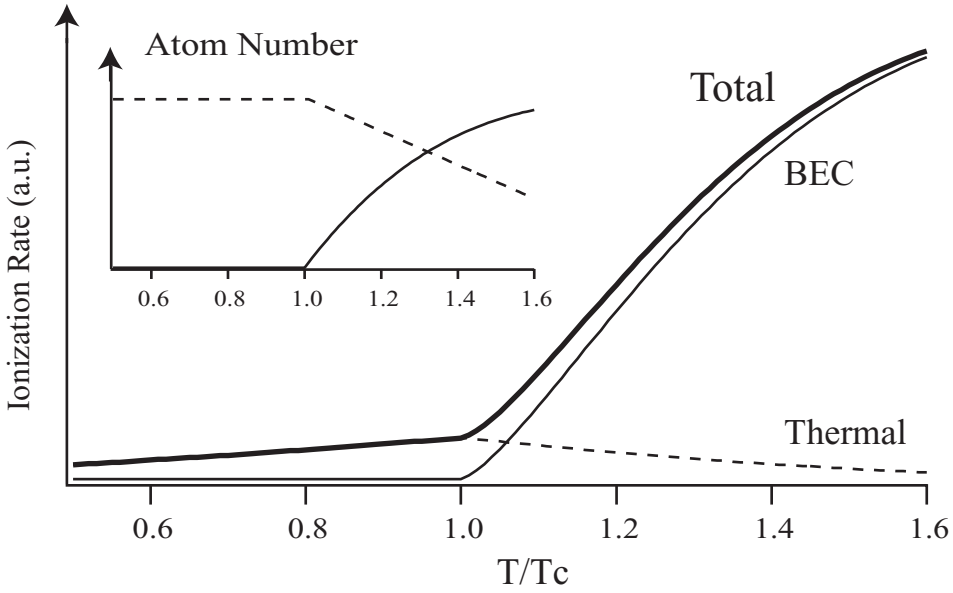

Figure 3.6: *A VERY simple model giving the evolution of the ionization rate for the BEC (thin solid line), for the thermal cloud (dashed line) and for both (thick solid line). The inset shows the evolution of the atom number for a BEC (solid line) and for a thermal cloud (dashed line). The horizontal axis is given in temperature normalized by T_c both for the main graph and the inset. We assume that the temperature decreases linearly with time.*

better model has been developed by O. Sirjean and can be found in chapter 4 in his thesis [37]. This model also assumes a linear decrease in temperature, but it takes into account losses due to inelastic processes, collisions between condensate and thermal cloud, and instead of using a simple Gaussian distribution for the thermal cloud, it uses the correct Bose function, which contains a term arising from interactions. The model neglects, however, atomic interactions between BEC and thermal cloud. The ionization rate obtained from this model is shown in Fig. 3.7. The break in the slope, defined from the derivatives (maximum curvature, or mathematically, where the 3rd derivative is zero, see later in this chapter), coincides with T_c, as it is defined for the ideal gas. Again, this is a confirmation of our above hypothesis.

Interactions and finite size

Both in the very simple and the more realistic model, we have used the ideal gas value for the critical temperature. We have shown that the break in the slope in the ionization rate corresponds to this temperature. In reality, T_c is shifted because of interactions and finite size effects, and the definition of BEC threshold becomes more subtle. For instance, the clear discontinuity

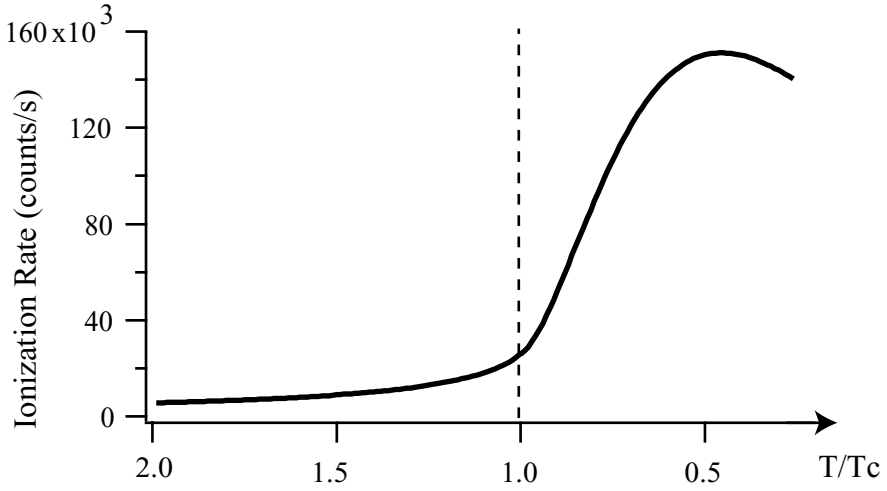

Figure 3.7: *Ion rate (solid line) calculated using a model developed by O. Sirjean [37]. This model is more realistic than the one discussed above, see text. The vertical dashed line indicates T_c, and also the point of break in the slope in the ionization rate (3rd derivative is zero).*

in the curve describing the condensed fraction (Fig. 3.5) is smeared out. Therefore it also becomes more difficult to locate the threshold point on the ionization rate.

We do not at the moment have a sophisticated model which takes this into account, and it is definitely worth studying more in detail. It would be interesting to know if, in such a model, the break in the slope in the ionization rate corresponds exactly to this – modified – critical temperature. However, we expect the correction to be small and without consequences for the result (the scattering length) obtained from an analysis based on the assumption. Nonetheless, in chapter 5, we will investigate the influence on the scattering length of an eventual shift in the critical point relative to the break in the slope in the ionization rate.

3.2.2 Establishing a "threshold curve"

In the following we will assume that the break in the slope in the ionization rate does correspond to threshold.

We will use this experimentally later, and we therefore look for a simple way to implement it. To do so, we will here establish an empirical relation between the ionization rate at BEC threshold and the corresponding frequency of the rf-ramp. With this relation, we will be able to switch off the trap when the cloud is exactly at BEC threshold.

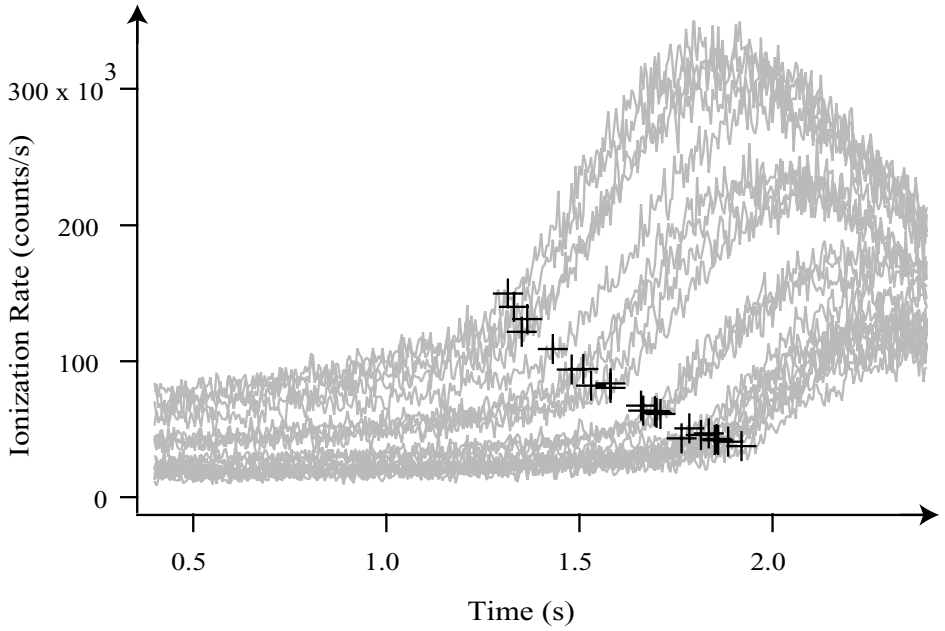

Figure 3.8: *Variation of the ionization rate as the atomic cloud is evaporatively cooled through the phase transition for various initial densities (gray curves). The rf-frequency at $t = 0$ is 2 MHz, and decreases monotonically until a pure BEC is formed (at 1 MHz). At the BEC transition, a sudden increase of the ionization rate occurs, indicated by the crosses.*

To establish this relation, we record different ion rates corresponding to clouds cooled through phase transition. To explore transition points corresponding to different ion rates (or equivalently, different densities), we vary the atom number of the sample. This is done by adjusting the parameters of the rf ramp. Our evaporation ramp is separated into 4 linear ramps, each with a different rate of frequency change, in a way that the overall shape of the rf change rate is exponential as a function of time. To modify the atom number we adapt the first 3 parts of the evaporation ramp (we never change the parameters of the 4th part of the ramp). The more rapidly we cool initially, the more atoms we lose. To give some numbers: if we divide the duration each time step in the first 3 evaporation ramps by a factor of two, the final atom number is generally also divided by a factor of two.

An example of a series of ion rates are shown in Fig. 3.8, the gray curves. For each curve, the break in the slope in the ionization rate is indicated by a cross. This point identified as the point where the second derivative of the curve has a global maximum and where the third derivative is zero. The "raw" ionization rate is not smooth enough to obtain precisely the derivatives, so we first fit the ionization rate, and then differentiate the fit. The fit function used is a high order polynomial (12 terms). An example of such

a fit is shown in Fig. 3.9 together with its second and third derivatives. The time for BEC threshold is indicated by the gray vertical line, which corresponds to the point, where the third derivative is zero. These threshold points, indicated by the crosses in Fig. 3.8, now give the time corresponding to the threshold point for different ion rates. Note that the points are obtained for a particular final evaporation ramp and a given bias field. If these parameters are changed, the transition points will be displaced accordingly.

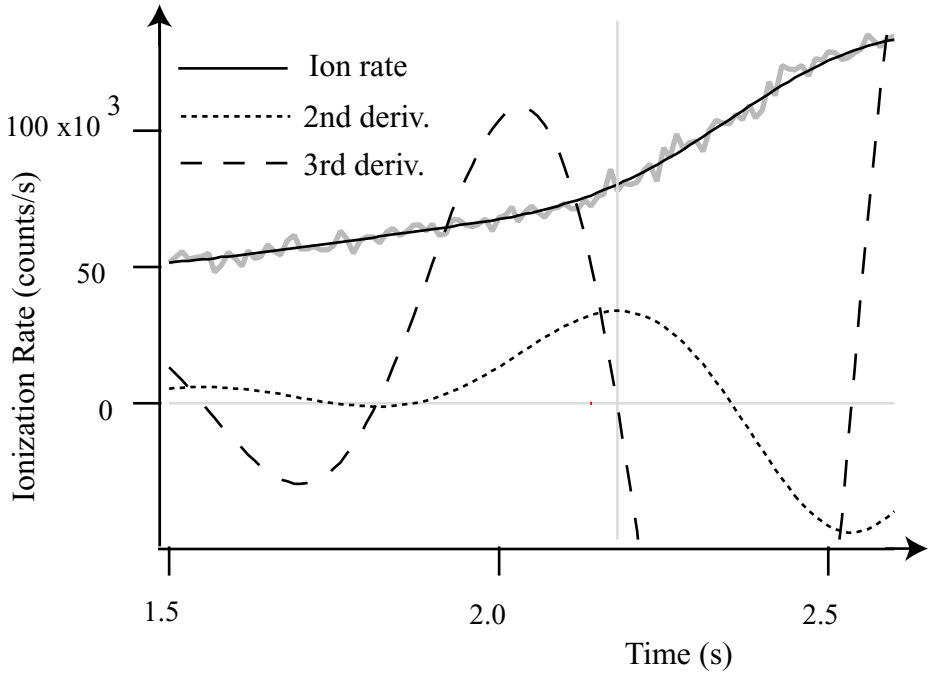

Figure 3.9: *The black solid line shows a 12-order polynomial fit of the ionization rate (gray curve). The short-dashed line is the 2nd derivative of the ionization rate while the long-dashed line is the 3rd derivative. The global maximum of the 2nd derivative (or equivalently the zero crossing of the 3rd derivative) indicates the break in the slope in the ionization rate, and therefore the onset of BEC)*

As this way of determining the BEC onset is essential to the work presented in chapter 5, we have repeated the experiment in order to increase the number of threshold points in Fig. 3.8. These data are shown in Fig. 3.10. As the time is directly related to the evaporation frequency (the frequency of the ramp decreases by 400kHz/s), we have substituted the increasing time scale by a decreasing frequency. The reason for doing this substitution is purely practical: in the experiment, we control the switch-off frequency and not the switch-off time. The points are then fitted by an exponential function, and thereby we establish in this way an empirical relation which

gives us the time of the onset of BEC for different ion rates[2]. We will in the following call this curve the "threshold curve". With this curve, for the particular evaporation ramp, we can know at which evaporation frequency we must switch off the trap, in order to observe a cloud at BEC threshold.

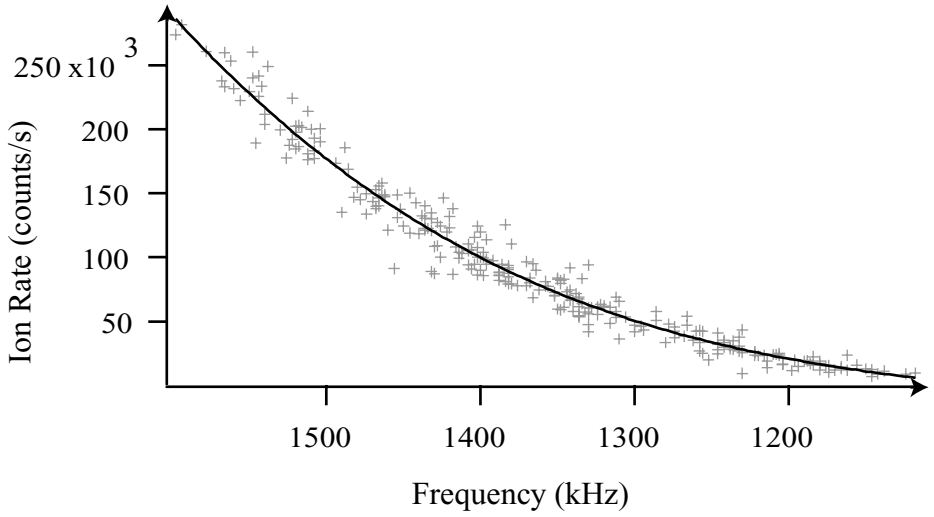

Figure 3.10: *Each point corresponds to the break in the slope of the ionization rate, and is here plotted as a function of the (switch-off) rf-frequency. Note that the frequency scale is reversed. The solid line corresponds to a fit of these points, and constitutes our empirical relation called the threshold curve.*

3.2.3 Fluctuations of the bias field

The dispersion of the points in Fig. 3.10 is mainly related to fluctuations in the bias field. A shift in the bias field gives rise to a shift in the transition point. Intuitively, this can be understood as explained in the following. We first define a parameter: $\eta = (h\nu - 2\mu_B B_0)/k_B T$. Here, B_0 is the bias field (the value of the magnetic field at the trap minimum), T is the temperature and ν is the frequency of the rf field responsible for the evaporative cooling. Therefore, η gives the ratio of the trap depth (determined by the rf-frequency) to temperature. During the evaporation, we expect η to be approximately constant. Now, by writing the condition for condensation $\eta k_B T_c = (h\nu_C - 2\mu_B B_0)$, where T_c is the critical temperature, we define ν_c as the rf-frequency at the transition point. If η is constant, a fluctuation

[2]There is no fundamental physics behind the choice of an exponential function, but it is chosen simply for empirical reasons.

in the bias field B_0 shifts ν_c accordingly: $\Delta\nu_c = 2\mu_B\Delta B_0/h$. A shift in B_0 would then displace the points horizontally in Fig. 3.10. To be rigorous, it is more complicated than so, because when the bias field fluctuates so does the density and therefore the transition point, but the above reasoning explains qualitatively why we see a significant dispersion in the transition points in Fig. 3.10.

In order to minimize this dispersion for the points in Fig. 3.10 we stabilized the bias field actively during the acquisition of these data: this was done by continuously monitoring the TOF signal corresponding to each ionization rate in Fig. 3.10. As seen in the figure, we cool the sample further down than necessary (i.e. far beyond the critical point). Actually, each time we continue the rf evaporation down to 1 MHz. The reason for doing that is that if the bias field corresponds to the desired value, a pure BEC is formed at this rf-frequency. Now if the cloud observed in the TOF signal starts to show thermal wings, we know that the bias field has decreased, and if the signal suddenly disappears, we know that the bias field has increased. If this happens, we compensate shot-to-shot for the changes by adapting the current in the coils, to bring the bias field back to its initial value, in order to observe a TOF signal showing a pure BEC. A change in the bias field (the total bias field is $\simeq 300$ mG) of more than 20 mG (or 25 kHz) is immediately revealed by the TOF signal, and can consequently be compensated. In this way we can limit the fluctuations of the points on the threshold curve to be less than ± 25 kHz, which corresponds to the dispersion of the points in Fig. 3.8. The threshold curve will be fully exploited in chapter 5, to obtain a cloud exactly at BEC threshold. The appealing thing about a cloud exactly at threshold is that the atom number can be deduced from the temperature. In our setup, even though we cannot measure the atom number precisely, we can measure the temperature. If we can be sure that we are at BEC threshold, the atom number of the cloud can then be deduced.

Chapter summary and outlook

In this chapter we have discussed qualitatively the dynamics of the cloud during formation and decay. This was done by observing the ionization rate assisted by the TOF signals. Of course, the ideal formation experiment consists of using a single one-shot ion signal during formation, and then translate this signal to the physically important parameter, the density. To do this, the rate constants for the ionizing collisions defined in chapter 1, are needed. The measurement of the rate constants will be our next step, and therefore the subject of the next chapter. However, due to difficulties in direct density measurements, the rate constants will first be given in terms of the scattering length, as we will explain in the next chapter. In chapter 5, by using the threshold curve discussed above, direct density measurements are no longer required, and the absolute values of the rate constants as well as the scattering length can be obtained.

CHAPTER 4

The ionizing rate constants

The ionization rate is a unique measurement tool, available only to clouds of metastable atoms. It is definitely worth trying to render it more quantitative by relating it to the density of the sample. The density is the important physical parameter, which we can compare with theory or measurements from other independent experiments. This motivates a measurement of the rate constants for different inelastic collisions present in the sample. If, however, we can show that only one type of density-dependent collision is present (i.e. for instance only two- *or* three-body processes) at the densities where we are performing our measurements, the translation between ionization rate and density simplifies. In this case, even though the particular rate constant is unknown, the value of the density within a multiplicative factor can be obtained from the ionization rate. This is unfortunately not the case. As we will show experimentally in this chapter, both two- and three-body collisions are present at the densities in the vicinity of Bose-Einstein condensation. Therefore, in order to translate the ionization rate to a density during BEC experiments, knowledge of the rate constants are unfortunately required. Until the beginning of our experiments, the rate constants had never been measured, and theoretically, only estimates were available (see chapter 1). Therefore we will measure these constants, and this is the main subject of the chapter. We will measure not only the ionization rates in a pure BEC, but also in a cold thermal cloud relatively far away from degeneracy. Measurements of ionizations rate from clouds at BEC threshold will be discussed later: chapter 5 is entirely dedicated to this subject.

4.1 Strategy

The "usual" way to determine rate constants corresponding to different loss processes is to record the number of atoms as a function of time for a decaying sample. From this decay curve, the rate constants describing the losses can be deduced. In this case, each measurement of the atom number constituting the decay curve is destructive. Recording a decay curve therefore requires a very high stability of the experiment. For our purposes, another inconvenient of this method is that we need the rate constants corresponding to *ionizing* losses, and not the rate constants corresponding to all loss processes. The problem is that one cannot distinguish ionizing and non-ionizing losses using this method. If non-ionizing collisions are present, losses due

to these processes will equally well be contained in the decay curve, and therefore in the deduced rate constants. To overcome the requirement of stability and to obtain the ionizing rate constants, we will use a different method. Remember the expression for the normalized ionization rate in a pure BEC, which was given in Eq. 1.45 in chapter 1:

$$\Gamma_{\mathrm{BEC}} = \frac{\Phi}{N} = \frac{1}{\tau_i} + \kappa_2 \frac{1}{2}\frac{4}{7}\beta\, n_0 + \kappa_3 \frac{1}{3}\frac{8}{21} L\, n_0^2. \tag{4.1}$$

Recall also that β and L are the two- and three-body rate constants, τ_i the ionizing lifetime. We have also defined κ_2 and κ_3 which are given by $\frac{1}{2!}$ and $\frac{1}{3!}$ for a pure BEC in the ideal gas approximation[1]. Therefore, by recording the ionization rate and corresponding density, for a large number of different densities, and fitting with Eq. 4.1, the rate constants can then be extracted. Each measurement of ionization rate versus density will be independent of the others, overcoming stability requirement. Moreover, as we here detect the ions and not a loss rate, the rate constants will arise from ionizing losses alone. Finally, also the form of the curve (linear or parabola), will give us useful information: it will inform us about the relative importance of contributions due to one- two- and three-body processes.

The measurements of ionization rate as a function of density can in principle be performed using a dense thermal cloud as well as a condensate, in order to deduce the rate constants. Nonetheless, as discussed in chapter 2 section 2.5.1, we are in general not able to measure correctly the density, because we only observe atoms which are transferred to the $m_J = 0$ level. Except in the case of a pure BEC. Here, the density can be obtained from the chemical potential (defined in chapter 2), which can be deduced directly from the width of a TOF signal. As this width can be measured correctly, so can the chemical potential. In general, for a thermal cloud, the density and width of the TOF signal are independent, and we cannot use the same trick to measure the density. Therefore, we have chosen to use a pure BEC to perform the above discussed measurements of the rate constants. Instead of measuring ionization rate and density, we then measure ionization rate and chemical potential, and from the latter, we deduce the density.

The only problem left is that the relation between chemical potential and density contains the scattering length, which was not very precisely known at the present time[2]. To begin, the strategy is therefore to determine the density, and thus the rate constants, as a function of the scattering length.

4.2 Corrections to the ionization rate

As mentioned above, for a BEC, κ_2 and κ_3 are given by $\frac{1}{2!}$ and $\frac{1}{3!}$. Even for a pure BEC (i.e. at zero temperature) is this only true within the mean

[1] By definition of the rate constants, $\kappa_2 = \kappa_3 = 1$ in a thermal cloud.

[2] The rate constant measurements here presented will later allow us to deduce the scattering length, see chapter 5.

field approximation. Beyond this approximation, quantum depletion must be considered and modifies these factors. In addition, our BEC is not truly pure; a small thermal fraction is often present. This also modifies κ_2 and κ_3 due to the presence of atoms in excited levels. To obtain precise values for the rate constants, these effects must be taken into account. This is the subject of this section.

4.2.1 Quantum depletion

Quantum depletion describes the fact that due to the interactions between the atoms in the sample, even at zero temperature, a certain fraction of the atoms are not in the condensate, see for instance Ref. [17]. The number of atoms outside the condensate at zero temperature N_{out} is given by

$$\frac{N_{\text{out}}}{N} = \frac{5\sqrt{\pi}}{8}\sqrt{n_0 a^3} \tag{4.2}$$

with a the s-wave scattering length and n_0 the peak density. As long as mean field theory is valid (i.e. $n_0 a^3 \ll 1$), quantum depletion is negligible. For metastable helium, the scattering length is large compared to other species used for BEC, as discussed in chapter 1. Consequently, the parameter $n_0 a^3$ is relatively large, and corrections due to quantum depletion will have a non-negligible influence on the values deduced for the rate constants.

Instead of changing the earlier given expressions for the ionization rate as a function of density, we will modify the factors κ_2 and κ_3 in order to account for these effects:

$$\kappa_2 \to \kappa_2 \times (1+\epsilon_2) \quad \text{and} \quad \kappa_3 \to \kappa_3 \times (1+\epsilon_3) \tag{4.3}$$

In the case of a homogeneous gas, the first order (in $n_0 a^3$) correction to the three-body rate has been calculated by G. Shlyapnikov [114]:

$$\epsilon_2 = \frac{1}{3} \times \frac{64}{\sqrt{\pi}}\sqrt{n_0 a^3} \quad \text{and} \quad \epsilon_3 = \frac{64}{\sqrt{\pi}}\sqrt{n_0 a^3} \tag{4.4}$$

For a harmonic potential, this correction must be modified. It has been calculated by O. Sirjean [37] and it becomes:

$$\epsilon_2 \simeq \frac{1}{3} \times 0.515 \times \frac{64}{\sqrt{\pi}}\sqrt{n_0 a^3} \quad \text{and} \quad \epsilon_3 \simeq 0.644 \times \frac{64}{\sqrt{\pi}}\sqrt{n_0 a^3} \tag{4.5}$$

These expressions are valid as long as the condensate is described by a Thomas-Fermi distribution – the corrections depend only on the density distribution. In the case of our largest condensates, we have $\epsilon_3 \sim 0.2$ and ϵ_2 about 3 times smaller.

4.2.2 Thermal excitation

The above corrections are valid for zero temperature. In reality, the temperature is not exactly zero. To be rigorous, when we speak about a pure BEC, we should rather say a quasi-pure BEC, because a small thermal fraction could be present. When the thermal fraction is less than about 10 %, it is not distinguishable in the TOF signal, even though it is present. In the above analysis, we have neglected the collisions between the condensate and the small thermal fraction. This introduces yet another correction, which again can be incorporated in κ_2 and κ_3. For example, for the three-body process, the correction $\Delta_3^{\rm th}$ modifies ϵ_3 such that it becomes

$$\epsilon_3 = \frac{64}{\sqrt{\pi}}\sqrt{n_0 a^3} \times (0.644 + \Delta_3^{\rm th}). \tag{4.6}$$

Using the Bogoliubov energy spectrum for the thermal cloud, $\Delta_3^{\rm th}$ can be estimated [37]. Its value depends on the thermal fraction (μ/k_BT). For a thermal fraction of 10%, $\mu/k_BT \sim 1.1$, and the correction for the three-body process is $\Delta_3^{\rm th} \sim 0.21$, three times weaker than the correction due to quantum depletion. The two-body correction, $\Delta_2^{\rm th}$, is even weaker, and is neglected in the analysis. It is interesting to note that even though the thermal excitation results in a larger fraction of atoms outside the condensate than does quantum depletion, the influence of the latter on κ_2 and κ_3 is much larger. Physically this is related to the spatial overlap of the excited atoms with the remaining condensate: thermally excited atoms are located as wings on the BEC and have only a small overlap with atoms in the BEC, while atoms being in excited levels due to quantum depletion have a larger overlap with the BEC.

The above corrections to κ_2 and κ_3 discussed here will be used for the data analysis given in section 4.5.

4.3 Density measurements

The density is as mentioned in the beginning of the chapter obtained from the TOF signal recorded on the MCP. As discussed several times, we cannot extract directly a reliable atom number or density from the TOF signal, so instead we extract the chemical potential, from which the peak density and atom number are deduced:

$$n_0 = \frac{m}{4\pi\hbar^2} \times \frac{\mu}{a}, \tag{4.7}$$

and

$$N = \frac{1}{15}\left(\frac{\hbar}{m\,\bar{\omega}}\right)^{1/2}\left(\frac{2}{\hbar\bar{\omega}}\right)^{5/2} \times \frac{\mu^{5/2}}{a} \tag{4.8}$$

The oscillation frequencies, entering through $\bar{\omega} = (\omega_\perp^2\omega_\parallel)^{1/3}$, are measured using the methods described in chapter 2. The above formulas also contain

the scattering length a, which we do not know. In the following, we will therefore give peak density and atom number parameterized by a.

4.3.1 The chemical potential

Some words justifying why the measured chemical potential gives the total number of atoms initially trapped, and not only the number of atoms falling on the MCP. First we must remember the reason why we cannot measure the atom number: only a certain fraction of the atoms are transferred to the magnetic field insensitive $m_J = 0$ level and fall on the detector. This means that the amplitude of the TOF signal does not correspond to the initial number of trapped atoms. Fortunately, the width of the TOF signal is independent of this transfer fraction. This is because of the following: in the trap, each atom has an interaction energy which reflects the mean field energy created by the presence of *all* the other atoms. After release of the trap, this energy is converted to kinetic energy, and the expansion of every single atom reflects the initial sample energy due to the presence of all the atoms. Therefore the expansion on the cloud will be independent of the number of atoms observed on the MCP. The amount of expansion is given by the width of the TOF signal. From this width, one can then determine the initial energy, and consequently the chemical potential, corresponding to the initial number of trapped atoms. The density deduced from Eq. 4.7 therefore gives the true atom number, and not only the number of atoms observed on the MCP.

4.3.2 A subtle factor of two

Some care must be taken when we determine the chemical potential from the width of the TOF signal. What we measure is an initial energy (arising from interactions) which is converted to kinetic energy during the beginning of the expansion[3]. Two regimes exist: if *all* the atoms are extracted, we measure the total internal energy of the sample, which is given by $E_{\text{internal}} = \frac{1}{2}\mu N$ ($\mu/2$ per atom). In the other regime, if very few atoms are extracted from the cloud, the energy for each of these atoms is by definition the chemical potential μ: it is the energy it takes to add an atom to the system. In this case, the total energy converted is given by $E_{\text{interaction}} = \mu N$. Importantly, note that N in both cases is the total number of atoms initially trapped.

The difference corresponding to the factor of two can be understood intuitively in the following way: when we extract one atom, its energy includes the interaction between itself and the remaining $N - 1 \simeq N$ atoms. This is correct as far as we extract only a small fraction of the atoms. If we count the interaction in the same way, while we extract all the atoms, each interaction would be counted twice: when atom 1 interacts with atom 2,

[3]The time for the conversion is approximately given by the inverse of the radial oscillation frequency $\simeq 1/1200$ Hz $\simeq$ 1ms.

and when atom 2 interacts with atom 1. Therefore, in order not to count the energy twice, we must multiply with a factor of $\frac{1}{2}$.

Note that the above results apply to a homogeneous gas. For a BEC in the Thomas-Fermi approximation, which is our case, the two regimes corresponds to $E_{\text{internal}} = \frac{2}{7}\mu N$ and $E_{\text{interaction}} = \frac{4}{7}\mu N$, respectively [17].

Free initial expansion of all atoms

Which formula should be used in our case? As we only extract a small fraction of atoms (about 10%), one could think that the interaction energy is given by $E_{\text{int}} = \frac{4}{7}\mu N$ (our BEC is described in the Thomas-Fermi approximation). This is the case in an experiment performed in the group of W. D. Phillips, where a small fraction of the atoms is extracted by transfer to an non-trapping state by Raman transition [115]. There, the remaining atoms stay trapped.

In our case the situation is different. Simultaneously with the transfer of a fraction of atoms to the non-trapping state, the trap potential is switched off, meaning that all the atoms, both $m_J = 0$ and $m_J = 1$, are released. In general, stray magnetic field due to eddy current will perturb the trajectories of the atoms in the $m_J = 1$ state, but in the very beginning of the expansion both $m_J = 0$ and $m_J = 1$ atoms expand freely together. The reason is that during the first ms of the expansion, the bias field decreases dramatically (the modulus *increases*) due to imperfections in the switch-off of the magnetic coils, see chapter 2 and [36]. This increase in the modulus of the bias field causes a dramatic relaxation of the radial oscillation frequencies (see chapter 2), and as a result, also the $m_J = 1$ atoms will expand nearly freely. The duration of the presence of the high bias field corresponds approximately to the time it takes for the interaction energy to be converted to kinetic energy, which is about 1 ms. Once the interaction energy is converted to kinetic energy, the energy of the atoms in the $m_J = 0$ state is no longer influenced by the behavior of the atoms in the $m_J = 1$ state, even though these atoms at later times during the expansion are perturbed by stray field and do not arrive on the MCP. As all the atoms expand together, the energy measured is then $E_{\text{internal}} = \frac{2}{7}\mu N$, even though only a small fraction is transferred to the $m_J = 0$ state. Note that the above conclusions are true only as long as the interaction between the different magnetic sub-states are the same: the scattering length corresponding to a collision between one atom in the $m_J = 0$ state and the other one in the $m_J = 1$ state must be approximately the same as the scattering length for a collision between two atoms in the $m_J = 0$ state. This is a reasonable assumption according to Ref. [116].

4.4 Experimental realization

The experiment is performed in the following way: during the last rf-evaporation ramp, we record the ionization rate until we have a pure BEC. The cloud is

then released from the trap, and the TOF signal is recorded. The very last value of the recorded ionization rate then corresponds to the cloud observed in the TOF signal. This is illustrated in Fig. 4.1, where an example of an ionization rate cooled until a time t_1 and the corresponding TOF signal are shown.

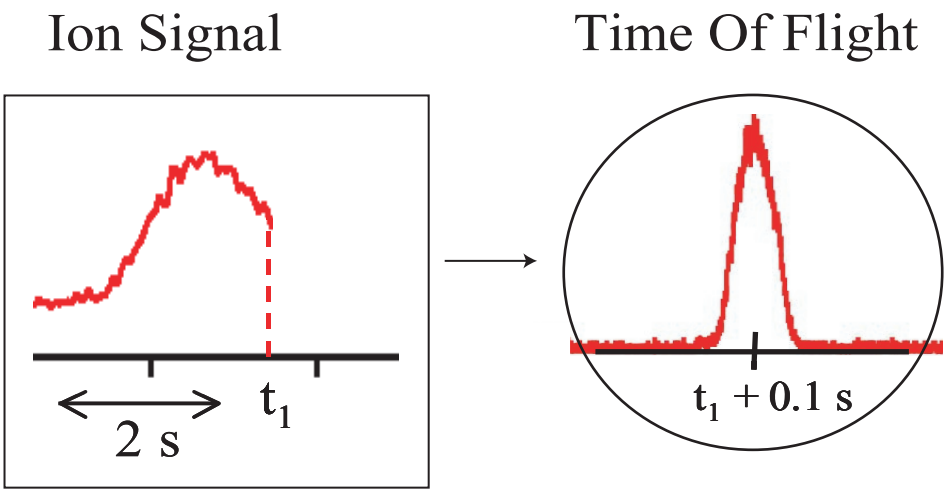

Figure 4.1: *The ion signal recorded during the last seconds of the rf-ramp. At time t_1 the atoms are released from the trap, and they arrive 0.1 s later on the MCP, and the TOF signal is recorded. In this way, the density corresponding to the ionization rate recorded at t_1 can be deduced.*

To obtain a better precision for the rate constant, we must explore a large range of densities. Therefore, the above procedure is then repeated for many clouds of different densities. The most dense samples are obtained by switching off the trap immediately after a pure BEC is reached. To decrease the density and still keep a pure BEC, we must lose atoms without any heating of the cloud. This is done by holding the atoms in the trap for a certain delay, with the rf-field kept on at the final value, which is around 50 KHz above the bottom of the trap. In practice, the rf-field is always switched off 100 ms before the trap is switched off, independent of the delay time, in order to measure the final ionization rate in the absence of the rf-field: this prevents an eventual perturbation of the ion rate.

4.4.1 Measurements of the ionization rate

The detected ionization rates in this experiment are around 3×10^4 counts per second, which is too low to be measured using the analog mode of our detector. Instead we use the high-gain counting mode. It has been checked that the detection process stays linear, both for the electronics as well as the detector itself, for detected ion rates up to 2×10^5, see chapter 2. We will therefore only produce samples for which the detected ionization rate do not exceed this value.

To obtain the real ionization rate, the ion detection efficiency must be known[4]. For a very cold cloud or a BEC, we can write the detected ionization rate as a function of the real ionization rate as $I_{\text{detected}} = \alpha \times I_{\text{real}}$, where α is a constant, expected to be around 0.42 (see chapter 2). The uncertainty of α will be obtained in chapter 5, but must at the present moment be considered unknown. We will therefore not include it in the uncertainty on the rate constants given in this chapter. Anyway, it is not before chapter 5 that we will be able to give the absolute values of the rate constants, and there the uncertainty on α will definitely be included in the final uncertainty on the rate constants.

4.4.2 Selection of pure Bose-Einstein condensates

In order to apply Eqs. 4.8 and 4.7, the cloud must be a pure BEC (i.e. a negligible thermal fraction). We use the following procedure to ensure that this is the case: first, we fit the TOF signal with an inverted parabola[5] over the whole non-zero range, and we obtain a chemical potential which we will denote by μ_{total}. We then fit again, this time excluding the wings of the TOF signal. In practice, we here include the central 90 % of the full Thomas-Fermi width obtained in the first fit. Thereby we obtain another chemical potential μ_{center}. Now, if the TOF signal does not contain thermal wings, the obtained two chemical potential should be identical. Therefore, we only retain data for which $0.9 < \mu_{\text{center}}/\mu_{\text{total}} < 1.1$. We can estimate the maximum thermal fraction that this procedure would accept. We do this by using an approximate fit function, which includes both a condensate and a thermal component, and which takes into account the influence of the mean field created by condensate on the thermal cloud, but not the effect of the thermal cloud on the condensate. We find that the above criterion rejects clouds with a thermal fraction larger than[6] 15%. In the following, when the thermal fraction is smaller than this value, we will refer to the

[4] In chapter 5 we will show that the results here obtained can be exploited quantitatively, even without knowing the absolute value of this efficiency, but for the present purpose, which is to deduce the rate constants, it must be known.

[5] This is the Thomas-Fermi function, see chapter 2.

[6] This number is not very precise: in addition to the uncertainty due to the fit function, which is only approximate, the fact that we here use the deduced amplitude of the thermal cloud requires knowledge of the fraction of atoms transferred to the $m_J = 0$ state, which we can only estimate.

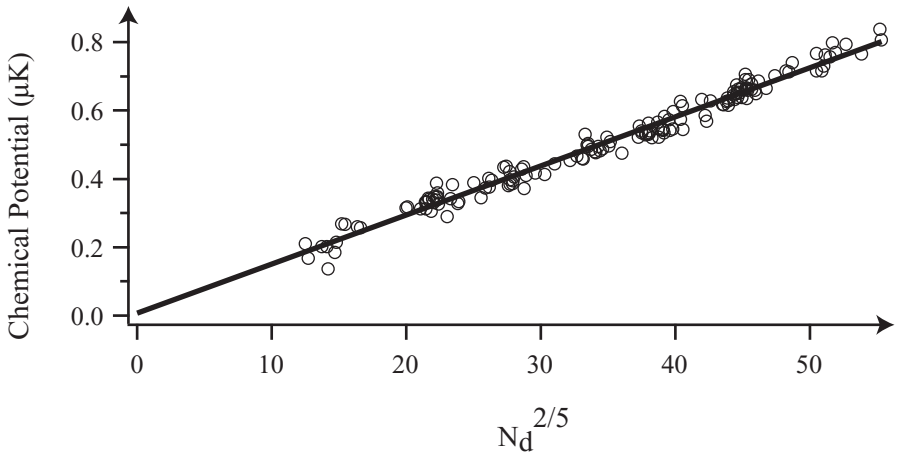

Figure 4.2: *Chemical potential μ vs $N_{\mathrm{d}}^{2/5}$, obtained for pure BEC. Note that N_{d} is the detected atom number, and therefore at least a factor of ten too small (to be discussed later in this chapter). The graph is linear in accordance with Eq. 4.8. This confirms that the detection in analog mode stays linear at least up to a detected atom of 2×10^4, and that we are able to exclude BECs containing a non-negligible thermal fraction*

condensate as a pure BEC, even though, rigourously speaking, we ought to call it a quasi-pure BEC. Thermal fractions smaller than 15% cannot be reliably detected in our experiment.

In contrast to the ion signal, the flux from the TOF signal is very high, around 10^7 atoms/s. In order to avoid saturation, the TOF signal is recorded in low-gain analogue mode. Therefore we lower the MCP gain at the moment of release of the atoms. To verify that we do not saturate the MCP while recording a TOF signal in this low gain mode, we graph the chemical potential as a function of the detected atom number to the power of 2/5. By detected atom number we mean the atom number deduced from the amplitude of the TOF signal, in contrast to the number deduced from the chemical potential. The graph of μ as a function of $N_d^{2/5}$ corresponds to Eq. 4.8 inverted. The result is shown in Fig. 4.2, and we observe a linear dependence. This indicates that the measurements of the chemical potential behaves as expected and that the detector does not saturate, even for the highest measured densities[7]. The small dispersion in the data in Fig. 4.2 also indicates that our procedure indeed allows us to select pure condensates, as

[7]Note that an eventual saturation would not influence the measurement of the chemical potential, as it is obtained from the base of an inverted parabola. The directly deduced atom number, obtained from the amplitude of the TOF signal, would. Therefore, a saturation would distort the straight line at high densities.

Eq. 4.8 is only valid when no thermal component is present.

4.5 Analysis of the results

We can now plot the ionization rate produced in the BEC as a function of peak density. This is done in Fig. 4.3. As the latest theoretical estimate for the scattering length is $a = 12^{+0}_{-4}$ nm (see Ref. [71] and chapter 1), we use this value to calculate the density. The two different symbols in the graph, black points and gray crosses, correspond to two different bias fields used during the data acquisition, and therefore two different longitudinal oscillation frequencies. For the black points $\omega_\perp/2\pi = 1200 \pm 50$ and for the crosses $\omega_\perp/2\pi = 1800 \pm 50$ Hz. In both cases, $\omega_\parallel/2\pi = 47 \pm 3$ Hz.

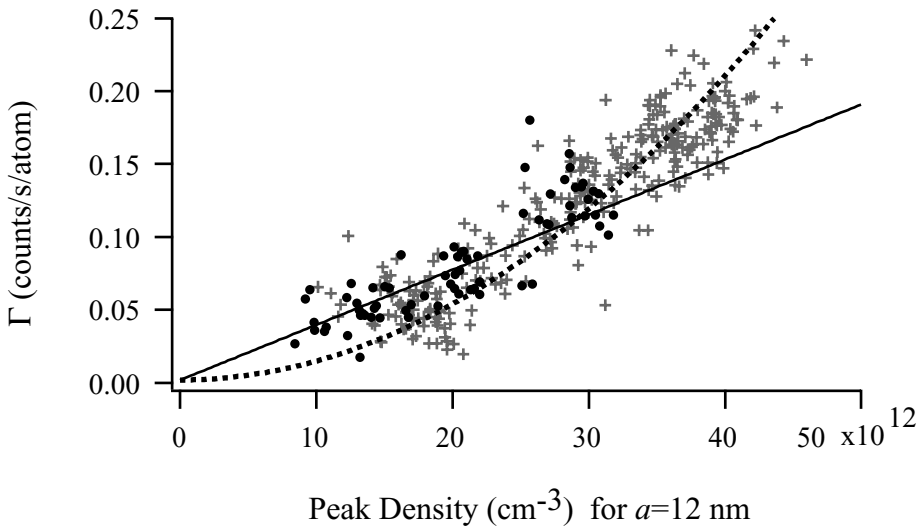

Figure 4.3: *Ion rate vs peak density for pure BEC. The density is calculated using the chemical potential and $a = 12$ nm. The gray crosses correspond to data obtained with $\omega_\perp/2\pi = 1800$ while for the black point $\omega_\perp/2\pi = 1200$. The solid line is a linear fit (neglects 3-body processes), while the dashed line is a parabola (neglects 2-body processes). None of the fits are very good, indicating that both 2- and 3- body processes must be included.*

The solid line is a fit which only takes into account background and two-body processes. This fit is linear in n_0 according to Eq. 4.1. The fit is clearly very bad (we obtain a normalized $\chi^2 \sim 1.4$), at least if we require that the curve intercepts the vertical axis at a non-zero value, i.e. a positive ionization

lifetime. We must conclude that at BEC densities (for the used oscillation frequencies), three-body processes are present and cannot be neglected. The dotted line takes only background and three-body processes into account. Again the fit does not describe the data very well ($\chi^2 \sim 1.2$). This is our first important result: at densities in the range $[10 - 50] \times 10^{12}$ cm^{-3} (see the scale of Fig. 4.3) both 2- and 3-body collisions are important! As both

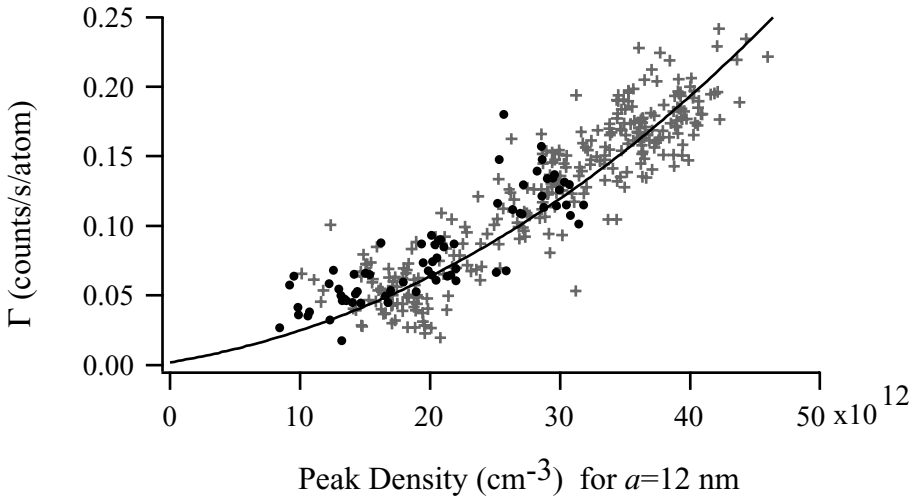

Figure 4.4: *Same data as in the preceding figure, but the fit includes both 2- and 3-body collisions.*

types of collisions are important, the translation from ionization rate to density is not a simple scaling, but requires the absolute value of the rate constants corresponding to both processes. To obtain the rate constants, we therefore fit the data presented in Fig. 4.3 again, but this time allowing for the presence of both 2- and 3-body collisions. The new fit is shown in Fig. 4.4, and this time it seems to describe very well the data (now we obtain a normalized $\chi^2 \sim 0.9$). The fit includes the corrections to κ_2 and κ_3 discussed above, which modifies the values of the rate constants, as we will discuss below. On the scale of the figure, the modification to the shape of the fit due to these corrections is invisible.

4.5.1 The obtained rate constants and their uncertainty

The obtained rate constants are shown in table 4.1. The error-bars are given in terms of the minimum and maximum values for each rate constant still compatible with a reasonable fit: they are obtained by considering the

rate constant	best fit	min	max
$\beta_{12}/10^{-14}\mathrm{cm}^3\mathrm{s}^{-1}$	1.1	0.2	2.0
$L_{12}/10^{-27}\mathrm{cm}^6\mathrm{s}^{-1}$	2.9	1.2	4.7

Table 4.1: *The rate constants obtained from the fit in Fig. 4.4. The range between the min and max gives the possible range for which the fit is still acceptable (see text), and is thus an estimation of the uncertainty on the rate constants. All rate constants are deduced assuming $a = 12$ nm, as indicated by their subscript. Note that the min and max value do not take into account the uncertainty due to the ion detection efficiency.*

quality of the fit as we minimize (maximize) one of the rate constants. We take the minimum and maximum values as being those just before the fit no longer is acceptable. Quantitatively, this corresponds to a reduced χ^2 value[8] of 1.1. For example, to calculate the minimum value of β, we leave L as a free parameter, and minimize β until $\chi^2 = 1.1$ This way of estimating the uncertainty results in error-bars on β and L which are highly correlated, because the decrease in β can be compensated by an increase in L. Therefore the minimum value of β is only possible by simultaneously taking the maximum value of L, decreasing the overall variation of the curve in Eq. 4.1. The curve using the minimum value for β and maximum value for L is shown in Fig. 4.5, solid line, while maximum β and minimum L corresponds to the dashed line. As we have calculated the rate constants for a given value of a, we have completely omitted the uncertainty due to this parameter. Nor do the minimum and maximum values take into account the systematic uncertainty on the ion detection efficiency. In chapter 5 we will estimate this uncertainty and include it in the error-bars of the rate constants (results presented later in this thesis are necessary to obtain this uncertainty). In chapter 5 we will also obtain the scattering length, allowing us to give the absolute values of the rate constants.

4.5.2 Dependence on the scattering length

Above we calculated the rate constants for $a = 12$ nm, but we can equally well deduce them for any value of a: we calculate the density as a function of a, and by repeating the fitting procedure we then deduce the rate constants for a range of possible values of a (8-16 nm). The results are shown in Fig. 4.6, black points. Now by fitting these points, we obtain the rate constants as a function of a. The fits are also shown in the figure as solid lines through the points, and the empirical fit functions giving the parameterization of the rate constants in terms of a are given in table 4.2. These empirical functions are valid in the range between 8 and 16 nm. Finally, the gray bands illustrate the error-bars of the rate constants, obtained as the

[8] χ^2 per degree of freedom, normally denoted by χ^2_ν even though we here call it χ^2

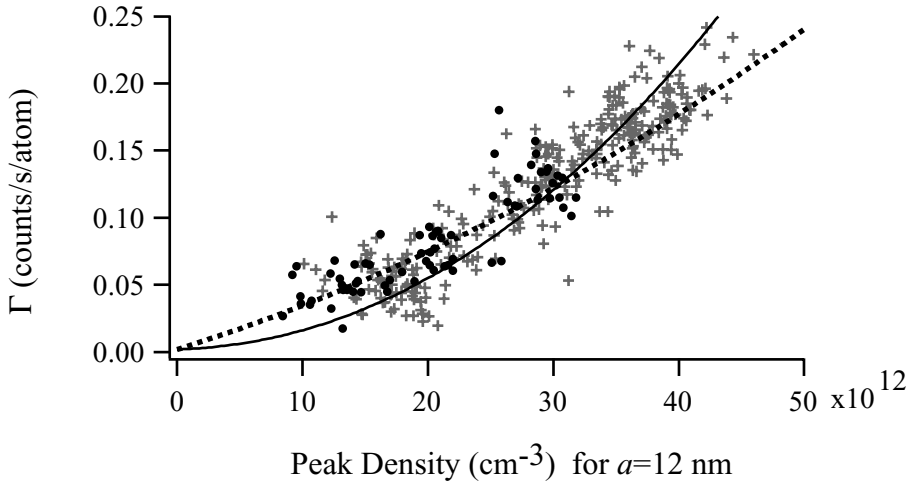

Figure 4.5: *The same data as in Fig. 4.3 and 4.4. The curves illustrates the error-bars: when using the minimum value for β and maximum value for L, one obtains the solid line, while maximum β and minimum L corresponds to the dashed line.*

minimum and maximum values described above.

Comparison with theory

A theoretical estimate of β as a function of a can be extracted from a graph in Ref. [116], and corresponds to the dashed line in Fig. 4.6 a. Taking into account the error-bars on the experimental data, we see a good agreement with theory.

For L there exists an approximate analytical expression given by $L \sim 11.7\hbar a^4/m$ [88]. This curve is indicated by a dashed line in Fig. 4.6 b.

$$\beta_a \simeq \beta_{12} \times \left(\tfrac{a}{12}\right)^2 \times \left(1 + 0.13\tfrac{a-12}{12}\right)$$

$$L_a \simeq L_{12} \times \left(\tfrac{a}{12}\right)^3 \times \left(1 - 0.28\tfrac{a-12}{12}\right)$$

Table 4.2: *Parameterization of the rate constants in terms of the scattering length in nm.*

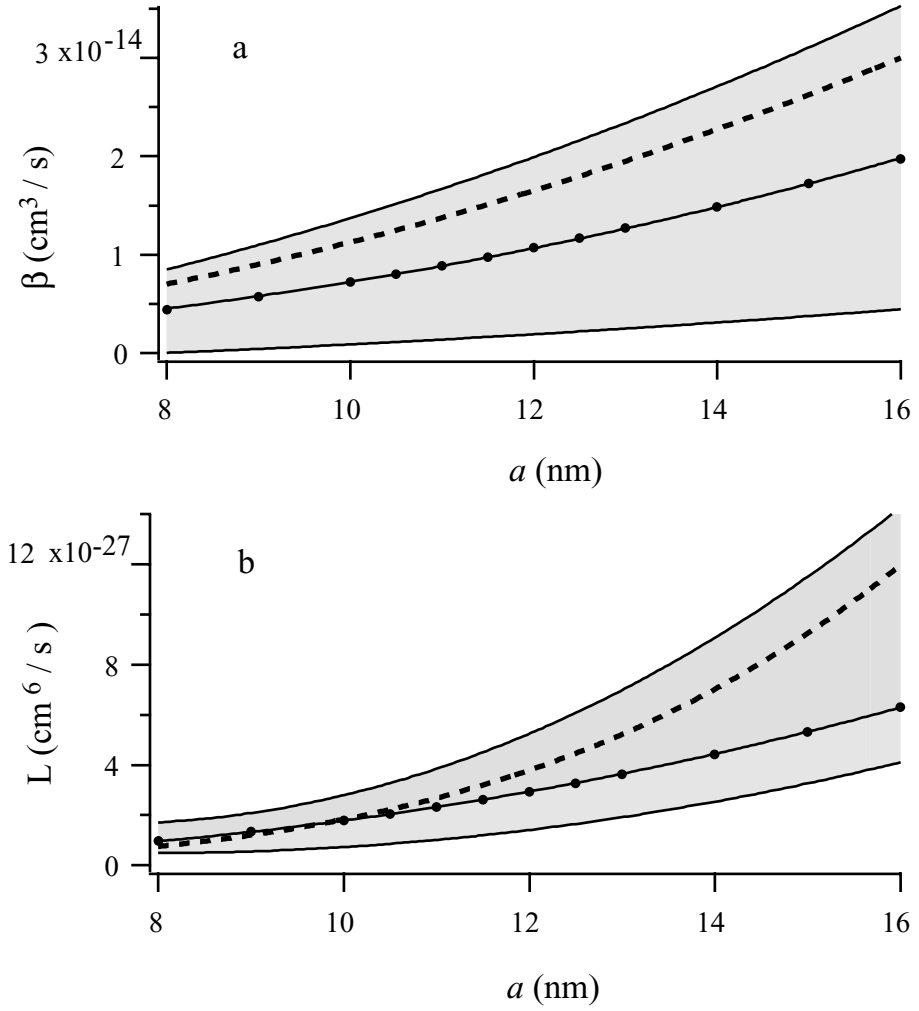

Figure 4.6: *The rate constants as a function of the scattering length. The black points corresponds to the data obtained with a BEC, and the solid line is a fit of these points. The gray band illustrates the error-bar on the measurements. The dashed lines give the theoretical values.*

Again we observe that within the error-bars, our measurements agree with the theoretical prediction. Especially for a scattering length between 8 and 11 nm, we notice an excellent agreement between data and theory.

4.6 Measurements in a cold thermal cloud

All data presented in this chapter have so far been obtained using a BEC. The reason is purely practical: we could measure the density by measuring the chemical potential. It is tempting to do the same kind of measurements with a thermal cloud - the rate constants should be the same, as long as the temperature of the cloud remains sufficiently low[9]. Of course, with a thermal cloud we cannot obtain the density using a chemical potential as we did for a BEC. Instead, we will use the unreliable, directly measured atom number, but then correct it by multiplying it with a given correction factor $\mathcal{F}$. In a first time we will obtain this factor from independent measurements using a BEC: it will be the ratio between the atom number deduced by the chemical potential (the "true" atom number N_{true}) and the atom number obtained by fitting the amplitude of the TOF signal (the measured atom number N_{meas}). This gives us a correction factor, which we will then use for the thermal clouds: we use it to multiply the atom number obtained from the amplitude of the TOF signals for the thermal clouds. Note that this amounts to assuming that this correction factor is the same for a BEC and a thermal cloud – and this will result in a disagreement between ionization rates in a BEC and a thermal cloud. Borrowing some of the results presented in chapter 5 will allow us to understand the source of disagreement and make the results coherent.

Recall Eq. 1.42 giving the ionization rate for thermal cloud deduced in chapter 1:

$$\Gamma_{\text{Th}} = \frac{1}{\tau_i} + \frac{1}{2}\beta\langle n\rangle + \frac{1}{3}\frac{8}{3\sqrt{3}}L\langle n\rangle^2. \tag{4.9}$$

In the BEC measurements, we replaced the average density by peak density, because this was the quantity deduced from the chemical potential. Here, this is no longer the case, so for simplicity, we keep the average density.

4.6.1 A naive correction factor: disagreement

To obtain a first (naive) value of the correction factor, we record a series of TOF signals corresponding to a pure BEC using exactly the same conditions as we will use for the experiments with a thermal cloud, in particular, we use the same voltage on the MCP. This is important, as the correction factor not only takes into account the fraction of atoms being transferred to the detectable state, but also an eventual default in the absolute calibration of the MCP in analogue mode. The correction factor $\mathcal{F} = N_{\text{true}}/N_{\text{meas}}$ is shown in Fig. 4.7, where we have used $a = 12$ nm to calculate the true atom number N_{true} using the chemical potential. We have plotted it as a function of the chemical potential. The average value turns out to be $\simeq 22$.

[9] Above 500 μK, the rate constant become temperature dependent, see [79].

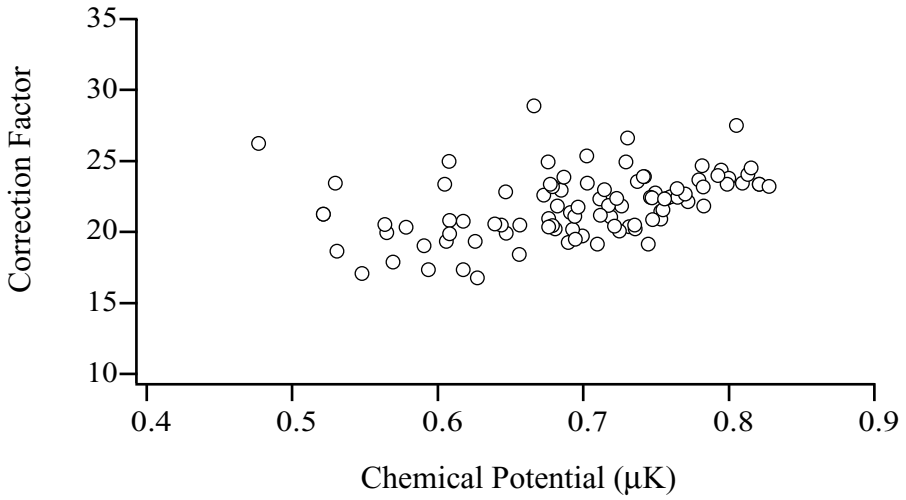

Figure 4.7: *The correction factor $N_{\text{true}}/N_{\text{meas}}$ obtained in a pure BEC. This is the ratio between the true atom number deduced by the chemical potential (with $a = 12$ nm) and the measured atom number obtained from the amplitude of the TOF signal. The factor is plotted as a function of the chemical potential. These measurements are independent of the measurements in the thermal cloud.*

We can now do the measurements of ionization rates versus density for a thermal cloud. The principle of the experiment is exactly the same as for a pure BEC, except that we must interrupt the evaporative cooling before the BEC threshold is reached. In general, we stop the rf-ramp around 1500 kHz and impose a delay without rf-shield, varying between 0 and 10 seconds, depending on the sample density desired: a delay decreases progressively the density. The temperature of the clouds varies between 2 and 5 μK. Fitting the amplitude of the TOF signals with a Gaussian function (assuming that we are far away from BEC threshold) and multiplying with the correction factor, we extract the density. For the obtained temperatures and densities, the phase space densities for the clouds varies between 0.1 and 0.8. We now plot the results: normalized ionization rate Γ as a function of the density. This is shown in Fig. 4.8, a. We have also plotted the theoretical curves from Eq. 4.9 using the rate constants which we obtained with a BEC. These are given as a function of the scattering length, and we have chosen to show three curves corresponding to $a = 20$, $a = 15$ and $a = 10$. From earlier measurements [8, 9] we know that a should be inside this range. Nonetheless we see that none of these curves agrees with the data. We also note a large dispersion of the data.

We suspect that the reason for this disagreement arises because the cor-

rection factor for a thermal cloud is different than for a BEC. If for example we assume that the detection efficiency is 1.5 higher for thermal atoms (this means that the correction factor is lower for a thermal cloud, so that thermal atoms are more efficiently transferred to the detectable level), we see that the data are compatible with a theoretical curve when the scattering length is somewhere between 10 and 15 nm, as shown in Fig. 4.8 b. Physically, the reason why the transfer fraction is different between a BEC and a thermal cloud might be the following: the magnetic field which is present during switch-off of the trap and which governs the transfer of atoms towards the detectable state, might be varying spatially. As the spatial extend of the thermal cloud is different from the BEC, the transfer could be different.

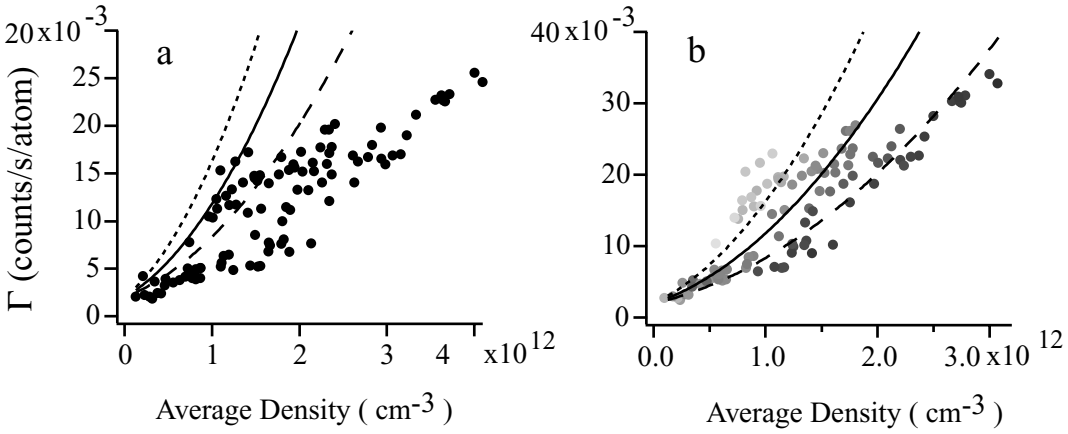

Figure 4.8: *The normalized ionization rate as a function of density for a thermal cloud. In a we have assumed the same correction factor for the thermal cloud as obtained with a BEC, while in b we assume the correction factor is 1.5 times higher. In b we have indicated the temperature of each cloud with colors: light gray corresponds to high temperature, while for dark points the temperature is low.*

Even when changing the correction factor, the data in Fig. 4.8 do not agree with the shape of the curve, and the large dispersion resists. We suspect that the transfer fraction varies with temperature, and consequently $\mathcal{F}$ will do. This is possible, because the spatial extent of a thermal cloud depends on its temperature. To investigate this we indicate the temperature corresponding to each data point. This is shown in the data in Fig. 4.8 b, where light gray corresponds to high temperatures, and dark gray to low temperatures. We see a clear systematic variation with temperature, which confirms the above hypothesis.

4.6.2 A better way to obtain the atom number

In the next chapter we will present a method to determine the true atom number for a thermal cloud at BEC threshold. This is possible by using thermodynamical relations valid for clouds exactly a BEC threshold. It will allow us to obtain not only the rate constants and the scattering length, but also a more reliable correction factor $\mathcal{F}$. In order to conclude this section about measurements in a cold, thermal cloud at this stage, we will use this factor, even though the reader must wait until the next chapter, to see how this factor is obtained experimentally. As suspected, $\mathcal{F}$ turns out to depend on temperature, as we will see below. We will also show that using this new $\mathcal{F}$ as a function of temperature will not only decrease the dispersion, but also make the theoretical curve agree with the data.

To obtain the new correction factor, we fit TOF signal obtained at BEC threshold, and we obtain the temperature T_c of these clouds. How this is done is discussed in detail in chapter 5. From the temperature of these clouds, we can calculate the true atom number, which we denote N_c (indicating that the cloud is at the critical point):

$$N_c = 1.202 \left(\frac{k_B T_c}{\hbar \overline{\omega}} \right)^3 \tag{4.10}$$

where $\overline{\omega} = (\omega_{\|} \omega_{\perp}^2)^{1/3}$ is the geometric average of the trap oscillation frequencies. We also extract an atom number from the fit (the amplitude) giving us the measured atom number N_{meas}. We then extract $\mathcal{F} = N_c / N_{\text{meas}}$. We plot this factor in Fig. 4.9 as a function of temperature (gray crosses). Only data for clouds being at BEC threshold according to their ionization rate (the final value is on the threshold curve, see chapter 3) are shown: in order to use Eq. 5.3, the data must indeed be at threshold. For comparison, we also show the correction factor for pure BEC (open circles). This is the same data as given in Fig. 4.7, but the scale of the axis is compressed.

The first thing we notice is that the correction factor is different for a BEC and a thermal cloud. This explains why the data for thermal clouds presented in Fig. 4.8 do not agree with the theory, when one simply applied the same correction factor as for the BEC. One also notice that for the thermal cloud, $\mathcal{F}$ increases linearly with temperature between 5 and 15 μK. A fit gives $\mathcal{F}(T) = 3.1 + 3.8\,T(\mu\text{K})$. Reporting this relation to our data for the thermal clouds, we can now correct the measured atom number to obtain the true atom number[10]. The result is shown in Fig. 4.10 b. For comparison, the data where the correction factor is assumed to be constant (the same as for the BEC), is shown in a. The two theoretical curves correspond to $a = 11$ nm (solid line) and $a = 12$ nm (dashed line). Two things to notice: first, the data seem to agree with the form of the theoretical curve for a scattering length between 11 and 12 nm, and second, the large dispersion

[10] This relies on the assumption the clouds at T_c behaves as thermal clouds away from threshold.

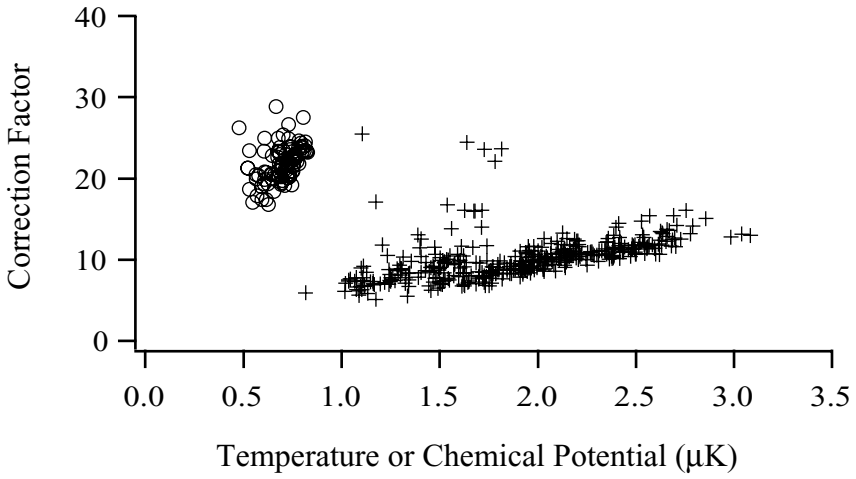

Figure 4.9: *The correction factor F for clouds at BEC threshold as a function of temperature*

is eliminated. Points corresponding to the highest densities do still not fall on the curve. This has an explanation: when we fitted the TOF signals, we used a Gaussian function, which is only valid far away from BEC threshold. This is not necessarily the case for the most dense clouds shown at the curve. We can confirm this by observing the Gaussian fits for these clouds. Two examples are shown in Fig. 4.11, the dotted lines. These fits are obviously very bad. The Gaussian function is not peaked enough to describe the data, and therefore the density deduced from the fit will be too low. Also the atom number will be estimated too low, and thus the ionization rate per atom too high. Consequently, fitting with a Gaussian will tend to displace the data towards densities, which are lower than in reality, and towards normalized ion rates, which are too high, exactly as we observe in Fig. 4.10.

In the vicinity of BEC threshold, the Gaussian function should be replaced by a Bose function. We therefore try to fit with a Bose function with the chemical potential fixed to its threshold value[11]: $\mu = \mu_c$. These fits are also shown in Fig. 4.11 as solid lines. But the Bose function does not fit any better. We conclude that we are too near the threshold to use a Gaussian function, but not close enough to impose the chemical potential to the threshold value. However, the poor quality of the Gaussian fit explains why the high-density data points in Fig. 4.11 b, do not lie on the theoretical curve.

In conclusion, due to the measurements at the BEC threshold, we have

[11]This function is only valid at BEC threshold, see chapter 5.

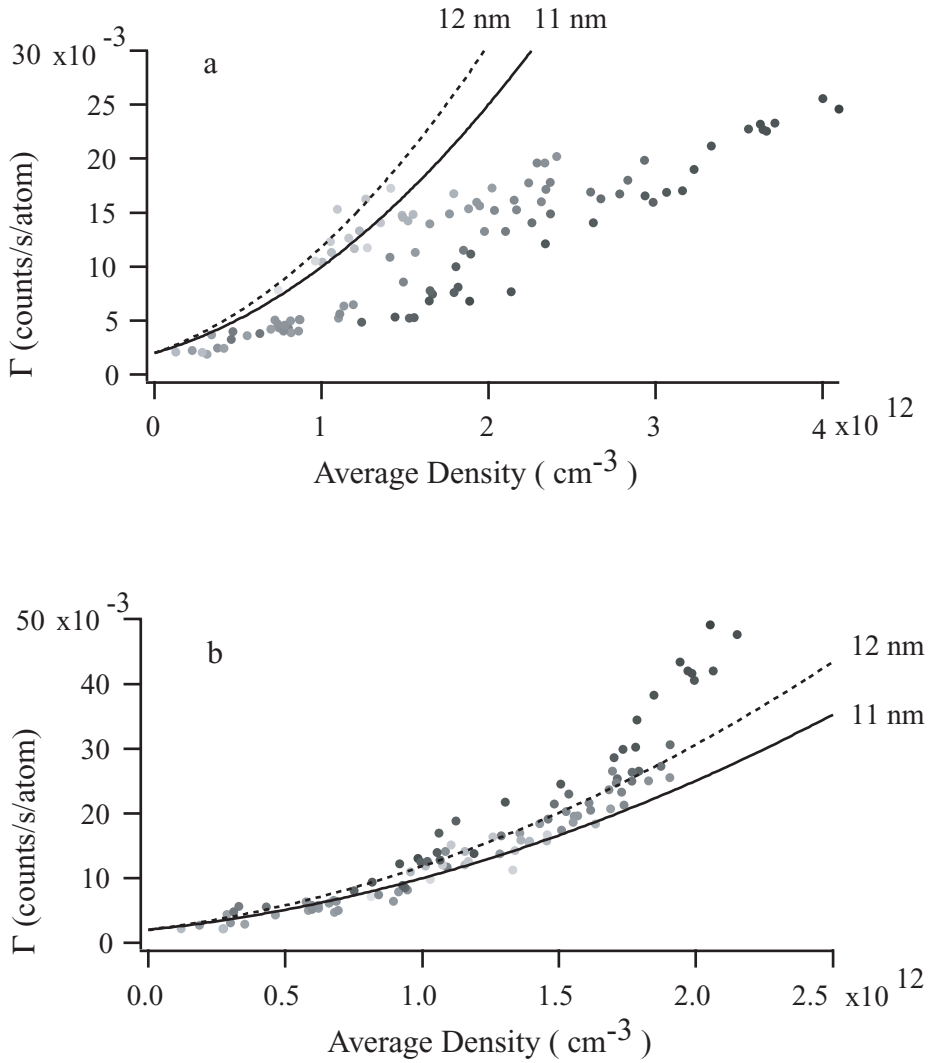

Figure 4.10: *Ion rate as a function of average density for a thermal cloud. The density is obtained by fitting the cloud with a Gaussian function. In a) we have used the correction factor obtained with a BEC, while in b) we have used the correction factor obtained for a thermal cloud at BEC threshold. The solid and dashed curves in both graphs give the ion rates for* $a = 10$ *and* $a = 11$ *nm respectively, using the rate constants determined in this chapter.*

managed to deduce the correction factor which seems to be valid for a thermal cloud in general. Due to this factor, we now understand the ionization rate data not only for a pure BEC, but also for a thermal cloud, at least in

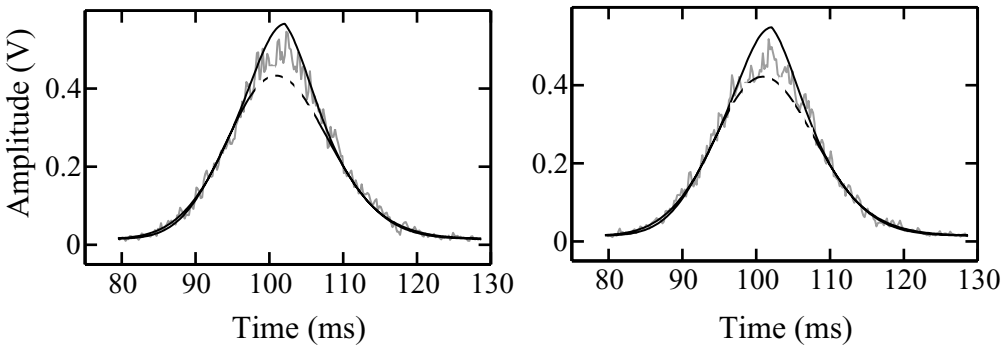

Figure 4.11: *Two examples of TOF signals and their fit corresponding to the highest density data in Fig. 4.10, a). The dashed curve is the Gaussian fit, which we use to deduce the density. The Gaussian fit is very poor, which explains why the data deviate from the curve in Fig. 4.10, a). The solid line is the Bose fit, which does not fit well the TOF signal either. The cloud is too close to threshold to be described by a Gaussian, but too far away to be a Bose function with a chemical potential corresponding to the threshold value.*

a given range of temperatures.

Chapter summary and outlook

We have presented our BEC measurements of the two- and three-body ionizing rate constants parameterized by the scattering length. The parameterization was necessary because we obtained the density of the BEC from measurements of the chemical potential – and these two quantities are related *via* the scattering length. The obtained rate constants agree with theory for all realistic values of the scattering length. We have also measured ionization rates in cold thermal clouds, and the results are consistent with the measurements for a pure BEC for a scattering length between 11 and 12 nm. In the next chapter we deduce the scattering length, and see that it is indeed in this interval.

CHAPTER 5

A measurement of the s-wave scattering length

In chapter 4 we obtained empirical expressions for the rate constants β and L in terms of the scattering length a. In this chapter, we will combine these results with independent measurements of the ionization rate. Together, these measurements will allow us to deduce a, and thus to give the absolute value for the rate constants. The independent ionization rate measurements are obtained with a cloud exactly at the BEC phase transition point[1]. We exploit the fact that for a cloud at this point, the density is related to the critical temperature. Therefore, at the critical point, density measurements can be replaced by temperature measurements. The reason why this is useful is that the temperature can be obtained from the width of the TOF signal, in the same way as the chemical potential for a BEC. The temperature however, in contrast to the chemical potential, gives the density independent of the scattering length[2]. In addition, as we have shown in chapter 3, we can locate the transition point by following the ion signal. We can therefore obtain measurements of the ionization rate at the transition point as a function of critical temperature. The data obtained are then fitted with the theoretical expression for the ionization rate, using a, which enters the expression *via* the rate constants $\beta(a)$ and $L(a)$, as a fit parameter. In this way, the value of a can be determined.

5.1 Ionization rates at Bose-Einstein phase transition

We will start by deriving an expression for the ionization rate as function of the temperature for a cloud at BEC threshold. If we in a first time neglect atomic interactions, the density of the cloud can be written in terms of a Bose function defined by $g_\alpha(x) = \sum_{i=1}^{\infty} \frac{x^i}{i^\alpha}$ [17]:

$$n(\mathbf{r}) = \frac{1}{\lambda^3(T)} g_{3/2}\left[\exp\left(-\frac{1}{k_B T}\, V(\mathbf{r}) - \mu\right)\right], \tag{5.1}$$

[1]The term "BEC threshold" or just "threshold" as well as "critical point" will in the following also be used to indicate the BEC phase transition.

[2]This is not exactly true: a small dependence on the scattering is present, but will not affect our final result, as we will discuss below.

where T is the temperature of the cloud, k_B is the Boltzmann constant, $\lambda(T)$ is the thermal de Broglie wavelength defined by $\lambda(T) = h/\sqrt{2\pi m k_B T}$, $V(r)$ is the harmonic trapping potential, and μ is the chemical potential. At BEC threshold, $\mu = 0$ when we neglect the interactions and zero point energy of the harmonic potential. Therefore, the critical density can be written as

$$n_{\rm c}(\mathbf{r}) = \frac{1}{\lambda^3(T_{\rm c})} g_{3/2}\left[\exp\left(-\frac{1}{k_B T_{\rm c}}\, V(\mathbf{r})\right)\right] \tag{5.2}$$

which depends only on the critical temperature $T_{\rm c}$ and the trapping potential. Also the total atom number depends only on $T_{\rm c}$:

$$N_{\rm c} = g_3(1)\left(\frac{k_B T_{\rm c}}{\hbar\overline{\omega}}\right)^3, \tag{5.3}$$

where $\overline{\omega} = (\omega_\parallel \omega_\perp^2)^{1/3}$ is the geometric average of the trap oscillation frequencies. Now recall the expression for the ionization rate discussed in chapter 1:

$$\Phi = \frac{N}{\tau_i} + \frac{1}{2}\beta \int n^2 d\mathbf{r} + \frac{1}{3} L \int n^3 d\mathbf{r}. \tag{5.4}$$

Now if we insert the above expressions for the critical density and atom number in this expression, the ionization rate at threshold $\Phi_{\rm c}$ can be deduced:

$$\Phi_{\rm c} = (\frac{\omega_{\rm c}}{\overline{\omega}})^3 \times \left[\frac{1}{\tau_i} 1.20 + \frac{\beta(a)}{\lambda_{\rm c}^3} 0.33 + \frac{L(a)}{\lambda_{\rm c}^6} 0.22\right]. \tag{5.5}$$

Here, $\omega_{\rm c} \equiv k_B T_{\rm c}/\hbar$ and $\lambda_{\rm c} \equiv \lambda(T_{\rm c})$. The numerical values appear in the calculations of the integrals of the Bose functions and are therefore independent of any parameters of the cloud.

Equation 5.5 gives us the ionization rate as a function of the critical temperature, and the rate constants are given in terms of the scattering length. By measuring $\Phi_{\rm c}$ as a function of $T_{\rm c}$, and fitting these data using Eq. 5.5, the scattering length can be obtained. This will be our strategy.

5.1.1 Ion detection efficiency

An advantage of this approach is that the value of a will be independent of the absolute *ion* detection efficiency α, which is not very well known. This can be understood in the following way: the detected ionization rate $\Phi_{\rm c,det}$ must be modified according to the efficiency so that $\Phi_{\rm c} = \Phi_{\rm c,det}/\alpha$. Now remember that the ionizing lifetime and the rate constants also were obtained by ionization rate measurements. This means that they were also corrected according to a detection efficiency α': $\tau_i = \alpha'\tau_{\rm det}$, $\beta = \beta_{\rm det}/\alpha'$ and $L = L_{\rm det}/\alpha'$. Inserting these expressions into Eq. 5.5, we get

$$\Phi_{\rm c,det}/\alpha = (\frac{\omega_{\rm c}}{\overline{\omega}})^3 \times \left[\frac{1}{\alpha'\tau_i} 1.20 + \frac{\beta_{\rm det}(a)/\alpha'}{\lambda_{\rm c}^3} 0.33 + \frac{L_{\rm det}(a)/\alpha'}{\lambda_{\rm c}^6} 0.22\right]. \tag{5.6}$$

It is now clear that if the detection efficiency has not changed since the earlier measurement, then $\alpha = \alpha'$, and Eq. 5.6 becomes independent of the detection efficiency. We expect this to be the case, and we will later show that we can confirm this experimentally.

5.1.2 Including the interactions and zero point energy

Equation 5.5 is an approximation in the sense that it does not take into account the atomic interactions and zero point energy[3]. In this section we will show that for our experimental parameters, these terms play a major role. We will therefore derive an expression for the ionization rate as a function of critical temperature, which takes the interactions into account. In this section, we will only outline how the calculations are done, a more complete derivation is given in Appendix B.

In the mean field approach, which includes the atomic interactions, the following expression for the density is obtained [17]:

$$n(\mathbf{r}) = \frac{1}{\lambda^3(T)} g_{3/2}\left[\exp\left(-\frac{1}{k_B T}\left(V(\mathbf{r}) + 2U\, n(\mathbf{r}) - \mu\right)\right)\right] \tag{5.7}$$

In addition to the parameters defined above, $U = 4\pi\hbar^2 a/m$ is the interaction constant. This includes a term in the density which depends on a. Therefore, the interactions introduce a dependence on a, in addition to the dependence *via* the rate constants. However, adding these a-dependent terms to the ionization rate given in 5.5, will not change the strategy discussed above.

As before, the ionization rate at the phase transition is derived from Eq. 5.4, now using Eq. 5.7 for the density. As the density now includes a term proportional to the density itself, no analytic expression can be derived, but a first order perturbation calculation is possible. The approach is similar to the one used in Ref. [51]. The calculations in this reference are for a fixed atom number: in our calculations, we fix the temperature instead of the atom number. We use the chemical potential of a gas in a harmonic potential at the BEC transition, valid to lowest order in a and for large atom numbers [51]:

$$\mu_c/k_B T_c = \frac{3}{2}\frac{\widetilde{\omega}}{\omega_c} + 4 g_{3/2}(1)\frac{a}{\lambda_c}. \tag{5.8}$$

We have used the notation $\widetilde{\omega} = (2\omega_\perp + \omega_\parallel)/3$ which is the arithmetic mean of the oscillation frequencies. The first term takes into account zero point energy while the second term arises from the interactions. When this chemical potential is inserted into Eq. 5.7, we obtain an expression for the critical density as a function of the critical temperature. We then make a first order expansion of the small terms due to interactions and the zero point energy

[3]The effect of the zero point energy is often referred to as finite size effects. This can be understood from the following: in the thermodynamical limit, the density $n = N/V$ is constant for $N \to \infty$. As the volume varies as $1/\bar{\omega}^3$, then $\bar{\omega} \to 0$ if we want the density to remain constant. If $\bar{\omega} = 0$, the zero point energy goes to zero in this limit.

of the potential. With this first order expression for the density, one can write the integrals in Eq. 5.4 in terms of integrals of Bose functions, which can be solved numerically. We finally obtain the critical ionization rate:

$$\begin{aligned}\Phi_{\rm c} = (\tfrac{\omega_{\rm c}}{\overline{\omega}})^3 \times \quad & [\ \tfrac{1}{\tau_i}(1.20 + 2.48\tfrac{\widetilde{\omega}}{\omega_{\rm c}} + 12.35\tfrac{a}{\lambda_{\rm c}}) \\ & + \tfrac{\beta(a)}{\lambda_{\rm c}^3}(0.33 + 1.81\tfrac{\widetilde{\omega}}{\omega_{\rm c}} + 6.75\tfrac{a}{\lambda_{\rm c}}) \\ & + \tfrac{L(a)}{\lambda_{\rm c}^6}(0.22 + 2.21\tfrac{\widetilde{\omega}}{\omega_{\rm c}} + 6.50\tfrac{a}{\lambda_{\rm c}})\Big]\end{aligned} \tag{5.9}$$

The terms proportional to a/λ_c account for the atomic interactions, while the corrections proportional to $\widetilde{\omega}/\omega_c$ take into account the effect of finite sample size. For the typical parameters of our experiment ($T_c \sim 2$ μK and $a = 12$ nm) we have $a/\lambda_c \simeq \widetilde{\omega}/\omega_c \simeq 0.02$. This means that for the term due to background collisions, the zero point correction is of the order of $0.02 \times 2.48/1.20 \sim 4\%$ and for interactions it is $0.02 \times 12.35/1.20 \sim 20\%$. For the 2-body process, the corrections are 11% and 40%, respectively, while for 3-body process, they are 20% and 60%.

Since these first order corrections are very large, in particular those due to interactions, we need to estimate the second order corrections. This is also done in Appendix B. We use an approach similar to Ref. [117], and we find that the second order corrections due to interactions are relatively small: for one-body collisions, the second order contribution is typically -4% of the ideal gas result, while for two- and three-body collisions, the corrections are 1.8% and -3%, respectively. As shown in Appendix B, also higher order corrections to zero point effects are small. In the analysis of our data these corrections turn out to be negligible, and it is therefore sufficient to use the first order approximation only.

We will later in this chapter use Eq. 5.9 to fit our data. This equation contains 3 parameters, β, L and a, but due to the parameterization of the rate constants in terms of a, can we do a simple one-parameter fit. This will give us a, and then, by substituting this a in the expression for the rate constants, they can also be deduced.

5.2 Experimental realization

The setup is the same as the one used to measure the collision constants described in chapter 4, and the experimental realization is similar: we record an ionization rate during a given time, and then we switch off the trap and record the TOF signal. Again, the last value of the measured ionization rate corresponds to the cloud observed in the TOF signal. The main difference is that we switch off the trap when the cloud is at the transition point instead of cooling it down until a pure BEC is obtained.

To identify the transition point, we use the break in the slope in the ionization rate. In chapter 3 we established a curve relating the break in the slope in the ionization rate (i.e. the threshold point) with the frequency of the rf-ramp (see Fig. 3.10 in chapter 3). This curve will allow us to switch off

the trap very close at the rf-frequency corresponding to the transition point. In this way, the last observed ionization rate and the corresponding TOF signal, will correspond to a cloud at BEC threshold. From the TOF signal, we get the critical temperature of the cloud. This procedure is illustrated in Fig. 5.1, where the ionization rate and the corresponding TOF signal are shown.

When we take the data, the experiment cycles continuously with a sequence lasting around 25 seconds. The ionization rate is fairly reproducible from run to run, but it fluctuates on a longer time scale[4]: after 3-4 runs, the ionization rate makes a jump which can be as large as 100.000 counts/s (see Fig. 5.1, a for comparison). The instabilities arise mainly from the fluctuations in the initial atom number in the magnetic trap, which we do not yet control very well. When the ionization rate changes, so does the rf-frequency corresponding to the transition point, according to the threshold curve. Consequently, when the ionization rate jumps, we must change the rf-ramp such that the cloud again is released when the ionization rate is on the threshold curve. In principle, the adaptation of the rf-ramps could be done real-time, by monitoring the initial value of the ionization rate, and accordingly change the interruption frequency during the run. It turns out to be simpler to chose in advance the interruption frequency, and take data until the ionization rate jumps. When it happens, we change the rf-ramp, and discard the last run, which did not produce a cloud at the transition point.

Another difference compared to the experiment in chapter 4, is the temperature of the cloud. In chapter 4, we used a pure BEC, while we here use a thermal cloud with a temperature around 2 μK. Remember that we must push the atoms in the $m_J = \pm 1$ state away from the MCP with magnetic gradients, in order to obtain a clean TOF signal. The higher the temperature is, the more kinetic energy the atoms have, and the more difficult it is to push away the $m_J = \pm 1$ atoms. Therefore, we increase the current in the coil which generates the horizontal magnetic gradient which pushes the atoms. In addition, to ensure that the $m_J = \pm 1$ atoms do not arrive on the MCP, we add a supplementary coil generating a vertical gradient. In this configuration, the atoms are pushed diagonally away from the MCP, and this turns out to be more effective.

A last difference between the pure BEC and the T_c measurements concerns the stabilization of the bias field. For the BEC experiments, after each run we observed the TOF signal corresponding to a pure BEC. From the signal, we could immediately identify a change of the bias field of 25 kHz or larger, by observing either thermal wings or a violent decrease in the signal. The TOF signal therefore allows us to continuously adapt the bias. With a thermal cloud, this is not possible, because the the form of the TOF signal is not considerably modified when the bias field fluctuates. Consequently

[4]It behaves like the Danish weather: the probability of the weather to be the same as the day before is 90 %, and still, the weather changes very often!

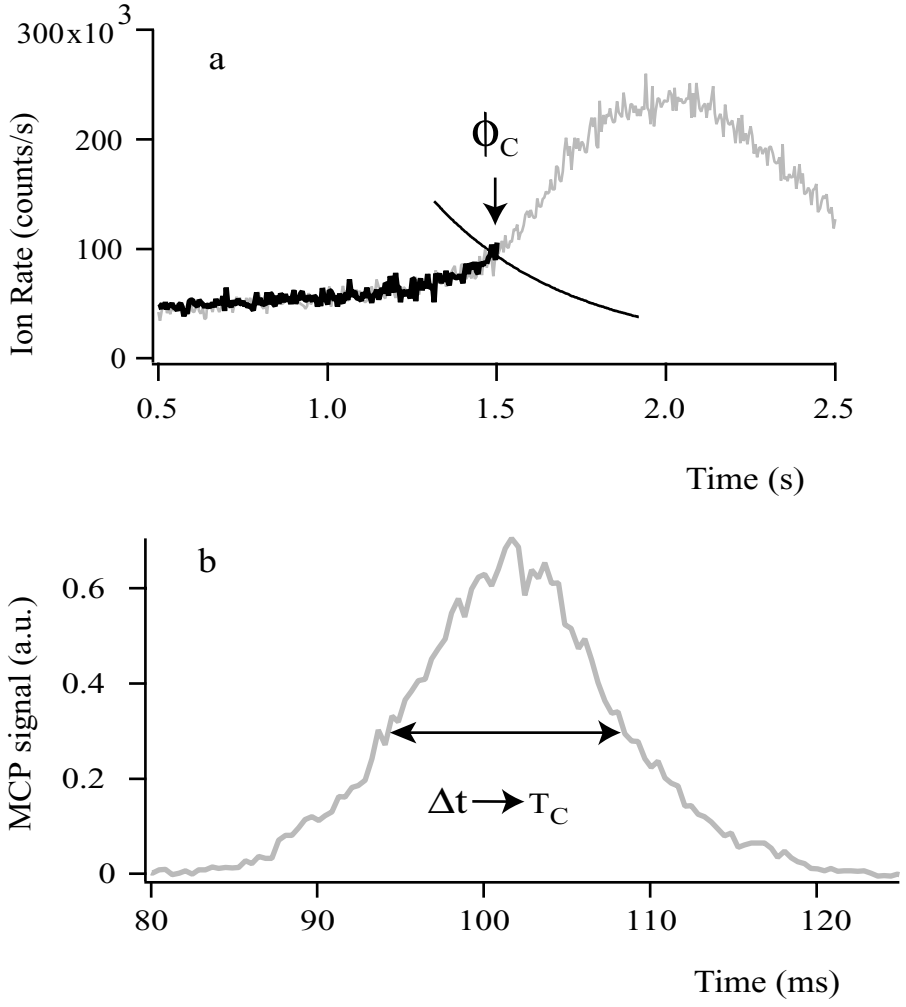

Figure 5.1: *In a we show an example of an ionization rate (gray curve). We use the threshold curve (black curve) to locate the threshold point. In the subsequent experimental run, we cut the trap at this point. The corresponding ionization rate is shown in black. The final value of the ionization rate Φ_c is the critical ionization rate. In b we show the TOF signal corresponding to the critical point. The fit of this TOF signal gives us the critical temperature T_c of the cloud.*

we cannot adapt the bias field from run to run. Instead, in every third run, we continue the evaporation down to 1 MHz. Here, a pure BEC should be

formed if the bias field has not derived. We can then adapt the bias field according to the above procedure. As a result, in this experiment, we only verify the bias field every third run, and consequently, fluctuations in the bias field are larger than in the BEC measurement. As explained in chapter 3, fluctuations in the bias field give rise to small fluctuations in the ionization rate[5], and therefore, according to the threshold curve, in the transition point as a function of rf-frequency. Consequently, in a large fraction of our runs, the evaporation is not interrupted at the threshold curve. After finishing the data acquisition, we discard all runs for which the interruption frequency was further than ± 25 kHz away from the threshold curve. In general, we often need to discard about 80 % of the data!

To explore a large range of critical temperatures and ion rates, the size of the cloud is varied. This is done by modifying the speed (the rate of change of the rf-frequency) of the first 15-20 seconds of the evaporation ramp. Note that the final part is never changed. The atom number left after these 15-20 seconds depends strongly on the speed of the ramp. If it is high, few atoms are left, while if it is low, more atoms will be left. We exploit this to adapt the evaporation ramp in order to obtain – as far as the uncontrolled fluctuations allow – the desired atom number.

5.3 Data analysis: the analysis

The starting point is the data set consisting of ionization rates and their corresponding TOF signals for clouds at the BEC transition point. These data have been selected by requiring the final ionization rate to be on the threshold curve, as explained in section 5.2. The following data analysis can be divided into three main parts: *i)* first we need to determine the ionization rate at the transition point from the recorded ion signal, *ii)* then we determine the temperature from the TOF signal, *iii)* and finally we verify by using the TOF signal if a cloud is at the transition point. If this is not the case, it should not be included in the analysis. Of course, in the ideal case, if the ionization rate is on the threshold curve, the cloud ought to be at threshold. However, a slight derivation of the bias field shifts the threshold curve relative to the one we recorded with the correct bias field, and therefore use for switching off the trap. Consequently it will happen that even though the ionization rate is on the initially recorded ionization rate, the cloud is not exactly at threshold. Therefore we also use the TOF signals for verification, and this point is the crux of the data analysis.

5.3.1 The ionization rate

As explained in section 5.1, the analysis relies on the fact that the ion detection efficiency has not changed since the measurements of the rate constants

[5]These small fluctuations are present in addition to the large jumps in the ionization rate discussed above.

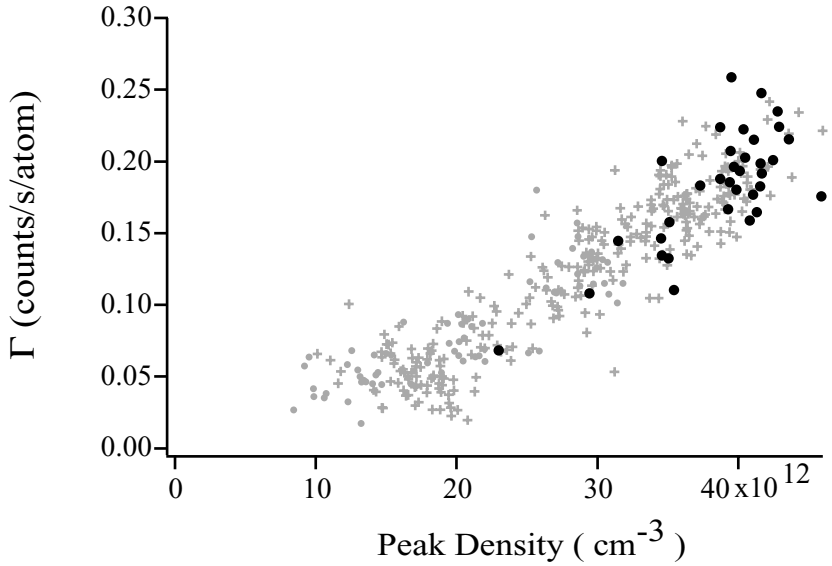

Figure 5.2: *The gray points (points and crosses) correspond to the data presented in chapter 4, and the black points are measurements discussed in section 5.3 obtained 1 year later. The absolute scale for the peak density was obtained by choosing $a = 12$ nm. Importantly, note that that the two different series of data are well superposed. This means that the detection efficiency has not changed between the two acquisition periods.*

performed 1 year earlier. One could imagine that due to extensive use, the properties of the surface might have changed or other similar degradations. If this has changed the detection efficiency, the measured ionization rate must be scaled accordingly. To verify if it is unchanged, we repeat first the measurement of ionization rate as a function of density for a pure BEC, presented in chapter 4, section 4.5. In Fig. 5.2, we plot the new measurement (black points) in addition to the measurements obtained 1 year earlier (gray points). We see that the two data sets are superposed, indicating that the detection efficiency has not changed.

The remaining analysis of the ionization rate is straightforward. To obtain the ionization rate at threshold, we take the average value of the last 5 points of the recorded ionization rate, in order to obtain less noise. This corresponds to averaging over the last 25 ms before the switch-off of the magnetic trap. We can do this because the cloud does not evolve significantly during 25 ms: assuming that the temperature decreases 2 μK per second (see section 5.6.1), 25 ms corresponds to a temperature change around 0.05μK, which is much smaller than the estimated temperature uncertainty. The ion detection is shot noise limited, so for a typical ionization rate of 100 $\times$

10^3 counts/s, the noise is $\sqrt{100 \times 10^3 \times 0.025}/0.025 = 2000$ counts/s $\simeq 2\%$. The error-bars arising from this contribution turn out to be approximately the size of the data points, and are therefore omitted in the following graphs.

5.3.2 Time-Of-Flight signal

To obtain the temperature, we fit the TOF signals. The function used for fitting is discussed in Appendix C. Briefly, it is obtained by combining Eq. 5.7 with the chemical potential fixed to the threshold value (Eq. 5.8) and performing a first order development of terms arising from atomic interactions. This gives a density distribution which describes the initial atomic density (i.e the density of the atoms in the trap). To obtain the fit function for the atoms arriving on the MCP, we have to modify the density distribution according to the expansion of the cloud. We assume that the cloud expands ballistically, i.e. no influence from collisions during the expansion, and we obtain thereby the fit function for the atoms arriving on the MCP. Later on we will refer to this as the Bose fit, even though this term rigorously is more general.

When we do the fit, each point in the TOF signal is weighted by an estimated uncertainty. A detailed derivation of this uncertainty is given in Appendix E. In summary, to estimate this uncertainty, we chose a set of TOF spectra which appeared to show no systematic deviation from their fits. The noise as a function of amplitude of the measured TOF signal was then estimated as the standard deviation between this TOF signal and the fit. We then established a relation between noise and amplitude, and this relation is used in the fitting procedure. As shown in Appendix E, we observed that this noise varies as the square root of the amplitude of the signal, indicating that also the atom detection is shot noise limited. When we fit, we exclude the central part of the TOF signal (it is given zero weight in the fit). The excluded window corresponds to half of the rms width of the TOF signal. The reason why we exclude the center of the TOF signal is to avoid the high density region, where the approximations used for deducing the fit function might no longer be valid.

The temperatures obtained from the fit are as mentioned obtained assuming a purely ballistic expansion of the cloud. This is an approximation, because we know that collisions are present and influence the first ms of the expansion of the cloud. When this is the case, the gas is in the *hydrodynamic regime*[6]. Instead of modifying the fit function in order to account for the collisions, we can maintain the fit function corresponding to a ballistic expansion, and simply modify the temperature obtained according to a scaling factor. This factor can be obtained as the solution to a set of differential equations, following the approach of by P. Pedri *et al.* [118]. How this is done in practice is discussed in Appendix D. For a temperature of 2 μK, the correction is $\simeq 0.1\ \mu K$.

[6]The opposite regime is referred to as the collisionless regime.

Since we use a fit function which takes into account interactions (Appendix C), the deduced temperature will also depend on the scattering length a. Fortunately, the changes on temperature are very small, when a is varied inside the range corresponding to realistic values. As shown in Appendix D, also the hydrodynamic correction depends slightly on the scattering length a. But as before, this dependence is quite weak, and the corresponding error introduced on a is very small. We will discuss these two errors when we list the uncertainties on a below.

Identification of transition point using the TOF signal

To improve our data selection, we will now use the second available criterion based on the TOF signal. The main point to realize is the following: since the Bose function, as defined in Appendix C, only is valid for a cloud exactly at BEC threshold, the quality of this fit will indicate how close the cloud is at the transition point. On the other hand, a Gaussian function is only valid for a cloud far away from quantum degeneracy. Consequently, if the cloud is at the transition point, a Gaussian function will not fit the data well. In Fig. 5.3 we show an example of a TOF signal corresponding to a cloud at BEC transition (gray curve). The solid black line is the Bose fit, while the dashed line is a Gaussian fit. In the example shown, a large window indicated by the vertical lines (corresponding to the rms width of the TOF signal) is excluded from both fits. The fact that the Bose function reproduces the central part of the TOF signal, even though it is given zero weight in the fit, confirms that the Bose function is the correct fit function, and therefore that the cloud is at the transition point. This conclusion is further supported by the fact that the Gaussian fit is very poor.

To render this criterion more quantitative, we will describe the fit in terms of a χ^2 value[7]. The value of χ^2 depends on the weight given to the different data points in the fit, which is inversely proportional to the uncertainty of the given points. This uncertainty is estimated in Appendix E. As this uncertainty is only approximate, the absolute values of χ^2 are somewhat arbitrary. Still, the χ^2 values can be used to classify the fits relative to each other, and can therefore be used to exclude the poorest fits. Because of the arbitrariness of the χ^2 values, we normalize all values according to the best of all our fits. We will use these χ^2 values in the analysis below, in particular, we will show how we can eliminate "outliers" by rejecting fits having a χ^2 higher than 2. A collection of fits and their χ^2 value is given in Appendix F.

In addition to a high χ^2 value, the fact that the Bose function is not the correct fit function can be revealed by the following procedure: we fit the TOF signal using the Bose function, excluding a window centered on

[7]We will in the following always use the reduced χ^2, which is the χ^2 per degree of freedom. For simplicity, we will denote it by χ^2, even though it is often denoted by χ^2_ν in literature. For a mathematical definition of the χ^2, see Appendix E.

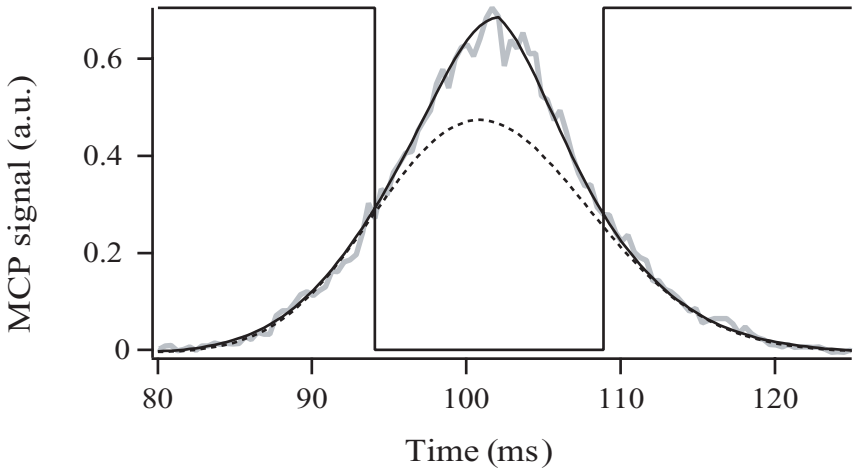

Figure 5.3: *A typical TOF signal (gray curve), fitted by the Bose function, see text, (solid line) and by a Gaussian function (dotted line). For both fits, we have excluded the central region indicated by the vertical lines (in this example it is the rms size of the cloud).*

the TOF signal. The width of this window is now varied, starting from 0 (we fit the entire TOF signal) and increased successively out the rms size of the cloud. The fits will then give us the temperature as a function of the size of the excluded window. Now if the fit function is the correct one, the temperature should be independent on the size of the window: the correct fit function should be able to reproduce the whole TOF signal, even when a part of it is excluded from the fit. To illustrate this in practice, we show in Fig. 5.4 two TOF signals: 1a shows a cloud that we expect to be at BEC threshold ($\chi^2 \simeq 1$ for the Bose fit) and 2a shows a cloud which is not at threshold ($\chi^2 \simeq 3.6$). The TOF signals and their Bose fit are shown to the left, and the temperature obtained from the fit as a function of the size of the hole is shown to the right. The hole size σ is normalized to the rms width of the TOF signal σ_0. We see that for the low χ^2 fit, the variation in the fitted temperature as the excluded window is increased is very small (a few percent), while for the large χ^2 fit, it is as high as 15%. In the example in Fig. 5.4, the temperature is decreasing, indicating that the cloud is above T_c. This can be understood in the following way: a cloud before T_c will be wider than a cloud at T_c. When we fit to the whole range, the procedure will tend to give a wide fit, and thus a relatively high temperature. When the center is excluded, only the wings will be considered, allowing the fit to be more

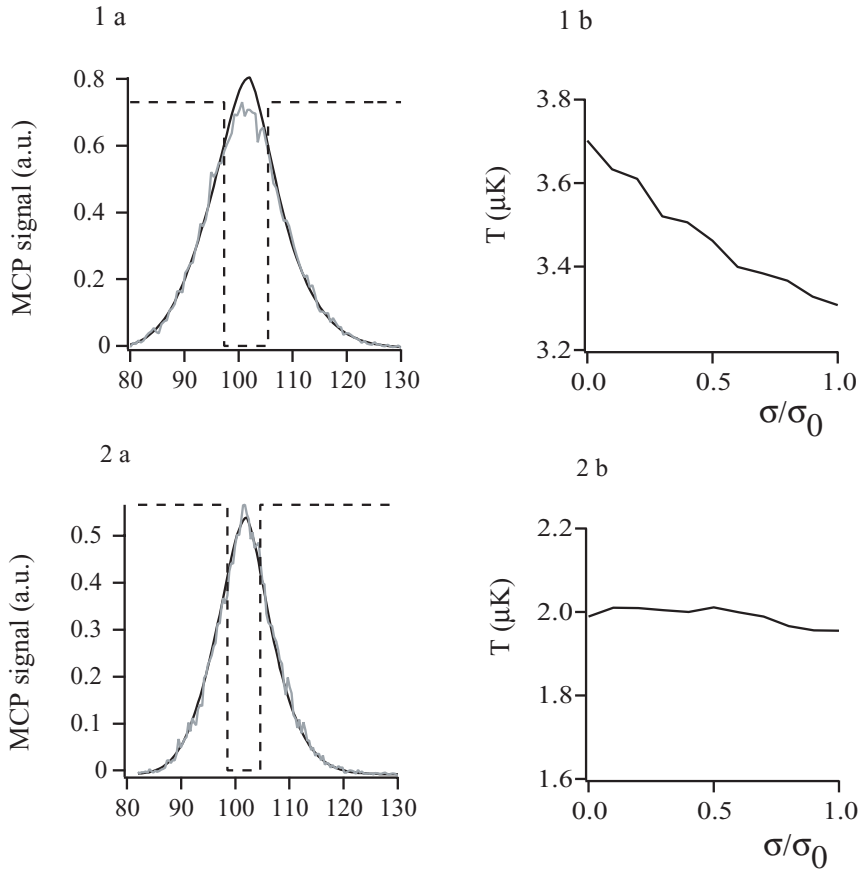

Figure 5.4: *Two examples of TOF signals fitted by the Bose function, see text. In 1a we show a fit with a* $\chi^2 = 3.6$ *, while in 2a,* $\chi^2 = 1.0$*. This is a general feature in our fits; when we qualitatively estimate that a fit is bad, the* χ^2 *is also high. Evolution of the temperature obtained by the two fits, as the excluded window is successively increased is shown in 1b and 2b respectively. The flat curve in 2b confirms the quality of the fit, while the decrease of temperature in 1b indicates that we are not at BEC threshold.*

peaked than the real TOF signal as is the case in the figure. This will give a lower temperature so the temperature appears to decrease as the exclusion window increases. In the same way, an increasing temperature indicates a cloud cooled beyond T_c: the fit excluding the center will be wider than the actual TOF signal, and the deduced temperature will be higher than when fitting to the total range. Our idea was to investigate the effect of discarding all fit for which the temperature varies more than 10 %. In practice, not very surprisingly, this criterion corresponds (almost) exactly to requiring χ^2

to be below 2, and we will therefore only apply this latter criterion.

Even though this temperature variation turns out to be redundant what data selection is concerned, it gives us information about the uncertainty on the temperature: it gives us an estimate of the uncertainty in temperature due to the fitting procedure. For this purpose we consider the fits corresponding to excluded windows ranging between 0 and the half of the rms size (instead of the entire rms size) of the TOF signal[8]. If we consider only fits with χ^2 below 2 (the data which we include in the final analysis), the temperature variation is ~ 5 %. This is our best estimate for the uncertainty on the temperature measurements[9].

In our approach the main principle of the data selection using TOF signals is the following: we fit with the Bose function, of which the chemical potential is fixed to the value at threshold, and then estimate if the fit is good or not. One could imagine another approach: we could fit the cloud with the temperature *and* the chemical potential as free variables, and then discard TOF signals for which the obtained chemical potential is different from the one corresponding to BEC threshold. Unfortunately, the temperature and chemical potential are not "orthogonal" variable in the fit function, in the sense that a variation in one, can be compensated by a variation in the other one. This gives rise to a very large uncertainty in the fitted value of these two parameters: the uncertainty in the chemical potential turn out to be about 100% of its value, which makes it useless as an indicator of BEC threshold. We therefore think that it is a better solution to fix the chemical potential to the value at BEC threshold, and then consider the quality of the fit, as we have done above.

5.4 Data analysis: the data

In the preceding section we have described the analysis: how we obtain the ionization rate and the temperature, and how we can define, by using the TOF signals, another criterion in addition to the ionization rate, to tell if a cloud is at threshold or not. In this section, we will finally present the data[10].

We will first consider the data points corresponding to all our data, selected only according to their ionization rate being on the threshold curve, i.e. a selection using the TOF signal has not yet been done. The critical ionization rate as a function of critical temperature for these data is plotted in Fig. 5.5, a. For comparison, we also show the theoretical curves (Eq. 5.9)

[8] When the excluded window approaches rms size, the quality of the fit starts to decrease.

[9] This assumes that we use the correct scattering length in the fit function, see section 5.5.1.

[10] This, and the preceding section title, were inspired by the name of the chapters "Nom de pays: le nom" and "Nom de pays: le pays" in "A la recherche du temps perdu" written by Marcel Proust. The two chapters are written in 1892-1895 and 1897, respectively.

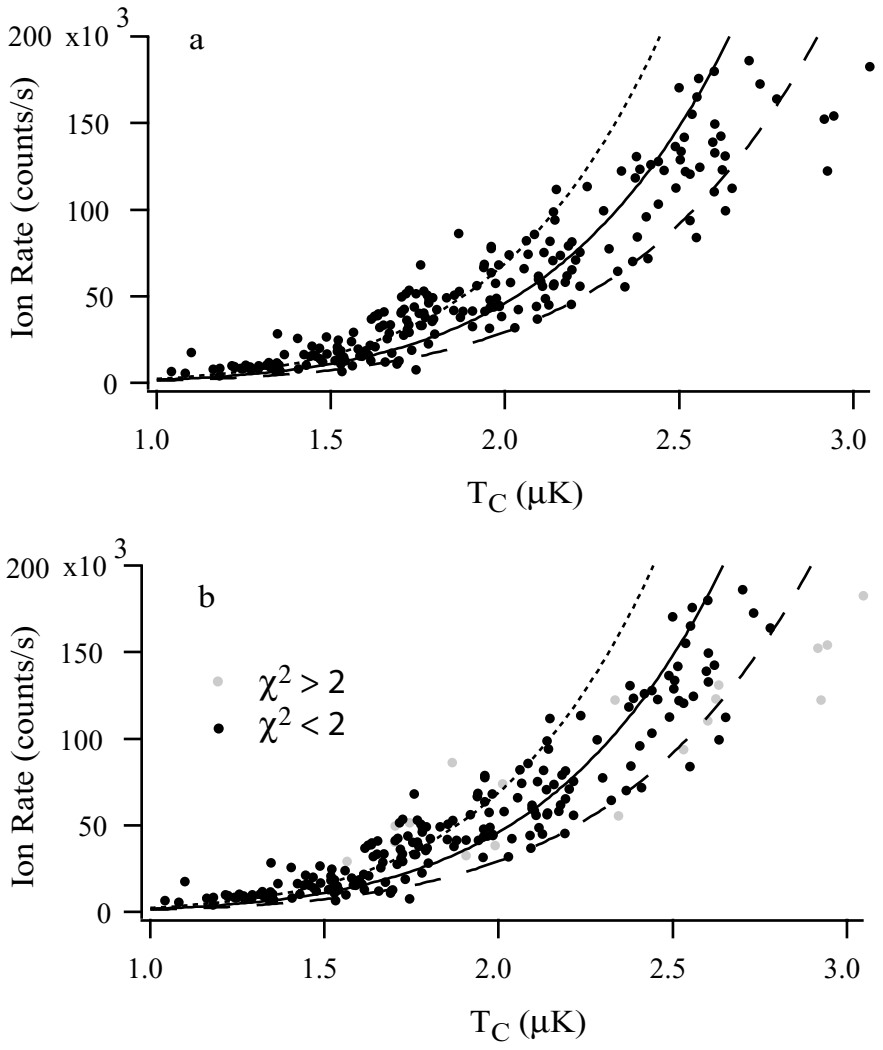

Figure 5.5: *Ion rate as a function of critical temperature. The dotted, solid, and dashed line correspond to the theoretical curves for* 14, 12 *and* 10 *nm. In a the data are selected only by imposing a criterion on the ionization rate (yet no requirements on the TOF signal), while in b the gray points correspond to TOF signals where the* χ^2 *is larger than two.*

corresponding to $a = 10$, 12 and 14 nm. The large separation of the three curves for the relatively small change in a underlines the sensitivity in the determination of a using this method. We observe that a large fraction of the data points falls between 10 and 14 nm. Looking at the data we observe that points at high temperatures show a tendency to fall near the 10 nm curve, while points at low temperatures fall near the 14 nm curve. We suspect that

this is due to the fact that even though the ionization rate indicates that the cloud is at BEC threshold, this is not exactly the case.

We then apply the second criterion for BEC threshold, related to the χ^2 value for the TOF signals. The black points in Fig. 5.5 b correspond to fits having a χ^2 value below 2, while for the gray points, this value is above 2. The black points considered alone show indeed a decreased dispersion. The 4 outlying gray points around $T_c = 3\ \mu K$, all have a χ^2 larger than 3, indicating that they are very far away from threshold.

Even when we eliminate data having a χ^2 larger than 2, some dispersion in the points remains. If we try to decrease further the cut-off value of χ^2 below 2, we essentially decrease the number of points without decreasing the dispersion. The remaining scatter in the data is larger than what can be accounted for by our estimates of the uncertainties in the ionization rate or temperature measurements. We therefore assume that is must be related to the fact that we are not exactly at condensation threshold, even though neither the ionization rate nor the fitting procedure reveals so.

5.5 Determination of the scattering length

Since we believe that points with a χ^2 higher than 2 do not correspond to clouds at BEC threshold, we exclude these points when we determine the scattering length. We fit the ionization rate as a function of T_c for the remaining points, using Eq. 5.9 given by

$$\begin{aligned}\Phi_c = (\tfrac{\omega_c}{\widetilde{\omega}})^3 \times \quad & [\ \tfrac{1}{\tau_i}(1.20 + 2.48\tfrac{\widetilde{\omega}}{\omega_c} + 12.35\tfrac{a}{\lambda_c}) \\ & + \tfrac{\beta(a)}{\lambda_c^3}(0.33 + 1.81\tfrac{\widetilde{\omega}}{\omega_c} + 6.75\tfrac{a}{\lambda_c}) \\ & + \tfrac{L(a)}{\lambda_c^6}(0.22 + 2.21\tfrac{\widetilde{\omega}}{\omega_c} + 6.50\tfrac{a}{\lambda_c})\Big]\end{aligned}$$

with a the fit parameter. All the points are given equal weight in the fit. Figure 5.6 shows the obtained fit (solid line). We obtain

$$a = 11.3 \text{ nm}.$$

This result is compatible with all earlier measurements as well as theory according to the discussion in chapter 1.

5.5.1 Uncertainty

Of course an experimental result is useless unaccompanied with its uncertainty. We believe that the main uncertainty of the scattering length *does not* comes from the uncertainty of the measurement of ionization rate and temperature, which can be measured very well[11]. We believe that the dominant uncertainty comes from the fact that a part of the clouds are not

[11] The uncertainty for the ionization rate and temperature is 2 and 5 %, respectively, see section 5.3.

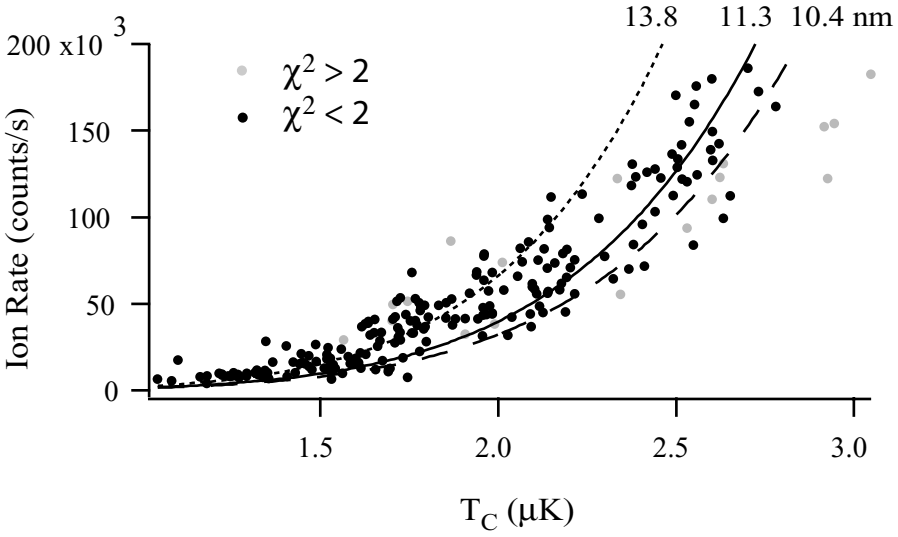

Figure 5.6: *The scattering length is obtained by fitting the black points (χ^2 less than 2), using Eq. 5.9. The fit gives* 11.3 *nm (solid line). The error-bars are estimated by fitting separately the data having a T_c below and above 2 μK (including the gray points). These fits are also shown (dotted and dashed line, respectively).*

exactly released at the BEC threshold, even though neither ionization rate nor TOF signal indicates that this is the case. It could be, for instance, that the break in the slope does not correspond exactly to BEC threshold, as we will discuss below. The resulting uncertainty on the scattering length is very difficult to estimate. As already mentioned, the trend in low temperature data to be above the fit and high temperature data to be below (see Fig. 5.6) arises probably from clouds not being exactly at BEC threshold. Therefore, we will estimate the resulting uncertainty on the scattering length by considering this trend in the data: we fit the data (including gray points) separately for T_c below and above 2 μK. We find $a = 13.8$ nm for the low temperature data and $a = 10.4$ nm for the high temperature data. The two fits are shown in Fig. 5.6, dotted and dashed line, respectively. Therefore, as we do not know if it is the low- or high temperature data or somewhere between which are "correct", the value of the scattering length could be somewhere between $a = 13.8$ nm and $a = 10.4$ nm. This is the main uncertainty.

Of course, other sources to uncertainty are present. In particular, the uncertainty on the rate constants contribute to the uncertainty on a, as well as the fact that the determination of the temperature actually depends

on a itself. We will in the following discuss these two sources, which turn out to be smaller than the error-bars estimated above. The uncertainty on the rate constants gives rise to an uncertainty on a of 0.5 nm, while the uncertainty due to the temperature determination turns out to be negligible (< 0.1 nm). Later, to obtain the total uncertainty on the scattering length, we will add quadratically the contribution arising from the rate constants to the uncertainty obtained from considering the high-low temperature trend in the data.

Uncertainties from the rate constants

First let us consider the contributions from the rate constants β and L. Fortunately, the uncertainties in β and L are highly correlated as discussed in chapter 4, and therefore their contribution to the uncertainty on a turns out to be small. To visualize this error, we show how the curve for $a = 11.3$ nm (which is obtained using the central value for the rate constants) is displaced according to the uncertainties on the rate constants. This is done in Fig. 5.7. The dashed line corresponds to using the upper limit of the value for the rate constant L and the lower limit for β, while the gray line is the opposite: lower limit for L and upper limit for β. To estimate quantitatively the influence on the scattering length, we first parameterize the extreme values of β and L in terms of a: for each a, we determine the upper and lower limit of the rate constant, in order to deduce them as a function of a. With these functions, we can then perform a fit to obtain a in the two extreme cases. In the first case (upper limit for β and lower limit for L) we obtain $a = 11.1$ nm, while in the opposite case, we obtain $a = 11.6$ nm. The uncertainty on a due to the uncertainty on β and L is thus 0.5 nm: this is much smaller than the errors-bars estimated above, but to be rigorous, we will add it quadratically to the error-bars estimated above, in order to obtain the total error-bars on the scattering length.

Uncertainty arising from the temperature determination

Our second source of uncertainty arises from the fact that the fit function depends on a itself. Therefore the temperature deduced from the fit will depend on the a used in the fit function, as discussed in Appendix C. In addition, the correction due to the hydrodynamic expansion depends on a. This is discussed in detail in Appendix D. We must therefore choose a value of a to obtain the temperature, before plotting our data. In the analysis above we have chosen $a = 12$ nm.

Nonetheless, the final value of a deduced from fitting the ionization rate depends only very weakly on the choice of a used in the analysis, in the case of a ranging between $a = 10$ nm and $a = 14$ nm, as we will show now. To do so, we will perform the analysis of the TOF signals again, now using, both for the initial fit function, and for the hydrodynamic corrections $a = 10$ nm. We then repeat the procedure, using $a = 14$ nm. We show the results

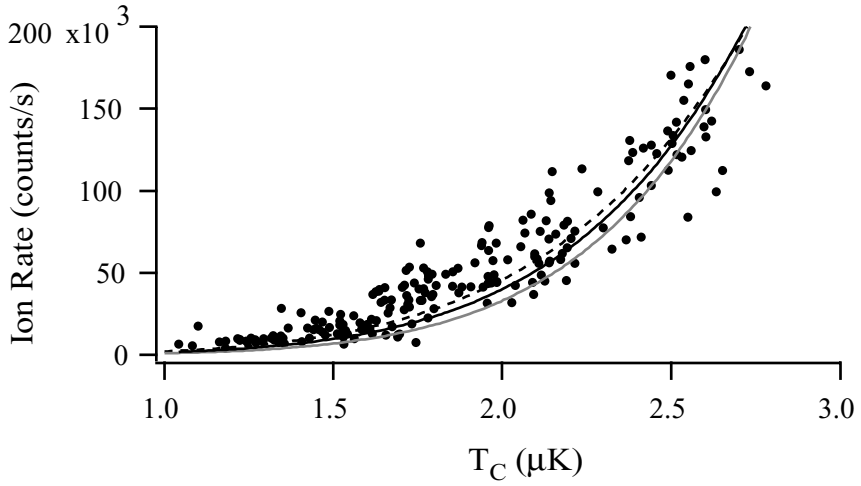

Figure 5.7: *Displacement of the curve corresponding to 11.3 nm (solid line), due to the uncertainty of the rate constants. The dashed curve corresponds to taking the upper limit for L and lower limit for β, both deduced for $a = 11.3$ nm. The gray curve is the contrary: L minimum and β maximum.*

in Fig. 5.8. Only points having a χ^2 less than 2 are shown. Gray points correspond to $a = 14$ nm, and black points to $a = 10$ nm. The physical reason why the gray points are shifted to the left, while black points are shifted to the right is the following: the higher a is, the lower the fitted temperature is, because for a high a, the expansion is expected to be due to interactions rather than thermal energy. Also the hydrodynamic correction is larger for a large a, because a higher elastic collision rate is expected in the first ms of the expansion – giving rise to a larger hydrodynamic effect. As the hydrodynamic corrections decrease the temperature, the points are displaced to the left. If we now fit the gray points, we obtain $a = 11.7$ nm, and for the black points we obtain $a = 11.1$ nm. The uncertainty due to this effect is smaller than these two limits however; by iteration, we conclude that a must be between 11 and 12 nm, and inside this interval, the corrections are nearly the same (the difference between using $a = 11$ and $a = 12$ nm changes the final value of a around 0.1 nm - and by further iteration this can be brought as small as desired). Therefore, this uncertainty is negligible compared to the errors-bars estimated above.

5.5.2 Final value for the scattering length

To obtain the final value for the uncertainty on a, we add in quadrature the non-negligible sources of uncertainty: the one estimated from the high-low temperature trend in the data and the error from the rate constants. We obtain

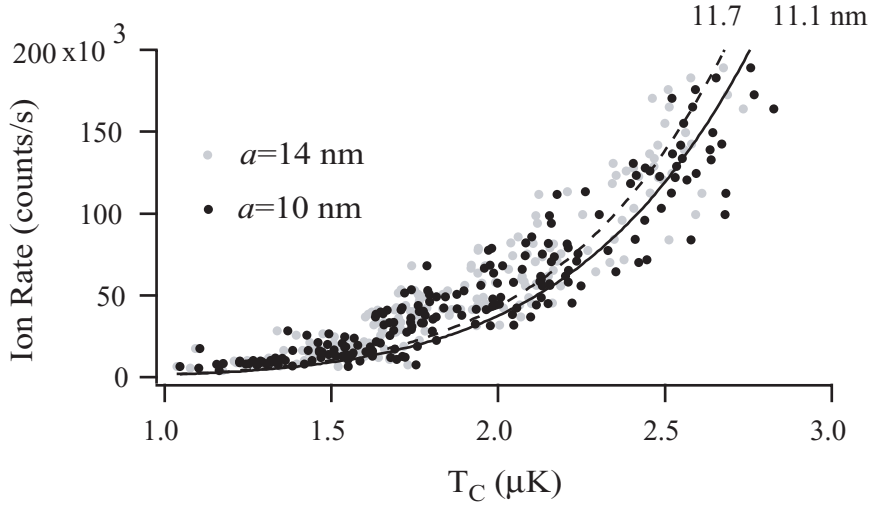

Figure 5.8: *Both the fit function and hydrodynamic corrections depend on the scattering length. In earlier analysis we have always taken* $a = 12$ *nm. In this figure we show the influence on the data points of this choice of scattering length: black points are obtained when* $a = 10$ *nm, and gray points correspond to* 14 *nm. To investigate the influence on the final deduced value of* a*, we fit the black and the gray points separately, and we obtain* $a = 11.1$ *and* $a = 11.7$ *nm (solid and dashed line, respectively).*

$$a = 11.3^{+2.5}_{-1.0} \text{ nm}$$

This is our final result for the scattering length. It is important to remember that this value, including the error-bars, rely on the assumption that the BEC threshold corresponds to the break in the slope in the ionization rate (see chapter 3). In the following, we will assume that the threshold is not exactly the break in the slope, and study the consequences on the scattering length.

5.6 If phase transition is shifted relative to the break in the slope

All our experimental tests confirm that the break in the slope indeed corresponds to the BEC threshold. Nevertheless, as discussed in chapter 3,

section 3.2.1, it has never been rigorously shown, using a model including interactions, that this is the case. Near BEC threshold, interactions start to play a role, and might result in a slight displacement of the threshold point relative to the break in the slope. In the following we will therefore assume that the threshold is not exactly at the break in the slope, and try to make some simple estimates on how this would influence our deduced value of the scattering length. To avoid confusion: in this section we will assume that all the clouds are released exactly at the break in the slope - what we will investigate is what happens if the break in the slope is *not* the threshold point.

5.6.1 If it were before the break in slope

Let us start by assuming that the BEC threshold is actually slightly before the break in the slope in the ionization rate. Before threshold, the ionization rate increases very slowly, and we will assume that it stays constant. The temperature, on the other hand, continues to drop, but we can estimate the cooling rate dT/dt. Our strategy is then to say that if the true threshold is shifted a time t_{shift} to the left of the break in the slope, then all the cloud are released too late, and the obtained temperatures are therefore too low: they are exactly $t_{\text{shift}} \times dT/dt$ too low. If the temperatures are too low, the deduced scattering length will also be too low. This is what we want to quantify in the following. First we need to estimate the cooling rate. To do so, we compare two different experimental runs, each with identical ion rates, but we have switched off the magnetic trap at different times (at t and $t + \Delta t$). In each case, we record the subsequent TOF signal and obtain the temperatures T_1 and T_2. This was done for three different ion rates, indicated by A, B and C in Fig. 5.9. The cooling rate is shown in the inset in the figure for each of the three pairs of ion rates. The cooling rate obtained is between 2 and 3 μK/s.

The data used to deduce the cooling rate correspond to relatively dilute clouds (the ionization rate is between 5×10^3 and 30×10^3 counts/s). In order to verify that the cooling rate is approximately the same also at higher densities, we can use the data obtained at T_c, presented earlier in this chapter. First, recall the parameter η describing the evaporative cooling:

$$\eta = h(\nu_{rf}(t) - \nu_0)/k_B T(t), \tag{5.10}$$

with $\nu_{rf}(t)$ the rf-frequency during the cooling, and ν_0 the bias field. This parameter was already used in chapter 4. We expect η to be constant during the evaporative cooling, at least up to the transition point[12]. The bias field, except small fluctuations, also remains constant. From the expression for η, the cooling rate can be found (assuming thermal equilibrium):

[12]This is the case for the rubidium experiments in our group, see for instance [60].

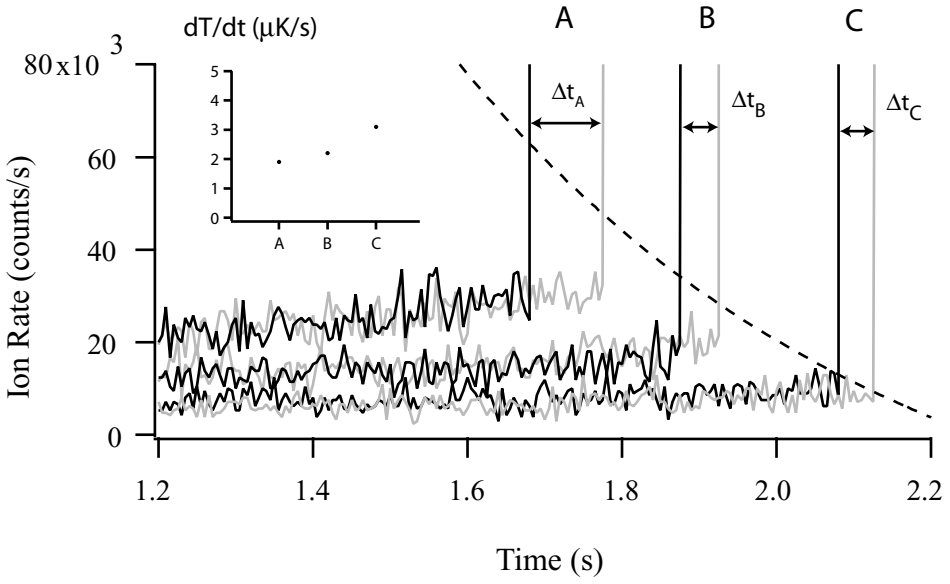

Figure 5.9: *Pairs of ionization rate curves (black and gray) having identical initial ion rates. These curves are used to estimate the cooling rate prior to threshold. In one case (gray curve) the trap was switched off a short time Δt after the other (black curve). For each of the two curves, the TOF signal obtained after the switch-off yields the corresponding temperatures T_1 and T_2, respectively, from which we obtain the cooling rate: $dT/dt = (T_2 - T_1/\Delta t)$. The inset shows this obtained cooling rate.*

$$\frac{\mathrm{d}T}{\mathrm{dt}} = \frac{h}{\eta k_B}\frac{\mathrm{d}\nu_{rf}}{\mathrm{dt}}. \tag{5.11}$$

The rate of change of frequency of the rf-ramp, $\frac{\mathrm{d}\nu_{rf}}{\mathrm{dt}}$, is an experimental adjustable parameter. In all our experiments, it is imposed to 400 kHz/s in the vicinity of T_c. We will in the following deduce η from our data, and therefrom we can obtain the cooling rate. We will use our data at T_c: for each cloud, we know the frequency of the rf-ramp ν_{rf} from the switch-off time of the ionization rate, and the temperature from the TOF signal. The bias field ν_0 is known to be approximately 950 kHz. Therefore, we can calculate a value for η for each cloud at T_c. The result is shown in Fig. 5.10, where we plot η as a function of temperature. First note the large dispersion in the data. In the plot, we have included all the data being at the threshold curve. Excluding data with $\chi^2 > 2$ does not decrease significantly the dispersion. Instead, we attribute the dispersion to bias field fluctuations, which influences directly η as seen from Eq. 5.10. We note that in particular for low temperatures, the dispersion is large, consistent with bias field fluctuations: the absolute values

of such fluctuations are independent of temperature, but a cold cloud is more sensitive to the bias field. Consequently, we use only the high temperature data (above 2 μK) to estimate η. We obtain an average value of ~ 9, which according to Eq. 5.11 gives a cooling rate of ~ 2 μK/s. This value agrees with the estimate obtained using data in Fig. 5.9. Finally note that the data are grouped together in separate, parallel decaying curves as illustrated in Fig. 5.10 a by a dashed line. This is nothing fundamental, but related to the way the experiment is done: for each chosen switch-off rf-frequency ν_{rf}, a series of data is recorded before changing the frequency to a new value. For ν_{rf} constant, η varies inversely with the temperature, as seen in Eq. 5.10. As the density varies from run to run, so does the critical temperature. This explains why the data in Fig. 5.10 resemble a set of $1/T$ curves.

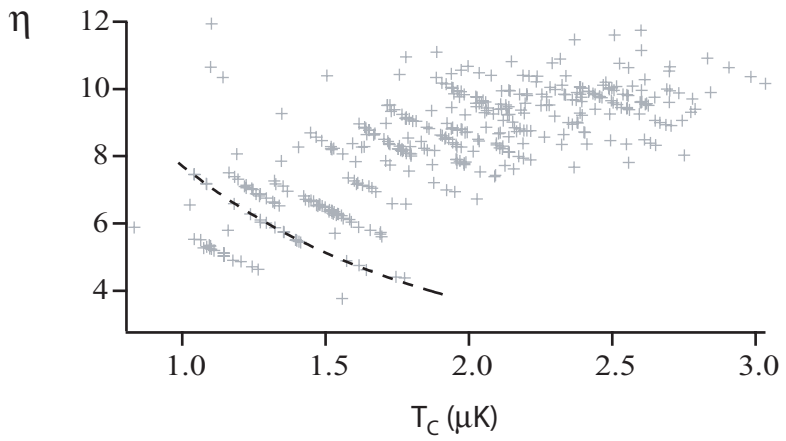

Figure 5.10: *The parameter η as a function of temperature. The data are the same as those used to deduce the scattering length (obtained at BEC threshold). The dispersion at low temperatures is due to fluctuations in the bias field. The dashed line is an eye guide line, see text for explanation.*

Using this cooling rate, we can calculate the expected temperature change for our data points in Fig. 5.6 assuming that the real transition point is not at our threshold curve, but at a time t_{shift} before. The measured temperature is changed by an amount $\delta T = t_{\text{shift}} \times 2\ \mu K$. This shifts all our data in Fig. 5.6 horizontally to the right, and thus the value of a obtained by fitting is decreased. Now for each value of t_{shift}, we calculate the scattering length that we would obtain, if the threshold were displaced by this amount. The result is shown in Fig. 5.11. The gray region indicates values of a which are allowed by the earlier announced lower limit ($a = 10.3$ nm). It is seen that a stays above this lower limit, as long as t_{shift} does not become greater than

$\sim$ 60 ms.

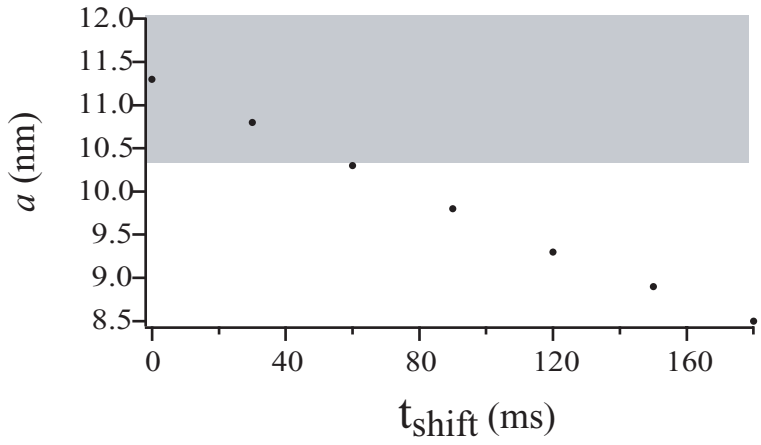

Figure 5.11: *We show the value which would be obtained for a if the real transition points were not situated at the threshold curve but a time* t_{shift} *before. The shaded gray area includes the values for a which are compatible with the lower error-bar.*

According to our experimental data, it must be considered unlikely, that the break in the slope is more than 60 ms away from the threshold point: in chapter 3 we compared a sequence of TOF signals with the ionization rate. In particular, we used the double structure in the TOF signal in order to locate the threshold point on the ionization rate – and it happened to correspond to the break in the slope in the ionization rate. What is important to note is that none of the TOF signals being released on threshold curve showed any indication of double structure. As we have investigated several TOF signals even closer than 60 ms to the break in the slope, and none of them contained a condensed part, we conclude that the uncertainty is below 60 ms, and therefore that a remains inside the earlier stated error-bars.

A question arises: is this an independent source of uncertainty, different from the others estimated above? If this is the case, even though this uncertainty contribution does not exceed the stated error-bar on a, it should be added to this one, enlarging the lower error-bar on a. We believe, however, that the high-low temperature trend in the data (see Fig. 5.6) actually is related to the fact that we do not identify perfectly well the threshold point. In this case, the error-bars estimated by fitting separately the high temperature and low temperature region take automatically this uncertainty into account, and it should therefore not be added to the given error-bars. In fact, we could initially have estimated our error-bars the other way around:

given the uncertainty in the break in slope, we get a minimum value for a (from Fig. 5.11), which we will take as our lower error-bar. The result, of course, is the same, as it should be, if our understanding of the sources to uncertainty is correct. We therefore keep our stated error-bars on the scattering length.

5.6.2 If it were after the break in slope

If the real transition point is located *after* the break in the slope, we must have interrupted the cooling too early. In this case, the temperatures obtained are overestimated, and the points in Fig. 5.6 are located more to the left, than they should be. This would lead to an overestimated value of a. Unfortunately, the simple temperature evolution assumed above is only a good approximation before threshold. After threshold, the temperature evolution becomes more complicated, and in addition, the ionization rate increases steeply, and this change cannot be neglected, as we did before. Instead, we estimate the consequences of a displaced threshold point experimentally. We have recorded a series of data (ion rates and TOF signals) for clouds cooled past the threshold curve. The ion rates are shown in Fig. 5.12 a. In b we show the ionization rate as a function of T_c for these points[13]. Also the fit (solid line) of the ionization rate as a function of T_c is shown, and we obtain $a = 14.7$ nm. This is quite far from our value $a = 11.3$ nm, but the fit of the TOF signals clearly indicate that threshold is passed: the fits using the Bose function, which is only valid at BEC threshold, is very bad. This indicates that we are indeed very far from threshold. Two of these TOF signals are shown in Fig. 5.12 c and d, and the clouds clearly show a narrow part indicating the presence of a condensed part. As expected the χ^2 values for the two fit are high (~ 4). This confirms that the threshold can not be as far away from the threshold curve as in the example in Fig. 5.12 a, and that the $a = 14.7$ nm is certainly excluded. If we note that the data points in Fig. 5.12 a, are recorded around 250 ms after the threshold curve, and that this gives $a = 14.7$ nm, we estimate that a varies $(14.7-11.3)/200 \sim 0.02$ nm per ms of displacement between break in the slope and the true threshold[14]. We have a temporal precision of the sequence of the TOF signals of at least 100 ms (see Fig. 3.1 in chapter 3). Therefore the uncertainty on the threshold is less 100 ms, and the corresponding uncertainty is maximum 2 nm. This is included in the upper error-bar on a (2.5 nm), estimated from the low temperature trend in the data.

[13] It should be noted that this temperature would only correspond to T_c if the clouds were at BEC threshold, and not after threshold, as we believe they are.

[14] Note that this is a very crude way of estimating it. However, if the threshold is actually after the break in the slope, the data that we analyze are before the threshold point, and assuming that the temperature, and therefore that a varies linearly with time, is not that wrong!

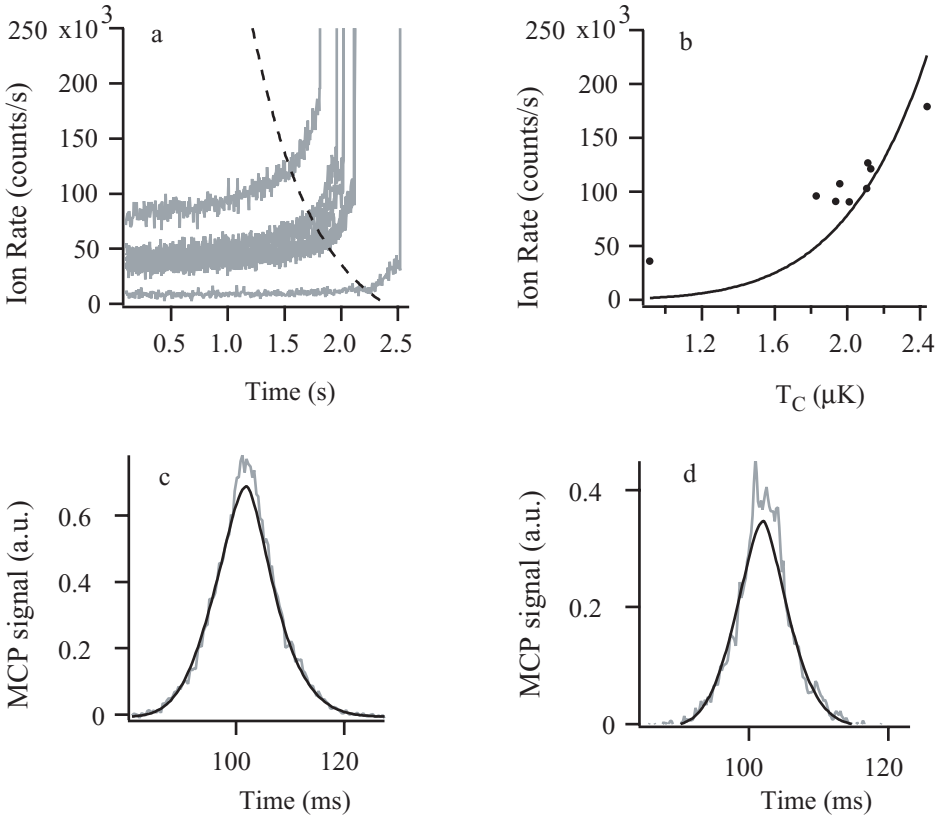

Figure 5.12: *a) A series of ion rates where the trap is switched off after threshold, according to the threshold curve. The final value of the ionization rate as a function of the temperature, obtained by fitting the TOF signal with the Bose function is shown in b). A fit of these data gives* $a = 14.7$ *nm (solid line). Finally, two typical TOF signal corresponding to these ion rates and their fit with a threshold Bose function are shown. In both cases, the TOF signal show a narrow peak, which is not present in the Bose fit.*

Before and after at the same time?

The reader might now ask him or herself why the data at low and high temperatures do not exhibit the same tendency, as seen in Fig. 5.6. The temperatures for low temperature data seem to be underestimated (the points lie left for fit curve). According to the discussion above, this could mean that the cloud is cooled past transition, and therefore that the true threshold point is located before the break in the slope. For the high temperature data it would be the opposite: the real threshold should be located after the break in the slope. How is this simultaneously possible? The reason might be related to the fact that for high temperature (high density and therefore

high ionization rate) the break in the slope in less abrupt (see for instance Fig. 5.12 a). One could imagine that for high temperatures, the threshold is not exactly the inflection point (where the threshold curve crosses the ionization rate in the figure) but somewhat later where the ionization rate starts to increase more steeply. For low temperature data on the contrary, the ionization rate changes more abruptly and the break in the slope is very neat. The reason why the threshold could be slightly before this break in the slope, is if some kind of delay between the threshold (the sharp increase in density) and the increase in the ionization rate. This cannot be explained by the time it takes for the ions to arrive to the micro-channel plate (less than a millisecond), but something else that we have not yet thought about.

5.7 The 23 of June 2003

The data presented in section 5.4 correspond to five days of data acquisition. Strangely, the trend for low temperature points to be below the fit curve and for high temperature points to be above is much more pronounced for one of the five days, namely the data acquired the 23 of June. The points corresponding to this day is indicated with black in Fig. 5.13 a, while the four other days are indicated with gray. It turns out that many of the fits (but not all) from the 23 of June, give a high χ^2, between 2 and 3. Therefore, if the data from this day is separated from the other data, we see a clear reduction in the dispersion of the remaining points. As before, we reject data having a χ^2 higher than 2, and as before the dispersion of the remaining points decreases. But now, in contrast to earlier, decreasing successively the cut-off value of χ^2 even further (to 1.5, 1.2 and 1, respectively), reduces successively the dispersion, until only a few points remain. This is shown in Fig. 5.13 b. To be sure that we really decrease the dispersion and not only the number of remaining points, we quantify the decreased dispersion as follows: we define a $\chi^2_{\text{ion rate}}$ corresponding to the fit of the ionization rate as a function of T_c. The subscript is given to avoid confusion with the χ^2 for the fits of the TOF signals. We normalize it with the value corresponding to the fit of the data set including TOF signals having a χ^2 below two. We obtain

Cut-off χ^2 for TOF	2	1.5	1.2	1.0
Obtained $\chi^2_{\text{ion rate}}$	1	0.8	0.3	0.1

The values for $\chi^2_{\text{ion rate}}$ decrease indeed when the cut-off value of χ^2 is reduced, indicating that the quality of fit increases due to a decreased dispersion of the points. This is in contrast to the case where we keep the data from the 23 of June: here we saw a reduction in the dispersion of the points when we chose the χ^2 to be less than 2, but a further decreasing

of this value only decreased the number of data points, not the dispersion ($\chi^2_{\text{ion rate}}$ stayed approximately constant). Consequently, we conclude that the 23 of June data represent some clouds which are not at BEC threshold, even though nor ion rate nor the corresponding χ^2 indicate this.

A dilemma is born: is it correct to reject data from the analysis (here the 23 of June), because they behave strangely compared to the remaining data? This is a profound question, but fortunately, we do not need to answer it here: the value of the scattering length varies very little according to what we do. Including the 23 of June in the analysis gives $a = 11.3$ nm, while we now obtain a varying between 11.5 and 11.3 nm, for a cut-off value of χ^2 ranging between 1 and 1.5.

5.8 New inelastic collision constants

In chapter 4 we gave the collision constants β and L in terms of the scattering length, because at that stage, we only had a very unprecise value for this constant. Now that we have deduced a much more accurate value of a, we can refit the data for pure BEC presented in chapter 4, using $a = 11.3$ nm. We obtain[15]

$$\beta = 0.9^{+2.0}_{-0.8} \times 10^{-14} \text{ cm}^3/\text{s}$$

$$L = 2.5^{+5.3}_{-1.7} \times 10^{-27} \text{ cm}^6/\text{s}$$

5.8.1 Modified error-bars

The quoted error-bars are significantly increased compared to those given in chapter 4. The reason is that we have included two contributions, which were not present in the earlier error-bars. The first additional contribution come from the uncertainty on a. Earlier, as the rate constants were given in terms of a, no uncertainty due to this parameter was to be taken into account. The uncertainty entering *via* a is now obtained by taking the minimum and maximum values for β and L corresponding to the upper and lower limits for a i.e. $a = 13.8$ and $a = 10.3$ nm, respectively. The obtained values are shown in table 5.1. The error-bars on β and L corresponding to this contribution are highly correlated: if we take for instance the upper bound for β corresponding to the maximum value of a, the minimum value of L must of course be taken for the same value of a, and not the overall minimum value. So taking into account these correlations, this part of the uncertainty would in practice be smaller than the error-bars stated.

The second supplementary contribution to the uncertainty comes from an eventual systematic error on the ion detection efficiency. We did not take it

[15] We have assumed the same detection efficiency as before, that is, 0.42.

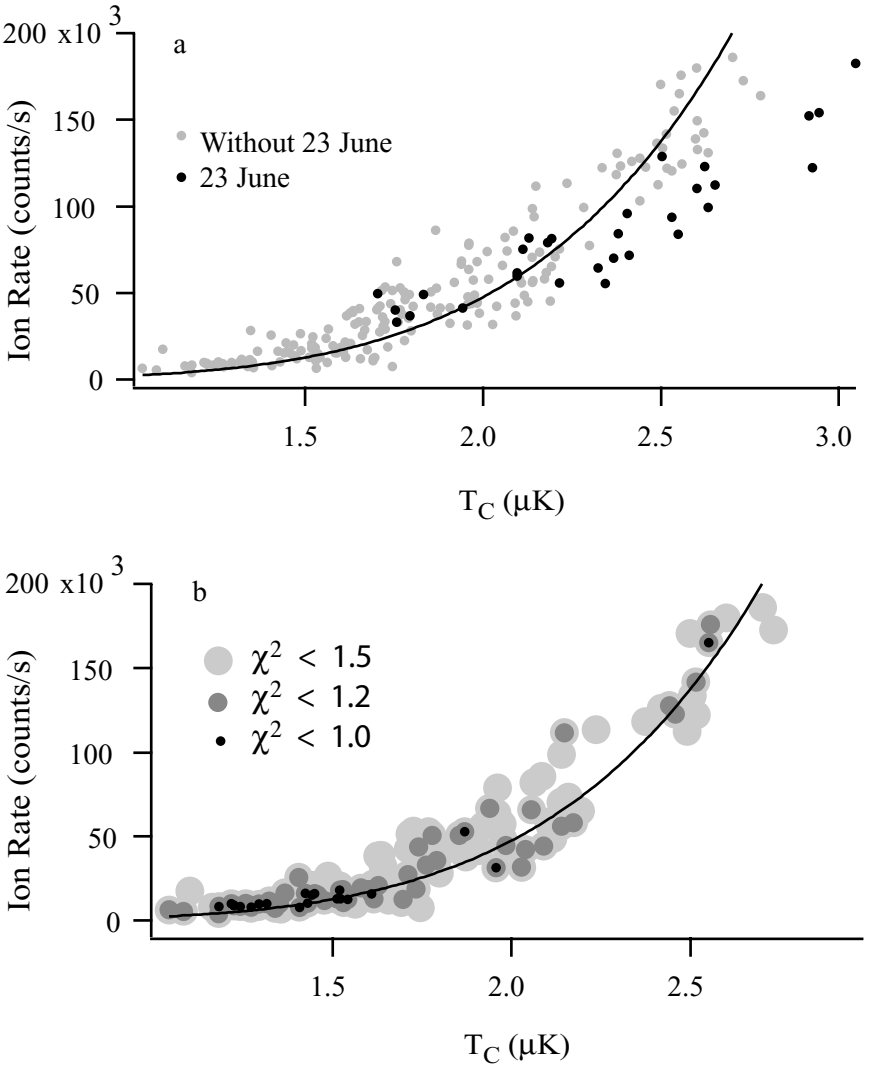

Figure 5.13: *The series of data from the 23 of June turns out to behave differently compared to the other data. In a, the black points correspond to data acquired the 23 June, and shows a systematic trend compared to the rest of the points. Excluding these data, the remaining data (gray points) show a decreased dispersion. When these points are fitted (black curve), we get* $a = 11.5$ *nm (solid line). In b we have completely omitted data from the 23 of June. Now by imposing a criterion on the* χ^2 *value for these points, we can decrease further the dispersion. The large gray circles correspond to* χ^2*<1.5, smaller gray circles to* $\chi^2_\nu < 1.2$ *and black points to* $\chi^2_\nu < 1$*. The black curve is present to guide the eye, and corresponds again to* $a = 11.5$ *nm.*

$a[nm]$	$\beta/10^{-14}$	$\beta_{max}/10^{-14}$	$\beta_{min}/10^{-14}$	$L/10^{-27}$	$L_{max}/10^{-27}$	$L_{min}/10^{-27}$
11.3	0.9	1.7	0.2	2.5	4.0	1.0
10.3	0.8	1.4	0.1	1.9	3.1	0.79
13.3	1.3	2.4	0.3	3.9	6.2	1.5

Table 5.1: *The rate constant β is given in* cm^3/s *while L is given in* cm^6/s. *Note that the uncertainty due to the ion detection efficiency is not included in the maximum and minimum value.*

into account to obtain the error-bars in chapter 4, because we did not have a good estimate of this uncertainty. But now that we have the absolute value for the rate constant, we can obtain a rigorous lower limit on the detection efficiency. To do this, we use a series of independent measurements of the atom number as a function of time for a decaying pure BEC. The experimental data are shown in Fig. 5.14. Now using the values for the rate constants, we can calculate the theoretical decay curve, corresponding to the losses from the ionizing collisions described by the rate constants. It is important to note that this theoretical curve does *only* include ionizing loss processes. Note also that as the rate constants depend on the assumed ion quantum detection efficiency, ϵ_{ion}, so does the theoretical curve. The central value of the rate constants above have been given assuming $\epsilon_{\mathrm{ion}} = 1$ (corresponding to a total ion detection efficiency α of 0.42) and the decay curve using these rate constants is indicated in Fig. 5.14, solid line. We have also plotted the theoretical curves corresponding to lower efficiencies: $\epsilon_{\mathrm{ion}} = 0.6$, 0.5 and 0.4 (long-dashed, dotted and gray curve, respectively). Now the crucial point is that the data points are only allowed to be *lower* than the theoretical curve. This just requires that other losses than those due to ionizing collisions are present. Therefore the theoretical curve can never be below the experimental data: this would mean that we lose less atoms than what is expected from the rate of ionizing collisions alone. Therefore the absolute lower limit compatible with the data is $\epsilon_{\mathrm{ion}} = 0.4$. According to literature [103, 106], the most probable value for ϵ_{ion} is 1, and we must therefore suppose that other losses are present, in order to explain why the experimental data are below the theoretical curve in Fig. 5.14. This is a reasonable assumption, because in order to keep the BEC pure, we apply during the decay an rf-field, to continuously eject hot atoms. Also non-ionizing inelastic collisions like spin-relaxation could be present and induce losses. Believing in the presence of other losses, we have used $\epsilon_{\mathrm{ion}} = 1$ to obtain the rate constants given above. We have nevertheless included in the error-bars the fact that ϵ_{ion} can be as low as 0.4, which must be considered a very conservative estimate. Note that this adds an asymmetric contribution to the error-bars on the rate constants.

Remember that this contribution to the error-bars of the rate constants does not contribute to the uncertainty of the scattering length. This is

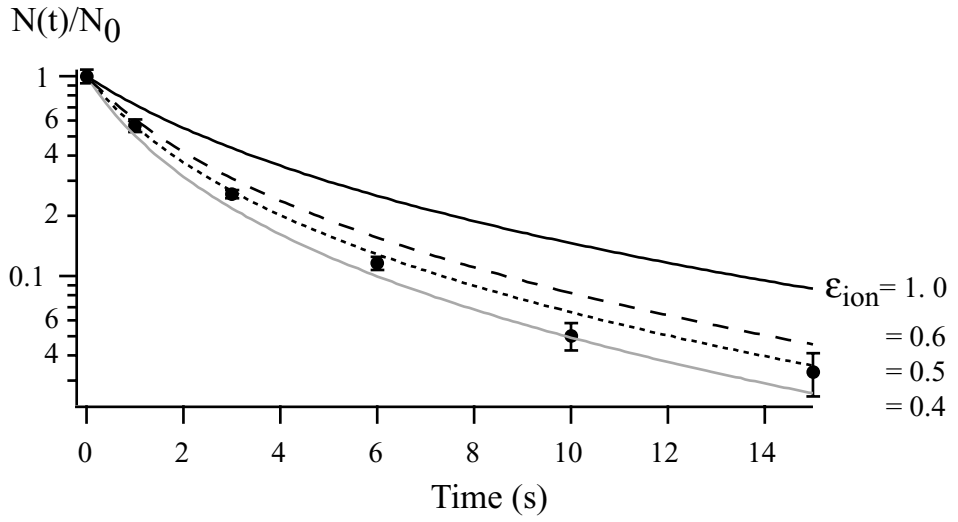

Figure 5.14: *Normalized atom number as a function of time for a decaying pure BEC. The atom number is obtained from the chemical potential, using* $a = 11.3$ *nm. Black points corresponds to experimental data. An rf-shield is present to prevent heating. The curves show the decay (theory) corresponding to ionizing losses alone (losses due to the rf-shield or other inelastic processes are not included). The rate constants used in all curves are for* $a = 11.3$ *nm, but the assumed ion detection efficiency (*$\epsilon_{\rm ion}$*) varies: we give it for* $\epsilon_{\rm ion} = 1$ *(corresponding to a total efficiency of 0.42), and for* $\epsilon_{\rm ion} = 0.6$, 0.5 *and 0.4. As none of the theoretical curves can be below the data points (see text), the rigorously lower limit for* $\epsilon_{\rm ion}$ *is 0.4. Finally note that the values for* $\epsilon_{\rm ion}$ *are given assuming that the intrinsic limitation in detection efficiency is* 0.42 *– this is, the total ion detection efficiency assumed for the theoretical curves is the product* $0.42 \times \epsilon_{\rm ion}$*. If the value* 0.42 *turns out to be wrong (see chapter 2), the values of* $\epsilon_{\rm ion}$ *indicated on the curves must be modified accordingly.*

because an eventual systematic error in the assumed ion detection efficiency also would be present for our measurement of the ionization rate leading to a, and cancels out, as explained earlier in this chapter.

Finally, using the graph 4.6 in chapter 4, we can compare the experimental values with the theoretical estimates for the rate constants for $a = 11.3$ nm. We find that our value of β is about 30% smaller than the theoretical one (but still within the experimental error-bars), while our value of L is 15% smaller than predicted by the theory.

5.8.2 Suppression of Penning collisions

In sounds amazing that it is possible to reach densities allowing BEC with a cloud of metastable atoms: one should think that ionizing collisions destroy the sample much faster than the duration of the evaporative cooling, which is generally more than half a minute! Fortunately, as discussed in chapter 1, due to the spin polarization in the magnetic trap, these inelastic collisions are forbidden. The prediction of this suppression encouraged the attempt to Bose-Einstein condense metastable helium, even though nobody knew in advance if it would be possible.

Now that we have obtained the value for the 2-body ionizing rate constant β, it is hard to resist the temptation of giving our experimental result for the suppression factor $\mathcal{F}_{\rm supp}$. We will use the value for the rate constant $\beta_{\rm non-pol}$ obtained in the group of W. Vassen [86]. They measured $\beta_{\rm non-pol} = 1.3(2) \times 10^{-10}$ cm^{-3}/s (in the absence of light). Therefore we obtain

$$\mathcal{F}_{\rm supp} = \frac{\beta}{\beta_{\rm non-pol}} = \frac{0.9 \times 10^{-14}}{1.3 \times 10^{-10}} \sim 7 \times 10^{-5}. \tag{5.12}$$

Including the dominating error-bars on β, we obtain a suppression factor in the range between $[6 - 15] \times 10^{-5}$. This value agrees with the estimates of Refs. [79, 80], which announce a suppression of five orders of magnitude.

5.9 Atomic interactions – an outlook

We have exploited the data at the critical point in order to extract the scattering length for metastable helium, because this constant was not very well known before these experiments. It is nonetheless interesting to note that if we have had the scattering length in advance, we could still have extracted important information from our data: the shift of the critical temperature due to the interactions [48, 49, 50, 51, 52, 53, 54, 55, 56, 57]. This is an exciting question, which has only been investigated experimentally a few times [58, 59]. Recall the critical ionization rate, which was given in Eq. 5.9

$$\begin{aligned}\Phi_{\rm c} = (\tfrac{\omega_{\rm c}}{\widetilde{\omega}})^3 \times \quad & [\ \tfrac{1}{\tau_i}(1.20 + 2.48\tfrac{\widetilde{\omega}}{\omega_{\rm c}} + 12.35\tfrac{a}{\lambda_{\rm c}}) \\ & + \tfrac{\beta(a)}{\lambda_{\rm c}^3}(0.33 + 1.81\tfrac{\widetilde{\omega}}{\omega_{\rm c}} + 6.75\tfrac{a}{\lambda_{\rm c}}) \\ & + \tfrac{L(a)}{\lambda_{\rm c}^6}(0.22 + 2.21\tfrac{\widetilde{\omega}}{\omega_{\rm c}} + 6.50\tfrac{a}{\lambda_{\rm c}})\Big]\end{aligned}$$

The terms proportional to a/λ_c account for the atomic interactions, and these terms shift significantly the ionization rate as shown in Fig. 5.15, where we show the ionization rate including interaction (solid line) and the ideal gas case (dashed line). In our analysis, we accounted for interactions using the perturbation theory discussed in Appendix B. Consequently, the deduced value of a relies on the validity of this theory. Now if an independent

measurement of a becomes available, the same kind of data can be used to probe the atomic interactions: if we imagine a is now known in the expression for the ionization rate, we could leave the constants multiplying the terms proportional to a/λ_c as free parameters in our fit. The obtained constants would give information of the importance of the interactions in the sample. Of course, if an independent measurement of a gives exactly 11.3 nm, then we would re-obtain the values corresponding to the coefficients used in the above expression. Of course, in addition to a precise, independent measurement of a, we would need to understand and eliminate the source to the dispersion of the points in Fig. 5.15, in order to use the ionization rate as a probe for atomic interactions.

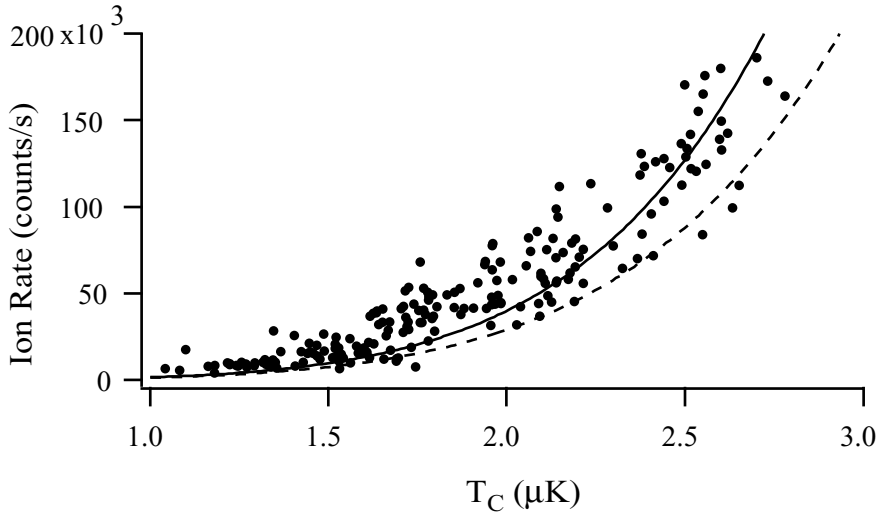

Figure 5.15: *The same data as presented in Fig. 5.5 and 5.6. The dashed line corresponds to the ideal gas, while the solid line takes into account interactions. Both lines correspond to 11.3 nm.*

Chapter summary

We have in this chapter deduced a new value for the scattering length, and we have given our best estimate for the error-bars on this measure. The result has permitted us to deduce the absolute value of the rate constants, which we in chapter 4 only could give in terms of the scattering length.

The measurement of the scattering length is 11.3 nm. This is almost a factor of two different from the first measure obtained in our group, though inside the error-bars: $a = 20 \pm 10$. There, the detection efficiency was

supposed to be the same for a thermal cloud and a BEC, even though we now know, that it typically differs a factor of two. This explains why the obtained value for the scattering length was too high.

As discussed in the introduction, photoassociation experiments are under progress in the ENS group. A spectroscopic measurement of the scattering length would provide the ultimate control of our result, and we hope that they will soon succeed in obtaining their result.

The End

Of course the ionizing rate constants and the s-wave scattering length for metastable helium are not among the quantities considered as fundamental constants of nature – and they do not have an intrinsic interest as does the gravitational acceleration or the fine structure constant. However, it is certain that in order to make quantum degenerate metastable helium a good candidate for studying fundamental processes, these constants are essential in the interpretation of the experimental results. And I hope that this thesis has convinced the reader that metastable helium *is* a unique and very advantageous system for investigating various physical phenomena. Therefore the amount of time spent on the measurements of these important constants should be justified. Also from a purely theoretical point of view, the measurement of these constants might be justified: both the rate constants, the scattering length and the suppression factor for Penning collision have been calculated, and by comparison with the experimental values, the validity of the theoretical models can be tested.

Several exciting experiments using metastable helium are in preparation, and I hope they will profit from the work here presented – in the preparation as well as in the understanding of the data. For instance, in Amsterdam, a new experiment using both fermionic ^{3}He* and bosonic ^{4}He* is being prepared [119]. As the s-wave collisions between identical fermions are suppressed, sympathetic cooling using ^{4}He* can be used to cool down the ^{3}He* atoms. Therefore, the magnitude of the ^{3}He$^* \leftrightarrow ^4$ He* scattering length (^{3-4}a) becomes crucial for the efficiency of the cooling process. It is therefore interesting to note that this scattering length can be deduced from the ^{4}He* scattering length (^{4-4}a) by a mass scaling approach [71]. In particular, the behavior of ^{3-4}a as a function of ^{4-4}a shows the position of a resonance centered around $a_{44} = 9.4$ nm: if ^{4-4}a is below this value, ^{3-4}a is large and positive, if ^{4-4}a is above this value, ^{3-4}a is large and negative. According to our measurement of ^{4-4}a, ^{3-4}a should therefore be large and negative! Quoting Ref. [119]: *"For a conservative estimate,* $9 < {}^{4-4}a$ (nm) < 13*, we find that* $^{3-4}a < -25$ *nm or* $^{3-4}a > 133$ *nm".* This means that for all realistic values of ^{4-4}a, the modulus of ^{3-4}a is large making the corresponding cross section for elastic collisions large. Sympathetic cooling should therefore be effective!

What is a bit more subtle is to predict with certainty the sign of ^{3-4}a given our error-bars on ^{4-4}a. Why is the sign important? If the quantum degenerate regime is reached simultaneously for ^{3}He* and ^{4}He* (i.e. a Fermi

sea for ^{3}He* and a Bose-Einstein condensate for ^{4}He*) the sign will tell us whether the two components will separate because of mutual repulsion (^{3-4}a positive) [120, 121] or stabilize each other in the mixture *via* attractive interactions (^{3-4}a negative). Our lower error-bar on ^{4-4}a corresponds to 10.3 nm. For this value, ^{3-4}a remains negative – as it will, as long as ^{4-4}a remains above 9.4 nm. Does that mean that we can rigourously exclude that ^{3-4}a is positive – and thereby assure the stability of the ^{3}He*-^{4}He* mixture? Well, this will all depend on the definition of our error-bar. Personally, I think we cannot, and I think my colleagues agree with me. We had to make some estimates to obtain the uncertainty, and it is therefore hard to tell if our error-bars correspond to one- or two sigma values. Anyway, as always in experimental physics, the chance that the true value is outside the given error-bars exists – and of course I would be happy to see an independent measurement from the group at Ecole Normale Supérieure which confirms our result.

As pointed out in the introduction, the engineering of the scattering length *via* Feshbach resonances is a field occupying a central position in atomic and condensed matter physics. In particular, the creation of bosons (molecules, loosely bound molecules or even Cooper-pairs) from two fermionic atoms is in focus at the moment. These studies can be situated in a larger context: liquid ^{4}He was the first manifestation of Bose-Einstein condensation, and later a superfluid state of ^{3}He was observed. Interpretation: two ^{3}He fermions form a Cooper pair, a boson, which can then condense. In 2001, the first Bose-Einstein condensate of ^{4}He* in the gas phase was observed. Would it not be fabulous, if a gaseous Bose-Einstein condensate of ^{3}He* *via* the creation of Cooper pairs using a Feshbach resonance could be made? Of course, ground state helium is fundamentally different from the metastable helium atom, so the above analogy should not be taken too literally. Also, the increase of Penning collisions in a sample which is not perfectly polarized might render the Feshbach resonances difficult to exploit. I find the idea is sweet, however!

From mercury lamps to metastable helium

New experiments are underway in our laboratory. Again experiments exploiting the metastability of the atoms. However, this time it is not the monitoring tool being the ionization rate which we used extensively throughout this thesis, but the fact that also the neutral atoms can be efficiently detected one by one using the micro-channel plate. What we want to do is an atom version of the famous photon correlation experiment performed by R. Hanbury-Brown and R. Q. Twiss, published in Nature in 1956 [122]. They measured the temporal second order correlation function for thermal photons generated by a mercury lamp, and they observed a bunching of the photons, i.e. a bump in the correlation function for short times. This effect is a consequence of the Bose-Einstein distribution, which is valid for a thermal

distribution. Laser photons on the other hand are described by a Poisson distribution, which means that the photons are statistically independent: the correlation function is flat for all times [123].

With metastable helium, we can detect the atom one by one in the same way as photons can be detected with a photomultiplier in photon counting mode. Moreover, with the same setup, we can obtain both the atom analogy to thermal light and a laser light: a thermal cloud and a Bose-Einstein condensate, respectively. And the photomultiplier is the micro-channel plate. We want to measure the two-body atom correlation function both for thermal and Bose-condensed atoms. A pioneering experiment was performed in 1996 by M. Yasuda and F. Shimizu [124]. In a heroic experiment, they managed to measure the two-body correlation function for thermal metastable neon, but as they did not have a Bose-Einstein condensate, they could not investigate this regime. With our setup, we hope to be able to obtain not only the correlation function for a thermal cloud and a Bose-Einstein condensate, but also to investigate the extremely interesting cross-over between these regimes.

In the quest for a good signal-to-noise ratio for these measurements, we have installed a new micro-channel plate detector. The new one, in contrast to the one used in the experiments discussed in this thesis, has a spatial resolution. It might appear strange that we need a good spatial resolution – after all, what we want to measure is the temporal correlations. However, the coherence area corresponding to the coherence volume of the cloud is smaller than the extent of the detector. This means that if we try to correlate all atoms falling on the micro-channel plate, most of them will necessarily be uncorrelated, and will tend to wash out the contrast of the bump in the correlation signal. With a spatially resolved micro-channel plate, we can deduce the correlation function pixel by pixel, and thereby be sure only to correlate atoms being inside the coherence volume. Afterwards, we can average over all pixels, and obtain a good signal-to-noise ratio. Finally, a position-sensitive detector could also allow one to observe the spatial 2-body correlation function. A beautiful experiment investigating spatial correlations was performed in the group of Eric Cornell and Carl Wieman [125]. Studying 3-body loss rates in rubidium, they could obtain the 3-body spatial correlation function. By using a spatially resolved micro-channel plate, one could measure it in a more direct way, and in addition, obtain the 2-body correlation function.

Of course, in reality, it is hard to obtain a micro-channel plate which has the desired temporal as well as spatial resolution, which can be put in vacuum, which can be baked out, which is compatible with low dead-time electronics and so on. It will necessarily be a compromise. The micro-channel plate we have chosen is hopefully the best one available for our purposes, and even though we cannot expect a perfect signal-to-noise ratio, calculations show that good results should be expected (these calculations are the subject of the thesis of my colleague J. Gomes.)

The new micro-channel plate has been installed recently, and is currently being tested by the next generation of Ph.D. students: R. Hoppeler, M. Schellekens and A. Perrin, assisted by the permanent members of the helium group. I hope they will soon succeed with this difficult experiment, and I wish them all the best luck.

A P P E N D I X A

The helium atom

All experiments performed in this thesis use ^{4}He in the metastable 2^3S_1 state. The atom is a spin-one boson without nuclear spin, and consequently without hyperfine splitting. The lifetime of the metastable state is ~ 9000 seconds.

The energy diagram for ^{4}He is shown in Fig. A.1. The optical transition used for the transverse molasses, the Zeeman slowing of the atomic beam, and for the magneto-optical trap (see chapter 2), is based on the transition between the 2^3S_1 level and the 2^3P_2 level. For optical pumping, we use

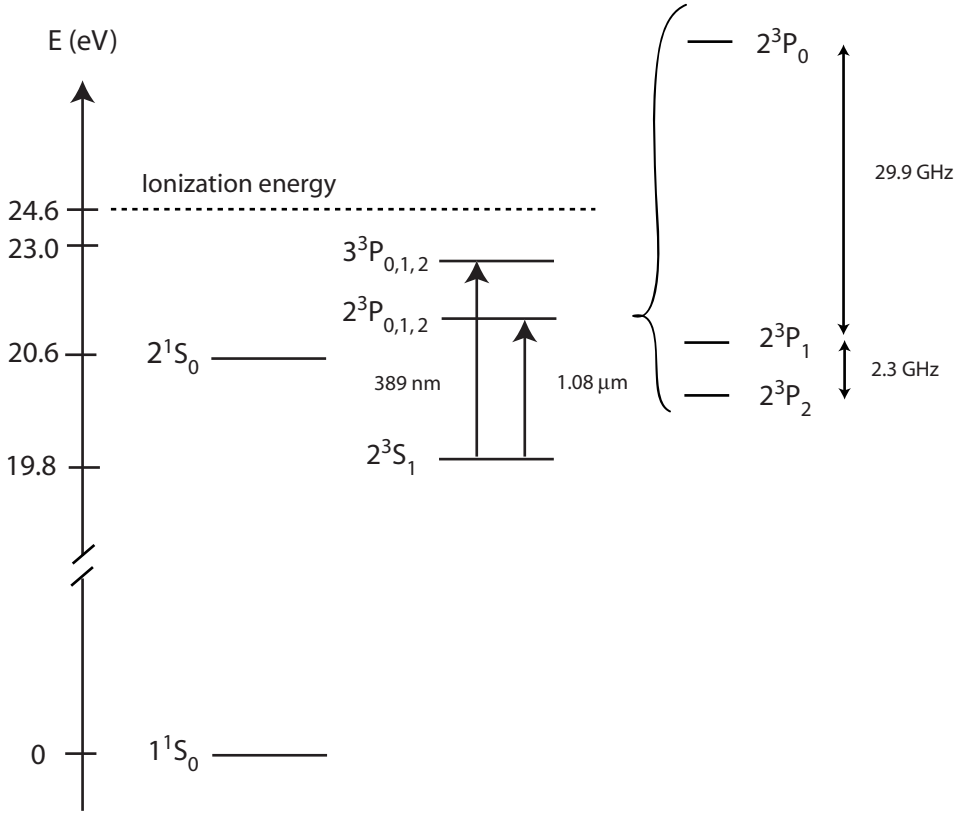

Figure A.1: *Energy diagram for ^{4}He.*

Parameter	Notation	Value	Unit
Mass	m	6.7×10^{-27}	kg
Wavelength of 2^3S_1 - 2^3P_2	λ	1.083	μm
Width 2^3S_1 - 2^3P_2	Γ	$1.6 \times 10^6 \times 2\pi$	rad/s
Saturation intensity	I_{sat}	0,16	mW/cm^2
Doppler temperture (1D)	T_{Dop}	38	μK
Recoil temperature	T_{rec}	4	μK
Ionization energy of the 1^1S_0 state	E_{ion}	24.6	eV
Excitation energy from 1^1S_0 to 2^3S_1	E_{exc}	19.8	eV

Table A.1: *Parameters concerning helium and the atomic transition used to manipulate helium in the metastable 2^3S_1 state.*

the transition between the 2^3S_1 level and the 2^3P_1 level. Both transitions correspond to 1.08 μm (infrared), and are quasi-closed: only a negligible fraction of the atoms decays from the excited levels to the 1^1S_0 level [35].

Another optical transition (from the 2^3S_1 level to the 3^3P_J level, with a transition energy of 389 nm, see Fig. A.1) is also available and has been implemented experimentally [126], but is not used in our experiments.

The characteristics of the ^{4}He atom and the different parameters describing the $2^3S_1 \rightarrow 2^3P_2$ transition used for optical manipulation is given in table A.1.

APPENDIX B

The ion rate at phase transition

In chapter 1 we showed explicitly how the ionization rate could be written in terms of the sample density. However, as discussed in chapter 2, we cannot measure directly the density of our cloud, because not all the atoms arrive on the micro-channel plate. Fortunately, there is a way to obtain the density for a cloud exactly at BEC threshold point: this is the main idea of chapter 5. For a cloud at this point, the density is related to the critical temperature T_c of the sample and the well-known oscillation frequencies. Therefore, at the threshold point, we can write an expression for the ionization rate, not as a function of density, but as a function of T_c. In chapter 5 we will use this expression to fit the data corresponding to the simultaneous measurements of ionization rate and critical temperature, in order to obtain the scattering length. In that chapter, we have already deduced the simple ideal gas expression for ionization rate as a function of T_c. Nonetheless, to achieve the desired precision on our final result, i.e. the scattering length, corrections arising from atomic interactions and finite size effects must be taken into account. This is the goal of the Appendix. In chapter 5, we will use this expression to fit the data corresponding to the simultaneous measurements of ionization rate and critical temperature in order to obtain the scattering length.

We will start by deducing the ionization rate limiting ourselves to first order effects. As we will see, the corrections turn out to be non-negligible. As these first order corrections are large, we also investigate second orders effects, but they turn out to be negligible for our purposes.

B.1 Interactions and zero point energy: 1st order calculations

In the mean field approach, above BEC threshold, the density is given by [17]:

$$n(T,\mu,\mathbf{r}) = \frac{1}{\lambda^3(T)} g_{3/2}\left[\exp\left(-\frac{1}{k_B T}\left(V(\mathbf{r}) + 2U\, n(T,\mu,\mathbf{r}) - \mu\right)\right)\right] \quad \text{(B.1)}$$

with T the temperature of the cloud, k_B the Boltzmann constant, $\lambda(T) = h/\sqrt{2\pi m k_B T}$ the thermal de Broglie wavelength, $V(r) = (m\omega_\perp^2 {r_\perp}^2 + m\omega_\parallel^2 {r_\parallel}^2)/2$

the trapping potential, $U = 4\pi\hbar^2 a/m$ the interaction constant[1], μ the chemical potential and $g_\alpha(x) = \sum_{\rho=1}^{\infty} \frac{x^\rho}{\rho^\alpha}$. By definition of the BEC threshold we have

$$\lambda_c^3 n(T_c, \mu_c, \mathbf{0}) \equiv \lambda_c^3 n_{c,0} = g_{3/2}(1), \tag{B.2}$$

where we have used the notation $\lambda_c = \lambda(T_c)$. This expression relates the density to temperature for a gas at BEC threshold. By replacing the density in this expression with Eq. B.1 and imposing $\mathbf{r} = 0$ and $T = T_c$, we obtain an expression for the chemical potential at T_c:

$$\mu_c = 2U n_{c,0} + V(\mathbf{0}) = 2U n_{c,0} + \frac{3}{2}\hbar\widetilde{\omega}. \tag{B.3}$$

We have here used the notation $\widetilde{\omega} = (2\omega_\perp + \omega_\parallel)/3$, which is the arithmetic mean of the oscillation frequencies. Reinserting this chemical potential in Eq. B.1, we get an expression for the critical density $n(T_c, \mu_c, \mathbf{r}) \equiv n_c(\mathbf{r})$:

$$\begin{aligned} \lambda_c^3 n_c(\mathbf{r}) &= g_{3/2}\left[\exp\left(-\frac{1}{k_B T_c}\left(V(\mathbf{r}) + 2U(\,n_c(\mathbf{r}) - n_{c,0}) - \frac{3}{2}\hbar\widetilde{\omega}\right)\right)\right] \\ &\equiv g_{3/2}\left[Ae^{-\epsilon}\right]. \end{aligned} \tag{B.4}$$

We have defined $A = e^{-V(\mathbf{r})/k_B T_c}$, and the small parameter $\epsilon = (2U(n_c(\mathbf{r}) - n_{c,0}) - \frac{3}{2}\hbar\widetilde{\omega})/(k_B T_c)$. We then use that

$$g_{3/2}[Ae^{-\epsilon}] = \sum_{\rho=1}^{\infty} \frac{A^\rho e^{-\rho\epsilon}}{\rho^{3/2}} \simeq \sum_{\rho=1}^{\infty} \frac{A^\rho(1-\rho\epsilon)}{\rho^{3/2}} = g_{3/2}(A) - \epsilon g_{1/2}(A).$$

This allows us to write

$$\begin{aligned} n_c(\mathbf{r})\lambda_c^3 &= g_{3/2}(A) - \epsilon g_{1/2}(A) \\ &= g_{3/2}(A) - \left[(2U(n_c(\mathbf{r}) - n_{c,0}) - \frac{3}{2}\hbar\widetilde{\omega})/(k_B T_c)\right] g_{1/2}(A) \\ &= g_{3/2}(A) + \left[(\zeta(3/2)g_{1/2}(A) - g_{3/2}(A)g_{1/2}(A)\right] \frac{4a}{\lambda_c} + g_{1/2}(A)\frac{3}{2}\frac{\widetilde{\omega}}{\omega_c}. \end{aligned}$$

In the last step we used that $g_{3/2}(1) = \zeta(3/2)$, and we have defined $\omega_c = k_B T_c/\hbar$. In the same way we find

$$\begin{aligned} n_c^2\lambda_c^6 &= g_{3/2}(A)\left[g_{3/2}(A) + 3g_{1/2}(A)\frac{\widetilde{\omega}}{\omega_c} + \left(\zeta(3/2) - g_{3/2}(A)\right) g_{3/2}(A)\frac{8a}{\lambda_c}\right] \\ n_c^3\lambda_c^9 &= g_{3/2}^2(A)\left[g_{3/2}(A) + \frac{9}{2}g_{1/2}(A)\frac{\widetilde{\omega}}{\omega_c} + \left(\zeta(3/2) - g_{3/2}(A)\right) g_{3/2}(A)\frac{12a}{\lambda_c}\right]. \end{aligned}$$

[1]Note that this constant often is called g, but to avoid confusion with gravity in Appendix C, we use U.

Note that these expressions include terms proportional to a/λ_c, which are the first order terms due to interactions, and terms proportional to $\widetilde{\omega}/\omega_c$, which are first order due to the zero point energy. The ionization rate at condensation threshold Φ_c is given by (see chapter 5)

$$\Phi_c = \frac{1}{\tau_i}\int n_c d\mathbf{r} + \frac{1}{2}\beta\int n_c^2 d\mathbf{r} + \frac{1}{3}L\int n_c^3 d\mathbf{r}. \tag{B.5}$$

We will now calculate the integrals over the density, using the expressions obtained above. To do this, we define the dimensionless constants

$$I_{\alpha\beta\ldots} = \int_0^\infty x^2 g_\alpha(e^{-x^2}) g_\beta(e^{-x^2})\ldots dx. \tag{B.6}$$

Writing the integral on this form, and making the substitution

$$\frac{4\pi}{\lambda_c^3}\left(\frac{2k_BT_c}{m\overline{\omega}}\right)^{3/2} = \frac{4}{\sqrt{\pi}}\left(\frac{k_BT_c}{\hbar\overline{\omega}}\right)^3 = \frac{4}{\sqrt{\pi}}\left(\frac{\omega_c}{\overline{\omega}}\right)^3, \tag{B.7}$$

where $\overline{\omega} = (\omega_\perp^2\omega_\parallel)^{1/3}$, we can write the integrals as follows:

$$\int n_c d\mathbf{r} = \frac{4}{\sqrt{\pi}}\left(\frac{\omega_c}{\overline{\omega}}\right)^3 \times \left[I_{\frac{3}{2}} + \frac{3}{2}\frac{\widetilde{\omega}}{\omega_c}I_{\frac{1}{2}} + \left[\zeta(3/2)I_{\frac{1}{2}} - I_{\frac{1}{2}\ \frac{3}{2}}\right]\frac{4a}{\lambda_c}\right],$$

$$\int n_c^2 d\mathbf{r} = \frac{1}{\lambda_c^3}\frac{4}{\sqrt{\pi}}\left(\frac{\omega_c}{\overline{\omega}}\right)^3 \times \left[I_{\frac{3}{2}\ \frac{3}{2}} + 3\frac{\widetilde{\omega}}{\omega_c}I_{\frac{1}{2}\ \frac{3}{2}} + \left[\zeta(3/2)I_{\frac{1}{2}\ \frac{3}{2}} - I_{\frac{1}{2}\ \frac{3}{2}\ \frac{3}{2}}\right]\frac{8a}{\lambda_c}\right],$$

and

$$\int n_c^3 d\mathbf{r} = \frac{1}{\lambda_c^6}\frac{4}{\sqrt{\pi}}\left(\frac{\omega_c}{\overline{\omega}}\right)^3 \times \left[I_{\frac{3}{2}\ \frac{3}{2}\ \frac{3}{2}} + \frac{9}{2}\frac{\widetilde{\omega}}{\omega_c}I_{\frac{1}{2}\ \frac{3}{2}\ \frac{3}{2}} + \left[\zeta(3/2)I_{\frac{1}{2}\ \frac{3}{2}\ \frac{3}{2}} - I_{\frac{1}{2}\ \frac{3}{2}\ \frac{3}{2}\ \frac{3}{2}}\right]\frac{12a}{\lambda_c}\right].$$

We evaluate the integral of the type defined in Eq. B.6 and get the ionization rate by adding the three contributions:

$$\begin{aligned}\Phi_c = (\frac{\omega_c}{\overline{\omega}})^3\times \quad & [\ \tfrac{1}{\tau_i}(1.20 + 2.48\tfrac{\widetilde{\omega}}{\omega_c} + 12.35\tfrac{a}{\lambda_c}) \\ & + \tfrac{\beta}{\lambda_c^3}(0.33 + 1.81\tfrac{\widetilde{\omega}}{\omega_c} + 6.75\tfrac{a}{\lambda_c}) \\ & + \tfrac{L}{\lambda_c^6}(0.22 + 2.21\tfrac{\widetilde{\omega}}{\omega_c} + 6.50\tfrac{a}{\lambda_c})\Big].\end{aligned}$$

This expression includes first order corrections due to atomic interactions (terms proportional to $\frac{a}{\lambda_c}$) and zero point energy (terms proportional to $\frac{\widetilde{\omega}}{\omega_c}$). For typical parameters such as $a = 12$ nm and $T_c = 2$ μK, $a/\lambda_c \sim \widetilde{\omega}/\omega_c \sim 0.02$. For these parameters, corrections due to the zero point energy constitute 4%, 10% and 20% of the ideal gas result, for one- two- and three-body collisions, respectively. For the corrections due to interactions, the numbers are higher: 20%, 40% and 60 %, respectively. These contributions are large and are therefore kept in the theoretical expression used to fit the ionization rate as a function of T_c, in order to deduce a, as explained in chapter 5.

B.2 Interactions: 2nd order contributions

As the first order corrections due to interactions are high, we must calculate the second order to see if it can be neglected or not. In the calculation of the ionization rate given above, we have used Eq. B.1 for the density, with the interaction constant U and the chemical potential μ only being to first order in a/λ_c. An expression for the density taking into account higher orders in a/λ_c is given in Ref. [117]. Including up to second order, this expression reads:

$$n(\mathbf{r}) = \frac{1}{\lambda_c}\left\{\sum_i \frac{\mathcal{Z}^i}{i^{3/2}} - \frac{2a}{\lambda_c}\sum_{ij}\frac{(i+j)\mathcal{Z}^{i+j}}{(ij)^{3/2}} + 8\left(\frac{a}{\lambda_c}\right)^2\sum_{ijk}(i+j+k)\right.$$
$$\left.\times\mathcal{Z}^{i+j+k}\left[\frac{1}{(ij)^{3/2}k^{1/2}} + \frac{1}{(i+k)(j+k)(ijk)^{1/2}}\right]\right\}, \quad \text{(B.8)}$$

where the indices in the sums all run from 1 to infinity. The fugacity $\mathcal{Z}$ is given by

$$\mathcal{Z} = \exp\{-\beta V(\mathbf{r})\}\bar{\mathcal{Z}},$$

with

$$\bar{\mathcal{Z}} = \exp\{-\beta\bar{\mu}_c\}.$$

Here, $\bar{\mu}_c$ is given by a second order expansion in terms of a/λ [117]:

$$\bar{\mu}_c = \left[\mu_c^{(1)}\frac{a}{\lambda_c} + \mu_c^{(2)}\left(\frac{a}{\lambda_c}\right)^2\right]k_B T_c, \quad \text{(B.9)}$$

where

$$\bar{\mu}_c^{(1)} = 4\zeta(3/2) = 4g_{3/2}(1) \simeq 10.45,$$

and

$$\bar{\mu}_{\rm c}^{(2)} = 32\pi\left[\ln\frac{32\pi^2 a}{\lambda} + C_1 - 72\pi^2 R\right],$$

with

$$C_1 \simeq -0.54410,$$

and

$$R = 0.001920(2).$$

As before, we calculate $\int n(\mathbf{r})\mathrm{d}\mathbf{r}$, $\int n(\mathbf{r})^2\mathrm{d}\mathbf{r}$ and $\int n(\mathbf{r})^3\mathrm{d}\mathbf{r}$, now using Eq. B.8. The spatial dependent part of $\mathcal{Z}$ can be integrated, and making the same substitution as in Eq. B.7, we obtain expressions which depends only on $\bar{\mathcal{Z}}$:

$$\int n_{\rm c}\mathrm{d}\mathbf{r} = \frac{4}{\sqrt{\pi}}\left(\frac{\omega_{\rm c}}{\overline{\omega}}\right)^3 \times \left\{\sum_i \frac{\bar{\mathcal{Z}}^i}{i^3} - 2\sum_{ij}\frac{\bar{\mathcal{Z}}^{i+j}}{(ij)^{3/2}(i+j)^{1/2}}\frac{a}{\lambda_{\rm c}}\right.$$
$$\left. +8\sum_{ijk}\frac{\bar{\mathcal{Z}}^{i+j+k}}{(i+j+k)^{1/2}}\left[\frac{1}{(ij)^{3/2}k^{1/2}} + \frac{1}{(i+k)(j+k)(ijk)^{1/2}}\right]\left(\frac{a}{\lambda_{\rm c}}\right)^2\right\},$$

$$\int n_{\rm c}^2\mathrm{d}\mathbf{r} = \frac{1}{\lambda_{\rm c}^3}\frac{4}{\sqrt{\pi}}\left(\frac{\omega_{\rm c}}{\overline{\omega}}\right)^3 \times \left\{\sum_{ij}\frac{\bar{\mathcal{Z}}^{i+j}}{[ij(i+j)]^{3/2}}\right.$$
$$-4\sum_{ijk}\frac{(i+j)\bar{\mathcal{Z}}^{i+j+k}}{[ijk(i+j+k)]^{3/2}}\frac{a}{\lambda_{\rm c}} + 4\sum_{ijkl}\frac{\bar{\mathcal{Z}}^{i+j+k+l}}{\sqrt{ijk}[l(i+j+k+l)]^{3/2}}$$
$$\left.\left[4(i+j+k)\left(\frac{1}{ij}+\frac{1}{(i+k)(j+k)}\right)+\frac{(i+j)(k+l)}{ijk}\right]\left(\frac{a}{\lambda_{\rm c}}\right)^2\right\},$$

and

$$\int n_{\rm c}^3\mathrm{d}\mathbf{r} = \frac{1}{\lambda_{\rm c}^6}\frac{4}{\sqrt{\pi}}\left(\frac{\omega_{\rm c}}{\overline{\omega}}\right)^3 \times \left\{\sum_{ijk}\frac{\bar{\mathcal{Z}}^{i+j+k}}{[ijk(i+j+k)]^{3/2}}\right.$$
$$-6\sum_{ijkl}\frac{(i+j)\bar{\mathcal{Z}}^{i+j+k+l}}{[ijkl(i+j+k+l)]^{3/2}}\frac{a}{\lambda_{\rm c}} + 12\sum_{ijklm}\frac{\bar{\mathcal{Z}}^{i+j+k+l+m}}{\sqrt{ijk}[lm(i+j+k+l+m)]^{3/2}}$$
$$\left.\left[2(i+j+k)\left(\frac{1}{ij}+\frac{1}{(i+k)(j+k)}\right)+\frac{(i+j)(k+l)}{ijk}\right]\left(\frac{a}{\lambda_{\rm c}}\right)^2\right\}.$$

We now make a second order expansion of $\bar{\mathcal{Z}}$:

$$\bar{\mathcal{Z}}^q = e^{-q\beta\bar{\mu}_\mathrm{c}} \approx 1 + q\beta\bar{\mu}_\mathrm{c} + \frac{q^2}{2}\beta^2{\bar{\mu}_\mathrm{c}}^2.$$

Keeping terms up to second order in a/λ_c, we can write

$$\begin{aligned}
\bar{\mathcal{Z}}^q &\approx 1 + q\left[\mu_\mathrm{c}^{(1)}\frac{a}{\lambda_\mathrm{c}} + \mu_\mathrm{c}^{(2)}\left(\frac{a}{\lambda_\mathrm{c}}\right)^2\right] + \frac{q^2}{2}\left[\mu_\mathrm{c}^{(1)}\frac{a}{\lambda_\mathrm{c}} + \mu_\mathrm{c}^{(2)}\left(\frac{a}{\lambda_\mathrm{c}}\right)^2\right]^2 \\
&\approx 1 + q\left[\mu_\mathrm{c}^{(1)}\frac{a}{\lambda_\mathrm{c}} + \mu_\mathrm{c}^{(2)}\left(\frac{a}{\lambda_\mathrm{c}}\right)^2\right] + \frac{q^2}{2}\left[\mu_\mathrm{c}^{(1)}\frac{a}{\lambda_\mathrm{c}}\right]^2.
\end{aligned}$$

We insert this expansion for $\bar{\mathcal{Z}}^q$ in the expressions for the integrals, and again we neglect all terms of order higher than $(a/\lambda_\mathrm{c})^2$. The above sums is then written as product between physical constants and purely geometric sums. The latter can be evaluated using the Euler-Maclaurin summation formula [127]. We also use that

$$\begin{aligned}
g_2(\bar{\mathcal{Z}}) &= \zeta(2) + \bar{\mu}_\mathrm{c} - \ln\bar{\mu}_\mathrm{c}, \\
g_3(\bar{\mathcal{Z}}) &= \zeta(3) + \zeta(2)\bar{\mu}_\mathrm{c} + \frac{3}{4}{\bar{\mu}_\mathrm{c}}^2 - \frac{{\bar{\mu}_\mathrm{c}}^2}{2}\ln\bar{\mu}_\mathrm{c}.
\end{aligned}$$

Finally we can write the three contributions as (note that the contribution corresponding $\int n_\mathrm{c}\mathrm{d}\mathbf{r} = N_\mathrm{c}$ has already been evaluated in Ref. [117]):

$$\int n_\mathrm{c}\mathrm{d}\mathbf{r} = \frac{4}{\sqrt{\pi}}\left(\frac{\omega_\mathrm{c}}{\overline{\omega}}\right)^3\left[0.53 + 5.47\frac{a}{\lambda_\mathrm{c}} + (0.73\bar{\mu}_\mathrm{c}^{(2)} - 42.779)\left(\frac{a}{\lambda_\mathrm{c}}\right)^2\right]$$

$$\int n_\mathrm{c}^2\mathrm{d}\mathbf{r} = \frac{1}{\lambda_\mathrm{c}^3}\frac{4}{\sqrt{\pi}}\left(\frac{\omega_\mathrm{c}}{\overline{\omega}}\right)^3\left[0.295 + 5.96\frac{a}{\lambda_\mathrm{c}} + (1.07\bar{\mu}_\mathrm{c}^{(2)} + 20.18)\left(\frac{a}{\lambda_\mathrm{c}}\right)^2\right]$$

$$\int n_\mathrm{c}^3\mathrm{d}\mathbf{r} = \frac{1}{\lambda_\mathrm{c}^6}\frac{4}{\sqrt{\pi}}\left(\frac{\omega_\mathrm{c}}{\overline{\omega}}\right)^3 \times \left[0.286 + 8.65\frac{a}{\lambda_\mathrm{c}} + (1.95\bar{\mu}_\mathrm{c}^{(2)} - 7.62)\left(\frac{a}{\lambda_\mathrm{c}}\right)^2\right].$$

Inserting these expressions in Eq. B.5 we obtain (for clarity, we seperate the terms corresponding to background, 2- and 3-body collisions):

$$\Phi_\mathrm{c}^{\mathrm{background}} = \frac{1}{\tau_i}\left(\frac{\omega_\mathrm{c}}{\overline{\omega}}\right)^3\left[1.20 + 12.35\frac{a}{\lambda_\mathrm{c}} + (1.65\bar{\mu}_\mathrm{c}^{(2)} - 96.54)\left(\frac{a}{\lambda_\mathrm{c}}\right)^2\right],$$

$$\Phi_\mathrm{c}^{2-\mathrm{body}} = \frac{\beta}{\lambda_\mathrm{c}^3}\left(\frac{\omega_\mathrm{c}}{\overline{\omega}}\right)^3\left[0.33 + 6.75\frac{a}{\lambda_\mathrm{c}} + (1.21\bar{\mu}_\mathrm{c}^{(2)} + 22.77)\left(\frac{a}{\lambda_\mathrm{c}}\right)^2\right],$$

and

$$\Phi_{\rm c}^{3-\rm body} = \frac{L}{\lambda_{\rm c}^6}\left(\frac{\omega_{\rm c}}{\overline{\omega}}\right)^3 \times \left[0.22 + 6.50\frac{a}{\lambda_{\rm c}} + (1.47\bar{\mu}_{\rm c}^{(2)} - 5.73)\left(\frac{a}{\lambda_{\rm c}}\right)^2\right].$$

For typical parameters ($a/\lambda \simeq 0.02$), we have $\bar{\mu}_{\rm c}^{(2)} \simeq -6.56$, and the second order contributions become -4%, 1.8% and -3% of the ideal gas result, for one- two- and three-body processes, respectively. These corrections are small, both compared to first order contributions and in absolute value, and it is therefore reasonable to neglect them in the analysis given in chapter 5.

B.3 Zero point energy: all higher order contributions

It turns out that it is simpler to include *all* higher order terms in the evaluation of effects due to the zero point energy, instead of considering the second order terms alone. We use the result of M. Naraschewski and R. J. Glauber [128] together with [89]. The exact density for a harmonically trapped ideal gas is given by:

$$n(\mathbf{r}) = \frac{1}{\pi^{3/2}\sigma_x\sigma_y\sigma_z}\sum_{\rho=1}^{\infty}\bar{\mathcal{Z}}^{\rho}\frac{\exp\left[-\left(\frac{x^2}{\sigma_x^2}\tanh\frac{\tau_x\rho}{2} + \frac{y^2}{\sigma_y^2}\tanh\frac{\tau_y\rho}{2} + \frac{z^2}{\sigma_z^2}\tanh\frac{\tau_z\rho}{2}\right)\right]}{\sqrt{(1-e^{-2\tau_x\rho})(1-e^{-2\tau_y\rho})(1-e^{-2\tau_z\rho})}}, \tag{B.10}$$

where $\tau_i = \hbar\omega_i/k_BT$ and $\sigma_i = \sqrt{\hbar/m\omega_i}$. Note that we have modified the definition of $\bar{\mathcal{Z}}$. It now reads:

$$\bar{\mathcal{Z}} = \exp\left\{\beta\left(\mu - \frac{3}{2}\hbar\tilde{\omega}\right)\right\},$$

with $\widetilde{\omega} = (2\omega_\perp + \omega_\parallel)/3$ defined as before. Note that we recover Eq. B.1 by making the following approximations: $\tanh\frac{\tau_i\rho}{2} \to \frac{\tau_i\rho}{2}$ and $(1-e^{-2\tau_i\rho}) \to 2\tau_i\rho$. The density corresponding to the atoms in the excited states $n_{\rm exc}(\mathbf{r})$ is

$$n_{\rm exc}(\mathbf{r}) = n(\mathbf{r}) - n_0(\mathbf{r}), \tag{B.11}$$

with $n_0(\mathbf{r})$ the ground state density given by:

$$n_0(\mathbf{r}) = \frac{1}{\pi^{3/2}\sigma_x^2\sigma_y^2\sigma_z^2}\exp\left[-\left(\frac{x^2}{\sigma_x^2} + \frac{y^2}{\sigma_y^2} + \frac{z^2}{\sigma_z^2}\right)\right]. \tag{B.12}$$

To deduce the density at BEC threshold, we will use the reasoning based on "saturation of excited states". As we will see below, there exists an upper limit for the density of atoms in the excited states $n_{\rm exc}^{\rm max}(\mathbf{r})$, and the

threshold is defined as the point, where the total density becomes equal to this density. First, we use Eq. B.11 together with Eq. B.10 and Eq. B.12 to write the density corresponding to the excited states:

$$n_{\mathrm{exc}}(\mathbf{r}) = \frac{1}{\pi^{3/2}\sigma_x\sigma_y\sigma_z}\sum_{\rho=1}^{\infty}\bar{\mathcal{Z}}^{\rho}\Big(\frac{\exp\left[-\left(\frac{x^2}{\sigma_x^2}\tanh\frac{\tau_x\rho}{2}+\frac{y^2}{\sigma_y^2}\tanh\frac{\tau_y\rho}{2}+\frac{z^2}{\sigma_z^2}\tanh\frac{\tau_z\rho}{2}\right)\right]}{\sqrt{(1-e^{-2\tau_x\rho})(1-e^{-2\tau_y\rho})(1-e^{-2\tau_z\rho})}} - \exp\left[-\left(\frac{x^2}{\sigma_x^2}+\frac{y^2}{\sigma_y^2}+\frac{z^2}{\sigma_z^2}\right)\right]\Big).$$

An upper bound is given by

$$n_{\mathrm{exc}}(\mathbf{r}) < n_{\mathrm{exc}}(\mathbf{r},\bar{\mathcal{Z}}=1) \equiv n_{\mathrm{exc}}^{\max}(\mathbf{r}). \tag{B.13}$$

By definition of BEC threshold we can then write

$$n_{\mathrm{c}}(\mathbf{r}) = n_{\mathrm{exc}}^{\max}(\mathbf{r}) = \frac{1}{\pi^{3/2}\sigma_x\sigma_y\sigma_z}\sum_{\rho=1}^{\infty}\Big(\frac{\exp\left[-\left(\frac{x^2}{\sigma_x^2}\tanh\frac{\tau_x\rho}{2}+\frac{y^2}{\sigma_y^2}\tanh\frac{\tau_y\rho}{2}+\frac{z^2}{\sigma_z^2}\tanh\frac{\tau_z\rho}{2}\right)\right]}{\sqrt{(1-e^{-2\tau_x\rho})(1-e^{-2\tau_y\rho})(1-e^{-2\tau_z\rho})}} - \exp\left[-\left(\frac{x^2}{\sigma_x^2}+\frac{y^2}{\sigma_y^2}+\frac{z^2}{\sigma_z^2}\right)\right]\Big).$$

Using this expression, we calculate numerically[2] $\int n(\mathbf{r})\mathrm{d}\mathbf{r}$, $\int n(\mathbf{r})^2\mathrm{d}\mathbf{r}$ and $\int n(\mathbf{r})^3\mathrm{d}\mathbf{r}$ and obtain the correction due to the finite size effects.

Obtained numerical results

From the numerical calculation, we obtain the corrections for finite size which includes all orders. Therefrom, we can obtain the result corresponding to all orders higher than 1, which we denote by $l^{\,2\mathrm{nd}+}$. From section B.1, we have the first order correction due to finite size ($l^{\,1\mathrm{st}}$). We can now give the correction $\mathrm{C}^{\text{finite size}} \equiv \frac{l^{\,2\mathrm{nd}+}}{l^{\,1\mathrm{st}}}$ for background, 2- and 3-body collisions:

- 1-body collisions: $\mathrm{C}^{\text{finite size}} \sim 0.05$
- 2-body collisions: $\mathrm{C}^{\text{finite size}} \sim 0.4$
- 3-body collisions: $\mathrm{C}^{\text{finite size}} \sim 0.5$

Even though the higher order corrections for 2- and 3-body collisions are relatively large compared to first order, neglecting them in the theoretical expression for the ionization rate does not change our final result in chapter 5. As mentioned, we use the expression for the ionization rate to obtain the s-wave scattering length for He*: including the higher order terms due to finite size effects in the expression for the ion rate only modifies a with 0.02 nm. Our experimental uncertainty on the scattering length turns out to be of the order of nm – and consequently, the uncertainty due to higher order finite size effects is negligible.

[2] Analytical expressions for the integrals can also be written, but the precision obtained by numerical evaluation is sufficient for our purpose.

APPENDIX C

Fit functions for Time-Of-Flight signals

The Time-Of-Flight signal recorded with the micro-channel plate, gives the atom flux as a function of arrival time of the atoms. The shape of this signal indicates qualitatively the state of the cloud:

- a Gaussian shape indicates a cold cloud still far from degeneracy,
- a more peaked shape indicates that the cloud approaches Bose-Einstein condensation threshold,
- the appearance of a double structure indicates that the cloud is cooled beyond threshold,
- and finally, an inverted parabolic shape corresponds to a (quasi) pure Bose-Einstein condensate.

To be more quantitative, we make a fit of the TOF signals with the theoretical expressions corresponding to the different types of clouds. From the width of the fit, the temperature (for a thermal cloud), or chemical potential (for a Bose-Einstein condensate), is obtained. From the amplitude of the signal, we can in principle deduce the atom number of the cloud[1].

This Appendix is intended to give the theoretical expressions for the Time-Of-Flight signals, which we use in this thesis. For conciseness we will list all of them, even though the expressions corresponding to an ideal thermal cloud has been discussed in Ref. [34], and the non-interacting cloud at BEC threshold as well as the pure BEC are given in Ref. [37]. We will here take a step further and add to the list the expression for a cloud at BEC threshold including interactions. This expression is needed in the data analysis in chapter 5.

[1] Note however that due to uncontrolled processes, the atom number obtained from the fit does not correspond to the number of atoms contained in the trap (see chapter 2).

C.1 Thermal cloud far from Bose-Einstein condensation threshold

Far from threshold, the velocity distribution of the atoms is a Maxwell-Boltzmann distribution $\mathcal{F}_{\rm MB}$ [107]:

$$\mathcal{F}_{\rm MB}(\mathbf{r},\mathbf{v},t=0)=\exp[-\beta(\frac{1}{2}mv^2+V(\mathbf{r}))],$$

where $\beta = 1/k_BT$ and $V(\mathbf{r})$ is the trapping potential before the trap is switched off[2]. Using this distribution function, and assuming that the initial cloud is a point source, the atom flux arriving on the MCP can be deduced (see [34] for details):

$$\frac{dN}{dt}(t) = N_0\sqrt{\frac{m}{2\pi k_BT}}\,\frac{h+\frac{1}{2}gt^2}{t^2}\,\exp\left(-\frac{m}{2k_BT}\,\frac{\left(h-\frac{1}{2}gt^2\right)^2}{t^2}\right)\times \left(1-\exp\left(-\frac{m}{2k_BT}\,\frac{R_0^2}{t^2}\right)\right) \quad . \tag{C.1}$$

The initial atom number is denoted by N_0, m is the atom mass, h is the distance between the trap center and the MCP (5 cm in our case), g the gravitational acceleration, k_B the Boltzmann constant, and R_0 is the radius of the MCP. The origin of time corresponds to the switch-off time of the trap potential. Rewriting this expression we obtain

$$\frac{dN}{dt}(t) = g\,t\,\frac{N_0}{\sqrt{2\pi}\,\sigma_x(t)}\times\frac{t_0^2+t^2}{2t^2}\times\exp\left(-\frac{x_0^2(t)}{2\,\sigma_x^2(t)}\right)\times\left(1-\exp\left(-\frac{R_g^2}{2\,\sigma_x^2(t)}\right)\right), \tag{C.2}$$

where we have defined the parameters t_0, $\sigma_x(t)$ and $x_0(t)$:

$$t_0=\sqrt{\frac{2h}{g}}\quad,\quad \sigma_x(t)\simeq\sqrt{\frac{k_BT}{m}}\times t \quad \text{et} \quad x_0(t)=h-\frac{1}{2}gt^2. \tag{C.3}$$

Two regimes exist: for high temperatures ($k_BT \gg mgh$) gravity is negligible and the cloud explodes symmetrically. In this case only a fraction corresponding to the solid angle of the MCP is detected, and the average arrival time is given by the temperature. In the other limit ($k_BT \ll mgh$) gravity alone determines the average arrival time ($\sim$ 100 ms). In this case, all the atom arrive on the MCP, and we can assume that R_0 is infinite, which simplifies Eq. C.2. The temperature can be obtained from the width of the Gaussian: $\Delta t = \sqrt{k_BT/mg^2}$.

[2] We assume that the switch off is instantaneous, and that the distribution of the atoms consequently do not change.

C.2 At Bose-Einstein condensation threshold: without interactions

In the vicinity of BEC threshold, the quantum nature of the particles becomes important, and the Maxwell-Boltzmann distribution is no longer valid. Instead we use the Bose-Einstein distribution [107] for a non-interacting gas:

$$\mathcal{F}_{\mathrm{BE}}(\mathbf{r},\mathbf{v},t=0)=\frac{1}{\exp[-\beta(\frac{1}{2}mv^2+V(\mathbf{r})-\mu)]-1}, \tag{C.4}$$

where μ is the chemical potential. This can also be written as

$$\mathcal{F}_{\mathrm{BE}}(\mathbf{r},\mathbf{v},t=0)=\sum_{\rho=1}^{\infty}\exp[-\rho\beta(\frac{1}{2}mv^2+V(\mathbf{r})-\mu)], \tag{C.5}$$

where we have used the fact that

$$\frac{1}{e^{\alpha}-1}=\sum_{\rho=1}^{\infty}e^{-\rho\alpha}.$$

The corresponding flux is given by [37]:

$$\frac{dN}{dt}(t)=\frac{1}{g_3(z)}\,g\,t\,\frac{N_0}{\sqrt{2\pi}\,\sigma_x(t)}\times\frac{t_0^2+t^2}{2t^2}\left(g_{5/2}\left[z\,e^{-\frac{x_0^2(t)}{2\sigma_x^2(t)}}\right]-g_{5/2}\left[z\,e^{-\frac{x_0^2(t)+R_0^2}{2\sigma_x^2(t)}}\right]\right), \tag{C.6}$$

where the Bose function is defined by $g_\alpha(x)=\sum_{\rho=1}^{\infty}\frac{x^\rho}{\rho^\alpha}$ and we have defined the fugacity $z=e^{\beta\mu}$. For an ideal gas at BEC threshold, $\mu=0$ so $z=1$. The factor $1/g_3(z)$ is a normalization factor obtained by requiring $N=1/(2\pi\hbar^2)\times\int\mathrm{d}\mathbf{r}\,\mathrm{d}\mathbf{v}\,\mathcal{F}_{\mathrm{BE}}$. For a typical temperature at threshold, the size of the cloud is approximatively the size of the MCP or slightly larger, and in general, we cannot neglect the finite size of the detector.

C.3 At Bose-Einstein condensation threshold: with interactions

The main steps necessary to include the interactions bear resemblance to the steps performed to include the interactions in the expression for the ionization rate in Appendix B. Therefore we will not go into detail with these steps, but only give the main ideas and the final result.

To take into account the interactions, we replace Eq. C.4 with:

$$\mathcal{F}_{\mathrm{BE}}(\mathbf{r},\mathbf{v},t=0)=\frac{1}{\exp[-\beta(\frac{1}{2}mv^2+V(\mathbf{r})-\mu+2Un(\mathbf{r}))]-1}, \tag{C.7}$$

with $U = 4\pi\hbar a/m$ the interaction constant (a is the scattering length), $n(\mathbf{r})$ the density, and μ the chemical potential. By using the fact that

$$\frac{1}{e^{\alpha}-1} = \sum_{\rho=1}^{\infty} e^{-\rho\alpha},$$

Eq. C.7 can be written as:

$$\begin{aligned}\mathcal{F}_{\mathrm{BE}}(\mathbf{r},\mathbf{v},t=0) &= \sum_{\rho=1}^{\infty} e^{\beta\rho[mv^2/2+V(\mathbf{r})]} e^{-\beta\rho[\mu-2Un(\mathbf{r})]} \\ &\simeq \sum_{\rho=1}^{\infty} e^{-\beta\rho[mv^2/2+V(\mathbf{r})]}\left(1+\beta\rho[\mu-2Un(\mathbf{r})]\right). \quad \text{(C.8)}\end{aligned}$$

In the last step we have assumed that[3] $mv^2/2+V(\mathbf{r}) \gg \mu-2Un(\mathbf{r})$. We then replace $n(\mathbf{r})$ with the non-interacting expression: $n^{(0)}(\mathbf{r}) = \frac{1}{\lambda^3(T)} g_{3/2}\left[\exp\left(-\frac{V(\mathbf{r})}{k_B T}\right)\right]$ and the expression can now be written as

$$\begin{aligned}\mathcal{F}_{\mathrm{BE}}(\mathbf{r},\mathbf{v},t=0) &= \sum_{\rho=1}^{\infty} e^{-\beta\rho[mv^2/2+V(\mathbf{r})]} \quad \text{(C.9)} \\ + \quad \beta\mu \sum_{\rho=1}^{\infty} \rho e^{-\beta\rho[mv^2/2+V(\mathbf{r})]} &- \frac{2\beta U}{\lambda^3} \sum_{(\rho,\rho')=1}^{\infty} \frac{\rho}{\rho'^{3/2}} e^{-\beta\rho mv^2/2} e^{-\beta(\rho+\rho')V(\mathbf{r})}.\end{aligned}$$

We have put $\mathcal{F}_{\mathrm{BE}}$ on a form which consist of three terms, the first two being similar to the non-interacting case given in Eq. C.5. We then use the fact that a distribution function of the form given in Eq. C.5 gives a flux corresponding to Eq. C.6. By identifying the coefficients in the Eq. C.5 with the coefficients in each of the first two term in Eq. C.9, we obtain the flux. The only differences are

- In the first term in Eq. C.9, the chemical potential μ is not present in the exponential. In the expression for the flux we must therefore set $z = 1$.
- The second term in Eq. C.9 is multiplied with $\mu\beta$, and so must the corresponding term for the flux be. Also an additional ρ is present in the sum, so the functions $g_{5/2}$ become $g_{3/2}$ in the expression for the flux.

The last term is for the moment kept as a sum. The flux therefore becomes

[3] The first exponential in Eq. C.8 decays much faster than the second one. Consequently for large values of ρ where the expansion would not be valid, the first exponential becomes very close to zero and "kills" the terms in the sum.

$$\frac{dN}{dt}(t) = C_{\rm int} \times g\, t\, \frac{N_0}{\sqrt{2\pi}\,\sigma_x(t)} \times \frac{t_0^2 + t^2}{2t^2} \tag{C.10}$$
$$\times \quad \left(g_{5/2}\left[e^{-\frac{x_0^2(t)}{2\sigma_x^2(t)}}\right] - g_{5/2}\left[e^{-\frac{x_0^2(t)+R_0^2}{2\sigma_x^2(t)}}\right] + \mu\beta\left\{ g_{3/2}\left[e^{-\frac{x_0^2(t)}{2\sigma_x^2(t)}}\right] - g_{3/2}\left[e^{-\frac{x_0^2(t)+R_0^2}{2\sigma_x^2(t)}}\right]\right\}\right.$$
$$\left. - \quad \frac{2\beta\, U}{\lambda^3} \sum_{\rho,\rho'=1}^{\infty} \frac{\exp[-\frac{\beta m\rho}{2t^2}(h - \frac{1}{2}gt^2)]}{[\rho'(\rho+\rho')]^{3/2}} \left[1 - e^{-\beta m\rho R_0/2t^2}\right] \right),$$

where the normalization constant now is given by

$$C_{\rm int} = \left[g_3(z) + \mu\beta g_2(z) - \frac{2\,\beta\, U}{\lambda} \sum_{\rho,\rho'=1}^{\infty} \frac{1}{\rho'^{3/2}(\rho+\rho')^{3/2}\rho^{1/2}} \right]^{-1}.$$

This expression remains valid as long as the absolute value of μ is small. At BEC threshold μ is indeed small and can be replaced be the expression $\mu = \frac{3}{2}\hbar\widetilde{\omega} + 2Un(0)$ with $\widetilde{\omega} = (2\omega_\perp + \omega_\parallel)/3$ (see Appendix B). The expression given in Eq. C.10 is the function which we use as fit function when we analyze the data corresponding to a cloud at threshold in chapter 5. The sum term in the normalization constant can be evaluated numerically, while the last sum term in Eq. C.10 is approximated by an analytical function.

Effect of the choice of scattering length on the temperature

Note that $\frac{2\beta U}{\lambda^3}$ in Eq. C.10 also can be written as $4a/\lambda$. This means that the fit function is slightly dependent on the scattering length a. Therefore one must choose an initial value of a before fitting the TOF signals. The fact that we do not know a prior to the analysis, results in an uncertainty on the temperature and consequently on the final value of a. We will here study the effect of the choice of scattering length on temperature; in chapter 5 we will investigate the influence on the final value of a. In Fig. C.1 we show how the temperature varies according to which a we use in the fit function: we show the temperature deduced for the experimental points presented in chapter 5, for 3 different values of a ($a = 10$, $a = 12$ and $a = 14$ nm), as a function of the temperature that we would obtain, if we did not include interactions in the fit function. For small temperatures (small densities) the temperature variations for different values of a are invisible on the scale of the graph, so we have only plotted the experimental points corresponding to the highest temperatures observed. In this way the estimates of the uncertainties from these points also become an upper limit. Note that the temperatures shown are not corrected for hydrodynamic effects (see Appendix D). The conclusion is that including interactions modifies significantly the temperature, but the variations inside the range of possible scattering lengths (a varying between

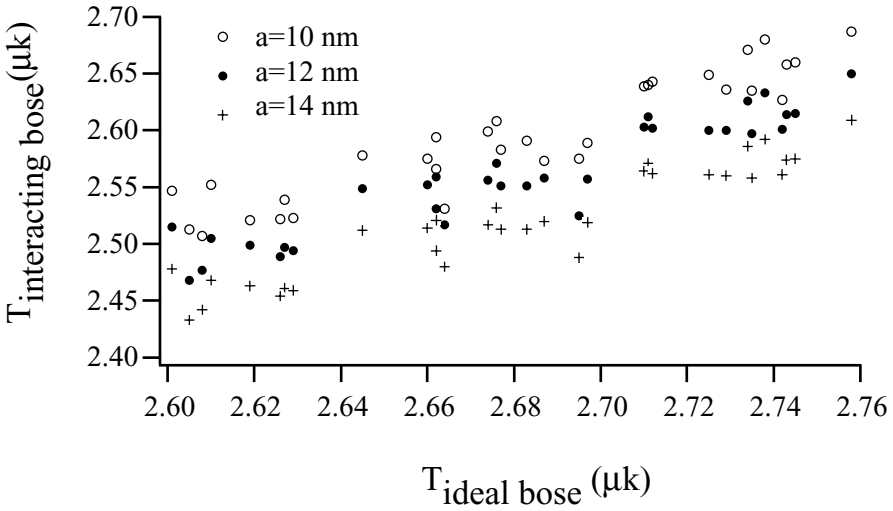

Figure C.1: *The temperatures deduced from the TOF signals using using a Bose function including interactions as a function of the temperature obtained with an ideal Bose function. As the interactions in the Bose function depend on the scattering length, so does the obtained temperature. We show the results for three different choices of scattering lengths. To reveal this effect alone, the temperatures are not corrected due to the hydro dynamic regime discussed in Appendix D. The dispersion in the points is due to the uncertainty in the fitting procedure. Finally note that only the highest temperatures data are shown. For lower temperatures, the difference arising from using* $a = 10$, $a = 12$ *or* $a = 14$ *nm becomes invisible.*

~ 12 nm and ~ 11 nm, are small, even for the highest temperatures, as seen in the graph.

C.4 A pure Bose-Einstein condensate

For completeness, let us add the last fit function used during the analysis of data presented in this thesis. It is the fit function that we use for the pure Bose-Einstein condensates, presented in chapter 4. We use the Thomas-Fermi distribution introduced in chapter 2 to describe the initial density in the trap. The derivation of the flux arriving on the micro-channel plate is given in Ref. [37]. Here, we will just state the final result:

$$\frac{dN_{\mathrm{BEC}}}{dt}(t) = \frac{15}{16}\, g\, N_{\mathrm{BEC}} \sqrt{\frac{m}{2\,\mu}}\ \max\left[\left(1 - \left(\frac{g}{2t}\sqrt{\frac{m}{2\,\mu}}\,(t_0^2 - t^2)\right)^2\right),\ 0\right]^2 \times \left(\frac{t^2 + t_0^2}{2\,t^2}\right).$$

By fitting the Time-Of-Flight signal corresponding to Bose-Einstein condensates with this function, we can obtain the chemical potential μ (introduced in chapter 2). From the chemical potential, the density of the cloud can be obtained, as discussed – and fully exploited – in chapter 4.

A P P E N D I X D

The hydrodynamic expansion

As explained in chapter 5, our determination of the scattering length relies partially on measurements of the temperature of clouds at Bose-Einstein phase transition. The temperature is obtained by fitting the Time-Of-Flight signal using the fit function described in Appendix C. However, this fit function is derived assuming a ballistic expansion of the cloud, i.e. no collisions present during the expansion. We know, however, that at high densities, these collisions play a role and modify slightly the expansion of the cloud – the cloud is influenced by *hydrodynamic effects*.

This is the case for a cloud of He^* at Bose-Einstein condensation threshold (for our choice of trapping potentials). Therefore, collisions during the first instants of the expansion must be taken into account: our gas is in the hydrodynamic regime. This happens when the rate of elastic collisions ($\sim 10^4$ per second for a threshold cloud with our parameters) is large compared to the inverse of the characteristic time for the conversion of interaction energy to kinetic energy, which happens during the initial expansion of the cloud. This time is given by the radial trap oscillation frequency (around 1 kHz, see chapter 2). The temperatures obtained using the "ballistic" fit function are therefore not exact. To correct for this, two possibilities exist: either we could modify the fit functions in order to account for the collisions during the expansion and obtain directly the correct temperature. Or, we can keep the fit function from Appendix C, and then posteriorly correct the obtained temperatures. As the hydrodynamic effect is only a small correction, the second solution turns out to be sufficiently precise, and easier to implement. This is what we will do in this Appendix, following the approach developed by P. Pedri *et al.* [118].

There is a subtle point however, similar to the one mentioned in Appendix C: the correction that we will apply to the temperature actually depends on the scattering length a, which we do not have prior to the analysis – we only have a given range, inside which a is confined, estimated from theory and earlier measurement. However, as we will show below, the temperature correction varies little, when a is varied inside this possible range, and even better, using an iterative procedure, we can render this variation as small as desired. This will be discussed below.

D.1 Corrections to the temperature

The value of the temperature T_0 of the trapped cloud (i.e. before expansion) can be extracted from the width of the TOF signal $R_{\rm th}(t)$, after an expansion time t. To describe the expansion, it is usual to define a scaling parameter:

$$R_i(t) = b_i(t) R_i(0)$$

with $i = x, y, z$. The width $R_i(0)$ is the equilibrium width of the cloud in the trap. The form of the scaling parameter is different for and ideal and interacting gas, as we will now show[1].

Ideal gas: a reminder

Let us see how the temperature is related to the width of the cloud for an ideal gas. The scaling parameter is given by:

$$b_i(t) = \sqrt{1 + (\omega_i t)^2}.$$

The initial size of the cloud is given by

$$R_i(0) = \sqrt{\frac{k_B T}{m\omega_i}},$$

and therefore

$$R_i(t) = \sqrt{1 + (\omega_i t)^2} \times \sqrt{\frac{k_B T}{m\omega_i}} = \sqrt{\frac{k_B T}{m}\left(1 + \frac{1}{(\omega_i t)^2}\right)} \times t.$$

For relatively hot clouds (~ 1 mK or above), the expansion time of the cloud is ~ 10 ms (or less), and we can neglect $1/(\omega_i t)^2$. We then obtain:

$$R_i(t) = \sqrt{\frac{k_B T}{m}} \times t$$

Therefore, for an ideal gas, the expansion is isotropic. This is because the initial velocity distribution is isotropic, and remains isotropic after release of the cloud.

Non-ideal gas

In a non-ideal gas it is more complicated. Due to collisions during the expansion, the velocity distribution does not remain perfectly isotropic in space, and the mean field energy during the expansion must be taken into account.

[1] In the following discussion we will assume that we measure a spatial width (the common case in BEC physics), even though that in reality, using an MCP, we measure a temporal width. How one can translate from spatial to temporal width is shown in [34].

A model including these effects have been developed by P. Pedri *et al.* [118], and is discussed in [60]. This is the approach that we will use, in order to deduce the scaling factors describing the expansion of our clouds at Bose-Einstein condensation threshold. In the following, we will briefly summarizes the main ideas behind this model. The approach is based on the Boltzmann equation

$$\frac{\partial f}{\partial t} + \frac{1}{m}\mathbf{p}\cdot\nabla_{\mathbf{r}} f - \nabla\left(2Un_{\mathrm{th}} + V_{\mathrm{ext}}(\mathbf{r},t)\right)\cdot\nabla_{\mathbf{p}} f = I_{\mathrm{coll}}[\ f]. \tag{D.1}$$

The function f describes the phase space distribution evolving under the action of three terms corresponding to a free expansion, the force $\mathbf{F} = \nabla\left(2Un_{\mathrm{th}} + V_{\mathrm{ext}}(\mathbf{r},t)\right)$ due to the interactions ($U = 4\pi\hbar^2 a/m$ and n_{th} is the density) and the trap potential, and the collision integral $I_{\mathrm{coll}}[\ f]$ which describes thermalizing collisions. For the steady state solution in the trap $I_{\mathrm{coll}}[\ f] = 0$, while during expansion $I_{\mathrm{coll}}[\ f] \neq 0$ and[2] $V_{\mathrm{ext}} = 0$. To determine f during the expansion, one assumes a scaling ansatz of the form

$$f(\mathbf{r},\mathbf{p},t) = \frac{1}{\prod_j b_j \theta_j^{1/2}} f_0\left(\left\{\frac{x_i}{b_i}\right\}, \left\{\frac{1}{\theta_i^{1/2}}\left(\frac{p_i}{m} - \frac{\dot{b}_i}{b_i}x_i\right)\right\}, t = 0\right), \tag{D.2}$$

where the presence of the dimensionless parameter θ_i allows it to include an eventual deformation of the velocity distribution in addition to the deformation in the density distribution expressed by b_i. The function f_0 is the distribution function at equilibrium satisfying $I_{\mathrm{coll}}[\ f_0] = 0$. The collision integral during expansion is written as

$$I_{\mathrm{coll}}[\ f] = -\frac{f - f_{le}}{\mathcal{T}_0}$$

where $\mathcal{T}_0$ is the collision relaxation time (related to the average time between the collisions, see below), and f_{le} is the so-called local equilibrium distribution function [118]. This approximation is referred to as the relaxation time approximation. Inserting Eq. D.2 in Eq. D.1 leads to a differential equation on $b_i(t)$, $\theta_i(t)$, $\nabla_{\mathbf{r}} f_0$ and $\nabla_{\mathbf{p}} f_0$. Using the fact that f_0 is the solution to Eq. D.1 with $I_{\mathrm{coll}} = 0$, we can obtain a set of differential equations the only variables being $b_i(t)$ and $\theta_i(t)$ [118, 129]:

[2] Note that we have not included gravity in this potential. Instead, we later modify the vertical z coordinate to account for the effect of gravity.

$$
\begin{aligned}
\frac{d^2 b_\perp}{d\tau^2} &= -\chi\left(\frac{\theta_\perp}{b_\perp} - \frac{1}{b_\perp\left(\prod_j b_j\right)}\right) - \frac{\theta_\perp}{b_\perp}, \\
\frac{d^2 b_\parallel}{d\tau^2} &= -\lambda^2\chi\left(\frac{\theta_\perp}{b_\parallel} - \frac{1}{b_\parallel\left(\prod_j b_j\right)}\right) - \lambda^2\frac{\theta_\parallel}{b_\parallel}, \\
\frac{d\theta_\perp}{d\tau} + 2\frac{db_\perp}{d\tau}\frac{\theta_\perp}{b_\perp} &= -\frac{1}{\mathcal{T}}\frac{\left(\theta_\perp - \theta_\parallel\right)}{3\tilde{\theta}\left(\prod_j b_j\right)}, \\
\frac{d\theta_\parallel}{d\tau} + 2\frac{db_\parallel}{d\tau}\frac{\theta_\parallel}{b_\parallel} &= +\frac{1}{\mathcal{T}}\frac{2\left(\theta_\perp - \theta_\parallel\right)}{3\tilde{\theta}\left(\prod_j b_j\right)},
\end{aligned}
\tag{D.3}
$$

We have introduced the dimensionless time $\tau = \omega_\perp t$ and the dimensionless collision relaxation time $\mathcal{T} = \omega_\perp \mathcal{T}_0$. We have also used the notation $\tilde{\theta} = (\theta_\parallel + 2\theta_\perp)/3$. The small parameter denoted χ is related to the mean values of interaction energy and the kinetic energy at equilibrium: $\chi = \langle Un\rangle_0/(\langle Un\rangle_0 + \langle p^2\rangle_0/2m)$. Finally we have defined the aspect ratio of the trap $\lambda = \omega_\parallel/\omega_\perp$. To predict the evolution of the cloud, we only need to determine 2 parameters: χ and $\mathcal{T}_0$. For a classical gas, we have [130]:

$$
1/\mathcal{T}_0 = \frac{2}{5} n_{\text{class}}(\mathbf{0})\sigma_{\text{el}} v_{\text{th}}, \tag{D.4}
$$

with $n_{\text{class}}(\mathbf{0})$ is the peak density corresponding to a Gaussian density distribution, $v_{th} = \sqrt{8k_B T/(m\pi)}$ and $\sigma_{el} = 8\pi a^2$.

For our purposes, the cloud must be described by a Bose-Einstein distribution. We calculate numerically χ using Eq. C.9, Appendix C. The parameter $\mathcal{T}_0$ is inferred from Eq. D.4 making 2 corrections: first, according to Ref. [131] $\mathcal{T}_0$ should be multiplied with 1.66 to take into account the fact that the density is not described by a Gaussian but a Bose function at the critical point. Second, the expression for n_{class} should correspond to a Bose function, which includes interactions (see Eq. B.4, Appendix B).

In practice, to correct the temperatures we solve numerically Eqs. D.3. We impose an initial temperature, and we obtain the size of the cloud (*via* $b(t)$). The temperature obtained is the correct hydrodynamic temperature T_{true} corresponding to a give size of the cloud. This is repeated for many temperatures, and we obtain the temperature as a function of the size of the cloud. These results are independent of our Time-Of-Flight signals or fit functions, they are just solutions to the Eqs. D.3. We then consider the temperatures T_{ball} as a function of width obtained from fits of our Time-Of-Flight signals assuming ballistic expansion. By comparing T_{true} with T_{ball} for the same values of the size of the cloud, we can thereby obtain a correction factor, which we can use to correct our temperatures

D.2 Scattering length dependent corrections

Before giving the values of the correction, note that as mentioned the solution to the differential equations depends on the scattering length a through σ_{el} ($\propto a^2$) and χ, which is proportional to a/λ_T. To make our corrections to the temperature, we have to give an initial estimate of a. To obtain this estimate, make an approximate analysis of the data from chapter 5, without taking into account the hydrodynamic expansion. This initial analysis confines the scattering length in the interval between 10 and 14 nm. Knowing that the hydrodynamic correction tends to lower the "ideal gas" temperatures and consequently the obtained scattering length (see for explanation chapter 5), we use $a = 12$ nm for the corrections applied the data presented in chapter 5. This value for the scattering length is also the best theoretical estimate available, see chapter 1.

Figure D.1 shows the "true" temperature T_{true} (calculated by including hydrodynamic corrections), as a function of the temperature we get, when we assume a purely ballistic expansion T_{ball} (gray curve). As we deduce the temperature from our TOF signal assuming ballistic expansion, we must multiply the obtained temperature with a factor $T_{\text{true}}/T_{\text{ball}}$ to obtain the correct temperature.

For comparison, we have shown not only the correction obtained for $a = 12$ nm, but also the correction corresponding to $a = 10$ and $a = 14$ nm (gray curves as well), and as a guide line for the eye, we have also added the non-interacting case, $T_{\text{true}} = T_{\text{ball}}$ (black curve). Even though the correction is rather large (0.2 μK) for the most dense sample, it does not vary much when a is varied in the interval between 10 and 14 nm, as seen in Fig. D.1. The inset shows a zoom of the graph, corresponding our highest observed temperatures: the highest temperatures corresponding to reliable points (χ^2 less than 2 for the TOF signal, see chapter 5) is around 2.7 μK. This corresponds to the most dense sample, and thus to the largest correction ($\sim 10\,\%$). Also the *difference* in the correction for different scattering lengths is greatest for these points. This will therefore give us an upper limit for the uncertainty in the correction, for a wrongly chosen value of the scattering length: the difference between choosing $a \sim 12$ nm and $a \sim 11$ nm (our final value for a) changes max the temperature about 0.02 μK. Therefore, the resulting error on a arising from the fact that we must "know a in advance" to do our corrections, is much smaller than the assumed error-bars due to other effects.

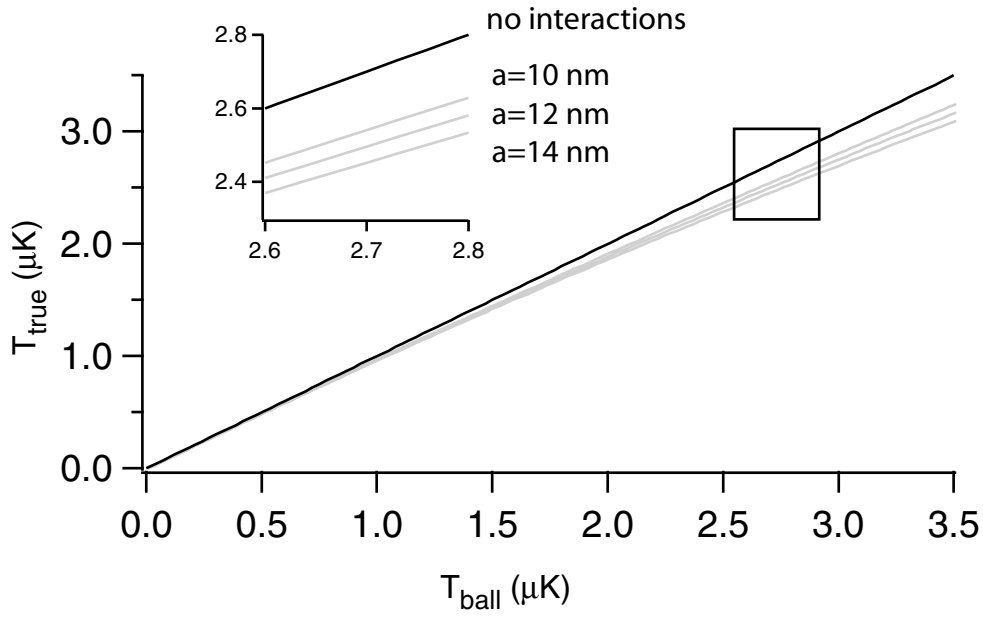

Figure D.1: *The true temperature (T_{true}) as a function of the temperature deduced from TOF signals assuming an ideal gas and ballistic expansion. To guide the eye, the non-interacting case has been shown $T_{\mathrm{true}} = T_{\mathrm{ball}}$ (black line). The inset is a zoom of the part corresponding to our highest measured temperatures.*

APPENDIX E

The noise in the Time-Of-Flight signal

For the data analysis in chapter 5, we need to determine if a cloud is exactly at Bose-Einstein condensation threshold. Our first criterion is based on the ionization rate: the break in the slope indicates the transition point. The second criterion is based on the quality of the fit of the Time-Of-Flight signal: we use a fit function, which is only valid for a cloud at BEC threshold, and the quality of the fit therefore tells how close the cloud is to the threshold point. To quantify this second criterion, we introduced in chapter 5 a χ^2 value for describing the fit. However, the χ^2 value will depend on the uncertainty attributed to the TOF signals. The subject of this Appendix is to describe how this uncertainty is estimated.

We will in the following use the reduced χ^2, which is defined by[1]:

$$\chi^2 = \frac{1}{m} \sum_i (d_i - f(t_i))^2 / \sigma_i^2.$$

Here, m is the number of degrees of freedom (the number of points in the fit plus the number of variables), d_i is the experimental data point in the TOF signal at a time t_i, $f(t_i)$ is the value of the fit for that time, and σ is the weight given to the particular data point. The summation is over all the points in the fit.

The weight given to a particular data point is inversely proportional to the uncertainty of the given point, which is related to the noise of the signal. This noise depends on the amplitude of the signal. To evaluate the χ^2 value, we therefore need an estimate of the behavior of the noise as a function of amplitude of the signal, as we will now deduce.

The easiest way to do this would be to record a constant signal during a certain time, and deduce the noise as the standard deviation of the signal from its average value. By repeating this procedure for many different amplitudes of the signal, the noise as a function of amplitude could be established. Now the problem is that we can not, with the atoms, keep a stable, constant signal during the time necessary for estimating the noise. Therefore we have chosen to use instead TOF signals, having intrinsically

[1] Note that for simplicity, we will denote it by χ^2, even though it is often denoted by χ^2_ν.

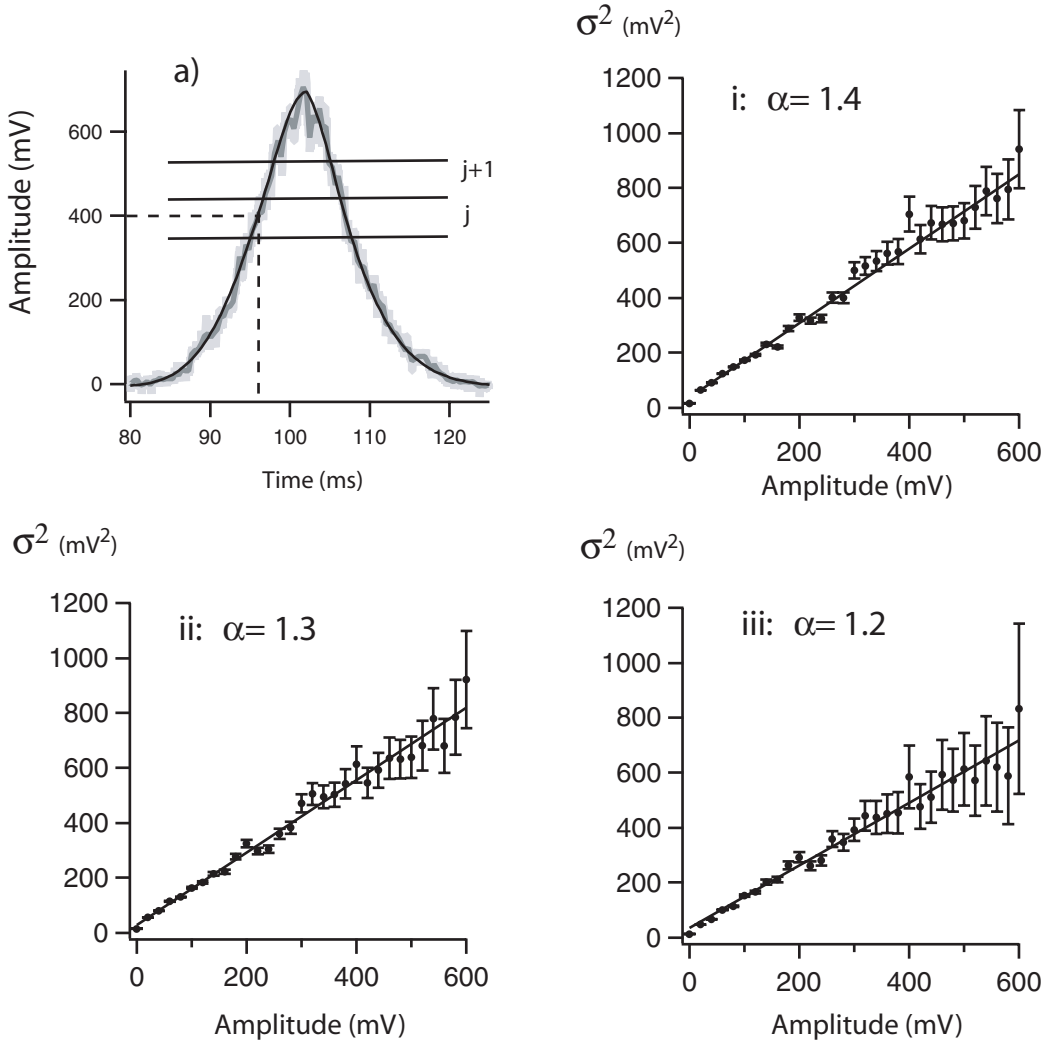

Figure E.1: *In a) we show a typical TOF signal and its fit, used for estimating the noise as a function of amplitude. We divide the TOF signal into intervals of 20 mV. Inside each interval, we obtain an average value for the noise (standard deviation of fit relative to TOF signal), corresponding to the central value of the amplitude. We then plot the noise squared as a function of the amplitude of the TOF signal. As the noise depends on the quality of the fits of the TOF signals using for the estimation, we have made three different plots (i,ii and iii) corresponding to increasing quality of the fits (see text).*

varying amplitudes, and use the deviation from the fits as a way to obtain the noise as a function of amplitude.

In practice, we do the following: we take a TOF signal and its corresponding fit, see Fig. E.1, a. The "raw" TOF signal (light gray in the figure) has been averaged (dark gray curve) within intervals corresponding to the bandwidth of the signal amplifier, which is 400 μs. We divide the TOF signal into horizontal slices (indexed by j) as shown in the figure, each corresponding to a certain central amplitude, as illustrated by the dashed line in the figure. In practice we choose 20 mV slices (for visibility the intervals in the figure are much larger than 20 mV), such that we estimate the noise for amplitudes corresponding to 0,10,30... mV. We then define the noise for the j-th amplitude interval as the mean value for all the data points inside this interval:

$$\sigma_j^2 = \frac{1}{N}\sum_{i=1}^{N}(d_i - f_{(t_i)})^2, \tag{E.1}$$

where each interval has N data points (indexed by i). The initial fit f has been obtained by fitting the data assuming an equal weight for all the data points.

To increase the precision, we do not only consider one TOF signal, but a set of P different TOF signals. This means that the noise estimation for each value of the amplitude is the mean value of P TOF signals. Indexing the TOF signals by k, the mean value is then

$$< \sigma_j^2 >= \frac{1}{P}\sum_{k=1}^{P}\sigma_{kj}^2.$$

We use the series of TOF signals obtained at T_c presented in chapter 5. The estimate of the noise will depend on the quality of the initial fit used in Eq. E.1. To quantify this we define three sets of TOF signals:

- i) a set consisting of all our TOF signals (400 TOF signals),
- ii) a set corresponding to the 200 best fits according to an initial χ^2 value,
- iii) a set corresponding to the 150 best fits[2].

We then plot, for the three cases, the corresponding σ^2, and we see that in each case, the data are well described by a straight line, as shown in Fig. E.1. The noise on these points ("the noise on the noise") is evaluated as the standard deviation defined by $\frac{1}{P}\sqrt{< \sigma_j^2 > - < \sigma_j >^2}$.

As expected, we see that the noise decreases when we choose a set of TOF signals with a lower χ^2 value, because the noise is indeed defined relative to the deviation of the TOF fit function. The slopes of the curves

[2]These initial χ^2 values are calculated giving equal weight to all points.

corresponding to all TOF signals, the 200 best fits and the 150 best fits are 1.4, 1.3 and 1.2, respectively, with an offset varying between 4 and 10.

We assume that that best estimation of the noise corresponds to the one using the best 150 fits. If we exclude more points, the estimation will be based on too few points. This means that the estimation of the noise we will use is then given by

$$\sigma^2(\mathrm{mV}^2) = 4\,\mathrm{mV}^2 + 1.16\,\mathrm{mV} \times A(\mathrm{mV}), \tag{E.2}$$

where A is the amplitude of the TOF signal. This will be the expression for the noise used when we fit the data presented in chapter 5. For each TOF we then obtain a χ^2 value. These values range from 0.6 to 3. As the absolute value of the χ^2 depends on which set of TOF signals we used to obtain the noise, the absolute value of χ^2 is somewhat arbitrary. For our discussion in chapter 5, we have therefore chosen to let the best fit have $\chi^2 = 1$ per definition, and normalize the remaining χ^2 values accordingly.

APPENDIX F

Fitting the Time-Of-Flight signals: examples

In the measurement of the ionization rate at Bose-Einstein condensation threshold, chapter 5, the analysis strongly depended on our ability to fit Time-Of-Flight signals. Not only to extract the temperature of the cloud, but also to determine if a given TOF signal represent a cloud which is really at threshold.

In chapter 5 we showed some examples of those fits, but only for some particular temperatures and χ^2 values. Moreover, as mentioned in Appendix E, the absolute value of χ^2 does not have a well-defined signification. Therefore, in order to give the reader an intuition for the relation between the quality of the fit and the χ^2 value, several representative examples of fits and their χ^2 values are shown in this Appendix.

We classify the fits into four groups according to:

- Low χ^2 and low temperature
- Low χ^2 and high temperature
- High χ^2 and low temperature
- High χ^2 and high temperature

For each group, we show six different TOF signals. We have excluded the 23 of June (see chapter 5) from these four groups, because this day shows some peculiar tendencies. Instead, we have added in the end of the appendix six fits, all coming from the 23 of June.

It is interesting to investigate the distribution of χ^2 values as a function of temperature. This is shown in Fig. F.1. The crosses corresponds to all the data, while the gray points corresponds to the 23 of June. In our analysis, we have decided to exclude all fits having a χ^2 above two. From Fig. F.1 we can see the temperature of the clouds excluded. As the high χ^2 valued fits correspond in general to higher temperatures than for the low χ^2 fits, we exclude essentially high temperature - and therefore high density clouds. At the moment we do not have a good explanation for this.

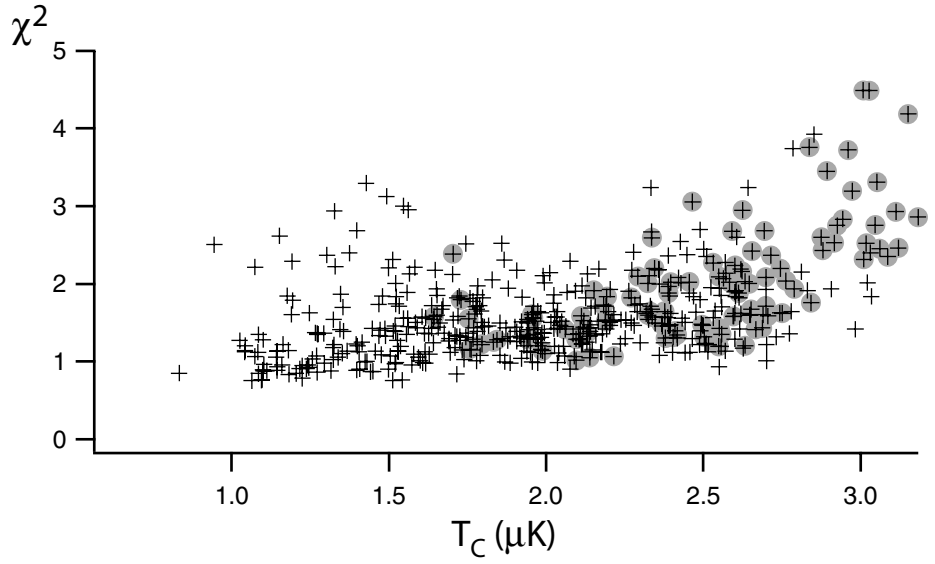

Figure F.1: χ^2 *as a function of temperature. The crosses corresponds to all data, while the gray points is the 23 of June.*

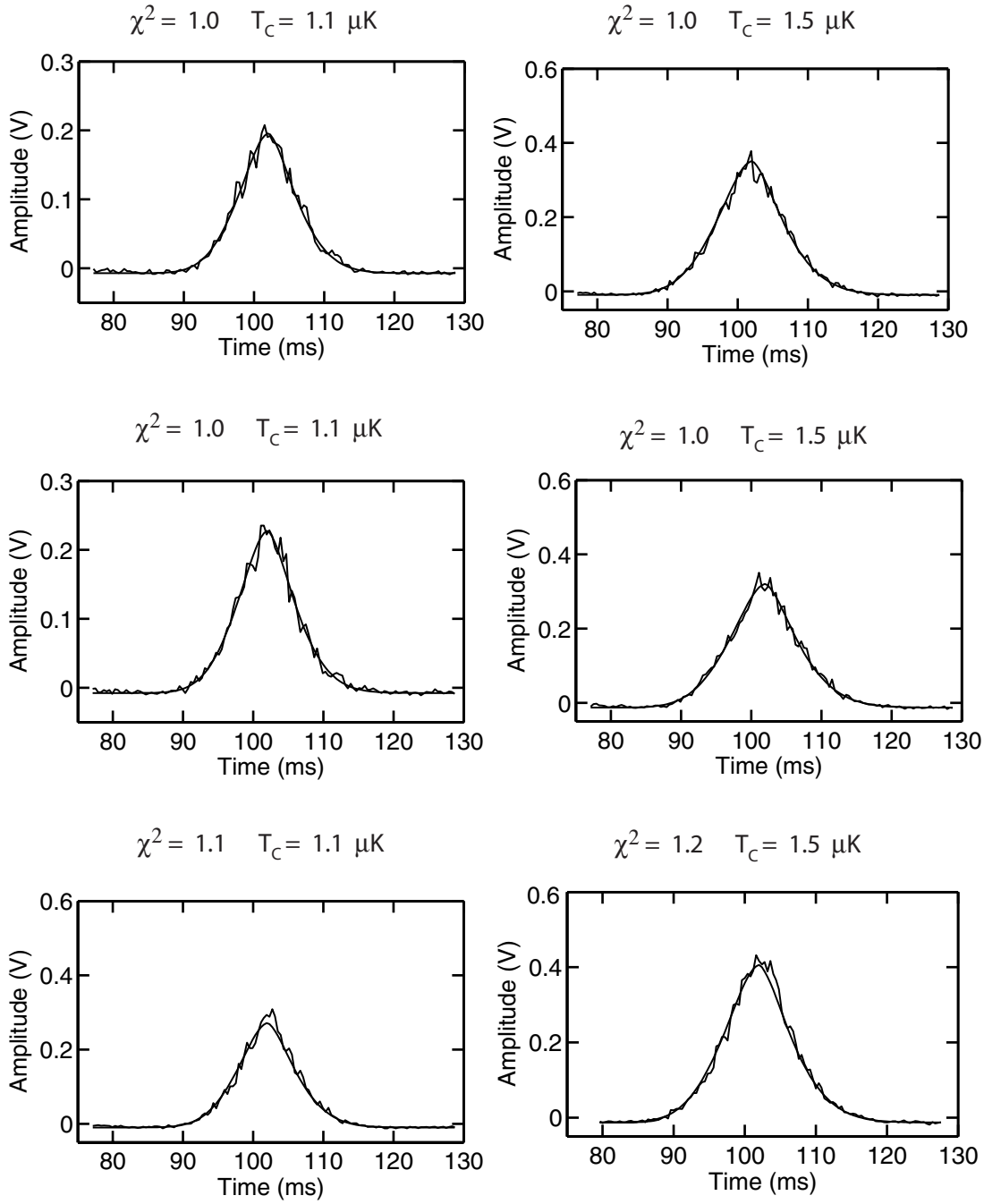

Figure F.2: *Time-Of-Flight signals and their fits corresponding to low χ^2 values and low temperatures. The graphs are ordered after a rising χ^2 value.*

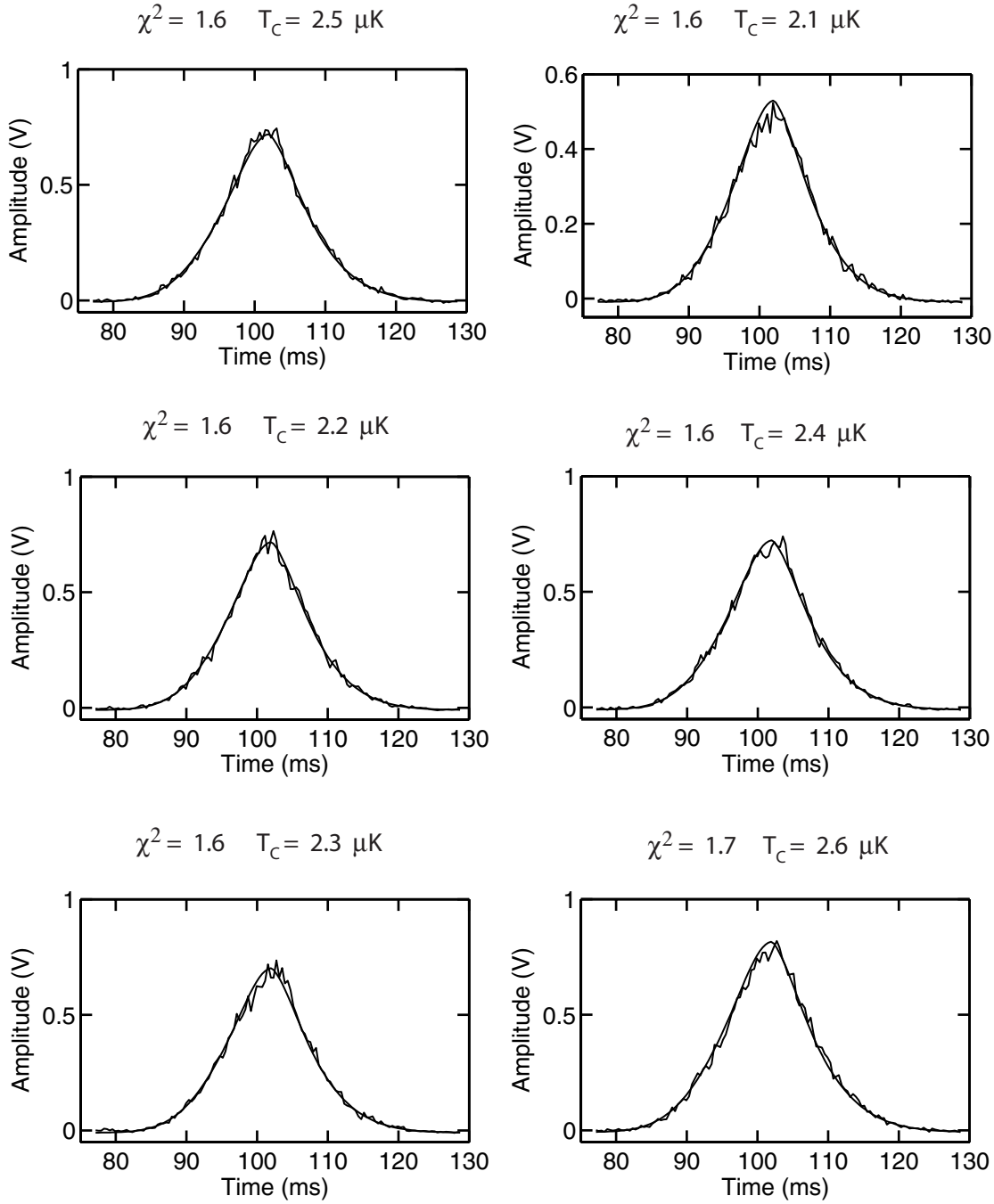

Figure F.3: *Low χ^2 values and high temperatures. The TOF signals are ordered after a rising χ^2 value.*

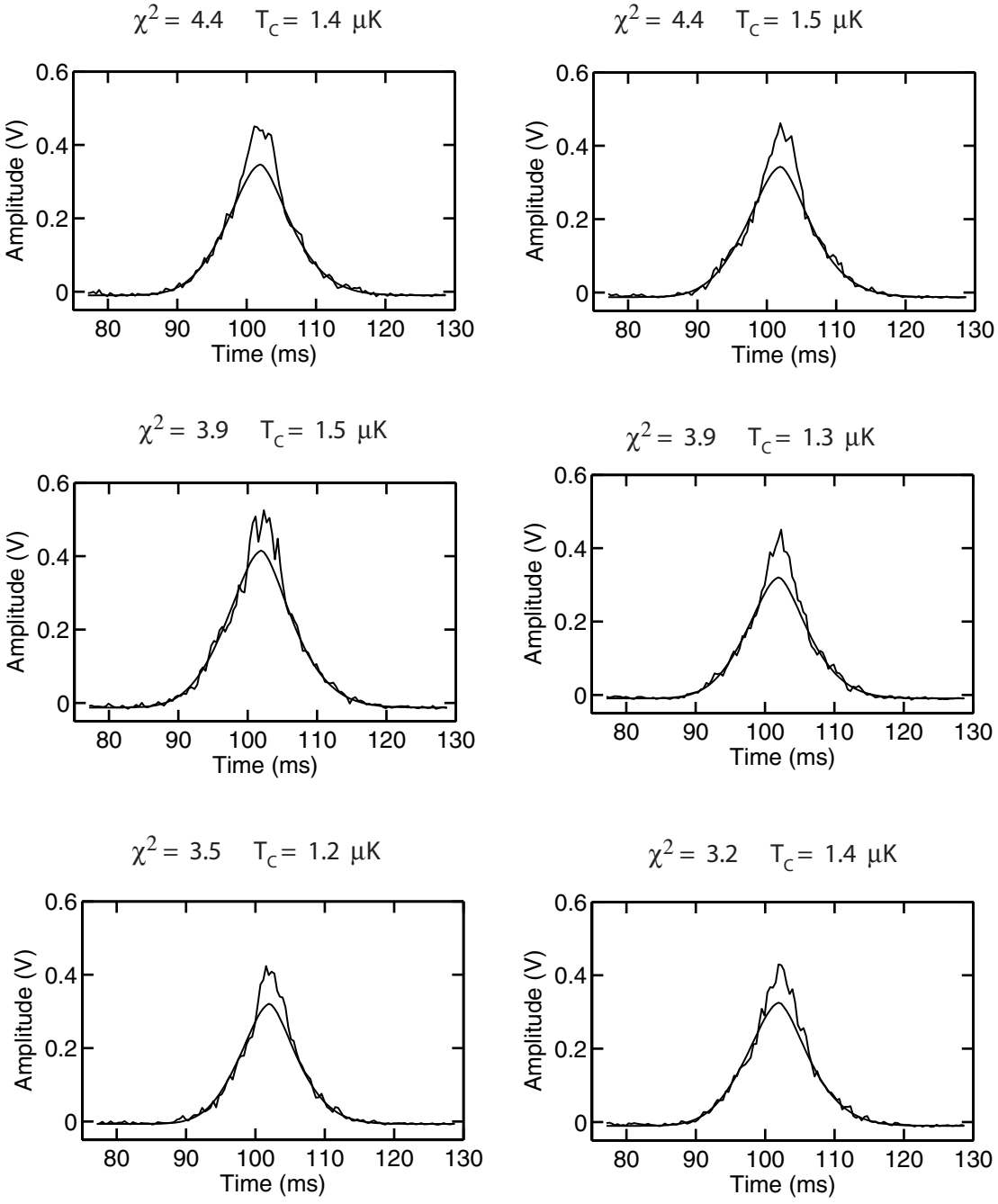

Figure F.4: *High χ^2 values and low temperatures. The TOF signals are ordered after a decreasing χ^2 value.*

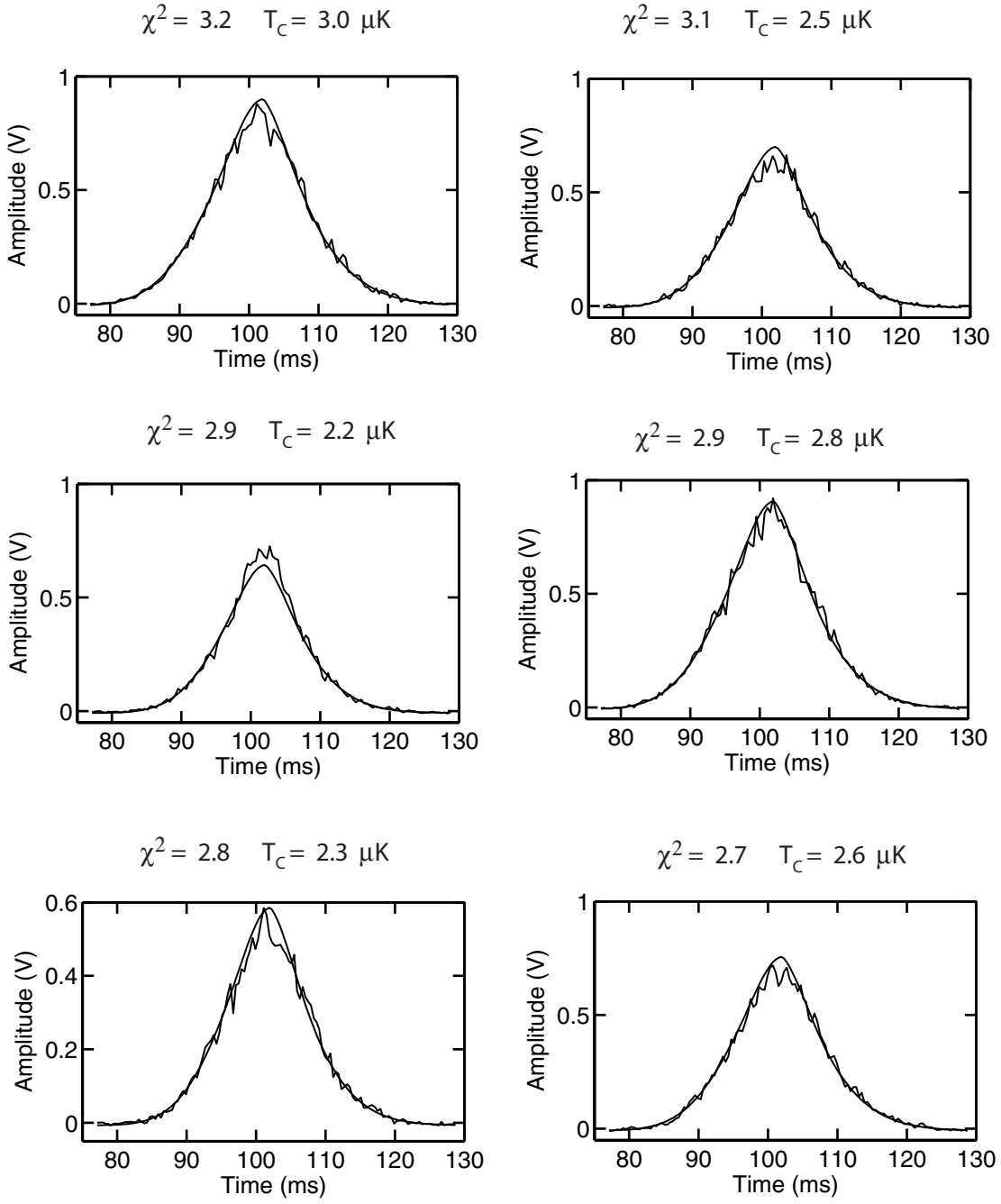

Figure F.5: *High χ^2 values and high temperatures. The TOF signals are ordered after decreasing χ^2 value.*

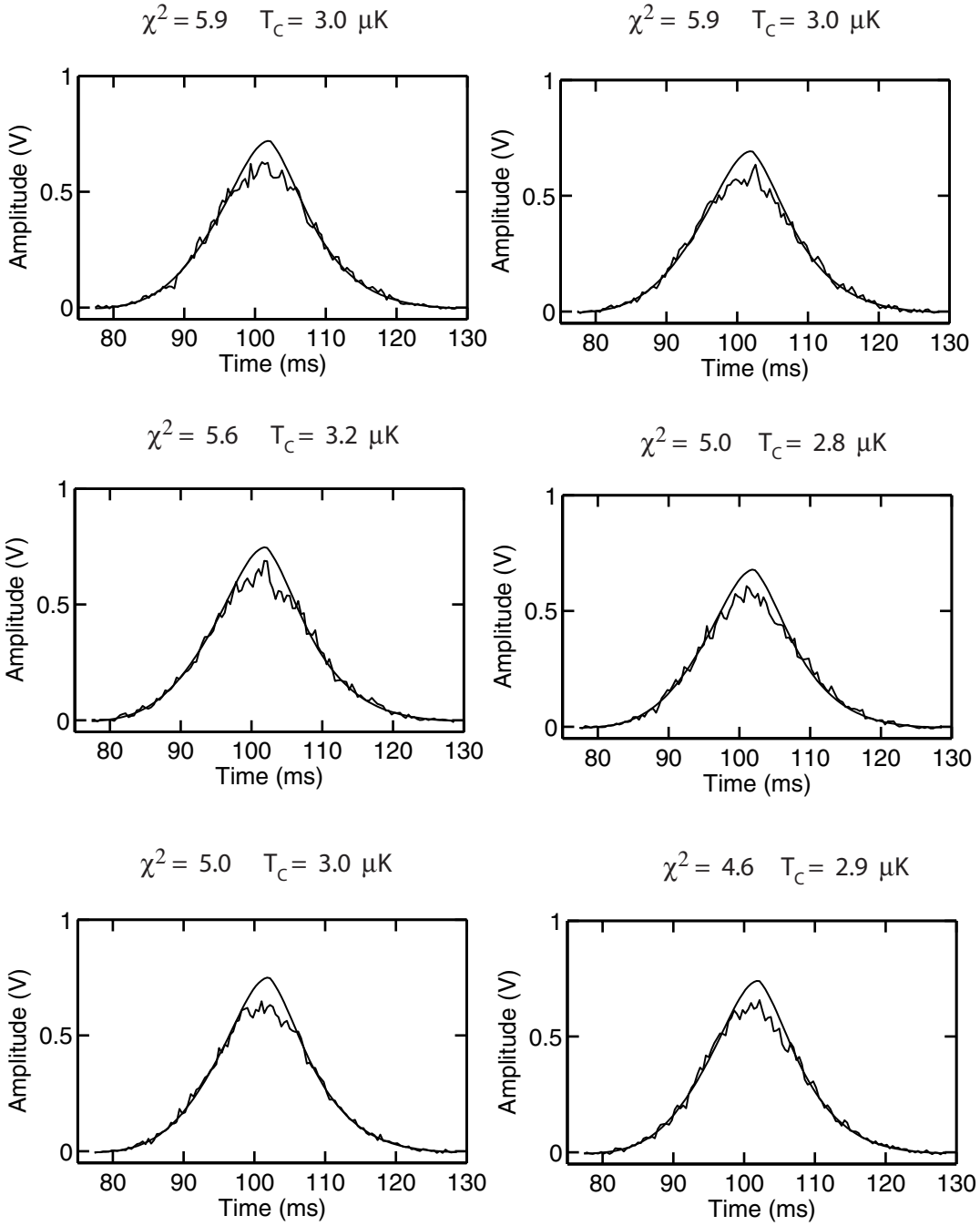

Figure F.6: *All the data are from the 23 of June. High χ^2 values and high temperatures. The TOF signals are ordered after decreasing χ^2.*

APPENDIX G

Articles

Ionization rates in a Bose-Einstein condensate of metastable helium

O. Sirjean, S. Seidelin, J. Viana Gomes, D. Boiron, C. I. Westbrook, A. Aspect and G. V. Shlyapikov

Physical Review Letters **89** 220406 (2002)

Using ion production to monitor the birth and death of a metastable helium Bose-Einstein condensate

S. Seidelin, O. Sirjean, J. Viana Gomes, D. Boiron, C. I. Westbrook and A. Aspect

Journal of Optics B **5** 112 (2003)

Getting the elastic scattering length by observing inelastic collisions in ultracold metastable helium atoms

S. Seidelin, J. Viana Gomes, R. Hoppeler, O. Sirjean, D. Boiron, A. Aspect and C. I. Westbrook

Physical Review Letters **93** 090409 (2004)

Ionization Rates in a Bose-Einstein Condensate of Metastable Helium

O. Sirjean, S. Seidelin, J. Viana Gomes,* D. Boiron, C. I. Westbrook, and A. Aspect
Laboratoire Charles Fabry de l'Institut d'Optique, UMR 8501 du CNRS, F-91403 Orsay Cedex, France

G. V. Shlyapnikov
FOM Institute for Atomic and Molecular Physics, Kruislaan 407, 1098 SJ Amsterdam, The Netherlands and Russian Research Center Kurchatov Institute, Kurchatov Square, 123182 Moscow, Russia
(Received 5 August 2002; published 12 November 2002)

We have studied ionizing collisions in a BEC of metastable He. Measurements of the ion production rate combined with measurements of the density and number of atoms for the same sample allow us to estimate both the two- and three-body contributions to this rate. A comparison with the decay of the atom number indicates that ionizing collisions are largely or wholly responsible for the loss. Quantum depletion makes a substantial correction to the three-body rate constant.

DOI: 10.1103/PhysRevLett.89.220406 PACS numbers: 34.50.–s, 05.30.–d, 67.65.+z, 82.20.Pm

The observation of Bose-Einstein condensation (BEC) of metastable helium (He in the 2^3S_1 state, denoted He*) [1,2] constituted a pleasant surprise for experimentalists although the possibility had been predicted theoretically [3]. Success hinged, among other things, on a strong suppression of Penning ionization in the spin-polarized, magnetically trapped gas. Too high a rate of ionization would have prevented the accumulation of sufficient density to achieve evaporative cooling. The ionization rate is not completely suppressed however, and when the atomic density gets high enough, a magnetically trapped sample of He* does produce a detectable flux of ions. As shown in [1], this signal can even be used as a signature of BEC. The observation of ions from the condensate opens the possibility of monitoring in real time the growth kinetics of a condensate [4]. This is an exciting prospect, but to quantitatively interpret the ion rate, one needs the contributions of two- and three-body collisions.

In this paper we use the unique features of metastable atoms to detect, in a single realization, the ionization rate, the density, and the atom number. This allows us to extract two- and three-body rate constants without relying on fits to nonexponential decay of the atom number, which require good experimental reproducibility [5–7] and are difficult to interpret quantitatively [5]. After estimating the ionization rate constants, a comparison with the decay of the atom number reveals no evidence for collisional avalanche processes. Thus, by contrast with ^{87}Rb [8], He* seems to be a good candidate for studying the "hydrodynamic" regime [9], as well as the effects of quantum depletion, i.e., a departure from the Gross-Pitaevskii wave function in the Bogoliubov theory, due to atomic interactions [10]. Indeed in our analysis of the three-body ionization process, quantum depletion makes a substantial correction [11].

Much theoretical [3,12] and experimental [1,2,13,14] work has already been devoted to estimating inelastic decay rates in He*. The dominant two-body decay mechanisms, called Penning ionization,

$$\mathrm{He}^* + \mathrm{He}^* \rightarrow \begin{cases} \mathrm{He}^+ + \mathrm{He}(1S) + e^- \\ \mathrm{He}_2^+ + e^- \end{cases} \quad (1)$$

are known to be suppressed by at least 3 orders of magnitude in a spin-polarized sample, but the total rate constant has not yet been measured. The three-body reaction,

$$\begin{aligned} \mathrm{He}^* + \mathrm{He}^* + \mathrm{He}^* &\rightarrow \mathrm{He}_2^* + \mathrm{He}^*(\sim 1\ \mathrm{mK}) \\ &\hookrightarrow \mathrm{He}^+ + \mathrm{He}(1S) + e^- \end{aligned} \quad (2)$$

proceeds via three-body recombination followed by autoionization of the excited molecule. Both reactions yield one positive ion which is easily detected. We define collision rate constants according to the density loss in a thermal cloud: $\frac{dn}{dt} = -\frac{n}{\tau} - \beta n^2 - L n^3$ with n the local density, τ the (background gas limited) lifetime of the sample, and β and L the two-body and three-body ionization rate constants defined for a thermal cloud [15]. The theoretical estimates of the rate constants at 1 μK are $\beta \sim 2 \times 10^{-14}\ \mathrm{cm^3\,s^{-1}}$ [3,12] and $L \sim 10^{-26}\ \mathrm{cm^6\,s^{-1}}$ [16], and the experimental upper limits were [1,2] $\beta \leq 8.4 \times 10^{-14}\ \mathrm{cm^3\,s^{-1}}$ and $L \leq 1.7 \times 10^{-26}\ \mathrm{cm^6\,s^{-1}}$.

For a pure BEC, in the Thomas-Fermi regime with a number of atoms N_0, and a peak density n_0, one can calculate the expected ionization rate per trapped atom:

$$\Gamma = \frac{\text{ion rate}}{N_0} = \frac{1}{\tau'} + \frac{2}{7}\kappa_2 \beta n_0 + \frac{8}{63}\kappa_3 L n_0^2. \quad (3)$$

The numerical factors come from the integration over the parabolic spatial profile and the fact that although two or three atoms are lost in each type of collision, only one ion is produced. The effective lifetime $\tau' \geq \tau$ is due to *ionizing* collisions with the background gas. The factors κ_i take into account the fact that the two- and three-particle local correlation functions are smaller than those of a

thermal cloud. For a dilute BEC $\kappa_2 = 1/2!$ and $\kappa_3 = 1/3!$ [7,11]. Because the He* scattering length (a) is so large, quantum depletion ($\sim \sqrt{n_0 a^3}$) leads to significant corrections [11] to the κ's as we discuss below.

Much of our setup has been described previously [1,17,18]. Briefly, we trap up to 2×10^8 atoms at 1 mK in a Ioffe-Pritchard trap with a lifetime (τ) of 90 s. We use a "cloverleaf" configuration [19] with a bias field $B_0 =$ 150 mG. The axial and radial oscillation frequencies in the harmonic trapping potential are $\nu_\parallel = 47 \pm 3$ Hz and $\nu_\perp = 1800 \pm 50$ Hz, respectively [$\overline{\omega}/2\pi = (\nu_\parallel \nu_\perp^2)^{1/3} =$ 534 Hz]. A crucial feature of our setup is the detection scheme, based on a two stage, single anode microchannel plate detector (MCP) placed below the trapping region. Two grids above the MCP allow us either to repel positive ions and detect only the He* atoms, or to attract and detect positive ions produced in the trapped cloud.

To detect the ion flux, the MCP is used in counting mode: the anode pulses from each ion are amplified, discriminated with a 600 ns dead time and processed by a counter which records the time delay between successive events. Typical count rates around BEC transition are between 10^2 and 10^5 s^{-1}. We have checked that the correlation function of the count rate is flat, indicating that there is no double counting nor any significant time correlation in the ion production. The dark count rate is of order 1 s^{-1}. By changing the sign of the grid voltage, we have checked that while counting ions, the neutral He* detection rate is negligible compared to the ion rate (less than 5%) even when the radio frequency (rf) shield is on. The intrinsic ion detection efficiency of the MCP for 2 keV He^+ ions is close to the open area ratio (60%) [20]. To estimate the total ion detection efficiency, we then multiply by the geometric transmission of the two grids $(0.84)^2$. Based on Refs. [20,21], we assume this (0.42) is an upper limit on our detection efficiency.

To find the values of N_0 and n_0 corresponding to the measured ion rate, we use the MCP to observe the time-of-flight (TOF) signal of the He* atoms released from the rapidly switched off trap. The instantaneous count rate can be as high as 10^6 s^{-1}, and the MCP saturates when used in counting mode. To avoid this problem, we lower the MCP gain, and record the TOF signal in analog mode with a time constant of 400 μs. Several tests were performed to verify the linearity of the detector.

In a typical run, evaporative cooling takes place for 40 s, down to an rf-knife frequency about 50 kHz above the minimum of the trapping potential. Near the end of the ramp, the ion rate increases sharply, signaling the appearance of a BEC (Fig. 4 in [1]). After reaching the final value, the rf knife is held on at that frequency. This constitutes an rf shield which eliminates hot atoms and maintains a quasipure BEC for up to 15 s (see Fig. 3). By quasipure we mean that we see no thermal wings in signals such as shown in the inset of Fig. 1. From tests of our fitting procedure, we estimate that the smallest thermal fraction we can distinguish is about 20%, with a temperature on the order of the chemical potential. Runs with visible thermal wings were discarded.

To acquire the TOF signals corresponding to a given ion rate, we turn off the rf shield, wait 50 ms, and then turn off the magnetic trap and switch the MCP to analog mode. To be sure that the rf has no influence on the ion rate, we use only the number of ions observed during the 50 ms delay to get the rate. We fit the TOF signals to an inverted parabola squared as expected for a pure BEC in the Thomas-Fermi regime and for a TOF width ($\sim$ 5 ms) narrow compared to the mean arrival time (100 ms) [1]. Under these assumptions, the chemical potential μ depends only on the TOF width, the atomic mass, and the acceleration of gravity [22], and thus can be measured quite accurately. Figure 1 shows that μ varies as expected as $N_d^{2/5}$ with N_d the number of detected atoms in the quasipure BEC. A fit on a log-log plot gives a slope of 0.39. Residuals from the linear fit do not show any systematic variation which is a good indication of the detection linearity and of the proportionality between N_d and N_0.

To determine the collision rate constants β and L, we need an absolute calibration of the number of atoms and the density. As discussed in Ref. [1], all the atoms are not detected, and the direct calibration has a 50% uncertainty which is responsible for the large uncertainty in the scattering length a. In fact the measurement of the chemical potential gives an accurate value for the product $n_0 a = \mu m/4\pi\hbar^2$, and with the value of $\overline{\omega}$ gives the product $N_0 a = (1/15)(\hbar/m\overline{\omega})^{1/2}(2\mu/\hbar\overline{\omega})^{5/2}$ as well. Therefore, in the hopes that the He* scattering length will be measured more accurately in the future, we shall express N_0 and n_0 in terms of a. In this paper, unless stated otherwise, we suppose that $a = 20$ nm, and in our conclusions we shall discuss how our results depend on a.

Figure 2 shows the ion rate per atom Γ versus the peak density. The densest sample corresponds to $N_0 = 2 \times 10^5$

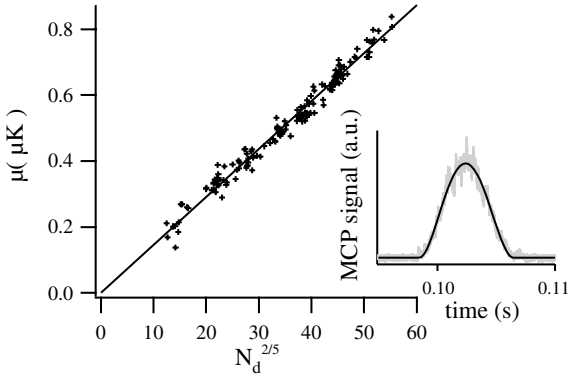

FIG. 1. Chemical potential versus number of detected atoms to the power $\frac{2}{5}$ and its linear fit. Data are for quasipure BEC. The inset shows a typical TOF signal and its inverted parabola squared fit.

atoms and $n_0 = 2.5 \times 10^{13}$ cm^{-3}. The corresponding Thomas-Fermi radii are $r_\perp \simeq 5$ μm and $r_\parallel \simeq 200$ μm. The vertical intercept in Fig. 2 corresponds to ionizing collisions with the background gas ($1/\tau'$). We have independently estimated this rate using trapped thermal clouds at 1 mK and 5 μK and found $1/\tau' \lesssim 5 \times 10^{-3}$ s^{-1}. This value is negligible at the scale of the figure.

The curvature in Fig. 2 shows that three-body ionizing collisions are significant. Before fitting the data to get β and L, we must take into account several effects. First, for three-body collisions, quantum depletion is important. For $T = 0$, on the basis of Ref. [11], we obtain a multiplicative correction to the factor κ_3 of $(1 + \epsilon) = (1 + 23.2 \times \sqrt{n_0 a^3})$ [23]. At our highest density $\epsilon \simeq 0.35$. Two-body collisions are subject to an analogous correction but approximately 3 times smaller. The fits in Fig. 2 include the density dependence of $\kappa_{2,3}$, associated with quantum depletion. The $n_0^{3/2}$ dependence introduced for two-body collisions is far too small to explain the curvature in the data. The density dependence of $\kappa_{2,3}$ does not improve the quality of the fit, but it significantly reduces the value of the fitted value of L (by 30%).

In addition, the fact that the sample probably contains a small thermal component means that collisions between the condensed and the thermal parts must be taken into account [6,11]. Assuming a 10% thermal population ($\frac{\mu}{k_B T} \simeq 1.5$), we find $\kappa_3 = \frac{1}{6}(1 + \epsilon + \epsilon')$, with an additional correction $\epsilon' \simeq 0.11$ for the densest sample [24].

Taking into account all these corrections, and assuming an ion detection efficiency of 0.42, the fitted values of the collision rate constants [15] are $\beta_{20} = 2.9(\pm 2.0) \times 10^{-14}$ cm^3 sec^{-1} and $L_{20} = 1.2(\pm 0.7) \times 10^{-26}$ cm^6 sec^{-1}, where the subscripts refer to the assumed value of a. These values are in good agreement with the theoretical estimates. The error bars are estimated as follows. We fix either β or L and use the other as a fit parameter. We repeat this procedure for different values of the fixed parameter and take the range over which we can get a converging and physically reasonable fit (i.e., no negative rate constants) as the uncertainty in the fixed parameter. These error bars are highly correlated since if β is increased, L must be decreased and vice versa. The error bars do not include the uncertainty in the absolute ion detection efficiency (see below).

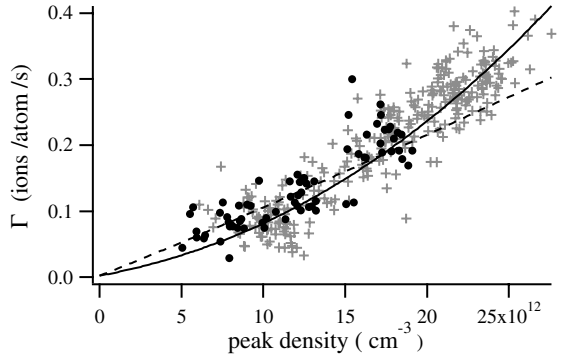

FIG. 2. Ion rate per trapped atom versus peak density for 350 different quasipure BEC's. Atom number and density are deduced from μ, $\overline{\omega}$, and a (here 20 nm). Data were taken for two different bias fields corresponding to $\nu_\perp = 1800$ Hz (crosses) and $\nu_\perp = 1200$ Hz (circles). The dashed line corresponds to the best fit involving only two-body collisions. The solid line is a fit to two- and three-body processes.

Until now we have assumed $a = 20$ nm, but current experiments give a range from 8 to 30 nm [1,2]. Using Eq. (3) and our parametrization of n_0 and N_0 in terms of a, one can see that, in the absence of quantum depletion, the values of β and L extracted from our analysis would be proportional to a^2 and a^3, respectively. Taking quantum depletion into account, no simple analytical dependence exists, but one can numerically evaluate β and L vs a and fit the results to expansions with leading terms in a^2 and a^3, respectively. The effect of quantum depletion is negligible for β [$\beta_a \approx \beta_{20}(\frac{a}{20})^2$]. For L, we find $L_a \approx L_{20}(\frac{a}{20})^3[1 - 0.21\frac{a-20}{20}]$ with a in nm.

To test the consistency of our measurements, we plot the decay of the atom number (Fig. 3). To acquire these data, we held the BEC in the trap in the presence of the rf shield for varying times. This study involves multiple BEC realizations, which typically exhibit large fluctuations in the initial atom number. We have been able to reduce this noise by using the ion signal to select only data corresponding to the same ion rate 500 ms after the end of the ramp. This time corresponds to $t = 0$ in the figure. We also plot the predicted decay curve (solid line) corresponding to ionization only. This curve results from a numerical integration of the atom loss due to ionization processes, calculated from the fitted values β_{20} and L_{20}. The fact that the error bars on β and L are correlated

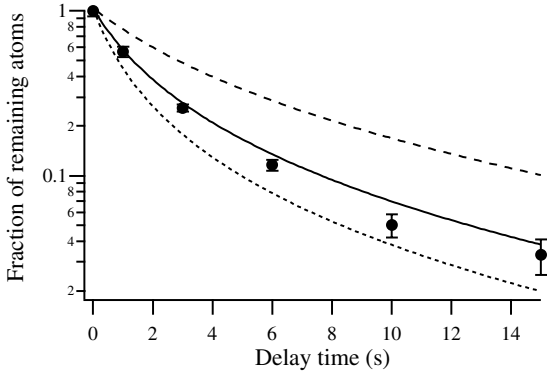

FIG. 3. Fraction of remaining atoms measured by TOF as a function of time. The rf shield is on and the cloud remains a quasipure condensate during the decay. The lines correspond to the predicted atom decay according to Eq. (3) with the fitted value of the two- and three-body rate constants for $a = 10$ nm (dashed line), $a = 20$ nm (solid line), and $a = 30$ nm (dotted line). The case of $a = 10$ nm is not necessarily excluded because other, nonionizing losses could be present.

leads to a small uncertainty on the solid curve that happens to be of the same order of magnitude as the typical error bars on the data. The observed decay agrees fairly well with the solid curve, and ionization apparently accounts for most of the loss. If the ion detection efficiency were actually lower than we assume, the predicted decay would be faster than the observed decay which is unphysical (assuming $a = 20$ nm). We conclude that our estimate of the ion detection efficiency is reasonable and does not lead to an additional uncertainty in β and L.

We also plot the curves obtained from the same analysis but with scattering lengths of 10 and 30 nm, assuming a detection efficiency of 0.42. The curve corresponding to $a = 30$ nm lies below the data points. Based on our analysis, this means that $a = 30$ nm is excluded. A scattering length of 25 nm is the largest one consistent with our data. In contrast, the decay predicted for an analysis with $a = 10$ nm is slower than the observed decay. This would mean that there are additional nonionizing losses (contributing up to half of the total loss), and/or that we have overestimated the ion detection efficiency by a factor as large as 2. In the latter case, β and L should be multiplied by the same factor. This results for $a = 10$ nm in a supplementary systematic uncertainty on β and L of a factor as large as 2.

In the event that our upper limit on the ion detection efficiency is too low, the rate constants β and L should be reduced by a factor as large as 2.4 ($= 0.42^{-1}$). In that case, our data would not exclude $a = 30$ nm and nonionizing losses could significantly contribute to the total loss.

Even though the peak densities of our BEC are small compared to those in alkalis, the elastic collision rate is high because of the large scattering length, and one must consider the possibility of collisional avalanches. For $a = 20$ nm our densest cloud has a mean free path of 7 μm and using the definition of [8] the collisional opacity is 0.8. With Rb atoms this would result in much increased loss due to avalanches [8]. Here we have to consider secondary collisions leading to both ion production and atom loss. However, for secondary ionization, mean free paths are at least 2 orders of magnitude larger than $r_{\|}$. Hence secondary ionization is unimportant. This conclusion is supported by our observation of no correlation in the time distribution of detected ions.

The good agreement between the data and the curve in Fig. 3 indicates that losses due to nonionizing collisional avalanches are not taking place either. This is in agreement with data on elastic collisions with He^+, He_2^+, and He($1S$), which have small cross sections [25]. Collisions with hot He* atoms from the reaction of Eq. (2) are more likely to play a role, but due to the higher velocity, the elastic cross section for these atoms is smaller. In Rb the situation is different because a d-wave resonance increases the total cross section [8].

The theoretical analysis shows that quantum depletion strongly affects the measured three-body rate constant. One way to experimentally demonstrate this effect would be to compare with similar measurements with thermal clouds. Absolute calibration of ion and atom detection efficiency should play no role in this comparison, if one could prove that they are the same for both situations.

We thank F. Gerbier for stimulating discussions. This work was supported by the European Union under Grants No. IST-1999-11055 and No. HPRN-CT-2000-00125, and by the DGA Grant No. 00.34.025.

*Permanent address: Departamento de Fisica, Universidade do Minho, Campus de Gualtar, 4710-057 Braga, Portugal.

[1] A. Robert *et al.*, Science **292**, 461 (2001).
[2] F. Pereira Dos Santos *et al.*, Phys. Rev. Lett. **86**, 3459 (2001); F. Pereira Dos Santos *et al.*, Eur. Phys. J. D **19**, 103 (2002).
[3] G.V. Shlyapnikov *et al.*, Phys. Rev. Lett. **73**, 3247 (1994); P.O. Fedichev *et al.*, Phys. Rev. A **53**, 1447 (1996).
[4] H.J. Miesner *et al.*, Science **270**, 1005 (1998); M. Köhl *et al.*, Phys. Rev. Lett. **88**, 080402 (2002).
[5] J.L. Roberts *et al.*, Phys. Rev. Lett. **85**, 728 (2000).
[6] J. Söding *et al.*, Appl. Phys. B **69**, 257 (1999).
[7] E.A. Burt *et al.*, Phys. Rev. Lett. **79**, 337 (1997).
[8] J. Schuster *et al.*, Phys. Rev. Lett. **87**, 170404 (2001).
[9] M. Leduc *et al.*, Acta Phys. Pol. B **33**, 2213 (2002).
[10] F. Dalfovo *et al.*, Rev. Mod. Phys. **71**, 463 (1999).
[11] Y. Kagan, B.V. Svistunov, and G.V. Shlyapnikov, JETP Lett. **42**, 209 (1985).
[12] V. Venturi *et al.*, Phys. Rev. A **60**, 4635 (1999); V. Venturi and I.B. Whittingham, Phys. Rev. A **61**, 060703(R) (2000).
[13] J.C. Hill *et al.*, Phys. Rev. A **5**, 189 (1972).
[14] N. Herschbach *et al.*, Phys. Rev. A **61**, 50 702 (2000).
[15] Collision rate constants are sometimes defined directly for a BEC ($\beta' = \beta/2$ and $L' = L/6$).
[16] P.O. Fedichev, M.W. Reynolds, and G.V. Shlyapnikov, Phys. Rev. Lett. **77**, 2921 (1996); P.F. Bedaque, E. Braaten, and H.W. Hammer, Phys. Rev. Lett. **85**, 908 (2000).
[17] A. Browaeys *et al.*, Phys. Rev. A **64**, 034703 (2001).
[18] S. Nowak *et al.*, Appl. Phys. B **70**, 455 (2000).
[19] M.O. Mewes *et al.*, Phys. Rev. Lett. **77**, 416 (1996).
[20] R.S. Gao *et al.*, Rev. Sci. Instrum. **55**, 1756 (1984).
[21] B. Deconihout *et al.*, Appl. Surf. Sci. **94/95**, 422 (1996).
[22] Y. Castin and R. Dum, Phys. Rev. Lett. **77**, 5315 (1996); Y. Kagan, E.L. Surkov, and G.V. Shlyapnikov, Phys. Rev. A **54**, R1753 (1996).
[23] The numerical factor $64/\sqrt{\pi}$ of [11] changes to 23.2 for a trapped bose gas.
[24] We have $\epsilon' = (\langle\langle 3n_0^2(n' + \alpha)\rangle\rangle + \langle 3n_0^2\langle n' + \alpha\rangle\rangle) \times \langle\langle n_0^3\rangle\rangle^{-1}$. The symbol $\langle\cdots\rangle$ denotes the integration over the condensate spatial region. The thermal part of the noncondensed density, n', and that of the anomalous average, α, are obtained in the local density approximation. This gives $\epsilon' = 7.7 \times \sqrt{n_0 a^3}$ for $(\mu/k_B T) = 1.5$.
[25] H.C.W. Beijerinck *et al.*, Phys. Rev. A **61**, 23 607 (2000).

INSTITUTE OF PHYSICS PUBLISHING JOURNAL OF OPTICS B: QUANTUM AND SEMICLASSICAL OPTICS

J. Opt. B: Quantum Semiclass. Opt. **5** (2003) S112–S118 PII: S1464-4266(03)55547-1

Using ion production to monitor the birth and death of a metastable helium Bose–Einstein condensate

S Seidelin[1], O Sirjean, J Viana Gomes[2], D Boiron, C I Westbrook and A Aspect

Laboratoire Charles Fabry de l'Institut d'Optique, UMR 8501 du CNRS, F-91403 Orsay Cedex, France

E-mail: signe.seidelin@iota.u-psud.fr

Received 29 October 2002
Published 2 April 2003
Online at stacks.iop.org/JOptB/5/S112

Abstract

We discuss observations of the ion flux from a cloud of trapped 2 $^3S_1$ metastable helium atoms. Both Bose–Einstein condensates (BEC) and thermal clouds were investigated. The ion flux is compared with time-of-flight observations of the expanded cloud. We show data concerning BEC formation and decay, as well as measurements of two- and three-body ionization rate constants. We also discuss possible improvements and extensions of our results.

Keywords: Cold atoms, Bose–Einstein condensate, metastable helium, condensate formation, Penning collisions

1. Introduction

Metastable helium (He^*) has recently joined the list of atomic species for which Bose–Einstein condensates (BEC) have been realized [1, 2]. Its major feature is the 20 eV internal energy of the metastable state. Although this metastability leads to additional possible loss channels, it has been shown that these are not a serious problem. Indeed, ionizing collisions are a benefit because their low rate is nevertheless easily detectable. Ion detection is thus a new, 'non-destructive' and real-time observation tool for studies of the phenomenon of BEC formation kinetics [3–7]. In this paper we will describe our progress toward rendering the ion signal quantitative.

Several loss mechanisms are specific to the metastable state. First, collisions with the background gas lead to Penning ionization of the background gas:

$$X + He^* \rightarrow X^+ + He + e^-.$$

The positive ion X^+ thus produced can be easily detected and if this is the dominant ion production mechanism, as it is for a dilute sample (for a density $n \lesssim 10^{10}\,\mathrm{cm}^{-3}$), the corresponding flux is proportional to the number of trapped He^* atoms. So for example we can easily measure the lifetime of a dilute, trapped sample. This linearity no longer holds when the density of the trapped cloud becomes high. Collisions between atoms in the cloud must be taken into account. The relevant ionization mechanisms involve both two-body processes:

$$He^* + He^* \rightarrow \begin{cases} He^+ + He(1S) + e^- \\ He_2^+ + e^- \end{cases} \quad (1)$$

and a three-body process:

$$\begin{aligned} He^* + He^* + He^* \quad &\rightarrow \quad He_2^* \quad +He^*(\sim 1\,\mathrm{mK}) \\ &\hookrightarrow \quad He^+ + He(1S) + e^-. \end{aligned} \quad (2)$$

When these processes are present, the ion flux is related to the spatial integral of n^2 and n^3. At BEC densities, the two- and three-body processes dominate the background gas ionization, and so detecting the ion flux in this case amounts to monitoring the atomic density.

In this paper, after a brief description of our experimental set-up, we present observations, via the ion flux, of the formation and the decay of a He* BEC. The observations are mainly qualitative, but we discuss some of the requirements for making them quantitative. We then discuss our measurements of the two- and three-body ionization rate constants both in a BEC [8] and in a thermal cloud. We discuss some of the systematic errors in these measurements and conclude with some ideas for avoiding these errors.

[1] Author to whom any correspondence should be addressed.
[2] Permanent address: Departamento de Fisica, Universidade do Minho, Campus de Gualtar, 4710-057 Braga, Portugal.

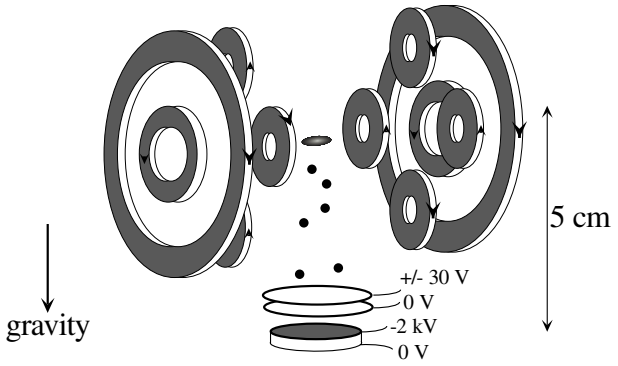

Figure 1. Experimental set-up. The cold atoms are trapped in a cloverleaf type magnetic trap. A special feature of our set-up is the MCP placed below the trapping region. Two grids above the MCP allow us either to repel positive ions and detect only the He* atoms suddenly released from the trap (TOF measurements), or to attract and detect the positive ions produced in the trapped cloud (ion rate measurements).

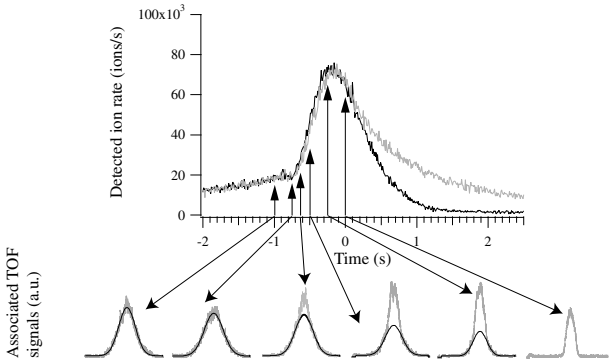

Figure 2. Single-shot measurements of the ion rate versus time and the corresponding TOF signals. Forced evaporative cooling takes place until $t = 0$ (only the last 2 s of the rf ramp are shown: from 1400 to 1000 kHz). The upper, lighter, ion curve corresponds to the case where we keep an rf shield on during the decay, while the lower, darker, decay curve is recorded without. The arrows indicate the time the trap was switched off to record the TOF. The dark curves superimposed on the TOF signals are Gaussian fits to the wings of the TOF.

2. Set-up and experimental procedure

Our set-up has been described previously [1, 8, 9]. Briefly, we trap up to 2×10^8 atoms at 1 mK in a Ioffe–Pritchard trap with a lifetime (τ) of 90 s. We use a 'cloverleaf' configuration (figure 1) [10] with a bias field $B_0 = 300$ mG. The axial and radial oscillation frequencies in the harmonic trapping potential are typically $\nu_\parallel = 47 \pm 3$ Hz and $\nu_\perp = 1200 \pm 50$ Hz respectively ($\overline{\omega}/2\pi = (\nu_\parallel \nu_\perp^2)^{1/3} = 408$ Hz). In a typical run, forced evaporative cooling takes place for 40 s and is divided into four linear ramps. The last ramp lasts for 5 s and the frequency decreases from 2000 kHz to a value between 1500 and 1000 kHz, depending on the condensed fraction wanted. A frequency of 1000 kHz (which is about 50 kHz above the minimum of the trapping potential) corresponds to the formation of a pure condensate.

A special feature of our set-up is the detection scheme, based on a two-stage, single-anode microchannel plate detector (MCP) placed 5 cm below the trapping region (figure 1). Two grids above the MCP allow us either to repel positive ions and detect only the He* atoms, or to attract and detect positive ions produced in the trapped cloud. To detect the ion flux, the MCP is used in counting mode [8]: the anode pulses from each ion are amplified, and processed by a counter which records the time delay between successive events. We can also use the MCP to record a time-of-flight (TOF) signal of the atoms released from the trap. Because the width of the TOF distribution is small (about 5 ms for a BEC) compared with the mean arrival time (100 ms), all of the atoms hit the detector with nearly the same final velocity of 1 m s^{-1}. The TOF spectra are then proportional to the spatial distribution along the vertical direction, integrated over the two horizontal directions. To record the TOF we use the MCP in analogue mode to avoid saturation due to the very high instantaneous flux [8].

3. Monitoring the evolution of a He* cloud

To monitor the evolution of an atomic cloud, one usually releases the cloud and measures the TOF signal. Such a technique is destructive, and one must repeat the cooling sequence for each measurement. The TOF signals are thus subject to fluctuations in the initial number of atoms. In our case, we have a supplementary signal: the ion rate. We can thus minimize these fluctuations, by selecting runs having identical ion rates from the time between the beginning of the last rf ramp until release.

Another type of observation is possible, however. We can use the evolution of the *value* of the ion rate, which is obtained in a single run, independent of any initial fluctuations. When the density is close to the density for BEC formation (i.e. $n \gtrsim 10^{12}$ cm^{-3}), two- and three-body collisions within the cloud dominate the ion production. Thus the ion rate is related to the density of the cloud via the two- and three-body rate constants. Under some conditions (see appendix A) a record of the ion rate followed by a TOF measurement at the end of the formation of the BEC allows one to monitor the evolution of all the parameters of the cloud. In such an observation, knowledge of the two- and three-body rate constants is essential. This is the aim of the experiments described in section 4.

3.1. Observation of condensate formation during the evaporation ramp

Before trying to do a quantitative experiment on BEC formation from of a non-equilibrium uncondensed cloud [3, 4], we can explore qualitatively what happens during our standard evaporation ramp. We show in figure 2 the evolution of the ion rate from 2 s before the end of the rf ramp to 2.5 s after it. In addition we show the TOF signals corresponding to various times before the end of the ramp, selected using their initial ion rate. Between times $t = -2$ and 0 s, the rf was ramped down linearly from 1.4 to 1 MHz. At $t = 0$ a pure condensate is formed. The comparison of the TOF and ion data first shows that the appearance of a narrow structure in the TOF spectrum corresponds, as closely as we can observe it, to an abrupt change in the slope of the ion signal. Thus, not only is the ion signal a reliable indicator of the presence of a BEC, but also a precise measure of the time of its appearance.

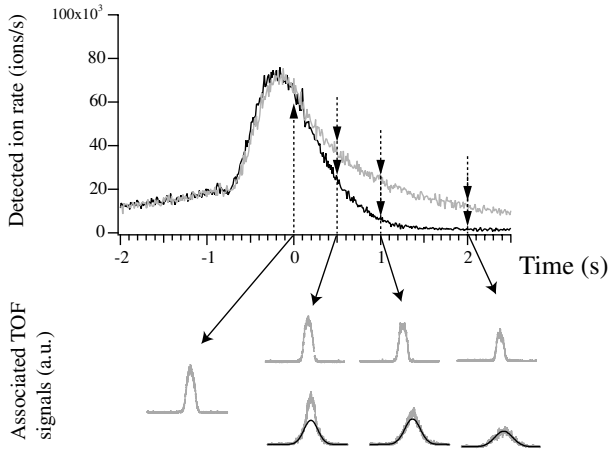

Figure 3. Same as in figure 2 except that we examine the decay of the ion signal after $t = 0$. The upper TOF curves correspond to the upper (lighter) ion decay curve (rf shield present). The lower TOF curves correspond to the lower (darker) ion curve (without rf shield). This shows that the rf shield is maintaining a quasi-pure BEC during the decay, and that in the absence of an rf shield the condensate rapidly heats up, causing the ion rate to drop even faster.

One's first reaction in looking at the ion rate signal is to assume that the higher the ion signal, the larger the BEC and the smaller the thermal cloud. Figure 2 shows, however, that this is not quite the case: the maximum in the ion signal arrives before the achievement of a pure BEC. In fact, computing the value of the ion signal is rather complex. First, as was discussed in [11, 12], as well as below, the indistinguishability of the atoms in the BEC renders the effective two- and three-body collision rate constants smaller than in the thermal cloud by factors of $1/2!$ and $1/3!$ respectively. Collisions between condensed and non-condensed atoms must also be taken into account [11] and the degree of overlap between the two clouds must be calculated. Thus it might be conceivable that the ion rate goes down when a BEC is formed. We show, however, in appendix A that for a fixed total number of atoms, the ion rate increases monotonically as a BEC becomes more and more pure. The observation in figure 2 is explained by the fact that, up until $t = 0$ in figure 2, the atoms are being evaporatively cooled as well as undergoing ionizing collisions and thus the total number of atoms must be decreasing. An explicit calculation including the atom loss is given in appendix A and agrees qualitatively with our observations.

3.2. Observing the decay of the condensate

Figure 3 shows a series of TOF spectra taken after the end of the rf ramp. Two situations are shown. In one case (upper, lighter ion curve) the rf knife was held on at the frequency corresponding to the end of the ramp. In the other case (lower, darker ion curve) the rf power was turned off completely at the end of the ramp. The data show that the condensate remains pure with the rf knife kept on. In the absence of the rf knife, the ion rate decays much faster and one sees that the sample rapidly acquires a thermal component. Since the total number of trapped atoms in the presence of a knife must be smaller than or equal to that in the absence of rf knife, we conclude that the rapid decline in ion rate is due to a loss of sample density and not of the total number of atoms. This conclusion is confirmed by a fit to the thermal wings, which reveals a heating as shown in figure 4.

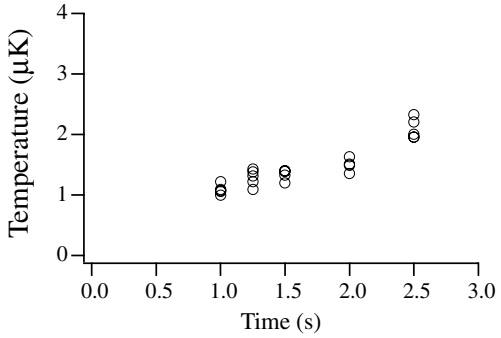

Figure 4. Heating of the condensate in the absence of an rf shield. The temperature increases from 1.1 to 2.2 μK in 1.5 s. The time $t = 0$ is the same as in figures 2 and 3. For each different time, four different TOFs have been acquired and fitted.

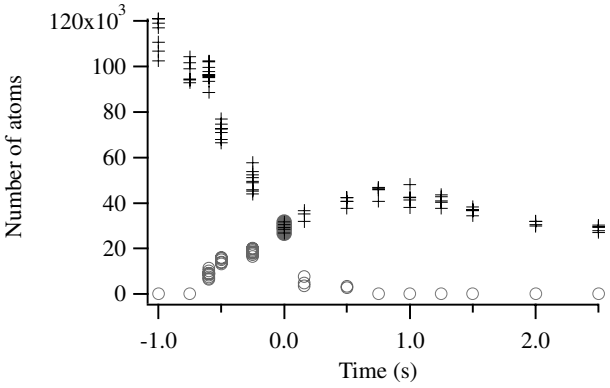

Figure 5. The measured number of atoms as a function of time. Crosses represent the total atom number, circles represent the number of atoms in the condensed part. The data come from the fits of the TOFs presented in figures 2 and 3 and correspond to the case where the rf knife is absent. The time scale indicated is the same as in figures 2 and 3. The increase in the total number after $t = 0$ is spurious (see text).

3.3. Measuring the total number of atoms

An attempt to measure the total number of atoms as a function of time is shown in figure 5. Both the total number and the condensed number as derived from fits to the TOF signals of figures 2 and 3 are plotted. Surprisingly the total number of atoms appears to increase between $t = 0$ and 1 s. There must be a systematic error, which we can account for by recalling that in our apparatus we only detect atoms which make non-adiabatic transitions to the (field insensitive) $m = 0$ state during the turn-off of the magnetic trap [1]. The fraction we observe is of the order of 10%. It is quite possible that this non-adiabatic transition does not occur with equal probability at every point in the trap. Thus clouds with different spatial distributions may be converted to the $m = 0$ state with different efficiencies. This could explain why atoms in the thermal cloud are observed with a higher efficiency than condensed atoms, as indicated in figure 5.

We conclude that our measurements of the absolute number of atoms contain uncontrolled systematic errors of the

order of a factor of two. So, even if we know the ionization rate constants, we cannot use the ion rate to study condensate growth kinetics because we need the absolute value of the initial number of atoms. It would also be useful to measure the variation in the number of atoms during formation. Such a study will have to wait for a more reliable method of releasing the atoms from the trap (see conclusion). However, the measurement of the ionization rate constants is a first step. For a BEC, we can circumvent the systematic error on the detection efficiency of the atoms to make a measurement of the ionization rate constants. This has been described in [8] and will be summarized in the following section. Afterwards, we will investigate the effect of this systematic error on the measurement for a thermal cloud.

4. Rate constants of ionizing collisions

The usual method of measuring the inelastic rate constants relies on fits to a non-exponential decay of the number of atoms. This method has some practical problems if the sample heats during the measurement: the density changes which complicates the fitting procedure. A way to avoid this heating is to apply an rf shield, but this causes atom losses, which are not due to collisions. What is even more inconvenient in our case is that what is measured in this kind of experiment is a decreasing atom number due to losses, which can be due to ionizing as well as non-ionizing collisions. We want to relate the ion rate to the density of the cloud, so what we need is the rate constants for *ionizing* two- and three-body collisions. We therefore use another method which consists of directly observing the products of the collisions, namely the number of ions, as a function of the density of the cloud.

As we have seen in section 3, there is a systematic error on the measurement of the number of atoms and thus of the density of the cloud. But we will see that we can circumvent it in the case of the BEC. Let us then assume first that we are able to measure the number of atoms accurately.

We use the MCP to detect both the ions and the TOF signal. In a single run we record the ion rate during the last seconds of the ramp until we switch off the magnetic trap and record the TOF signal (to obtain the atom number N and the density). The very last value of the ion rate recorded corresponds to ions produced by the cloud observed with the TOF signal. We repeat this sequence many times with different numbers of atoms in the cloud. The way to vary this number is to keep the atoms in the trap with an rf shield kept on. In this way we reduce the atom number and keep the temperature of the cloud constant. As explained in appendix A, the relation between ion rate and density is quite complex in the case of the presence of collisions between atoms in the condensed part and atoms in the thermal part. We therefore only examine the case of a pure BEC *or* a pure thermal cloud. In that case we can write the ion rate per atom Γ as follows:

$$\frac{\text{ion rate}}{N} = \Gamma = \frac{1}{\tau'} + \frac{1}{2}\kappa_2\beta\langle n\rangle + \frac{1}{3}\kappa_3 L\langle n^2\rangle \qquad (3)$$

where $\langle n\rangle = \frac{1}{N}\int n^2\,\mathrm{d}\boldsymbol{r}$ and $\langle n^2\rangle = \frac{1}{N}\int n^3\,\mathrm{d}\boldsymbol{r}$, n being the local density. We have also introduced the two- and three-body ionizing collision rate constants, β and L respectively, defined according to their effect on the density loss in a thermal gas[3]: $(\frac{\mathrm{d}n}{\mathrm{d}t})_{ionization} = -\frac{n}{\tau'} - \beta n^2 - Ln^3$. The effective lifetime $\tau' \geqslant \tau$ is due to *ionizing* collisions with the background gas. The numerical factors come from the fact that although two or three atoms are lost in each type of collision, only one ion is produced. The factors κ_2 and κ_3 take into account the fact that the two-and three-particle local correlation functions are different depending on whether it is a BEC or a thermal cloud. For the thermal cloud $\kappa_2 = \kappa_3 = 1$, while for a dilute BEC, one has $\kappa_2 = 1/2!$ and $\kappa_3 = 1/3!$ [11, 12]. When the sample is very dense, quantum depletion must be taken into account, which modifies these factors [11]. A measurement of β and L would allow us to test experimentally the theoretical values of κ_2 and κ_3 [8].

4.1. Rate constants for a BEC

To determine the ionizing collision rate constants β and L, we need an absolute calibration of the number of atoms in the condensate, N_0, and the peak density, n_0, in order to calculate $\langle n\rangle$ and $\langle n^2\rangle$. As discussed above, we do not have a good calibration of these quantities. In the case of a BEC, however, the measurement of the chemical potential μ obtained by a fit of the TOF signal gives an accurate value for the product $n_0 a = \mu \mathrm{m}/4\pi\hbar^2$, a being the scattering length. With the value of $\overline{\omega}$ we also obtain the product $N_0 a = (1/15)(\hbar/m\overline{\omega})^{1/2}\,(2\mu/\hbar\overline{\omega})^{5/2}$. Experimentally we confirm that $\mu \propto N_d^{2/5}$ where N_d is the number of detected atoms [8]. This is a good indication that our detector is linear and that the detection efficiency for a BEC is indeed independent of μ. Assuming a value of the scattering length ($a = 20$ nm), we therefore have an accurate measurement of n_0 and N_0. We have measured the rate constants β and L for a condensate [8]. We obtain by a fit to equation (3) (having corrected for the effect of quantum depletion and the fact that the BEC also contains a small thermal fraction) $\beta = 2.9(\pm 2.0) \times 10^{-14}$ cm^3 s^{-1} and $L = 1.2(\pm 0.7) \times 10^{-26}$ cm^6 s^{-1}. These values agree with the theoretical estimates [13, 14]. The scattering length is not well known [1, 2], so we have also given β and L for different values of a [8].

4.2. Rate constants for a thermal cloud

To determine the rate constants for a thermal cloud we need, as before, to determine the atom number and density. We cannot use the same trick as in section 4.1 to avoid systematic errors in the detection efficiency. If we want to use the above experimental method for a thermal cloud we must rely on a fit of the TOF to find the atom number and the temperature T. In appendix B, we propose a method to determine the rate constants which is independent of an absolute detection efficiency, but at this stage we will concentrate on the same technique as used for a BEC.

As we have shown above, the detection efficiency is expected to be different for a thermal cloud and we can investigate the effect of this systematic error on these measurements. We repeat the above described experiment, this time with a pure thermal cloud. To begin with, we assume that the detection efficiency is the same for a BEC and a thermal cloud. We

[3] Collision rate constants are sometimes defined directly for a BEC ($\beta' = \beta/2$ and $L' = L/6$).

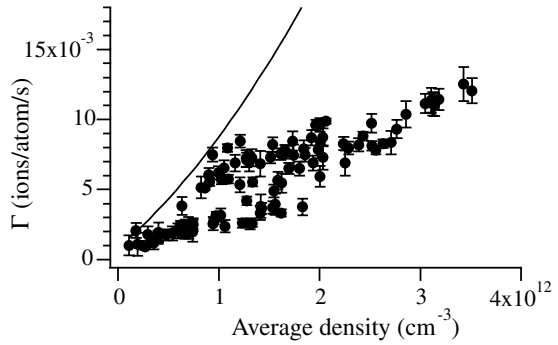

Figure 6. Ion rate per trapped atom (Γ) in a thermal cloud versus average density. The full curve corresponds to the value of β and L deduced from the condensate measurements.

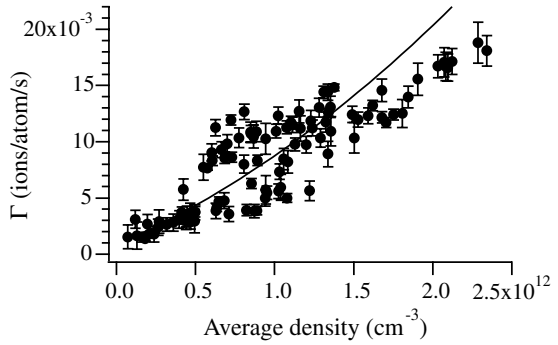

Figure 7. Same as figure 6 but assuming a detection efficiency of the thermal cloud a factor of 1.5 higher relative to the BEC. The data have simply been rescaled along both axes; the full curve is the same as in figure 6.

plot the ion rate per atom as a function of $\langle n \rangle$ in figure 6. We can extrapolate the data to obtain the vertical intercept, which corresponds to $1/\tau'$. For densities corresponding to the moment of formation of BEC, the corresponding ion rate N/τ' is negligible compared with the total ionization rate, meaning that we are dominated by two- and three-body processes (see figures 2 and 5). To compare with the results obtained for the BEC, we have also plotted the curve we would expect using the above values of β and L. It is clear that the data do not agree with this curve. Moreover, no possible pair of β and L taken within their error bars (see [8]) can transform the curve so that it agrees with the data. Nor can assuming a different scattering length. What *can* make the curve agree with the data is assuming a different detection efficiency for atoms in the thermal cloud. If we assume for example that the detection efficiency is a factor of 1.5 higher for a thermal cloud relative to a BEC (which is consistent with figure 5), the curve agrees better with the data as shown in figure 7.

The dispersion of the data points is quite large. This dispersion can be understood by examining figure 8 in which we have plotted the same data as in figure 6, but now indicating the temperature corresponding to each different point on the graph. There is a clear systematic variation with temperature. One possible explanation is that the detection efficiency is temperature dependent. This agrees with the above idea that the efficiency depends on the spatial extent of the cloud which is indeed related to the temperature. We do not know the form of the detection efficiency as a function of temperature, but comparing these data (indicating that cold atoms are better

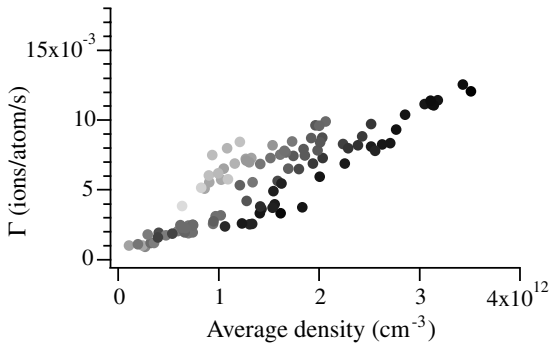

Figure 8. Same data as in figure 6 but with the different temperatures indicated. The lighter circles correspond to the point with higher temperatures (the maximum temperature is 5.5 μK), the darker circles with lower temperatures (minimum temperature 1.8 μK).

detected) with the fact that a thermal cloud is better detected than a BEC, leads us to conclude that there exists a certain temperature giving a maximal detection efficiency. Therefore the correction to the detection efficiency for thermal atoms is not just a simple factor, but rather a function of temperature. Without knowing this correction, we cannot use this method to determine the collision constants for a thermal cloud. Still, these results are a consistency check on the rate constants measured using a BEC.

5. Conclusion

We have seen that the benefits of ion detection are twofold. First, the ion rate can be used to select BECs with very similar parameters out of a sample with large fluctuations. Second, the ion rate itself can give information on the condensate on a single-shot basis. Quantitatively, we still have some difficulties interpreting the data due to systematic errors in the detection calibration.

One way to overcome this problem is to release the atoms from the trap by the mean of Raman transitions. It should be possible to transfer close to 100% of the atoms into the $m = 0$ state. This will eliminate the temperature dependence of the detection efficiency and allow us to obtain more precise measurements of β and L, both for the BEC by improving the value of the scattering length and for the thermal cloud by making the detection efficiency temperature independent.

Acknowledgments

We thank A Villing and F Moron for their assistance with the electronics. This work is supported by the European Union under grants IST-1999-11055 and HPRN-CT-2000-00125, and by the DGA grant 00.34.025. JVG thanks Fundação para a Ciência e a Tecnologia and SS acknowledges Danish Research Training Council and Danish Research Agency for financial support.

Appendix A. Predictions of the ion rate during the formation of the BEC

The two- and three-body ion rates (I_{2b} and I_{3b} respectively) in a sample containing both a BEC and a thermal cloud are given by [11]:

$$I_{2b} = \frac{1}{2}\frac{\beta}{2!}\int \mathrm{d}\boldsymbol{r}\,[n_0^2(\boldsymbol{r}) + 4n_0(\boldsymbol{r})n_{th}(\boldsymbol{r}) + 2n_{th}^2(\boldsymbol{r})] \quad (A.1)$$

$$I_{3b} = \frac{1}{3}\frac{L}{3!}\int \mathrm{d}\boldsymbol{r}\,[n_0^3(\boldsymbol{r}) + 9n_0^2(\boldsymbol{r})n_{th}(\boldsymbol{r}) + 18n_0(\boldsymbol{r})n_{th}^2(\boldsymbol{r}) + 6n_{th}^3(\boldsymbol{r})] \quad (A.2)$$

where $n_0(\boldsymbol{r})$ is the local density of the BEC and $n_{th}(\boldsymbol{r})$ is the local density of the thermal cloud. Here we have taken into account the symmetrization factors, but neglected quantum depletion.

Four parameters are needed to determine the densities of the two clouds: N_0, μ, N_{th} and T_{th}. In the Thomas–Fermi approximation, however, the BEC density depends only on μ:

$$n_0(\boldsymbol{r}) = \max\left[0, \frac{\mu - U(\boldsymbol{r})}{g}\right] \quad (A.3)$$

with $U(\boldsymbol{r})$ the harmonic trapping potential and $g = 4\pi\hbar^2 a/m$ the interaction strength. The density of the thermal cloud depends on two parameters. But, if thermodynamic equilibrium is reached, taking into account the interactions between the BEC and the thermal cloud (and neglecting the interaction energy of the thermal cloud), we can write:

$$n_{th}(\boldsymbol{r}) = \frac{1}{\lambda_{dB}^3} g_{3/2}\left(\exp\left(-\frac{1}{k_B T}(U(\boldsymbol{r}) + 2gn_0(\boldsymbol{r}) - \mu)\right)\right) \quad (A.4)$$

where λ_{dB} is the thermal de Broglie wavelength and $g_{3/2}(x) = \sum_{n=1}^{+\infty} \frac{x^n}{n^{3/2}}$. In that case, given μ, n_{th} only depends on one additional parameter.

A.1. Comparison between the ion rates created by a thermal cloud at $T = T_C$ and a pure BEC

Before trying to calculate the ion rate for any T, which requires numerical calculation, let us first examine the ion rate created by a thermal cloud at $T = T_C$ with a number of atoms N and that created by a pure BEC ($T = 0$) with a number of atoms ηN ($\eta < 1$).

In the case of two-body collisions, the ratio R_{2b} of the ion rates created by a pure BEC (I^{BEC}) and by a thermal cloud (I^{th}) is related to the ratio of the peak densities. For three-body collisions the ratio (R_{3b}) is related to the square of that ratio. Using the above equations we find:

$$\left(\frac{n_0}{n_{th}}\right) = C_0 \eta^{2/5} N^{-1/10}\left(\frac{\overline{\sigma}}{a}\right)^{3/5} \quad (A.5)$$

$$R_{2b} = \frac{I_{2b}^{BEC}}{I_{2b}^{th}} = C_2 \eta^{7/5} N^{-1/10}\left(\frac{\overline{\sigma}}{a}\right)^{3/5} \quad (A.6)$$

$$R_{3b} = \frac{I_{3b}^{BEC}}{I_{3b}^{th}} = C_3 \eta^{9/5} N^{-2/10}\left(\frac{\overline{\sigma}}{a}\right)^{6/5} \quad (A.7)$$

where $\overline{\sigma} = \sqrt{\frac{\hbar}{m\overline{\omega}}}$. The numerical factors $C_0 \simeq 0.78$, $C_2 \simeq 1.05$ and $C_3 \simeq 0.49$ are independent of the atom considered and only assume that the cloud is trapped in a 3D harmonic trap. The maximum ratios are reached in the case of no loss ($\eta = 1$). Using the typical values of our experiment ($a \simeq 20$ nm, $N \simeq 4 \times 10^5$ and $\overline{\omega} \simeq 2\pi \times 408$ Hz), we find $(\frac{n_0}{n_{th}})_{max} \simeq 4$, $(R_{2b})_{max} \simeq 5$ and $(R_{3b})_{max} \simeq 12$.

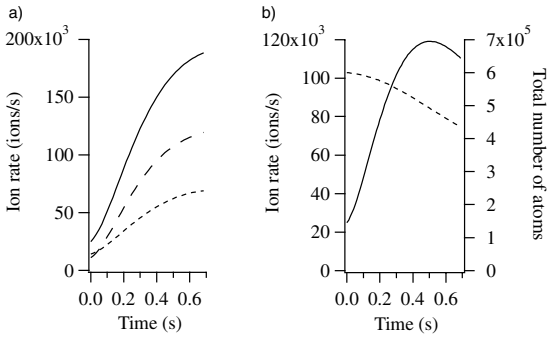

Figure A.1. Evolution of the ion rate with time. In (a) the total number of atoms is constant. We show the different contributions to the total ion rate (continuous curve) of the ion rate created by two-body collisions (short dashed curve) and three-body collisions (long dashed curve). In (b) the total number of atoms (dashed curve) decreases due to ionizing collisions. Here the ion rate exhibits a maximum before the formation of a pure BEC. For both graphs, the initial number of atoms is 6×10^5 and a linear evolution of the temperature between T_C and 0 is imposed. The rates have been calculated with the values of rate constants measured in [8].

If the total number of atoms decreases during the formation of the BEC, these ratios rapidly fall. For instance, if the number of atoms decreases by a factor of 3.5 during the last 750 ms of evaporation as shown in figure 5, we would not have seen an increase of ionization rate but roughly the same ion rate at $t = -750$ and 0 ms! This is an additional evidence of the difference of neutral atom detection efficiency for a thermal cloud and BEC (i.e. the total number of atoms decreased by less than 3.5).

A.2. Evolution of the ion rate between $T = T_C$ and $T = 0$

Using equations (A.1) and (A.2), we have numerically calculated the ion rates for all temperatures. If the cloud is at thermodynamic equilibrium all the parameters of the cloud are deduced from two parameters, for example the total number of atoms and the temperature. To simulate a time evolution of the ion rate we thus need a model for the variation of these parameters. In this appendix we will assume a linear evolution of the temperature between $T = T_C$ and 0 in 0.7 s. This is of course a simplification, but given the linearity of the evaporative cooling ramp, it is quite a good approximation.

In figure A.1(a) we show the evolution of the ion rates assuming a constant total number of atoms. The ion rate increases monotonically. We also see that the number of ions produced and thus also the number of lost atoms is not necessarily negligible compared with the total.

We can attempt to take into account these losses in our model. In the experiments described in the text, the losses are not only due to the ionizing collisions but also to the rf knife. In addition, losses not only lead to a decrease in the total number of atoms but also to a change in the temperature because these collisions change the condensed fraction. Thus, modelling the ion rate can be quite complicated. Here we wish simply to illustrate the effect of loss, so we assume that losses are only due to ionizing collisions, and we will neglect losses due to the rf knife. Figure A.1(b) shows the results. The atom number decreases by only 30% and the ion rate reaches a local

maximum before the formation of the pure BEC, as in our experiment. Extensions of our model to include losses due to the rf knife would allow one to monitor all the parameters of the cloud using the ion signal.

Appendix B. Proposed measurement of rate constants independent of absolute neutral atom detection efficiency

We will assume in this section that the absolute ion detection efficiency is known, and that two- and three-body losses are ionizing collisions [13]. The idea behind this method is that two TOF signals separated by a given time can measure the relative atom loss during this time, while the ion rate can measure the absolute atom loss. These data allow one to extract the rate constants without relying on an absolute calibration of the neutral atom detection efficiency. The method works if the neutral detection efficiency is unknown but independent of temperature. Otherwise, we must also assume that the cloud does not heat during the measurement or that we know the variation of detection efficiency with temperature.

To simplify the discussion we will neglect three-body reactions and assume that the sample does not heat during the measurement. This will allow us to derive analytical expressions, but the results are easily generalized to include heating as well as three-body reactions. We can then write the ion rate $I(t)$ as:

$$I(t) = \frac{\epsilon N(t)}{\tau'} + \frac{\beta\epsilon}{2V_{eff}} N(t)^2 \tag{B.1}$$

with τ' the lifetime due to ionizing collisions, $N(t)$ the absolute atom number, V_{eff} defined by $\langle n\rangle = N/V_{eff}$ and ϵ the ion detection efficiency. We write $N_d(t) = \alpha N(t)$ where $N_d(t)$ is the number of atoms detected and α is the neutral atom detection efficiency. Then

$$I(t) = \frac{\epsilon N_d(t)}{\alpha\tau'} + \frac{\epsilon\beta}{\alpha^2 2V_{eff}} N_d(t)^2. \tag{B.2}$$

We can also write an equation for the atom number

$$\frac{\mathrm{d}N(t)}{\mathrm{d}t} = -\frac{N(t)}{\tau} - \frac{\beta}{V_{eff}} N(t)^2 \tag{B.3}$$

with τ the total lifetime of the sample that we can measure independently at lowest density. The solution is:

$$\frac{N(t)}{N(t_0)} = \frac{1}{\left(1 + \frac{\beta}{V_{eff}} N(t_0)\tau\right)\mathrm{e}^{(t-t_0)/\tau} - \frac{\beta}{V_{eff}} N(t_0)\tau}. \tag{B.4}$$

Substituting again $N_d(t) = \alpha N(t)$ we have:

$$\frac{N_d(t)}{N_d(t_0)} = \frac{1}{\left(1 + \frac{\beta}{\alpha V_{eff}} N_d(t_0)\tau\right)\mathrm{e}^{(t-t_0)/\tau} - \frac{\beta}{\alpha V_{eff}} N_d(t_0)\tau}. \tag{B.5}$$

Thus we can measure an initial ion rate and the corresponding detected atom number $N_d(t_0)$ by a TOF signal, let the system evolve for a certain time and then again measure the ion rate and the atom number $N_d(t)$. With the evolution of the ion rate, we can deduce $\epsilon/\alpha\tau'$ and $\epsilon\beta/\alpha^2 V_{eff}$ from equation (B.1), and from the evolution of the atom number we can deduce $\beta/\alpha V_{eff}$ using equation (B.5). With the value of V_{eff} and ϵ, we can obtain the value β. We can also obtain the detection efficiency α.

If we allow for three-body reactions, the method can still be used but (B.4) is no longer analytical and must be integrated numerically. If the sample heats during the measurement, we only have to recalculate the volume V_{eff} for each TOF measurement.

The reason why we have not yet been able to apply this method is, as indicated above, that the sample is heating so that the detection efficiency changes during the measurement. As we have not been able to measure the temperature dependence of $\alpha(T)$ the above equations cannot be solved. We hope to render the detection efficiency temperature independent in the near future by using Raman transitions as mentioned in the conclusion.

References

[1] Robert A, Sirjean O, Browaeys A, Poupard J, Nowak S, Boiron D, Westbrook C I and Aspect A 2001 *Science* **292** 461

[2] Pereira D S F, Léonard J, Junmin W, Barrelet C J, Perales F, Rasel E, Unnikrishnan C S, Leduc M and Cohen-Tannoudji C 2001 *Phys. Rev. Lett.* **86** 3459

[3] Miesner H J, Stamper-Kurn D M, Andrews M R, Durfee D S, Inouye S and Ketterle W 1998 *Science* **270** 1005

[4] Köhl M, Hänsch T W and Esslinger T 2002 *Phys. Rev. Lett.* **88** 080402

[5] Kagan Yu M, Svistunov B V and Shlyapnikov G V 1992 *Sov. Phys.–JETP* **75** 387

[6] Gardiner C W, Zoller P, Ballagh R J and Davis M J 1997 *Phys. Rev. Lett.* **79** 1793

[7] Bijlsma M J, Zaremba E and Stoof H T C 2000 *Phys. Rev.* A **62** 063609-1

[8] Sirjean O, Seidelin S, Viana Gomes J, Boiron D, Westbrook C I, Aspect A and Shlyapnikov G V 2002 *Phys. Rev. Lett.* **89** 220406

[9] Browaeys A 2000 Thèse de l'Université Paris-Sud available at http://ccsd.cnrs.fr/

[10] Mewes M O, Andrews M R, van Druten N J, Kurn D M, Durfee D S and Ketterle W 1996 *Phys. Rev. Lett.* **77** 416

[11] Kagan Yu M, Svistunov B V and Shlyapnikov G V 1985 *JETP Lett.* **42** 209

[12] Burt E A, Ghrist R W, Myatt C J, Holland M J, Cornell E A and Wieman C E 1997 *Phys. Rev. Lett.* **79** 337

[13] Shlyapnikov G V, Walraven J T M, Rahmanov U M and Reynolds M W 1994 *Phys. Rev. Lett.* **73** 3247
Fedichev P O, Reynolds M W, Rahmanov U M and Shlyapnikov G V 1996 *Phys. Rev.* A **53** 1447

[14] Venturi V, Whittingham I B, Leo P J and Peach G 1999 *Phys. Rev.* A **60** 4635
Venturi V and Whittingham I B 2000 *Phys. Rev.* A **61** 060703(R)

Getting the Elastic Scattering Length by Observing Inelastic Collisions in Ultracold Metastable Helium Atoms

S. Seidelin, J. Viana Gomes,* R. Hoppeler, O. Sirjean, D. Boiron, A. Aspect, and C. I. Westbrook
Laboratoire Charles Fabry de l'Institut d'Optique, UMR 8501 du CNRS, F-91403 Orsay Cedex, France
(Received 13 January 2004; published 27 August 2004)

We report an experiment measuring simultaneously the temperature and the flux of ions produced by a cloud of triplet metastable helium atoms at the Bose-Einstein critical temperature. The onset of condensation is revealed by a sharp increase of the ion flux during evaporative cooling. Combining our measurements with previous measurements of ionization in a pure Bose-Einstein condensate, we extract an improved value of the scattering length $a = 11.3^{+2.5}_{-1.0}$ nm. The analysis includes corrections that take into account the effect of atomic interactions on the critical temperature, and thus an independent measurement of the scattering length would allow a new test of these calculations.

DOI: 10.1103/PhysRevLett.93.090409 PACS numbers: 03.75.Hh, 34.50.–s, 67.65.+z

Understanding and testing the role of interparticle interactions in dilute Bose-Einstein condensates (BEC) is an exciting area of current research. Although measurements of the interaction energy and the spectrum of excitations of a BEC have confirmed the validity of the Gross-Pitaevskii equation [1], there are still relatively few quantitative tests of other aspects, such as the effect of interactions on the value of the critical temperature (T_c) or the condensed fraction [2,3]. The success in condensing metastable helium atoms (He^*) [4,5] was greeted with interest in the community partly because the metastability offers new detection strategies unavailable with other species. To fully use these strategies, however, we are still missing an accurate value of the s-wave scattering length a, the atomic parameter which determines all elastic scattering behavior at low energies. An accurate value of a would also be useful to help clarify some puzzling results concerning measurements of He^* in the hydrodynamic regime, in which two different ways of measuring the elastic scattering rate appeared to be in contradiction [6]. Also, because He is a relatively simple atom, theoretical predictions of a are already in a rather narrow range [7,8] and these calculations should be tested.

A straightforward method to determine a is to use ballistic expansion of a BEC to measure the chemical potential for a known atom number. This was done in Refs. [4,5], but the measurements were limited by the calibration of the number of atoms. The reported values for a are 20 ± 10 and 16 ± 8 nm, respectively. A recent estimate, limited by similar effects, is $a = 10 \pm 5$ nm [9]. In this Letter, we report a new measurement of a which makes extensive use of a unique feature of He^*, spontaneous Penning ionization within the sample.

We exploit two specific situations in which the absolute atom number N is simply related to a and measured quantities: (i) for a pure BEC, the number is deduced directly from the chemical potential μ and a, and (ii) for a cloud at the BEC threshold, it is simply related to T_c. Both μ and T_c are accurately deduced from time of flight (TOF) measurements. Comparison of ion rates from a pure BEC of known chemical potential and from a cloud at T_c allows us to extract a and the ionization rate constants. The deduced value of a is independent of the absolute ion detection efficiency, assuming that this efficiency is the same in the two measurements. The ion signal is also used in another novel way: since it provides a real-time observation of the onset of BEC [10], we use it to reliably produce a cloud at threshold.

A dense cloud of He^* produces a steady flux of ions due to various ionization processes. Density losses due uniquely to *ionizing* collisions depend on the local density n according to $(dn/dt)_{\text{ionizing}} = -(n/\tau_i) - \beta n^2 - Ln^3$, with τ_i the lifetime due to ionizing collisions with the background gas and β and L the 2-body and 3-body ionization rate constants defined for a thermal cloud. The total ion rate from a thermal cloud is given by

$$\Phi = \frac{N}{\tau_i} + \frac{1}{2}\beta \int n^2 d\mathbf{r} + \frac{1}{3} L \int n^3 d\mathbf{r}. \tag{1}$$

The numerical factors reflect the fact that although two (three) atoms are lost in 2-body (3-body) collisions, only one ion is produced. Ionization measurements on a pure BEC were reported in Ref. [11], and, as a was not precisely known, β and L were given in terms of a.

For a precise measurement of a, corrections due to interactions must be taken into account. In the mean-field approach, the density is given by [1]

$$n(\mathbf{r}) = \frac{1}{\lambda^3(T)} g_{3/2}\left[\exp\left(-\frac{1}{k_B T}[V(\mathbf{r}) + 2gn(\mathbf{r}) - \mu]\right)\right], \tag{2}$$

with $\lambda(T)$ the thermal de Broglie wavelength, T the temperature k_B the Boltzmann constant, V the trapping potential $g = 4\pi\hbar^2 a/m$ the interaction constant, μ the chemical potential, and $g_\alpha(x) = \sum_{i=1}^{\infty} x^i/i^\alpha$.

The ion rate at the phase transition Φ_c can be derived from Eq. (2) by a first order perturbation theory similar to Ref. [12] but with a fixed temperature rather than a fixed atom number. We use the chemical potential of a gas in a harmonic potential at the BEC transition:

$$\mu_c/k_B T_c = \frac{3}{2}\frac{\tilde{\omega}}{\omega_c} + 4g_{3/2}(1)\frac{a}{\lambda_c}. \quad (3)$$

This gives

$$\Phi_c = \left(\frac{\omega_c}{\overline{\omega}}\right)^3\left[\frac{1}{\tau_i}\left(1.20 + 2.48\frac{\tilde{\omega}}{\omega_c} + 12.35\frac{a}{\lambda_c}\right) + \frac{\beta}{\lambda_c^3}\left(0.33 + 1.81\frac{\tilde{\omega}}{\omega_c} + 6.75\frac{a}{\lambda_c}\right) + \frac{L}{\lambda_c^6}\left(0.22 + 2.21\frac{\tilde{\omega}}{\omega_c} + 6.50\frac{a}{\lambda_c}\right)\right], \quad (4)$$

with $\tilde{\omega} = (2\omega_\perp + \omega_\parallel)/3$, $\overline{\omega} = (\omega_\parallel \omega_\perp^2)^{1/3}$, $\omega_c = k_B T_c/\hbar$, and $\lambda_c = \lambda(T_c)$. The numerical values come from the calculation of arithmetic series and are independent of any parameters of the cloud. The terms proportional to a/λ_c account for the atomic interactions, while the corrections proportional to $\tilde{\omega}/\omega_c$ take into account the effect of finite sample size. For the typical parameters ($T_c \sim 2\ \mu$K and $a = 12$ nm) we have $a/\lambda_c \simeq \tilde{\omega}/\omega_c \simeq 0.02$, corresponding to an interaction correction of 20%, 40%, and 60% in the three successive terms in Eq. (4). Even though the first order corrections are large, we find, using an approach similar to Ref. [13], that the second order corrections are negligible: -4%, 1.8%, and -3%, respectively. Note that finite size corrections are always smaller than those due to interactions.

Our setup has been described in Ref. [11]. Briefly, we trap up to 2×10^8 atoms at 1 mK in an Ioffe-Pritchard cloverleaf trap with τ_i estimated to be >500 s. In a typical run, forced evaporation for 30 s cools a cloud to a temperature near the phase transition. At this point, the rf-knife frequency is decreasing at a rate of 400 kHz/s. The axial and radial oscillation frequencies in the harmonic trapping potential are $\omega_\parallel/2\pi = 47 \pm 3$ Hz and $\omega_\perp/2\pi = 1225 \pm 20$ Hz, respectively. A 2-stage, single anode microchannel plate detector (MCP) is placed 5 cm below the trapping region. Two grids above the MCP allow us either to repel positive ions and detect only the He^* atoms or to attract and detect positive ions produced in the trapped cloud. As explained in Ref. [11], to detect the ion flux, the MCP is used in counting mode, whereas we record the TOF signal at low gain (analog mode) to avoid saturation. As explained in Ref. [4], the TOF signal is due to atoms in the $m = 0$ state which are insensitive to the magnetic field. However, atoms in magnetic field sensitive states are still present, and their trajectories are affected by uncontrolled residual fields. Therefore, during the time of flight, we apply a magnetic gradient in order to push these atoms away from the detector. The ratio between the detected atoms in the $m = 0$ state and the initial number of atoms in the cloud is not well known [10], so we use the TOF only to get the temperature.

The crux of the experiment is to obtain a cloud of atoms at the phase transition. To identify the BEC threshold point, we monitor the ion signal. We have shown in Ref. [10] that the onset of BEC is heralded by a sudden increase of the ion rate associated with the increased density of the condensate. More precisely, the BEC threshold corresponds to the rapid change in slope of the ion rate vs time or the maximum of the 2nd derivative [14]. Figure 1 shows a series of such ionization rates during evaporation through the BEC transition. From these curves we can determine an empirical relation between the time of the onset of condensation and the ion rate preceding it. This relation stays valid only as long as we keep the same evaporation ramp and bias field. We will refer to this as the "threshold curve." Because of fluctuations of the bias field, we observe fluctuations of the time of BEC onset from run to run. These correspond to approximately ± 60 ms in time or ± 25 kHz in frequency, a value which agrees with independent measurements of the fluctuations of the bias field.

Having established this relation, we can interrupt an evaporation sequence very close to the BEC threshold and record the instantaneous ion rate as well as the corresponding TOF signal. Only runs closer than ± 60 ms to the threshold curve are used in the analysis.

We fit the associated TOF spectrum to determine the temperature (Fig. 2). We use Eq. (2) together with μ_c given in Eq. (3) for the initial atomic density and then assume purely ballistic expansion of the cloud after the switching off of the trap. We refer to this fit as the Bose fit. The fits are weighted by an estimated uncertainty in each point of the TOF curve. To make this estimate, we chose a set of TOF spectra which appeared to show no systematic deviation from their fits and used them to estimate the amplitude of the noise. This noise varies as the square root of the amplitude of the signal, indicating that we are limited by the shot noise of the atom detection. Our procedure is only an approximate indicator of the error bars. The chi square per degree of freedom χ^2 for the fits

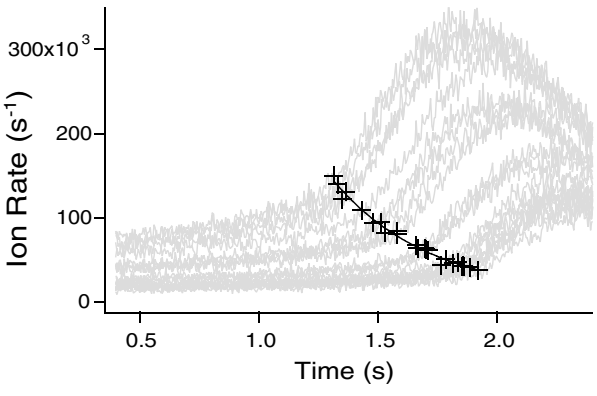

FIG. 1. Variation of the ion rate as the atomic cloud is cooled through the phase transition for various initial densities (gray curves). The rf-knife frequency at $t = 0$ is 2 MHz. The sudden increase of the ion rate (crosses) occurs at the BEC transition. The solid line passing through the transition points constitutes our empirical relation, named threshold curve.

deduced in this way ranges from 0.8 to 3. We then exclude a successively larger window (up to the rms of the TOF signal) from the fit (see Fig. 2). For all runs, we observe a variation of less than 5% and in most cases less than 3% of the temperature as the excluded window is increased.

In Fig. 2, we show an example of a typical TOF spectrum where the wings are fitted by a Gaussian and the Bose function described above. The ability of the Bose function to reproduce the center of the distribution without including it in the fit, unlike the Gaussian, confirms that the cloud is indeed close to the BEC threshold. In the following, we use the temperature given by the fit with an excluded window of half the rms width of the TOF signal in order to avoid the possibility of a small condensate component or other high density effects distorting our analysis.

Before plotting the ion rate as a function of the critical temperature, we correct the observed temperature to account for the hydrodynamic expansion of the cloud (see [2] and references therein). This is done in the spirit of Ref. [15], which uses the Boltzmann equation approach to take into account collisions during the expansion. The collision rate in Ref. [15] is calculated using a Gaussian density profile. We rather use the value calculated for an ideal Bose gas [16], which we have adapted to take interactions into account. This correction depends on the scattering length but the effect on the final value of a is only of order 0.3 nm for a ranging from 10 to 14 nm. We therefore simply assume $a = 12$ nm for this correction in the following. Due to the additional anisotropy of the expanding cloud in the horizontal (detector) plane, the fitting function should be modified; but a simulation of this effect shows that the correction to the temperature is less than 0.1%.

Finally, we correct the detected ion rate $\Phi_{c,det}$ to account for the detection efficiency α such that $\Phi_c = \Phi_{c,det}/\alpha$. It should be noted that the rate constants were

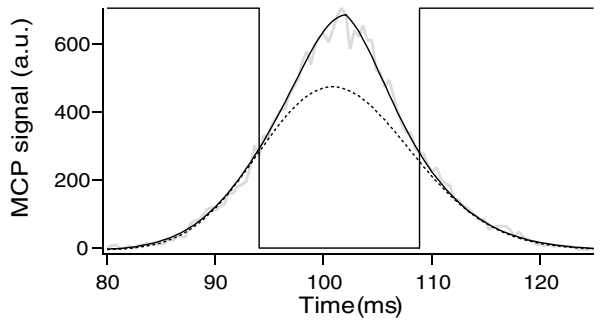

FIG. 2. Time of flight signal corresponding to a cloud released from the trap (at $t = 0$) when its ion rate is on the threshold curve. Here we have fitted the data with an excluded window indicated by the vertical lines (width equal to the rms width of the TOF signal). A Gaussian function (dotted line) does not describe the central part of the data well, while the Bose function as defined in the text (solid line) does, indicating that the cloud is close to threshold.

obtained by ion rate measurements [11]. This means that they were also corrected: $\beta = \beta_{det}/\alpha'$ and $L = L_{det}/\alpha'$. Equation (4) shows that, as long as $\alpha = \alpha'$, the detection efficiency cancels out and does not have any impact on the determination of a. We have checked experimentally that $\alpha = \alpha'$. To allow comparison with figures in earlier publications, all the figures have been corrected using the same α as earlier, namely, $\alpha = 0.42$ [10,11].

The results are plotted in Fig. 3. Curves corresponding to the expected variation for three values of the scattering length are also shown. We see that a large fraction of the data falls between $a = 10$ and 14 nm. The points at the highest temperatures, however, show a tendency to fall near the theoretical curve for $a = 10$ nm, while those at lower temperatures fall near $a = 14$ nm. To analyze this tendency further, we examine the TOF fits more closely using the χ^2 value as an indicator of the confidence level of each measurement. A large χ^2 could mean that the Bose function with μ imposed to μ_c is not the right fit function and, therefore, that the cloud is not sufficiently close to T_c. As shown in Fig. 3, outliers tend to be correlated with a large χ^2. Note, however, that the remaining scatter in the data is too large to be accounted for by our *a priori* estimates of the uncertainties in our ion rate or temperature measurements. We presume that it is due to fluctuations in the determination of the BEC threshold.

To determine the scattering length, we fit the black points in Fig. 3 with a as a free parameter and using β and L parametrized by a as in Ref. [11]. The fit gives (all points are given equal weight) $a = 11.3$ nm. Our chief estimated uncertainty stems from the fact that our data show a systematic tendency to fall above the best fit at low temperature and below it at high temperature. To estimate this uncertainty, we fit the data (including gray points) separately for T_c below and above 2 μK. We find $a = 13.8$ nm for the low temperature data and $a = 10.4$ nm for the high temperature data. The uncertainties in the measurements of β and L also contribute to the uncertainty in Eq. (4) used for fitting. In fact, the uncertainties in β and L are highly correlated [11] and their contribution to the uncertainty is less than 0.5 nm.

The error bars are obtained by summing quadratically the sources of uncertainties. Our final result for the scattering length is thus $a = 11.3^{+2.5}_{-1.0}$ nm. This result may be compared with the calculation in Ref. [8]. This work leads to $a = 8$ nm using the potential curves of Ref. [17]. From Ref. [8] one also finds that a 0.5% shift of the repulsive part of that potential would bring the theoretical value into agreement with our result. This 0.5% shift corresponds to the estimated uncertainty in the potential of Ref. [17]. Another theoretical treatment [7] gives a scattering length between 8 and 12 nm, also consistent with our results.

Our result also allows one to give values for the 2- and 3-body ionization rate constants. The error bars of Ref. [11] are modified to take into account the uncertainty

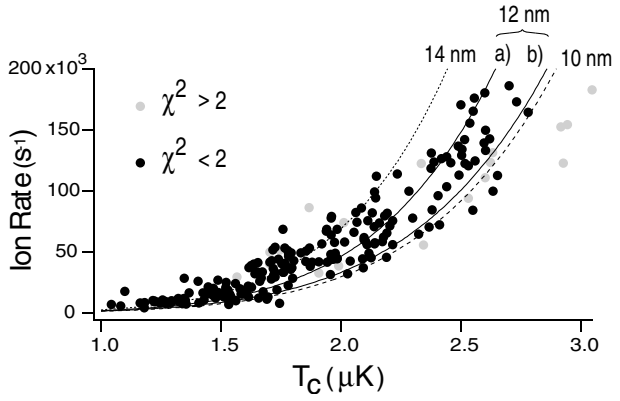

FIG. 3. Ion rate versus critical temperature. The points correspond to the results of 280 runs for which the ion rate was deemed sufficiently close to the condensation threshold. Gray indicates runs for which χ^2 in the TOF fits was above 2. The dashed line is the theoretical estimate for $a = 10$ nm, the dotted line for $a = 14$ nm [both including interaction corrections of Eq. (4)]. The two solid lines correspond to $a = 12$ nm, (*a*) with interactions and (*b*) without interactions, and illustrate the size of their effect.

of a. The uncertainty in the ion detection efficiency also contributes to the uncertainty in the rate constants. As discussed in Ref. [11], we will assume $\alpha = 0.42$ to get the central values of the rate constants. We will include a one-sided contribution to the error bars to account for the possibility, also discussed in [11], that α could be a factor of 2 smaller. We finally get $\beta = 0.9^{+1.7}_{-0.8} \times 10^{-14}$ cm^3/s and $L = 2.5^{+4.5}_{-1.7} \times 10^{-27}$ cm^6/s. The rate constants are in good agreement with theoretical predictions [8,18].

As shown in Fig. 3, curves *a* and *b*, our value of a is significantly shifted by the nonideal gas corrections of Eq. (4). Thus, when an independent measurement of the scattering length becomes available, our results can be used as a test of these corrections [19]. Note, however, that corrections to the critical temperature beyond mean-field theory [20] are small when one parametrizes the critical point in terms of an average density [13]. But an examination of the critical density measured in a local way, by imaging the ions from a cloud, for example, is sensitive to critical fluctuation phenomena which go beyond mean-field theory similar to the homogenous case [20]. Thus, refinements of the ionization measurements described here promise to continue to provide new tests of BEC physics.

This work is supported by EU Grants No. IST-2001-38863 and No. HPRN-CT-2000-00125 and by the INTAS Project No. 01-0855. S. S. is supported by the Danish Research Agency and J. V. G. by the Portuguese Foundation for Science and Technology.

*Permanent address: Departamento de Fisica, Universidade do Minho, Campus de Gualtar, 4710-057 Braga, Portugal.

[1] F. Dalfovo, S. Giorgini, L. P. Pitaevskii, and S. Stringari, Rev. Mod. Phys. **71**, 463 (1999).
[2] F. Gerbier, J. H. Thywissen, S. Richard, M. Hugbart, P. Bouyer, and A. Aspect, Phys. Rev. Lett. **92**, 030405 (2004).
[3] J. R. Ensher, D. S. Jin, M. R. Matthews, C. E. Wiemann, and E. A. Cornell, Phys. Rev. Lett. **77**, 4984 (1996).
[4] A. Robert, O. Sirjean, A. Browaeys, J. Poupard, S. Nowak, D. Boiron, C. I. Westbrook, and A. Aspect, Science **292**, 461 (2001).
[5] F. Pereira Dos Santos, J. Léonard, Junmin Wang, C. J. Barrelet, F. Perales, E. Rasel, C. S. Unnikrishnan, M. Leduc, and C. Cohen-Tannoudji, Phys. Rev. Lett. **86**, 3459 (2001).
[6] M. Leduc, J. Léonard, F. P. Dos Santos, E. Jahier, S. Schwarz, and C. Cohen-Tannoudji, Acta Phys. Pol. B **33**, 2213 (2002).
[7] A. S. Dickinson, F. X. Gadéa, and T. Leininger, J. Phys. B **37**, 587 (2004).
[8] P. Leo, V. Venturi, I. Whittingham, and J. Babb, Phys. Rev. A **64**, 042710 (2001).
[9] P. J. J. Tol, W. Hogervorst, and W. Vassen, Phys. Rev. A **70**, 013404 (2004).
[10] S. Seidelin, O. Sirjean, J. Viana Gomes, D. Boiron, C. I. Westbrook, and A. Aspect, J. Opt. B **5**, 112 (2003).
[11] O. Sirjean, S. Seidelin, J. Viana Gomes, D. Boiron, C. I. Westbrook, A. Aspect, and G. V. Shlyapnikov, Phys. Rev. Lett. **89**, 220406 (2002).
[12] S. Giorgini, L. P. Pitaevskii, and S. Stringari, Phys. Rev. A **54**, R4633 (1996).
[13] P. Arnold and B. Tomàšik, Phys. Rev. A **64**, 053609 (2001).
[14] O. Sirjean, Ph.D. thesis, Université Paris XI, 2003, available at http://tel.ccsd.cnrs.fr/documents/archives0/00/00/30/88
[15] P. Pedri, D. Guéry-Odelin, and S. Stringari, Phys. Rev. A **68**, 043608 (2003).
[16] G. M. Kavoulakis, C. J. Pethick, and H. Smith, Phys. Rev. A **61**, 053603 (2000).
[17] J. Stärck and W. Meyer, Chem. Phys. Lett. **225**, 229 (1994).
[18] G. V. Shlyapnikov, J. T. M. Walraven, U. M. Rahmanov, and M. W. Reynolds, Phys. Rev. Lett. **73**, 3247 (1994); P. O. Fedichev, M. W. Reynolds, and G. V. Shlyapnikov, Phys. Rev. Lett. **77**, 2921 (1996); P. F. Bedaque, E. Braaten, and H. W. Hammer, Phys. Rev. Lett. **85**, 908 (2000).
[19] A measurement using photoassociation spectroscopy is in progress at the Ecole Normale Supérieure in Paris [M. Leduc (private communication)].
[20] M. Holzmann, J. N. Fuchs, G. Baym, J. P. Blaizot, and F. Laloë, C. R. Phys. **5**, 21 (2004); N. Prokof'ev, O. Ruebenacker, and B. Svistunov, Phys. Rev. A **69**, 053625 (2004), and references therein.

Bibliography

[1] M. H. Anderson, J. R. Ensher, M. R. Matthews, C. E. Wieman, and E. A. Cornell, "Observation of Bose-Einstein Condensation in a Dilute Atomic Vapor", *Science* **269**, 198 (1995).

[2] K. B. Davis, M.-O. Mewes, M. R. Andrews, N. J. van Druten, D. S. Durfee, D. M. Kurn, and W. Ketterle, "Bose-Einstein condensation in a gas of sodium atoms", *Phys. Rev. Lett.* **75**, 3969 (1995).

[3] C. C. Bradley, C. A. Sackett, J. J. Tollett, and R. G. Hulet, "Evidence of Bose-Einstein condensation in an atomic gas with attractive interactions", *Phys. Rev. Lett.* **75**, 1687 (1995), *ibid.* **79**, 1170 (1997).

[4] S. L. Cornish, N. R. Claussen, J. L. Roberts, E. A. Cornell, and C. E. Wieman, "Stable ^{85}Rb Bose-Einstein condensate with widely tunable interactions", *Phys. Rev. Lett.* **85**, 1795 (2000).

[5] G. Modugno, G. Ferrari, G. Roati, R. J. Brecha, A. Simoni, and M. Inguscio, "Bose-Einstein condensation of potassium atoms by sympathetic cooling", *Science* **294**, 1320 (2001).

[6] T. Weber, J. Herbig, M. Mark, H.-C. Nägerl, and R. Grimm, "Bose-Einstein condensation of cesium", *Science* **299**, 232 (2003).

[7] D. G. Fried, T. C. Killian, L. Willmann, D. Landhuis, S. C. Moss, D. Kleppner, and T. J. Greytak, "Bose-Einstein condensation of atomic hydrogen", *Phys. Rev. Lett.* **81**, 3811 (1995).

[8] A. Robert, O. Sirjean, A. Browaeys, J. Poupard, S. Nowak, D. Boiron, C. I. Westbrook, and A. Aspect, "A Bose-Einstein Condensate of Metastable Atoms", *Science* **292**, 461 (2001), and Sciencexpress/www.sciencexpress.org/22 March 2001/page 1/10.1126/science.1060622.

[9] F. Pereira Dos Santos, J. Léonard, J. Wang, C. Barrelet, F. Perales, E. Rasel, C. S. Unnikrishnan, M. Leduc, and C. Cohen-Tannoudji, "Bose-Einstein condensation of metastable helium", *Phys. Rev. Lett.* **86**, 3459 (2001).

[10] Y. Takasu, K. Maki, K. Komori, T. Takano, K. Honda, M. Kumakura, T. Yabuzaki, and Y. Takahashi, "Spin-singlet Bose-Einstein condensation of two-electron atoms", *Phys. Rev. Lett.* **91**, 040404 (2003).

[11] M. Zinner, P. Spoden, T. Kraemer, G. Birkl, and W. Ertmer, "Precision measurement of the metastable $^3P_2$ lifetime of neon", *Phys. Rev. A* **67**, 010501 (2003).

[12] S. J. M. Kuppens, J. G. C. Tempelaars, V. P. Mogendorff, B. J. Claessens, H. C. W. Beijerinck, and E. J. D. Vredenbregt, "Approaching Bose-Einstein condensation of metastable neon: Over 10^9 trapped atoms", *Phys. Rev. A* **65**, 023410 (2002).

[13] H. C. W. Beijerinck, E. J. D. Vredenbregt, R. J. W. Stas, M. R. Doery, and J. G. C. Tempelaars, "Prospects for Bose-Einstein condensation of metastable neon atoms", *Phys. Rev. A* **61**, 023607 (2000).

[14] S. Bose, "Plancks Gesetz und Lichtquantenhypothese", *Z. Phys.* **26**, 178 (1924).

[15] A. Einstein, "Quantentheorie des einatomigen idealen Gase", *Sitzungsberg. Kgl. Preuss. Akad. Wiss.* 261 (1924).

[16] A. Einstein, "Quantentheorie des einatomigen idealen Gase. Zweite Abhandlung", *Sitzungsberg. Kgl. Preuss. Akad. Wiss.* 3 (1925).

[17] F. Dalfovo, S. Giorgini, L. Pitaevskii, and S. Stringari, "Theory of Bose-Einstein condensation in trapped gases", *Rev. Mod. Phys.* **71**, 463 (1999).

[18] E. A. Donley, N. R. Claussen, S. Thompson, and C. E. Wieman, "Atom-molecule coherence in a Bose-Einstein condensate", *Nature* **417**, 529 (2002).

[19] K. E. Strecker, G. B. Partridge, , and R. G. Hulet, "Conversion of an Atomic Fermi Gas to a Long-Lived Molecular Bose Gas", *Phys. Rev. Lett.* **91**, 080406 (2003).

[20] C. A. Regal, C. Ticknor, J. L. Bohn, and D. S. Jin, "Creation of ultracold molecules from a Fermi gas of atoms", *Nature* **424**, 47 (2003).

[21] S. Jochim, M. Bartenstein, A. Altmeyer, G. Hendl, C. Chin, J. H. Denschlag, and R. Grimm, "Pure Gas of Optically Trapped Molecules Created from Fermionic Atoms", *Phys. Rev. Lett.* **91**, 240402 (2003).

[22] J. Cubizolles, T. Bourdel, S. J. J. M. F. Kokkelmans, G. V. Shlyapnikov, and C. Salomon, "Production of Long-Lived Ultracold Li_2 Molecules from a Fermi Gas", *Phys. Rev. Lett.* **91**, 240401 (2003).

[23] K. Xu, T. Mukaiyama, J. R. Abo-Shaeer, J. K. Chin, D. E. Miller, and W. Ketterle, "Formation of Quantum-Degenerate Sodium Molecules", *Phys. Rev. Lett.* **91**, 210402 (2003).

[24] M. Greiner, C. A. Regal, and D. S. Jin, "Emergence of a molecular Bose-Einstein condensate from a Fermi gas", *Nature* **426**, 537 (2003).

[25] M. W. Zwierlein, C. A. Stan, C. H. Schunck, S. M. F. Raupach, S. Gupta, Z. Hadzibabic, and W. Ketterle, "Observation of Bose-Einstein Condensation of Molecules", *Phys. Rev. Lett.* **91**, 250401 (2003).

[26] M. Bartenstein, A. Altmeyer, S. Riedl, S. Jochim, C. Chin, J. H. Denschlag, and R. Grimm, "Crossover from a Molecular Bose-Einstein Condensate to a Degenerate Fermi Gas", *Phys. Rev. Lett.* **92**, 120401 (2004).

[27] N. Vanhaecke, W. de Souza Melo, B. L. Tolra, D. Comparat, and P. Pillet, "Accumulation of Cold Cesium Molecules via Photoassociation in a Mixed Atomic and Molecular Trap", *Phys. Rev. Lett.* **89**, 063001 (2002).

[28] T. Bourdel, L. Khaykovich, J. Cubizolles, J. Zhang, F. Chevy, M. Teichmann, L. Tarruell, S. J. J. M. F. Kokkelmans, and C. Salomon, "Experimental Study of the BEC-BCS Crossover Region in Lithium 6", *Phys. Rev. Lett.* **93**, 050401 (2004).

[29] M. W. Zwierlein, C. A. Stan, C. H. Schunck, S. M. F. Raupach, A. J. Kerman, and W. Ketterle, "Condensation of Pairs of Fermionic Atoms near a Feshbach Resonance", *Phys. Rev. Lett.* **92**, 120403 (2004).

[30] C. A. Regal, M. Greiner, and D. S. Jin, "Observation of Resonance Condensation of Fermionic Atom Pairs", *Phys. Rev. Lett.* **92**, 040403 (2004).

[31] M. Bartenstein, A. Altmeyer, S. Riedl, S. Jochim, C. Chin, J. H. Denschlag, and R. Grimm, "Collective Excitations of a Degenerate Gas at the BEC-BCS Crossover", *Phys. Rev. Lett.* **92**, 203201 (2004).

[32] A. Simoni, F. Ferlaino, G. Roati, G. Modugno, and M. Inguscio, "Magnetic Control of the Interaction in Ultracold K-Rb Mixtures", *Phys. Rev. Lett.* **90**, 163202 (2003).

[33] F. Ferlaino, E. de Mirandes, G. Roati, G. Modugno, and M. Inguscio, "Expansion of a Fermi Gas Interacting with a Bose-Einstein Condensate", *Phys. Rev. Lett.* **92**, 140405 (2004).

[34] A. Browaeys, *Piégeage magnétique d'un gaz d'Hélium métastable : vers la condensation de Bose-Einstein*, Thèse de doctorat, Université de Paris VI, 2000, available at http://tel.ccsd.cnrs.fr.

[35] J. Poupard, *Mesure de deux caractéristiques de l'hélium métastable importantes pour le refroidissement radiatif*, Thèse de doctorat, Université Paris-Sud, 2000.

[36] A. Robert, *Réalisation d'un condensat de Bose-Einstein d'Hélium métastable*, Thèse de doctorat, Université de Paris XI, 2001.

[37] O. Sirjean, *Collisions ionisantes: un nouveau diagnostic pour les condensats d'hélium métastable*, Thèse de doctorat, Université de Paris XI, 2003, available at http://tel.ccsd.cnrs.fr.

[38] D. J. Griffith, *Introduction to quantum mechanics* (Prentice Hall, New Jersey, 1995).

[39] C. J. Joachain, *Quantum collision theory* (North Holland, Amsterdam, 1983).

[40] J. Dalibard, in *Proceedings of the International School of Physics - Enrico Fermi*, edited by M. Inguscio, S. Stringari, and C. Wieman (IOS Press, 1999), p. 321.

[41] D. J. Heinzen, in *Proceedings of the International School of Physics - Enrico Fermi*, edited by M. Inguscio, S. Stringari, and C. Wieman (IOS Press, 1999), p. 351.

[42] K. T. Hecht, *Quantum Mechanics* (Springer, 2000).

[43] B. H. Bransden and C. J. Joachain, *Physics of atoms and molecules* (Longman Scientific and Technical, England, 1983).

[44] J. L. Roberts, N. R. Claussen, J. J. P. Burke, C. H. Greene, E. A. Cornell, and C. E. Wieman, "Resonant Magnetic Field Control of Elastic Scattering in Cold ^{85}Rb", *Phys. Rev. Lett.* **81**, 5109 (1998).

[45] C. Pethick and H. Smith, *Bose-Einstein Condensation in Dilute Gases* (Cambridge University Press, Cambridge, UK, 2002).

[46] C. C. Bradley, C. A. Sackett, and R. G. Hulet, "Bose-Einstein Condensation of Lithium: Observation of Limited Condensate Number", *Phys. Rev. Lett.* **78**, 985 (1997).

[47] H. Stoof, "Atomic Bose gas with a negative scattering length", *Phys. Rev. A* **49**, 3824 (1994).

[48] W. Krauth, "Quantum Monte Carlo Calculations for a Large Number of Bosons in a Harmonic Trap", *Phys. Rev. Lett.* **77**, 3695 (1996).

[49] G. Baym, J.-P. Blaizot, M. Holzmann, F. Laloë, and D. Vautherin, "The transition temperature of the dilute interacting Bose gas", *Phys. Rev. Lett.* **83**, 1703 (1999).

[50] M. Holzmann, G. Baym, J.-P. Blaizot, and F. Laloë, "Nonanalytic dependence of the transition temperature of the homogeneous dilute Bose gas on scattering length", *Phys. Rev. Lett.* **87**, 120403 (2001).

[51] S. Giorgini, L. P. Pitaevskii, and S. Stringari, "Condensate fraction and critical temperature of a trapped interacting Bose gas", *Phys. Rev. A* **54**, R4633 (1996).

[52] S. Giorgini, L. P. Pitaevskii, and S. Stringari, "Thermodynamics of a trapped Bose-condensed gas", *J. Low Temp. Phys.* **109**, 309 (1997).

[53] S. Giorgini, L. P. Pitaevskii, and S. Stringari, "Scaling and thermodynamics of a trapped Bose-Condensed gas", *Phys. Rev. Lett.* **78**, 3987 (1997).

[54] M.-O. Mewes, M. R. Andrews, N. J. van Druten, D. M. Kurn, D. S. Durfee, and W. Ketterle, "Bose-Einstein condensation in a tightly confining dc magnetic trap", *Phys. Rev. Lett.* **77**, 416 (1996).

[55] D. J. Han, R. H. Wynar, P. Courteille, and D. J. Heinzen, "Bose-Einstein condensation of large number of atoms in a magnetic time-averaged orbiting potential", *Phys. Rev. A* **57**, R4114 (1998).

[56] O. Maragò, G. Hechenblaikner, E. Hodby, and C. Foot, "Temperature dependence of damping and frequency shifts of the scissors mode of a trapped Bose-Einstein condensate", *Phys. Rev. Lett.* **86**, 3938 (2001).

[57] F. Schreck, L. Khaykovich, K. L. Corwin, G. Ferrari, T. Bourdel, J. Cubizolles, and C. Salomon, "Quasipure Bose-Einstein Condensate Immersed in a Fermi Sea", *Phys. Rev. Lett.* **87**, 080403 (2001).

[58] J. R. Ensher, D. S. Jin, M. R. Matthews, C. E. Wieman, and E. A. Cornell, "Bose-Einstein condensation in a dilute gas: Measurement of energy and ground-state occupation", *Phys. Rev. Lett.* **77**, 4984 (1996).

[59] F. Gerbier, J. H. Thywissen, S. Richard, M. Hugbart, P. Bouyer, and A. Aspect, "Critical Temperature of a Trapped, Weakly Interacting Bose Gas", *Phys. Rev. Lett.* **92**, 030405 (2004).

[60] F. Gerbier, *Condensat de Bose-Einstein dans un piège anisotrope*, Thèse de doctorat, Université Paris VI, 2003, available at http://tel.ccsd.cnrs.fr.

[61] G. Woestenenk, *Photoassociation of Cold Metastable Helium Atoms*, Ph.d. thesis, Universiteit Utrecht, 2001.

[62] J. Léonard, *Photo-association de l'hélium métastable au voisinage de la condensation de Bose-Einstein et formation de dimères géants*, Thèse de doctorat, Université Paris VI, 2003, available at http://tel.ccsd.cnrs.fr.

[63] J. Weiner, V. S. Bagnato, S. Zilio, and P. S. Julienne, "Experiments and theory in cold and ultracold collisions", *Rev. Mod. Phys.* **71**, 1 (1999).

[64] N. Vanhaecke, *Molécules froides : formation, piégeage et spectroscopie*, Thèse de doctorat, Ecole polytechnique, 2003, available at http://tel.ccsd.cnrs.fr.

[65] Sakurai, *Modern Quantum Mechanics* (Addison-Wesley, New York, 1994).

[66] L. D. Landau and E. M. Lifshitz, *Theoretical Physics, Quantum mechanics* (Edition Mir, Moscou, 1988), Vol. 3.

[67] E. R. I. Abraham, W. I. McAlexander, C. A. Sackett, and R. G. Hulet, "Spectroscopic Determination of the s-Wave Scattering Length of Lithium", *Phys. Rev. Lett.* **74**, 1315 (1995).

[68] J. Stärck and W. Meyer, "Long-range interaction potential of the $^5\Sigma_g^+$ state of He_2", *Chemical Physics Letters* **225**, 229 (1994).

[69] V. Venturi and I. B. Whittingham, "Close-coupled calculation of field-free collisions of cold metastable helium atoms", *Phys. Rev. A* **61**, 060703 (2000).

[70] F. X. Gadea, T. Leininger, and A. S. Dickinson, "Calculated scattering length for spin-polarized metastable helium", *Journal of Chemical Physics* **117**, 7122 (2002).

[71] A. S. Dickinson, F. X. Gadea, and T. Leininger, "Scattering length for spin-polarized metastable helium-3 and helium-4", *J. Phys. B: At. Mol. Opt. Phys.* **37**, 587 (2004).

[72] N. Herschbach, P. J. J. Tol, W. Vassen, W. Hogervorst, G. Woestenenk, J. W. Thomsen, P. van der Straten, and A. Niehaus, "Photoassociation Spectroscopy of Cold He(2^3S) Atoms", *Phys. Rev. Lett.* **84**, 1874 (2000).

[73] P. J. J. Tol, W. Hogervorst, and W. Vassen, "Theory of evaporative cooling with energy-dependent elastic scattering cross section and application to metastable helium", *Phys. Rev. A* **70**, 013404 (2004).

[74] H. L. Anderson, *Physics Vade Mecum : A physicist's desk reference* (American Institute of Physics, 1989).

[75] F. Penning, *Naturwissenschaften* **15**, 818 (1927).

[76] F. Bardou, O. Emile, J.-M. Courty, C. I. Westbrook, and A. Aspect, "Magneto-optical Trapping of Metastable Helium: Collisions in the Presence of Resonant Light.", *Europhys. Lett.* **20**, 681 (1992).

[77] H. Mastwijk, *Cold Collisions of Metastable Helium Atoms*, Ph.d. thesis, Universiteit Utrecht, 1997.

[78] M. W. Müller, A. Merz, M.-W. Ruf, H. Hotop, W. Meyer, and M. Movre, "Experimental and theoretical studies of the Bi-excited collision systems $He^*(2\,^3S) + He^*(2\,^3S, 2\,^1S)$ at thermal and subthermal kinetic energies", *Z. Phys. D Atoms, Molecules and Clusters* **21**, 89 (1991).

[79] P. O. Fedichev, M. W. Reynolds, U. M. Rahmanov, and G. V. Shlyapnikov, "Inelastic decay processes in a gas of spin-polarized triplet helium", *Phys. Rev. A* **53**, 1447 (1996).

[80] G. S. Shlyapnikov, J. T. M. Walraven, U. M. Rahmanov, and M. W. Reynolds, "Decay Kinetics and Bose Condensation in a Gas of Spin-Polarized Triplet Helium", *Phys. Rev. Lett.* **73**, 3247 (1994).

[81] V. Venturi, I. B. Whittingham, P. J. Leo, and G. Peach, "Close-coupled calculation of collisions of magnetostatically trapped helium atoms", *Phys. Rev. A* **60**, 4635 (1999).

[82] P. S. Julienne and F. H. Mies, "Collisions of ultracold trapped atoms", *J. Opt. Soc. Am. B* **6**, 2257 (1989).

[83] H. C. Mastwijk, J. W. Thomsen, P. van der Straten, and A. Niehaus, "Optical Collisions of Cold Metastable Helium Atoms", *Phys. Rev. Lett.* **80**, 5516 (1999).

[84] H. C. Mastwijk, M. van Rijnbach, J. W. Thomsen, P. van der Straten, and A. Niehaus, "Photo-induced collisions with laser cooled He^* atoms", *Eur. Phys. J. D.* **4**, 131 (1998).

[85] M. Kumakura and N. Morita, "Laser Trapping of Metastable ^{3}He Atoms: Isotopic Difference in Cold Penning Collisions", *Phys. Rev. Lett.* **82**, 2848 (1999).

[86] P. J. J. Tol, N. Herschbach, E. A. Hessels, W. Hogervorst, and W. Vassen, "Large numbers of cold metastable helium atoms in a magneto-optical trap", *Phys. Rev. A* **60**, R761 (1999).

[87] A. Browaeys, J. Poupard, A. Robert, S. Nowak, W. Rooijakkers, E. Arimondo, L. Marcassa, D. Boiron, C. I. Westbrook, and A. Aspect, "Two body loss rate in a magneto-optical trap of metastable He", *Eur. Phys. J. D.* **8**, 199 (2000).

[88] P. O. Fedichev, M. W. Reynolds, and G. V. Shlyapnikov, "Three-Body Recombination of Ultracold Atoms to a Weakly Bound s Level", *Phys. Rev. Lett.* **77**, 2921 (1996).

[89] Y. Castin, in *Coherent atomic matter waves, Lecture Notes of Les Houches Summer School*, edited by R. Kaiser, C. Westbrook, and F. David (EDP Sciences and Springer-Verlag, 2000), p. 1, e-print cond-mat/0105058.

[90] in *Proceedings of the International School of Physics - Enrico Fermi*, edited by M. Inguscio, S. Stringari, and C. Wieman (IOS Press, 1999).

[91] R. Kaiser, *Manipulation par laser d'hélium métastable : effet Hanle mécanique, refroidissement sous le recul d'un photon*, Thèse de doctorat, Université de Paris VI, 1990.

[92] G. Labeyrie, *Deux outils pour l'optique atomique : Jet intense d'hélium métastable et Miroir à onde évanescente exaltée*, Thèse de doctorat, Université de Paris XI, 1998.

[93] N. Vansteenkiste, C. Gerz, R. Kaiser, L. Hollberg, C. Salomon, and A. Aspect, "A frequency-stabilized LNA laser at 1.083 μm : application to the manipulation of helium 4 atoms", *J. Phys. II France* **1**, 1407 (1991).

[94] W. Rooijakkers, W. Hogervorst, and W. Vassen, "Laser deceleration and trapping of metastable helium atoms", *Opt. Commun.* **135**, 149 (1997).

[95] J. Nellessen, J. H. Müller, K. Sengstock, and W. Ertmer, "Large-angle deflection of a laser-cooled sodium beam", *J. Opt. Soc. Am. B* **6**, 2149 (1989).

[96] W. D. Phillips, "Laser cooling and trapping of neutral atoms", *Rev. Mod. Phys.* **70**, (1998).

[97] E. Raab, M. Prentiss, A. Cable, S. Chu, and D. Pritchard, "Trapping of Neutral Sodium Atoms with Radiation Pressure", *Phys. Rev. Lett.* **59**, 2631 (1987).

[98] P. Lett, W. Phillips, S. Rolston, C. Tanner, R. Watts, and C. Westbrook, "Optical molasses", *J. Opt. Soc. Am. B* **6**, 2084 (1989).

[99] F. Pereira Dos Santos, F. Perales, J. Léonard, A. Sinatra, J. Wang, F. S. Pavone, E. Rasel, C. S. Unnikrishnan, and M. Leduc, "Production of a Bose-Einstein Condensate of Metastable Helium atoms", *Eur. Phys. J. D* **14**, 15 (2002).

[100] M. O. Mewes, M. R. Andrews, N. J. V. Druten, D. M. Kurn, D. S. Durfee, C. G. Townsen, and W. Ketterle, "Collective excitations of a Bose-Einstein condensate in a magnetic trap", *Phys. Rev. Lett.* **77**, 988 (1996).

[101] W. Petrich, M. H. Anderson, J. R. Ensher, and E. A. Cornell, "Stable, Tightly Confining Magnetic Trap for Evaporative Cooling of Neutral Atoms", *Phys. Rev. Lett.* **74**, 3352 (1995).

[102] J. Wiza, "Microchanel plate detectors", *Nucl. Instr. and Meth.* **162**, 587 (1979).

[103] R. Gao, P. Gibner, J. Newman, K. Smith, and R. Stebbings, "Absolute and angular efficiencies of a microchanel-plate position-sensitive detector", *Rev. Sci. Instrum.* **55**, 1756 (1984).

[104] B. Deconihout, P. Gerard, M. Bouet, and A. Bostel, "Improvement of the detection efficiency of chanel plate electron multiplier for atom probe application", *Appl. Surf. Sci.* **94/95**, 422 (1996).

[105] *MCP assembly* (Hamamatsu, 1994).

[106] J. Oberheide, P. Wilhelms, and M. Zimmer, "New results on the absolute ion detection efficiencies of a microchannel plate", *Meas. Sci. Technol.* **8**, 351 (1997).

[107] T. Guénault, *Statistical Physics* (Chapman & Hall, London, 1995).

[108] M. Kasevich, D. S. Weiss, E. Riis, K. Moler, S. Kasapi, and S. Chu, "Atomic velocity selection using stimulated Raman transitions", *Phys. Rev. Lett.* **66**, 2297 (1991).

[109] H. J. Lee, C. S. Adams, M. Kasevich, and S. Chu, "Raman Cooling of Atoms in an Optical Dipole Trap", *Phys. Rev. Lett.* **76**, 2658 (1996).

[110] H.-J. Miesner, D. M. Stamper-Kurn, M. R. Andrews, D. S. Durfee, S. Inouye, and W. Ketterle, "Bosonic stimulation in the formation of a Bose-Einstein condensate", *Science* **279**, 1005 (1998).

[111] I. Schvarchuck, C. Buggle, D. S. Petrov, K. Dieckmann, M. Zielonkowski, M. Kemmann, T. Tiecke, W. Von Klitzing, G. V. Shlyapnikov, and J. Walraven, "Bose-Einstein condensation in non-equilibrium states studied by condensate focusing", *Phys. Rev. Lett.* **89**, 270404 (2002).

[112] M. Köhl, M. J. Davis, C. W. Gardiner, T. W. Hänsch, and T. Esslinger, "Growth of Bose-Einstein condensates from thermal vapor", *Phys. Rev. Lett.* **88**, 080402 (2002).

[113] P. Spoden, *Stoßwechselwirkungen in einem kalten Gas metastabiler Neonatome*, Ph.d. thesis, Universitât Hannover, 2004.

[114] Y. Kagan, B. V. Svistunov, and G. V. Shlyapnikov, "Effect of Bose condensation on inelastic processes in gases", *Sov. Phys. JETP Lett.* **42**, 209 (1985).

[115] E. W. Hagley, L. Deng, M. Kozuma, J. Wen, K. Helmerson, S. L. Rolston, and W. D. Phillips, "A well-collimated quasi-continuous atom laser", *Science* **283**, 1706 (1999).

[116] P. J. Leo, V. Venturi, I. B. Whittingham, and J. Babb, "Ultracold collisions of metastable helium atoms", *Phys. Rev. A* **64**, 42710 (2002).

[117] P. Arnold and B. Tomàšik, "T_C for trapped dilute Bose gases: A second-order result", *Phys. Rev. A* **64**, 053609 (2001).

[118] P. Pedri, D. Guéry-Odelin, and S. Stringari, "Dynamics of a classical gas including dissipative and mean-field effects", *Phys. Rev. A* **68**, 043608 (2003).

[119] R. J. W. Stas, J. M. McNamara, W. Hogervorst, , and W. Vassen, "Simultaneous Magneto-Optical Trapping of a Boson-Fermion Mixture of Metastable Helium Atoms", *Phys. Rev. Lett.* **93**, 053001 (2004).

[120] K. Mølmer, "Bose Condensates and Fermi Gases at Zero Temperature", *Phys. Rev. Lett.* **80**, 1804 (1998).

[121] P. Capuzzi and E. S. Hernández, "Phase separation and response of ^{3}He-^{4}He mixtures within a magnetic trap", *Phys. Rev. Lett.* **66**, 035602 (2002).

[122] R. Hanbury-Brown and R. Q. Twiss, *Nature* **177**, 27 (1956).

[123] L. Mandel and E. Wolf, *Optical coherence and quantum optics* (Cambridge University Press, Cambridge, MA, 1990).

[124] M. Yasuda and F. Shimizu, "Observation of two-atom correlation of an ultracold neon atomic beam", *Phys. Rev. Lett.* **77**, 3090 (1996).

[125] E. A. Burt, R. W. Ghrist, C. J. Myatt, M. J. Holland, E. A. Cornell, and C. E. Wieman, "Coherence, correlations, and collisions: What one learns about Bose-Einstein condensates from their decay", *Phys. Rev. Lett.* **79**, 337 (1997).

[126] A. S. Tychkov, J. C. J. Koelemeij, T. Jeltes, W. Hogervorst, and W. Vassen, "Two-color magneto-optical trap for metastable helium", *Phys. Rev. A* **69**, 055401 (2004).

[127] M. R. Spiegel, *Shaum's outline series: Mathematical handbook of formulas and tables* (McGraw-Hill, United States of America, 1968).

[128] M. Naraschewski and R. J. Glauber, "Spatial coherence and density correlations of trapped Bose gases", *Phys. Rev. A* **59**, 4595 (1999).

[129] D. Guéry-Odelin, "Mean-field effects in a trapped gas", *Phys. Rev. A* **66**, 033613 (2002).

[130] D. Guéry-Odelin, F. Zambelli, S. Stringari, and J. Dalibard, "Collective oscillations of a classical gas in a harmonic trap", *Phys. Rev. A* **60**, 4851 (1999).

[131] G. M. Kavoulakis, C. J. Pethick, and H. Smith, "Collisional relaxation in difuse clouds of trapped bosons", *Phys. Rev. A* **61**, 053603 (2001).

Résumé

Cette thèse présente des résultats obtenus par des méthodes originales sur les nuages d'atomes ultra-froids au voisinage de la condensation de Bose-Einstein. Les atomes qui constituent les nuages utilisés dans ces expériences sont particuliers du fait de leur métastabilité. Plus précisément, ce sont des atomes d'hélium métastable. Grâce à l'énergie interne qu'ils possèdent, ces atomes peuvent être détectés électroniquement de façon efficace par une galette de micro-canaux. L'utilisation de l'hélium métastable pour l'étude de la dégénérescence quantique est également particulière du fait de la présence de collisions ionisantes au sein de l'échantillon atomique. Les ions He+ créés lors d'une collision inélastique peuvent être détectés "en temps réel", ce qui constitue un diagnostic nouveau et intéressant. En particulier, il est possible d'identifier très précisément le seuil de condensation de Bose-Einstein, c'est-à-dire le moment où commencent à s'accumuler les atomes dans l'état quantique fondamental. L'avantage d'utiliser le taux d'ions comme outil d'observation est sa nature "non-invasive". Contrairement à la technique d'observation habituelle qui exige que les atomes soient lâchés du piège pour permettre leur observation, la mesure du taux d'ions produits par l'échantillon ne change en rien le comportement naturel du nuage. En utilisant cette méthode de diagnostic originale, une mesure des paramètres collisionnels régissant le comportement du nuage a été obtenue : constantes de collisions ionisantes et longueur de diffusion de l'atome d'hélium métastable.

Mots-clés

Hélium métastable - Atomes froids - Condensation de Bose-Einstein - Seuil de condensation - Galette de micro-canaux - Collisions Penning - Collisions élastiques - Longueur de diffusion.

Abstract

This thesis presents an experimental study of an atomic cloud in the vicinity of Bose-Einstein condensation. The atoms used in our experiment are special in the sense that they are metastable – we use metastable helium. The metastability opens the door for using new and original detection methods. Due to their internal energy, the atoms can be detected electronically by means of a micro-channel plate. The use of metastable helium is also interesting due of the presence of ionizing collisions in the sample. The He+ ions produced in collisions between the metastable atoms can be detected in real-time, and the ion signal constitutes an alternative and useful diagnostic. In particular, this signal allows one to identify very precisely the Bose-Einstein condensation threshold. One of the advantages of using this signal to probe the cloud, is its "non-invasive" nature: observing the ions does not at all alter the natural evolution of the cloud, in contrast to the ordinary detection technique which consists of releasing the atoms from the trap and then imaging the cloud. In this thesis, by using the new diagnostics based on the ion signal, we have measured some important parameters governing the collisions, and thereby the behavior of the cloud: the ionizing rate constants and the scattering length.

Mots-clés

Metastable helium - Cold Atoms - Bose-Einstein condensation - Condensation threshold - Micro-channel plate - Penning collisions - Elastic collisions - Scattering length.